The permeation and moisture transmission properties of a thermosensitive membrane barrier for chemical protective clothing

Phannaphat Phromphen

Submitted in accordance with the requirements for the degree of
Doctor of Philosophy

The University of Leeds
School of Design
August 2015

The candidate confirms that the work submitted is her own, except where work which has formed part of jointly authored publications has been included. The contribution of the candidate and the other authors to this work has been explicitly indicated below. The candidate confirms that appropriate credit has been given within the thesis where reference has been made to the work of others.

Publication title: Liquid permeation and water vapour transmission properties of a temperature-sensitive NIPAAM-g-PVDF barrier membrane.
Authors: Phannaphat Phromphen, Ningtao Mao, Stephen J. Russell, and Parikshit Goswami
Conference title: 15thAUTEX World Textile Conference 2015
Relevant chapter: Chapter 4 and 7
Co-author contributions: Advisory

Acknowledgements

This work would not have been possible without the support of The Royal Thai Government. I would like to thank you **Dr Ningtao Mao** who supervised, guided and encouraged me in doing this research and **Dr Parikshit Goswami** who gave me useful comments on chemistry subject.

Special thanks to **DuPont Company** and **Microgard Company** for providing the commercial chemical protective clothing.

I also would like to thank to **Dr Jianguo Qu** and other colleagues in the performance textiles and clothing research group for the great help in the experiments, **Mr. Leslie Johnson** for all his helps in the experimental set up and the training session, **Dr Carlos Grattoni** for the mercury porosimetry testing, **Ms. Susanne Patel** for the BET testing, **Mr. Simon A. Barrett** the NMR testing and **Mr. John Harrington** and **Dr Algy Kazlauciunas** for the SEM images and elemental analysis.

Thank you to my family for being so supportive and for convincing me no matter what. Thank you all my friends in Thailand for the encouragement and special thanks to all the friends I've made in Leeds. It is great to have another place which I feel like home.

Abstract

The liquid chemical permeation properties and water vapour transmission properties of temperature sensitive poly(vinylidene fluoride) (PVDF) grafted N-isopropylacrylamide (NIPAAM) (NIPAAM-g-PVDF) copolymer membranes as a smart barrier layer in chemical protective clothing are studied in this research. Both modified thermally induced method and modified plasma induced method are employed to oxidise PVDF polymer for its copolymerisation with NIPAAM monomers.

In the thermal induced method, NIPAAM-g-PVDF polymer materials are synthesised via the copolymerisation of ozone activated PVDF polymer with NIPAAM monomers below a lower critical solution temperature of NIPAAM (30°C). An effective supercritical carbon dioxide drying method is used as an alternative drying method to remove the solvent from the ozone activated PVDF polymer in conventionally copolymerisation is successfully applied and a new direct copolymerisation route by adding NIPAAM polymer into ozone activated PVDF in solutions without the drying process of the activated PVDF polymers. The NIPAAM-g-PVDF made by the new copolymerisation process is much simpler than the conventional method and the processing time needed is much shorter.

In the oxygen plasma induced copolymerisation method, the porous PVDF membranes produced from the phase inversion method are treated oxygen plasma before they were copolymerised with NIPAAM monomer in N,N-dimethylformamide (DMF) solvent aqueous solution below the lower critical solution temperature of NIPAAM (30°C).

The structural characteristics of heat-pressed NIPAAM-g-PVDF nanoporous membranes produced from the above two methods are investigated. The influence of the microstructure of the nanoporous copolymer membranes on both their water vapour transfer properties and dynamic permeation rate has been studied. The mechanisms of liquid/vapour permeation through the thermal sensitive copolymer nanoporous membranes are analysed and investigated.

In this study, it is found that the breakthrough time and permeation rate of nanoporous NIPAAM-g-PVDF membranes are influenced by the proportion of NIPAAM components, the membrane thickness, the crystallinity and the porous structure of the NIPAAM-g-PVDF membranes.

It is also found that the water vapour permeability of the heat-pressed NIPAAM-g-PVDF membranes at both 20°C and 40°C are influenced by the membrane thickness, the total pore volume and the porosity of the membranes. The water vapour permeability coefficient of the NIPAAM-g-PVDF nanoporous membranes is determined by both the proportion of thermal sensitive NIPAAM components and associated porous structure of the copolymer membranes.

Table of Contents

List of Figures

List of Tables

Symbols and notations

A	.....	Surface area of sample (m^2)
a_1	.....	Fractional surface areas occupied by material and air in a plane unit area
A_φ	.....	Area of the fabric specimen contacted with chemical challenge agent (cm^2)
ATR-FTIR	.....	Attenuated total reflectance- Fourier transform infrared spectroscopy
B	.....	A constant in solubility of permeant in membrane equation
BET	.....	Brunauer-Emmett-Teller
BS	.....	British standards
C	.....	Concentration gradient across the membrane (mg cm^{-3})
c	.....	A constant related to the difference between the molar free energy of adsorption of the first layer and the liquefaction one.
C_0	.....	Water vapour concentration of the bottom outgoing stream (kg m^{-3})
C_1	.....	Water vapour concentration of the bottom incoming stream (kg m^{-3})
C_f	.....	Convective heat change in Fanger's equation
c_i	.....	Concentration of test chemical in collection medium (µg dm^{-3})
Cs	.....	Steady-state concentration of permeant in collection medium
CuCl	.....	Copper(I)chloride
$CuCl_2$	.....	Copper(II)chloride
D	.....	Diffusion coefficient (cm^2 min^{-1})
d_0	.....	Average pore diameters before grafting NIPAAM (nm)

δ^2 ..... Hansen 3-D solubility parameter

D_a ..... Fabric porosity

δ_d ..... Dispersion solubility parameters ($cal^{-1/2}$ $cm^{-3/2}$)

D_f ..... Dispersion force between solvent molecules and polymer

d_g ..... Average pore diameters after grafting NIPAAM (nm)

δ_η ..... Hydrogen-bonding solubility parameters ($cal^{-1/2}$ $cm^{-3/2}$)

ΔH ..... Enthalpy change of the unknown specimen

ΔHa ..... Enthalpy change of the pure amorphous standard

ΔHc ..... Enthalpy change of the pure crystalline standard

DMF ..... N,N-dimethylformamide

D_∞ ..... Bulk diffusivity of the fluid depending on the temperature

D_{NIPAAM} ..... Diffusivity of NIPAAM (cm^2 s^{-1})

$D_{NIPAAM\text{-}hexane}$ ..... Diffusivity of NIPAAM in n-hexane (cm^2 s^{-1})

δ_p ..... Polar solubility parameters ($cal^{-1/2}$ $cm^{-3/2}$)

dP ..... Differential pressure along the conduit length (Pa)

DPPH 2,2-diphenyl-1-picrylhydrazyl

D_{PVDF} ..... Diffusivity coefficient of PVDF (cm^2 s^{-1})

$D_{PVDF\text{-}hexane}$ ..... Diffusivity of PVDF in hexane (cm^2 s^{-1})

DSC	.....	Differential scanning calorimetry
ΔP_{hexane}	.....	Pressure of n-hexane between two sides of the membrane
ΔP_{wv}	.....	Water vapour pressure differences between two sides of the membrane (Pa)
ΔT	.....	Temperature difference between two sides of fabric (K)
ε	.....	Porosity (%)
E_f	.....	Evaporative heat loss in Fanger's equation
EN	.....	European standards
E_p	.....	Energy of activation for permeation (kJ mol^{-1})
E_{sk}	.....	Evaporative heat exchange (W m^{-2})
F	.....	A pore filling ratio
FESEM	.....	Field emission scanning electron microscopy
G	.....	Weight change (g)
γ_{Hg}	.....	surface tension of mercury (0.48 N m^{-1})
GC	.....	Gas chromatography
GCMS	.....	Gas chromatography mass spectroscopy
γ_{LV}	.....	Interfacial tension that exists between liquid and vapour
γ_{SL}	.....	Interfacial tension that exists between solid and liquid
γ_{SV}	.....	Interfacial tension that exists between solid and vapour

η ..... viscosity of the water vapour (Pa s)

H_{tf} ..... Heat transfer between the clothing surface and the environment by conduction, convection, and radiation (W m^{-2})

H_f ..... Hydrogen force between solvent molecules and polymer

i ..... An indexing number to indicate the specific concentration c_i that was measured at time t_i

ISO ..... International organization for standardization

J_0 ..... Constant factor

J_D ..... Diffusion flux (mg cm^{-2} min^{-1})

φ_i ..... Dynamic permeation rate at time t_i, (µg cm^{-2} min^{-1})

J_p ..... Permeability coefficient (µg mm^{-1} cm^{-2} min^{-1})

J_{NIPAAM} ..... water permeability coefficient through the NIPAAM component of the membrane (cm^3 cm^{-2} s^{-1} $(Pa/cm)^{-1}$)

Jpore ..... water permeability coefficient through the pores in the membrane (cm^3 cm^{-2} s^{-1} $(Pa/cm)^{-1}$)

J_{PVDF} ..... Water vapour permeability coefficient through the PVDF component (cm^3 cm^{-2} s^{-1} $(Pa/cm)^{-1}$)

J_s ..... Steady-state permeation rate (µg cm^{-2} min^{-1})

J_{total} ..... Permeation coefficient of water vapour permeation through of membrane (cm^3 cm^{-2} s^{-1} $(Pa/cm)^{-1}$)

$J_{total\text{-}hexane}$ ..... Total permeation of n-hexane transport through the membrane (cm^3 cm^{-2} s^{-1} $(Pa/cm)^{-1}$)

K ..... Specific permeability (m^2)

K_{20} ..... Specific permeability at 20°C

K_{40} ..... Specific permeability at 40°C

k	.....	Thermal conductivity of material (W m^{-1} K^{-1})
KBr-FTIR	.....	Potassium Bromide- Fourier transform infrared spectroscopy
K_f	.....	Conductive heat change in Fanger's equation
K_{eff}	.....	A hydrodynamic factor due to the surface interaction between the pore wall and the fluid.
λ	.....	Ratio of the diameters of the fluid molecules to the diameter of the pores
L	.....	Thickness of membrane (mm)
LCST	.....	A lower critical solution temperature
m	.....	weight of effective PVDF (g)
M_0	.....	Mass of the membrane before conditioning
M_1	.....	Mass of the membrane after conditioning
MD	.....	Machine direction
M_f	.....	Metabolic rate in Fanger's equation
MVA	.....	Moisture vapour absorbency
N/A	.....	Not Applicable
N/C	.....	Not calculation because other values are infinity
N/F	.....	No formation of molten droplets, burning does not continue
NFPA	.....	National fire protection association
NIPAAM	.....	N-isopropylacrylamide

NMP ..... N,N-dimethylformamide

NMR ..... Nuclear magnetic resonance spectroscopy

OSHA ..... Occupational safety and health administration

Φ ..... Partition coefficient caused by steric restriction

P_{Hg} ..... An external pressure applied on mercury flow (bar)

P ..... Permeability coefficient (mg mm cm^{-2} min^{-1})

$\frac{P}{P_0}$ ..... Gas pressure relative to its saturation pressure (Pa)

p_{air} ..... Saturation water vapour partial pressure of the air in the test enclosure (Pa)

p_a ..... Ambient water vapour pressure (kPa)

PBS ..... Phosphate buffered saline

PEG ..... Polyethylene glycol

PET ..... Polyethylene

P_f ..... Polar force between solvent molecules and polymer

P_{df} ..... Water vapour diffusivity of air

PID ..... Photo Ionization Detector

PPE ..... Personal protective equipment

p_s ..... Saturation water vapour partial pressure at the surface of the measuring unit (Pa)

p_{sk} ..... Skin water vapour pressure (kPa)

PTFE	.....	Polytetrafluoroethylene
PU	.....	Polyurethane
PVC	.....	Polyvinyl chloride
PVDC	.....	Polyvinylidene chloride
PVDF	.....	poly(vinylidene fluoride)
θ	.....	Equilibrium contact angle
q	.....	Heat flux flow through textile fabric per unit area (J s^{-1})
Q	.....	Volumetric flow rate (m^3 s^{-1})
$Q_{J_{NIPAAM}+J_{total}}$	.....	The percentage of water permeability coefficient through the pores and the water permeability coefficient through the NIPAAM component of the membrane
θ_{Hg}	.....	Contact angle between mercury and the membrane specimen, (~141.3°)
Q_s	.....	Volumetric flow rate of the fluid flow through a unit cross-section area in the porous structure (m^3 s^{-1})
Q_{steady}	.....	Supplied steady state heating power (W)
q_v	.....	Flow rate of fresh collection medium through the cell (dm^3 min^{-1})
θ_ω	.....	Thermodynamic contact angle on a smooth surface of material
R	.....	Ideal gas constant
R^2	.....	Coefficient of determination
ρ	.....	Bulk density of the fabric (kg m^{-3})
R_b	.....	Boundary air layer thermal resistance at clothing surface (m^2 °C W^{-1})

R_{ct} ..... Fabric thermal resistance (m^2 °C W^{-1}) l_{cl}

R_{ct0} ..... Apparatus constant for measurement of thermal resistance ($m^2 \cdot K \cdot W^{-1}$)

R_{et} ..... Evaporative resistance of clothing and the boundary air layer (kPa m^2 W^{-1})

R_{et0} ..... Apparatus constant of water-vapour resistance of bare plate (m^2 Pa W^{-1})

R_f ..... Radiative heat change in Fanger's equation

RH ..... Relative humidity (%)

R_{hexane} ..... Dynamic permeation rate of the membranes

$R_{J_{NIPAAM}+J_{Pore}}$ ..... Ratio of J_{NIPAAM}+ J_{pore} between 20°C and 40°C

r_p ..... An inner radius of a cylindrical pore (nm)

ρ_σ ..... True density of the fabric (kg m^{-3})

$R_{J_{total}}$ ..... Ratio of the total of water vapour permeability through the membrane between 20°C and 40°C

r_w ..... Roughness factor

ρ_{wv} ..... Density of water vapour (g cm^{-3})

R_{WVTR} ..... Ratio of water vapour transmission rate between 40°C and 20°C

S ..... Solubility coefficient (cm^3)

sccm ..... Standard cubic centimetres per minute

SEM ..... Scanning electron microscopy

S_f ..... Heat storage in Fanger's equation

SGHP	.....	Sweating guarded hotplate method
S_{NIPAAM}	.....	Solubility of NIPAAM in water ($cm^3\ cm^{-3}\ Pa^{-1}$)
$S_{NIAAM\text{-}hexane}$	.....	Solubility of NIPAAM in n-hexane at 25°C ($cm^3\ cm^{-3}\ Pa^{-1}$)
Sp	.....	Solubility of a permeant in membrane ($kg\ m^{-3}$)
S_{PVDF}	.....	Solubility coefficient of PVDF in water ($cm^3\ cm^{-3}\ Pa^{-1}$)
$S_{PVDF\text{-}hexane}$	.....	Solubility of PVDF in hexane ($cm^3\ cm^{-3}\ Pa^{-1}$)
T_k	.....	An absolute temperature (K)
t	.....	Testing duration (hour)
T	.....	content of initiator brought about by a gram of ozone activated PVDF (mole of peroxide per gram of ozonized polymer)
T_a	.....	Temperature of air in the wind channel (°C) (T_a = 20°C)
t_{cl}	.....	Clothing surface temperature (°C)
t_i	.....	Time elapsed beginning with the initial chemical contact and end with the measurement of concentration c_i (minutes)
T_m	.....	Melting temperature (°C)
ToF-SIMS	.....	Time-of-flight secondary ion mass spectrometry
T_s	.....	Temperature of the skin model (°C)
t_{sk}	.....	Mean skin temperature (°C)
v	.....	Volume of adsorbed gas (cm^3)
V_0	.....	Volume of pore before grafting NIPAAM (cm^3)

VDF-TeFE	.....	Vinylidene fluoride–tetrafluoroethylene
VDF-TrFE	.....	Vinylidene fluoride–trifluoroethylene
V_g	.....	volume of grafted PNIPAAM polymer in the pore (cm^3)
v_m	.....	Volume of a monolayer of the gas (cm^3)
w	.....	Skin wettedness
w/w	.....	Weight by weight
W_0	.....	Weight of the membrane before grafting (g)
Wa_0	.....	Weight of assembled cup before test (g)
Wa_1	.....	Weight of assembled cup after test (g)
W_g	.....	Weight of the membrane after grafting (g)
$WVTR$	.....	Water vapour transmission rate ($g\ m^{-2}\ 24h^{-1}$)
X	.....	Proportions of in NIPAAM-g- PVDF membrane (%)
x	.....	Final DPPH concentration ($g\ dm^{-3}$)
x_0	.....	Initial DPPH concentration ($g\ dm^{-3}$)
x_1	.....	concentration of DPPH in solution ($g\ dm^{-3}$)
XD	.....	Cross-machine direction
X_p	.....	Polar bonding contribution to the solubility parameters of the membrane
XPS	.....	X-ray photoelectron spectroscopy

XRD	.....	X-Ray diffraction
Y	.....	Proportions of NIPAAM in NIPAAM-g-PVDF membrane (%)
Yg	.....	Grafting yield (%)
y_1	.....	Absorbance of ultraviolet-visible spectroscopy at 516 nm
Y_h	.....	Hydrogen bonding contribution to the solubility parameters of the membrane
Z_d	.....	Dispersive bonding contribution to solubility parameters of membrane
θ_{cb}	.....	Cassie-Baxter contact angle for a rough surface

Chapter 1 Introduction

1.1 Background

Chemical protective clothing is classified as one of the technical textile products which aim to provide functionality rather than aesthetical properties. Most of the chemical protective clothing are used by the industrious workers to protect themselves from hazardous chemicals. The products are especially used in the oil and gas industries, the construction and manufacturing industries as well as in pharmaceutical industries. Chemical protective clothing are mostly consumed in the developed countries specifically in the United States and the Nordic region [1]. Moreover, it has been forecasted the consumption of chemical protective clothing will increase at about 6.7% compound annual growth rate (CAGR) over the period of 2014-2019 [2].

In the past, the most important requirement of the chemical protective clothing has been used to efficiently protect workers working in hazardous chemical environments from harmful chemical exposure for certain amount of times or even for longer time. Prolonged chemical exposures and thermal stress problems are unavoidable to the workers working in most industries; therefore, it is necessary for researchers to continue improving the level of protection while balancing the comfort, functionality and other ergonomics aspects [3].

Despite protection, the chemical protective clothing in the modern days are expected to offer comfort, neatness, inspiration, and motivation to the workers. The clothing are also expected to reinforce the team spirit among the workers and play the part of the company's image as well as shaping its external perception. If well engineered, the chemical protective clothing may influence the worker's better working mood, and possibly higher concentration with safer and faster reactions towards hazardous tasks [4].

1.2 Purpose of the research

The purpose of this research is to develop a smart barrier membrane to be used as a protection layer in chemical protective clothing while improving the moisture management property of the membrane in order to provide improved thermal comfort performance to the wearer of the chemical protective clothing.

1.3 Scope of the research

The scope of this research is categorised into three parts as discussed below:

The first part of the research studies microstructures, liquid chemical permeation properties and the thermophysiological properties of some typical commercially available chemical protective fabrics in the market. The study would help to establish the requirements for the barrier membrane and to identify ways to improve thermophysiological properties of the barrier membrane while maintaining its chemical permeation properties.

The second part of the research involves preparing a prototype of the smart barrier membrane from thermo-responsive material. In this study, NIPAAM is proposed as the molecular formation of macroscopic aggregates due to a hydrophobic interaction among the collapsed polymer chains at the temperature around 32°C, this temperature is known as the lower critical solution temperature (LCST) [5]. Since its LCST value falls between human body temperature and the environmental temperature, it can therefore exhibit reversible swelling and shrinkage when the temperature changes. Applying NIPAAM on the fabric may therefore change the water vapour transmission rates and permeability [6]. For these reasons, NIPAAM is particularly suitable for the development of smart materials for clothing applications [7]. In this study, NIPAAM and PVDF are copolymerised by using the thermally induced graft copolymerisation method and the oxygen plasma induced copolymerisation method to synthesis NIPAAM-g-PVDF copolymers. These smart NIPAAM-g-PVDF copolymer barrier membranes could possibly change the water vapour permeability properties with change of environment or body temperature while maintaining the required liquid chemical permeation properties.

The third part of the research looks at the influence of heat-pressed processing on the microstructures of the heat-pressed NIPAAM-g-PVDF membranes, and the influences of the microstructure of the heat-pressed NIPAAM-g-PVDF membranes on their liquid chemical permeation properties. Furthermore, thermal sensitive water vapour transfer properties are also investigated in order to understand the mechanisms of liquid/vapour permeation through the smart copolymer barrier membranes.

Chapter 2 Literature review

This critical literature review covers state of the art research and product development in the barrier membrane of chemical protective clothing in relation to both its chemical protection and thermophysiological comfort properties, in order to:

1. Identify any gaps between the performance of existing chemical protective clothing products, and the methods for characterising the structures and properties of the barrier materials used in chemical protective clothing.

2. Identify the mechanism of the chemical protection and thermophysiological comfort properties of chemical protective clothing.

3. Identify potential methods for synthesis of a copolymer membrane for use as a smart barrier material in chemical protective clothing.

2.1 Chemical protective clothing

In Personal Protective Equipment at Work Regulations 1992 [8], personal protective equipment (PPE) is defined as all the equipment (including clothing affording protection against weather) which is intended to be worn or held by a person at work and which protects him/her against one or more risks to his/her health or safety and any addition or accessory designed to meet that objective. Chemical protective clothing is one type of PPEs and its purpose is "to shield or isolate individuals from the chemical, physical, and biological hazards that may be encountered during hazardous materials operations" [9].

2.1.1 Types of chemical protective clothing

Chemical protective clothing has wide applications in various industries (e.g., chemical engineering, agriculture, military, pharmaceutical, and healthcare industries) to protect the wearer from different forms of hazards (e.g., vapours, liquids, and particles). It is classified as four categories based on the capability of permeation of water vapour, chemical vapour, and chemical liquids/aerosols through the barrier materials used in the clothing. These classifications are: air-permeable materials, semi-permeable materials, selective permeable materials, and impermeable materials as illustrated in Figure 2.1 [10].

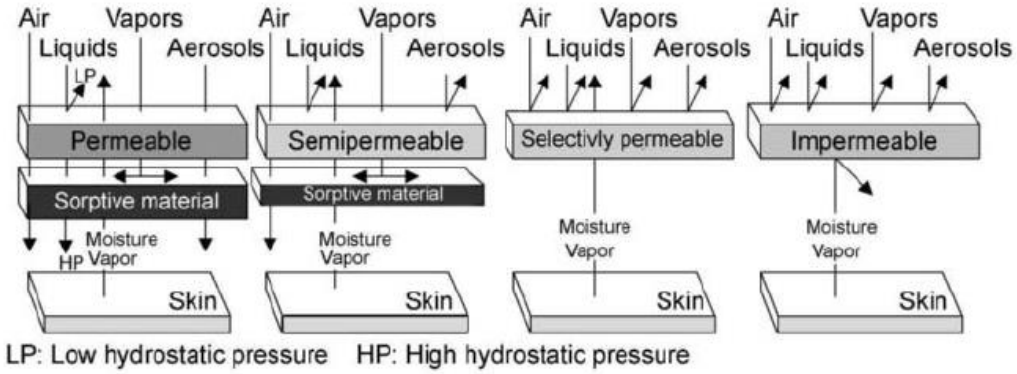

Figure 2.1 Types of chemical protective clothing [10]

However, in terms of the transport of moisture vapour from skin to the environment and the inhibition of aerosols and liquid chemicals, the semi-permeable materials and the selectively permeable materials are similar if the permeation of chemical vapour is not considered in this research. Therefore, barrier materials could be divided into three categories, i.e., air-permeable, semi-permeable, and impermeable materials.

2.1.1.1 Air-permeable barrier materials

Air-permeable barrier materials used in the outer shell layer of air-permeable chemical protective clothing products are usually heavy woven cotton or cotton/nylon mix fabrics, and are used as the repellent layer against liquid states [11]. The air-permeable barrier fabrics are usually used with a layer of sorptive material and a liner fabric in the protective clothing. The sorptive material, usually either an activated carbon layer or a charcoal layer, also plays a role as an additional protection layer to absorb the hazardous chemical liquids/aerosols and its vapour penetrated through the pores of the permeable barrier materials. At the same time, it allows heat, air, and water vapour exchange between the fabric and its environment [2]. The inner layer is used as a supportive layer of excess protection and comfort to the wearer. However, the chemical protective clothing products using the air-permeable barrier materials inherently bulky, and thus have greater thermal resistance properties [12].

2.1.1.2 Semi-permeable (selectively permeable) materials

A thin, lightweight, less bulky and flexible semi-permeable (selectively permeable) polymeric barrier membrane without using an activated carbon adsorptive layer is developed for some chemical protective clothing products. Based on a similar mechanism used in gas separation and reverse osmosis membranes, this type of membrane allows the selective permeation of water vapour while preventing the larger organic chemical molecules transport through the materials [13], [14]. Examples of

semi-permeable materials include hydrophilic polyurethane (PU) [15], polytetrafluoroethylene (PTFE), polyester, polyether, polyamide, polyacrylate, copolyether ester and copolyether amides [16].

2.1.1.3 Impermeable materials

Impermeable materials are the barrier against the penetration of chemical and biological agents in the form of liquid, vapour, and aerosol particles. Air and water vapour transport through impermeable fabric materials is also prohibited as the fabrics are coated or laminated by using butyl rubber, neoprene, and plastic film such as polyethylene (PET), chlorinated PET, PTFE, polyvinyl chloride (PVC), polyvinylidene chloride (PVDC). The impermeable barrier materials usually consist of fabrics made of PET, polyamide, cotton, as well as their blends; and the bicomponent coating/lamination constructions such as fluoroelastomer/butyl, fluoroelastomer/neoprene, PVDC/PET and neoprene/PVC [17]. The structure of one impermeable barrier fabric material from Microchem 4000 chemical protective clothing is shown in Figure 2.2 below [18].

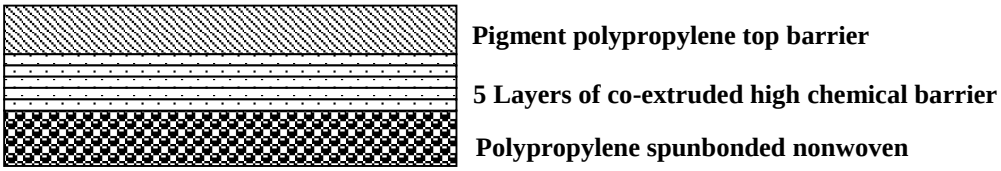

Figure 2.2 Microchem 4000 construction

2.1.2 Performance requirements of chemical protective clothing

Performance requirements of chemical protective clothing are legislated by laws and legislations which are based on many years' research in multiple disciplines. In the United States, the Occupational Safety and Health Administration (OSHA) mandate worker protection with a guideline for the selection of chemical protective clothing products in order to communicate the characteristics of their performance [19], and the National Fire Protection Association (NFPA) defined two performance requirements-based standards, NFPA 1991 and NFPA 1992, for chemical protective clothing uses during chemical emergency responses, both of which are explained below.

1. NFPA 1991 (Standard for vapour-protective ensembles for hazardous materials emergencies) require that the protective clothing shall be tested for their permeation resistance in accordance with ASTM F739-12 (Standard test method

for permeation of liquids and gases through protective clothing materials under conditions of continuous contact) [20] for at least a duration of 3 hours and the minimum detected permeation rate shall be less than or equal to 0.10 µg cm^{-2} min^{-1} for a list of designated chemicals [21].

2. NFPA 1992 (Standard for liquid splash-protection ensemble and clothing for hazardous materials emergencies) require that the chemical protective garment and items shall be tested for penetration resistance by ASTM F903-10 (standard test method for resistance of materials used in protective clothing to penetration by liquids: procedure C after flexing and abrasion) [22]. It shall exhibit no penetration for at least 1 hour for acetone, ethyl acetate, 50% w/w sodium hydroxide, 93.1% w/w sulphuric acid, and tetrahydrofuran or additional chemical or specific chemical mixture for which the manufacturer is certifying [23].

PPE in the European Union is governed by Directive 89/686/EEC, which is designed to ensure PPE meets common quality and safety standards by setting out their basic safety requirements as well as conditions for its placement on the market. PPE covers ‘any device or appliance designed to be worn or held by an individual for protection against one or more health and safety hazards [24]. The European Union has identified six levels of protection to facilitate the effective choice of chemical protective clothing [25], and the six types of chemical protective clothing are categorised as follows:

Type 1 (gas-tight chemical protective suits): The minimum requirement for chemical protective clothing which is suitable for emergency teams including component parts such as gloves and boots based on EN 943-1:2002 [26].

Type 2 (non-gas-tight chemical protective suits): Specify the minimum requirement for ventilated and non-ventilated, used and reusable chemical protective suits which meet the requirement of EN 943-1:2002.

Type 3 (liquid-tight clothing): According to EN 14605:2005 [8], the performance requirements for liquid-tight clothing, and the specific minimum requirement for full-body protective clothing or partial body protection garments offering protection against permeation of chemical liquids to specified parts of the body.

Type 4 (spray-tight clothing): As with type 3, EN 14605:2005, the performance requirements for liquid-tight clothing, the specific minimum requirement for full-

body protective clothing or partial body protection garments offering protection against permeation of chemical liquids to specified parts of the body.

Type 5 (chemical protective clothing resistant to penetration by air bone solid particles): Based on ISO 13982-1:2004 [27], this is the minimum requirement for full-body protection items including trunk, arms, and legs, with or without hoods, visors, and foot protection.

Type 6: Limited-performance, limited-use, and reusable materials used in case of potential exposure to light sprays, liquid aerosols, or low-pressure, low-volume splashes which does not require a complete liquid permeation barrier. The scope is based on BS EN 13034:2005 [10]. Performance requirements for chemical protective clothing offering limited protective performance against liquid chemicals for both chemical protective suits (type 6) and partial body protection garments (type PB (6) equipment).

CE Marking is required for protective clothing which meets or exceeds the minimum requirement for materials' physical and chemical properties and pass one or more garment type test [6].

No matter how permeable, semi-permeable, and impermeable chemical protective clothing is designed, the ultimate objectives, and performance criteria of the clothing is to achieve both maximum protection performance and minimum thermal physiological burdens simultaneously according to the requirement from ISO 16602:2007 (Protective clothing for protection against chemicals: classification, labelling and performance requirements) [28].

2.1.3 Summary of existing commercial chemical protective clothing

To identify gaps between the technical performance of existing commercial chemical protective clothing products and the performance requirements of ideal chemical protective clothing identified in Section 2.1.2, seven chemical protective clothing samples available in the market from two companies are compared in Figure 2.3 and Figure 2.4 . The characteristics of the protective fabrics used in these chemical protective clothing products are summarised in Table 2.1.

According to the categories of chemical protective clothing described in Section 2.1.1, Tyvek and Microgard 2500 are made from air-permeable fabrics. Tychem C2 and Microchem 3000 are semi-permeable and Tychem F, Tychem F2, and Microchem 4000 are made from impermeable materials. The fabric structure and physical

properties of these commercial chemical protective clothing products obtained from their producers' instruction leaflets are summarised and compared in Table 2.1 and Table 2.2 respectively.

The permeation resistance of chemical liquids based on the requirement of NFPA 1991 (Standard on vapour-protective ensembles for hazardous materials emergencies, and liquid), one of the key chemical protection properties of the chemical protective clothing, is reported in Table 2.3 . It is noticed that the permeation properties of those fabrics reported in the leaflet are not tested in unified testing conditions and are thus difficult to be compared; in addition, not all of the chemicals listed in NFPA 1991 were reported in their instruction leaflets. It may be reasonable to assume that those fabrics were not tested against those specific chemicals, and that they therefore do not resist penetration by them. Nevertheless, it might be necessary to compare the permeation properties of those fabrics through examination of their permeation rate and breakthrough time against one specific chemical liquid in the same testing conditions.

It is also noted that the thermal and thermophysiological comfort properties of these existing chemical protective clothing products are not available in their instructions, and thus unable to be compared. It is therefore necessary to examine and compare the thermal and thermophysiological properties of these fabrics to find out how the chemical protection and thermophysiological comfort performances of the existing commercial clothing products are balanced.

Therefore, both the permeation test and thermal comfort properties of these fabrics will be investigated in Chapter 3.

Tyvek

Tychem C2

Tychem F

Tychem F2

Figure 2.3 Selected chemical protective clothing products from Du Pont[1]

Microgard 2500

Microchem 3000

Microchem 4000

Figure 2.4 Selected chemical protective clothing products from Microgard[2]

[1] http://www.dupont.com

[2] http://www.microgard.com/

Table 2.1 Fabric structures of chemical protective clothing [18],[29],[30],[31],[32],[33],[34]

Company	Commercial name	Basic structure	Applications
Dupont	Tyvek	A high density polyethylene spunbonded web	- Non-hazardous particle & aerosol - Non-hazardous liquid splash such as oil & grease, lubricants, fertilizer, sewage - Hazardous particles such as fertilizer, pesticide, asbestos, lead, chromium, beryllium, mould, fibreglass, carbon, radioactive particles - Hazardous aerosol
	Tychem C2	Tyvek with a polymeric coating, 120 g m^{-2}	Protection against concentrated inorganic chemicals and biohazards
	Tychem F	Tyvek with polymeric coating and laminating film, 120 g m^{-2}	- Chemical-Biological and warfare agents - Moderate liquid chemical splash - Light chemical splash & aerosols - Bloodborne pathogens & biohazards - Protection against concentrated inorganic chemicals and biohazards
	Tychem F2	Tyvek with polymeric coating, 120 g m^{-2}	- Protection against organic and highly concentrated inorganic chemicals and biohazards
Microgard	Microgard 2500	A microporous polypropylene laminated fabric	- Viral contaminated areas - Avian influenza - Part of business continuity kit

			- Centres for disease control - Decontamination processes - Low hazard chemical spray - Emergency services - Veterinary services - Industrial paint spraying
	Microchem 3000	Spunbonded polypropylene fabric laminated with barrier film	- Chemical handling or transportation - Oil based mud protection - Offshore drilling - Pesticide/insecticide spraying - Land reclamation and clean-up - Food industry caustic clean downs
	Microchem 4000	Polypropylene nonwoven spunbonded laminated with a multi-layer barrier lightweight textile	For hazardous areas where protection against concentrated chemicals and biological agents is required, such as; - Chemicals - Oil & Petrochemicals - Pharmaceutical - Mining - Agriculture - Industrial & tank cleaning - Sewage purification installations - Emergency Services

Table 2.2 Physical properties of chemical protective clothing [18],[29],[30],[31],[32],[33],[34]

	Test method	**Tyvek**	**Tychem F**	**Tychem F2**	**Tychem C2**	**Microgard 2500**	**Microchem 3000**	**Microchem 4000**
Colour	-	White	Orange	Grey	Yellow	White	Yellow	Green
Abrasion resistance (cycles)	EN 530:1994 (method2)	100	>2000	>2000	>1500<2000	>100	>500	2000
Flex cracking resistance (cycles)	EN ISO 7854/B: 1997	>100000	>1000<2500	>1000<2500	>2500<2000	>40000	>100000	40000
Trapezoidal tear resistance (MD/XD) (N)	EN ISO 9073-4:1997	26.1/30.6	22.9/28.1	66.0/54.6	74.8/50.9	43.1/35.7	44.0/29.0	88.0/44.0
Tensile strength (max. tear) (MD/XD) (N)	EN ISO 13934-1:1999	N/A	248.9/259.6	327.4/298.4	224.4/202.5	109.0/113.5	172.0/62.0	164.7/84.0
Burst resistance (kPa)	EN ISO 13938-2: 1999 ISO 2960 (50 cm^2)	108.0	201.7	306.4	220.2	110.7	90.0	116.0
Puncture resistance (N)	EN 863: 1995	10.8	22.4	25.2	20.5	15.23	10.0	16.0

Hydrostatic head (kPa)	EN 20811:1992	N/A	>100	>100	>100	>500	>350	>692
Stability to heat	EN 25978: 1993	-	No blocking	No blocking	No blocking	-	No blocking	-
Resistance to flame	EN 13274-4: 2001 (method 3)	-	N/F	N/F	N/F	N/F	N/F	-

[1]MD=Machine Direction, XD=cross-machine direction

N/A = Not Applicable, N/F = No formation of molten droplets, burning does not continue

Table 2.3 Liquid permeation resistance of existing chemical protective clothing [35], [36]

Chemicals	**Tyvek**	**Tychem F**	**Tychem F2**	**Tychem C2**	**Microgard 2500**	**Microchem 3000**	**Microchem 4000**
1. Acetone	N/A	>480	-	Immediate	Immediate	28	>540
2. Acetonitrile	N/A	>480	>480	N/A	Immediate	Immediate	>540
3. Anhydrous ammonia (gas)	N/A	-	-	-	Immediate	3	60
4. 1,3 butadiene	-	>480	-	N/A	N/A	-	-
5. Carbon disulfide	-	>480	-	N/A	5	Immediate	2
6. Chlorine (gas)	-	>480	-	N/A	Immediate	10	>540
7. Dichloromethane	-	Immediate	-	N/A	Immediate	Immediate	9
8. Diethylamine	-	>480	-	N/A	Immediate	Immediate	Immediate
9. Dimethyl formamide	-	>480	-	N/A	N/A	>480	-
10. Ethyl acetate	-	>480	-	N/A	Immediate	Immediate	>540
11. Ethylene oxide	-	64	-	N/A	N/A	N/A	>480

12. Hexane	N/A	>480	>480	-	N/A	N/A	>480
13. Hydrogen chloride	-	>480	-	N/A	Immediate	8	>540
14. Methanol	N/A	>480	>480	-	Immediate	>540	>540
15. Methyl chloride (gas)	-	>480	-	N/A	N/A	N/A	N/A
16. Nitrobenzene	-	>480	-	N/A	N/A	>480	>480
17. Sodium hydroxide (42%)	N/A	N/A	-	>480	>480	>540	>540
18. Sulphuric acid	-	N/A	-	N/A	>480	>540	>540
19. Tetrachloroethylene	-	>480	-	N/A	N/A	N/A	218
20. Tetrahydrofuran	-	>480	-	N/A	Immediate	Immediate	5
21. Toluene	N/A	>480	>480	>480	Immediate	Immediate	>540

N/A = Not Applicable,

- = No data available

2.2 Permeation of chemical liquids through barrier fabrics used in chemical protective clothing

When hazardous liquid contacts PPE materials, there are various mechanisms involved in the liquid permeation into PPE materials. These mechanisms include liquid wetting and spreading, liquid sorption and desorption, and liquid permeation and diffusion.

2.2.1 Liquid wetting and spreading on the surface of barrier fabrics

The interaction of liquids and textiles depends on the wettability of fibres, their surface geometry, the capillary geometry of the fibrous assembly, the amount and nature of the liquid, and external forces. After that the capillary penetration, the adsorption on fibre, and the diffusion of liquid into fibre may occur concurrently [37]. Wetting is a thermodynamic process involving the replacement of a solid-liquid or liquid-air interface with a liquid-liquid interface, and a solid-air interface with a solid-solid interface, it depends on the surface roughness and surface free energy of the solid surface. The wetting property of the solid surface is classified on a scale between lyophobic and lyophilic. A lyophilic surface is a surface that attracts liquids, while a lyophobic surface repels liquid. A sub-class of lyophobic and lyophilic conception is designated hydrophobic and hydrophilic which is restricted to wetting properties for water [38].

Contact angle is the net effect of three interfacial tensions that exists between solid and vapour, solid and liquid, and liquid and vapour respectively. When a liquid drop is placed on an ideal flat solid surface (smooth, homogenous, impermeable, and non-deformable), it comes to an equilibrium state corresponding to the minimization of interfacial free energy of the system. The relationship between the interfacial tensions involved in the equilibrium of wetting is given by Young's equation in equation (2-1).

$$\gamma_{SV} - \gamma_{SL} = \gamma_{LV} \cos\theta \qquad (2\text{-}1)$$

where
γ_{SV} is the solid-vapour interfacial tension,
γ_{SL} is the solid-liquid interfacial tension,
γ_{LV} is the liquid-vapour interfacial tension,
θ is the equilibrium contact angle,
$\gamma_{LV}\cos\theta$ is the adhesion tension or specific wettability.

For a rough surface, it was proposed that the actual surface area is greater than the geometric surface area and that the difference of the surface areas between a rough surface and a flat smooth surface leads to a considerable difference between the apparent and intrinsic contact angle. Surface roughness enhances both the hydrophilicity of hydrophilic surfaces and the hydrophobicity of hydrophobic surfaces. The roughness factor (r_w) is proposed in Wenzel's equation [39].

$$r_w = \frac{Actual\ surface\ area}{Geometric\ surface\ area} \quad (2\text{-}2)$$

From Young's equation (2-1) this is rewritten in equation (2-3)

$$\cos\theta_w = r_w \cos\theta \quad (2\text{-}3)$$

where
θ_w is the thermodynamic contact angle on a smooth surface of material.

Additionally, the apparent contact angles for a heterogeneous porous surface are suggested by Cassie and Baxter's equation [40] as equation (2-4) below

$$\cos\theta_{cb} = a_1 \cos\theta_1 - a_2 \quad (2\text{-}4)$$

where
a_1 are the fractional surface areas occupied by the material and the air in a plane unit area,
θ_1 is the corresponding intrinsic contact angle on the solid surface, and
θ_{cb} is the Cassie-Baxter contact angle for a rough surface [41].

2.2.2 Process of liquid permeation through a membrane

After a liquid wets a membrane surface, it might permeate through the membrane material. Permeation is the process which a liquid or gas chemical moves through a membrane material on a molecular level [42]. There are three steps involved in the process of liquid permeation through polymeric membranes [43].

(1) The first step of liquid permeation is the sorption of the challenge chemical molecules on the outer surface of the membrane material into the liquid-membrane contact surface; this depends on the solubility of the chemicals in the polymer membrane.

(2) The diffusion of the chemical molecules through the membrane material is considered as the second step of the permeation process [45], it occurs straight after the solvent molecules are absorbed on the outer surface.

(3) The desorption of molecules from opposite surfaces of membrane material.

As the desorption step is not the major process we are interested in our study of the permeation process [45], the chemical permeation through a polymeric membrane is usually described as the solution-diffusion process [46] as shown in Figure 2.5.

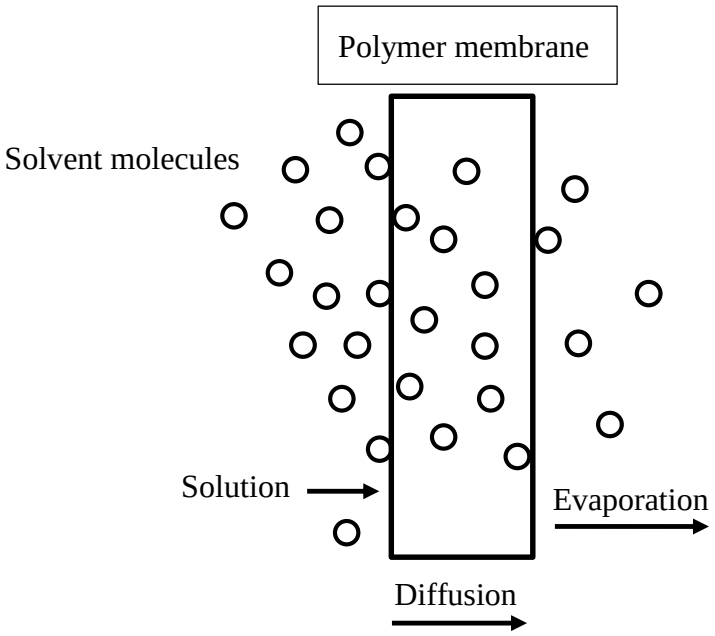

Figure 2.5 Process of liquid permeation through a polymeric membrane [47]

Steady-state permeation occurs after chemicals break through the barrier membrane materials when the chemical contact is continuous and all forces affecting permeation has reach equilibrium. The steady-state permeation rate (J_s) is defined in the equation (2-5) below.

$$J_s = \frac{C_s Q}{A} \tag{2-5}$$

where

Cs is the steady-state concentration of permeant in the collection medium,

Q is the flow rate of the collection medium,

A is the surface area of the sample.

Theoretically, the permeation rate, J_s , is related to the permeability coefficient, *P*, and the membrane thickness, *L*, as shown in the equation (2-6) below [48]

$$J_s = \frac{P}{L} \tag{2-6}$$

where

P is the permeability coefficient,

L is the thickness of the membrane.

It was also proposed that the permeability coefficient is a function of both solubility and diffusivity as defined by Henry's law as the equation (2-7) below [49].

$$P = S \cdot D \tag{2-7}$$

where

P is the permeability coefficient (mg mm cm^{-2} min^{-1}),

S is the solubility coefficient (cm^3),

D is the diffusion coefficient (cm^2 min^{-1}).

Solubility: Solubility is defined as the amount of chemical absorbed by a given amount of polymeric materials [50]. It is determined by various molecular interaction forces [47] including the dispersion force between solvent molecules and the polymer, the polar force between solvent molecules and the polymer and the hydrogen force between solvent molecules and the polymer, all of which were used to predict the solubility of a polymer material in a solvent. The Hansen 3-D solubility parameter (δ^2) was shown in equation (2-1) [51].

$$\delta^2 = \delta_p^2 + \delta_h^2 + \delta_d^2 \tag{2-8}$$

where

δ_p is the polar solubility parameters ($cal^{-1/2}$ $cm^{-3/2}$),

δ_h is the hydrogen-bonding solubility parameters ($cal^{-1/2}$ $cm^{-3/2}$),

δ_d is the dispersion solubility parameters ($cal^{-1/2}$ $cm^{-3/2}$).

Then, the solubility of the permeant in the membrane is proposed by the equation (2-9) below [52].

$$S = \frac{B}{(\delta_p - X_p)^2 + (\delta_h - Y_h)^2 + (\delta_d - Z_d)^2} \quad (2\text{-}9)$$

where
S is the solubility of a permeant in the membrane,
B is a constant,
X_p is the polar bonding contribution to the solubility parameters of the membrane,
Y_h is the hydrogen bonding contribution to the solubility parameters of the membrane,
Z_d is the dispersive bonding contribution to the solubility parameters of the membrane.

In the process of chemical liquids permeation through barrier polymeric membranes in protective clothing, solubility is a significant factor which refers to the ability of the polymer to protect against a given solvent [53]. Generally, a highly soluble chemical will rapidly permeate through the barrier materials, which might lead to a shorter breakthrough time and greater permeation rate, but this is not always true as the permeation rate also depends on the diffusion coefficient. For instance, gas has a low solubility but a high diffusion coefficient and may permeate the material at rates several times greater than a liquid with moderate to high solubility in the material [54].

Diffusion: The chemical liquids' diffusion through polymer membranes occurs straight after the solvent molecules absorbed into the outer surface. The solvent diffuses through the polymer membrane above their glass transition temperature as described by the Fick's equation in (2-10) below [55].

$$J_D = -D\frac{dC}{dL} \quad (2\text{-}10)$$

where
J_D is the diffusion flux (mg cm^{-2} min^{-1}),
D is the diffusion coefficient of chemical through polymer membrane,
(cm^2 min^{-1})
C is the concentration gradient across the membrane (mg cm^{-3}),

L is the fabric thickness (m).

There are many other factors that affect the chemical permeation rate including environmental temperature, the thickness of barrier materials, and multi-components of challenge liquids as discussed below.

Temperature: While most chemical permeation tests for chemical protective clothing are conducted at 20-25°C, the actual polymer-solvent permeation situations often occur at higher temperatures in field use. The permeation coefficient usually increases with an increase in environmental temperature, and Arrhenius's equation (see equation (2-11) below) is usually used to predict the effect of temperature on permeation coefficient over a small range of temperatures (25-50°C) [46].

$$J_s = J_0 exp(-\frac{Ep}{RT_k}) \quad (2\text{-}11)$$

where

J_s is the permeability coefficient (μg mm^{-1} cm^{-2} min^{-1}),

J_0 is the constant factor,

E_p is the energy of activation for permeation (kJ mol^{-1}),

R is the ideal gas constant,

T_k is the absolute temperature (K).

Membrane thickness: It is found that an increase in the thickness of barrier materials leads to an increase in breakthrough time and reduction of the permeation rate but has no effect on normalized breakthrough time for many chemicals including methylene chloride and perchloroethylene [56].

Multi-component challenge liquids: The mixture of chemicals can be significantly more aggressive towards chemical protective materials than any one of the components alone. A study of the permeation of aromatic hydrocarbons including benzene, toluene, ethyl benzene, and *p*-xylene through the test nitrile gloves was found that the slowly permeating component of a mixture of chemicals break through nitrile gloves earlier than its pure form. If the single pure solvents could permeate through the protective glove, the steady state permeation rates of multi-component

mixtures will depend on their molecular volume and mole fraction in composition [57].

Once the chemicals begin to diffuse into barrier materials, they would continue to diffuse even after the chemicals on the outside surface were removed. This is the result of the concentration gradient established within the barrier materials which drives the chemicals to move towards the areas of lower concentration of the chemicals [58].

2.2.3 Methods for characterisation of liquid chemicals' permeation and penetration through membrane barrier materials

The chemical liquids' permeation and penetration through membrane barrier materials for protective clothing are characterised by using three types of standard methods [59]: degradation resistance [23], penetration resistance [60] and permeation resistance [42].

2.2.2.1 Chemical degradation resistance

The degradation is defined in ASTM F23 standard [61] and ISO 6529:2013 standard [42] as the deleterious change of physical properties of the polymer membrane material as a result of chemical exposure. The physical properties include fabric weight, dimensions, tensile strength, hardness, and any other characteristics related to the material's performance. The chemical degradation resistance testing does not measure the liquid permeation/penetration directly and it is an indirect characterisation method. It is thus typically used as a screen test before any further chemical penetration and permeation testing.

The international standard test methods are available for the chemical degradation resistance, such as ASTM D 471-12a (Standard test method for rubber property-effect of liquids) or ASTM D 543-06 (Standard practices for evaluating the resistance of plastics to chemical reagents).

2.2.2.2 Chemical penetration resistance

Chemical penetration through chemical protective clothing is considered as the process through which solid, liquid or gas chemicals flow through the textile structure including closure, seams, interstices and pinholes or other imperfections on a non-molecular level [63]. BS ISO 13994:1998 (Determination of the resistance of protective clothing materials to penetration by liquids under pressure) [64] and ASTM

F903-03(2004) (Standard test method for resistance of materials used in protective clothing to penetration by liquids) [22] are used to determine the penetration resistance property of the protective clothing [23].

In BS ISO 13994:1998, the fabric's ability to resistance the liquid penetration under external pressure is determined by subjecting the material to the liquid for a specified time and pressure sequence in a specified penetration cell, which contains a chamber containing the challenge liquid and a restraining ring which holds a fabric specimen, the fabric specimen acts as a partition separating the chemical liquid which penetrates through the fabrics as shown in Figure 2.6 . The testing sequence defined in BS ISO 13994:1998 is summarised in Table 2.4 and the sequence in ATM F 903-03 is shown in Table 2.4. If any visible penetration of liquid through the fabric specimen is observed, the fabric fails the liquid penetration test.

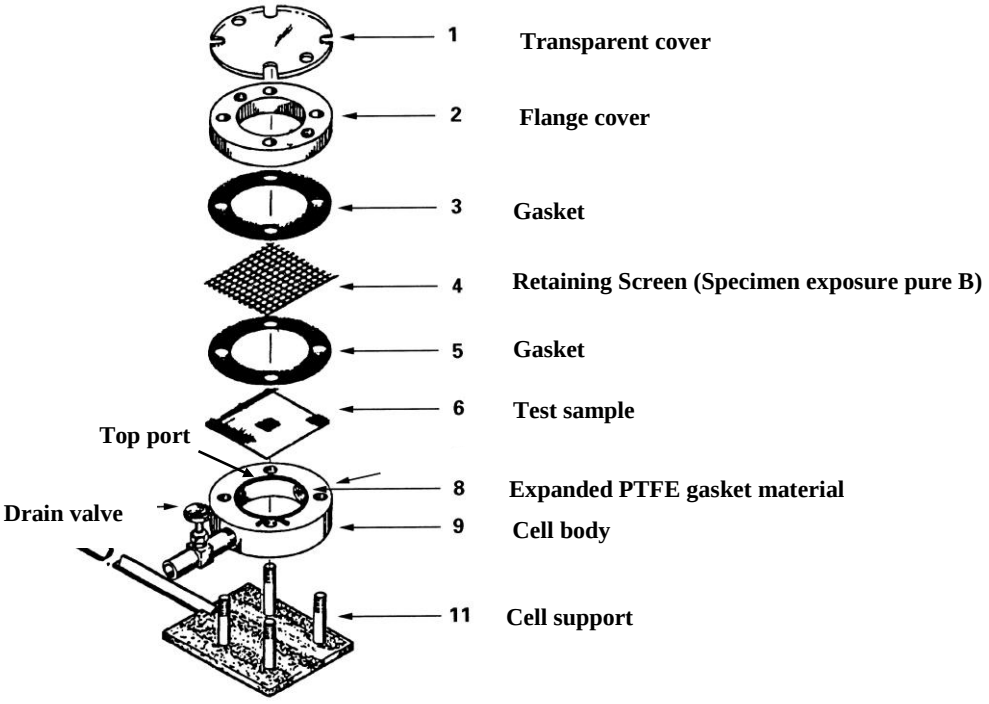

Figure 2.6 Penetration cell with retaining screen (exploded view) [64]

Table 2.4 Pressure/time sequences and conditions for selected circumstances of the liquid penetration testing

Procedure	Pressure/time sequence	Circumstances
A	0 kPa for 5 min, followed by 13.8 kPa for 10 min.	Used for selecting protective clothing materials, seams and closures, to limit exposure to liquid splashes.
B	0 kPa for 5 min, followed by 6.9 kPa for 10 min.	Used for selecting protective clothing materials (such as gloves) to limit exposure to liquid splashes.
C1	0 kPa for 5 min, followed by 13.8 kPa for 1 min, followed by 0 kPa for 54 min. A retaining screen is not used to support the sample.	Used for selecting protective clothing materials, seams and closures, to limit exposure of fire service personnel to liquid splashes during emergency responses.
C2	0 kPa for 5 min, followed by 13.8 kPa for 1 min, followed by 0 kPa for 54 min. A retaining screen is used to support the sample.	Used for selecting protective clothing materials, seams and closures, to limit exposure of fire service personnel to liquid splashes during emergency responses; applied instead of C1 when specimen requires additional support.
D	Include in the report, the time and pressure sequence used if different from procedure A, B, or C.	Use for other specified needs or circumstances.

2.2.2.3 Chemical permeation resistance

The chemical permeation is the process which liquids and gases move through the membrane materials in molecular level of the material without passing through any void or imperfection part of the membrane [64]. The permeation property of chemical barrier membrane is used to classify the level of performance of the chemical protective clothing.

Liquid permeation testing methods are defined in many international standards including BS EN 374-3:2003 [65], EN ISO 6529:2013, ASTM F739-12 [20], and ASTM F1383-12 [66]. The comparison of each standard is shown in Table 2.5.

Table 2.5 Standard methods for determination of liquid permeation through protective clothing [53]

Test method	**Diameter of permeation cell (mm)**	**Flow rate of collection medium**	**Detection Limit (μg cm^{-2} min^{-1})**
BS EN 374-3:2003	51	Five volume changes of collection	1
ISO 6529:2013	25 or 51		0.1 or 1
ASTM F739-12	51	50-150 cm^3 min^{-1}	0.1 (open loop) 0.25 (closed loop)

BS EN 374-3 is used to determine the protective gloves against chemical and micro-organism resistance to permeation by potentially hazardous non-gaseous chemicals under the condition of continuous contact. The permeation test cell used is the same as the one defined in EN ISO 6529:2013; the chemical molecules permeation through the fabric specimen is collected in a collection media flow and the concentration of the chemicals in media flow are measured. The collection medium could be dry air, nitrogen or a dry, non-flammable inert gas or water or other liquid which does not influence the resistance of a material to permeation or other collecting media may be used such as porous polymers in powder form when a chemical cannot be collected either by gaseous or liquid collecting media. The determination of breakthrough time of a chemical (or mixture) is estimated to have occurred when the sum of the permeation rates of each individual component reaches the rate of either 0.1 or 1 μg cm^{-2} min^{-1}.

ASTM F 1407-99a is a standard test method for determining the resistance of chemical protective clothing materials to liquid [67] which is less sensitive and less toxic than the ones used in ASTM F 739-99a while ASTM D5886 is a standard test method for determining the rate of fluid permeation through geomembranes [68]. Gas chromatography (GC) and gas chromatography mass spectroscopy (GCMS) are proposed to measure the multicomponent fluid such as mixture of gas, aqueous solution of organic salt, mixture of organic, aqueous solution of organic and aqueous solution of organic and inorganic species.

Generally, the permeation resistance is reported by three testing results: permeation rate, the breakthrough time and cumulative permeation [69]. The dynamic permeation rate of the liquid chemicals permeation through the membrane, i.e., the mass flux through a unit area of the membrane material within a unit time, is measured (see Figure 2.7). In the case of chemical protective clothing, either the steady-state or maximum observed permeation rate are reported. The breakthrough time is defined as the time elapsed from the start of the test to the sampling time at which the test chemical was first detected at the normalised permeation rate of either 0.1 or 1 μg cm^{-2} min^{-1} [70].

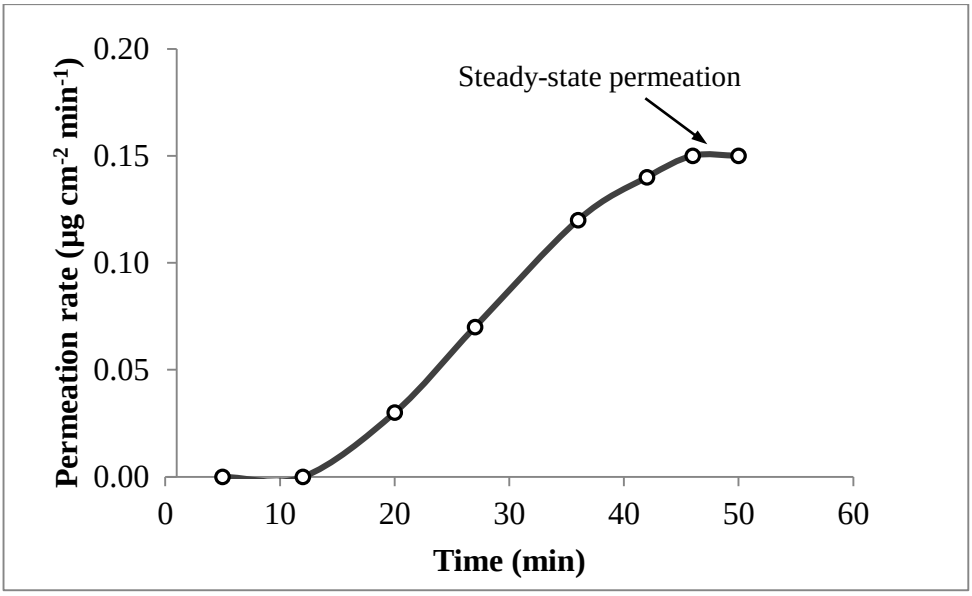

Figure 2.7 The most typical of permeation behaviour where the permeation rate stabilized at the steady-state value

2.3 Thermal and thermophysiological comfort properties of barrier fabrics used in chemical protective clothing

Thermophysiological comfort is both a psychological and physical phenomenon, and it is defined as the condition of mind which expresses satisfaction with the thermal environment [71], it is achieved when human body is in a state of heat balance and where heat loss is approximately equal to heat production. The heat balance can be described by Fanger's equation [72] shown in the equation (2-12) below.

$$M_f = \mathrm{E}_f \pm C_f \pm K_f \pm R_f \pm S_f \qquad (2\text{-}12)$$

where

M_f is metabolic rate,
E_f is evaporative heat loss,
C_f is convective heat change,
K_f is conductive heat change,
R_f is radiative heat change,
S_f is heat storage.

Human body maintains thermal comfort through its thermoregulation system to control heat losses and maintain thermal balance in four ways: sweating, shivering, vasodilatation and vasoconstriction [73]. Clothing system play an important role in supporting the human body's thermoregulation by controlling radiation, conduction, and convection heat transport, as well as managing insensible heat transfer via evaporation of sweat, through its component fabrics to the surrounding environment [10], [74].

When an intensive activity is carried out in a hot environment, a human body enclosed with chemical protective clothing generates a significant amount of metabolic heat and produces moisture and sweat, which impose a thermal burden on the human body if the heat and moisture cannot be transferred away from the body [75]. The removal of heat and sweat away from the human body through chemical protective clothing is related to the thermal resistance and water vapour transmission resistance of its component fabrics.

In permeable protective clothing, both wind in the environment and air movement produced by human movement help convective heat transport and moisture transfer through the porous fabrics. Air permeability of the fabrics is strongly related to both their convective heat loss and water vapour transmission rate [76]. An increase in fabric air permeability reduces the heat strain level of protective clothing. [77].

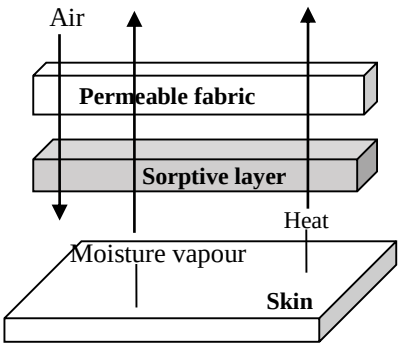

Figure 2.8 Schematic of heat and water vapour transfer through porous fabrics in permeable protective clothing

Air permeability in semi-permeable chemical protective clothing is usually low and most of the heat transport through this type of chemical protective clothing is via moisture vapour transfer through semi-permeable barrier membranes. Moisture transport through semi-permeable fabrics is divided into two types: nanoporous and solution-diffusion (monolithic) membranes. In nanoporous membranes, the moisture vapour passes through the membrane via Knudsen diffusion.

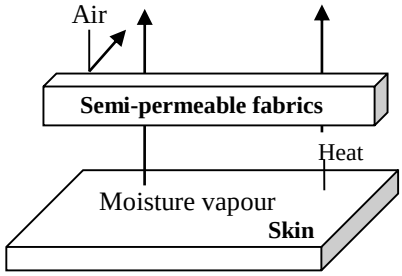

Figure 2.9 Schematic of heat and water vapour transfer in a semi-permeable material

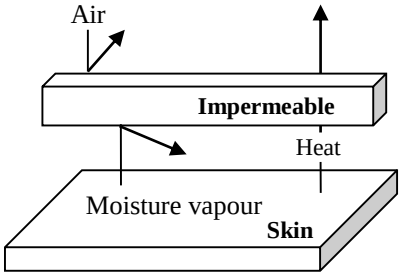

Figure 2.10 Schematic of heat and water vapour transfer through impermeable protective clothing

Hardly any water vapour can transmit through impermeable fabrics [78]. Within the microclimate formed within impermeable protective clothing worn on a human body, water vapour pressure gradually builds up and eventually reaches the saturation pressure (100% relative humidity). A significant increase in microclimate air temperatures as well as skin temperatures may then be seen [79].

Heat transfer from clothing surface to environment via convection, radiation, and evaporation. The heat flow from skin to clothing surface, and heat flow from the clothing surface to the environment, are all shown as the equation (2.13).

$$\boldsymbol{H_{tf}} = \frac{\boldsymbol{t_{sk}} - \boldsymbol{t_{cl}}}{\mathbf{R}} = \frac{\boldsymbol{t_{cl}} - \boldsymbol{t_q}}{\boldsymbol{R_b}} = \frac{\boldsymbol{t_{sk}} - \boldsymbol{t_a}}{\mathbf{R} + \mathbf{R}_{\boldsymbol{b}}} \qquad (2\text{-}13)$$

where

H_{tf} is the heat transfer between the clothing surface and the environment by conduction, convection, and radiation (W m^{-2}),

t_{sk} is the mean skin temperature (°C),

t_{cl} is the clothing surface temperature (°C),

t_a is the ambient temperature (°C),

R is the fabric thermal resistance (m^2 °C W^{-1}),

R_b is the boundary air layer thermal resistance at clothing surface (m^2 °C W^{-1}).

Under steady state conditions, the heat evaporation exchange takes place via the transfer of latent heat of evaporated sweat from the skin to the environment as expressed by the equation (2-14) [79].

$$\boldsymbol{E_{sk} = \frac{p_{sk} - p_a}{R_{et}} = w \cdot \frac{p_{sk,s} - p_a}{R_{et}}} \qquad (2\text{-}14)$$

where

E_{sk} is evaporative heat exchange (W m^{-2}),

p_{sk} is skin water vapour pressure (kPa),

p_a is ambient water vapour pressure (kPa),

w is skin wettedness,

R_{et} is evaporative resistance of clothing and the boundary air layer

(kPa m^2 W^{-1}).

Therefore, the thermal comfort of the chemical protective clothing depends on the heat and moisture vapour transport through its component textile fabrics. This is usually influenced by the fabric structures (fabric density, thickness, porosity, thermal conductivity, etc) including the single and multilayer structure [80], the enclosed still air, and the external air movement.

2.3.1 Heat and moisture transfer through textile fabrics

Dry heat transport through textile fabrics and membranes is the net result of the combination of radiant, conductive, and convective heat transfer, and is described by

using thermal conductivity and thermal resistance. The thermal conductivity of a fabric quantifies its heat transfer ability as shown in equation (2.15) [81].

$$\boldsymbol{k = q \cdot \frac{L}{A \cdot \Delta T}} \qquad (2\text{-}15)$$

where
k is thermal conductivity of the material (W m^{-1} K^{-1}),
q is heat flux flow through the textile fabric per unit area across its thickness (J s^{-1}),
A is cross-sectional surface area (m^2),
ΔT is temperature difference between the two sides of the fabric (K),
L is thickness of the fabric through which heat transfers (m).

Thermal resistance characterises the thermal insulation properties of the fabric as defined in equation (2-16) and depends on both thermal conductivity and thickness of the fabric [82].

$$\boldsymbol{R = \frac{L}{k}} \qquad (2\text{-}16)$$

where
R is thermal resistance (m^2 K W^{-1}),
L is thickness of the fabric through which heat transfers (m),
k is thermal conductivity of the fabric (W m^{-1} K^{-1}).

Moisture vapour transfer through porous textile fabrics and semi-permeable membranes involves water vapour diffusion in the pore space, moisture vapour sorption and desorption in fibres and diffusion through fibres, evaporation, and capillary effects [83].

Moisture vapour permeation through nanoporous semi-permeable polymeric barrier membranes follows the same solution-diffusion mechanism as chemical liquids through polymeric membranes described in Section 2.2.1.

For membranes having macro-porous structures, there are three mechanisms for moisture vapour transporting through textile fabrics and porous membranes: Knudsen diffusion, molecule diffusion flow, and viscous flow [84]. Knudsen diffusion happens via the collision between vapour molecule and pore wall in pores less than 70 nm wide. Molecular diffusion occurs via the collision between moisture vapour molecules

and gas (i.e. air) molecules. Viscous flow is driven by the external pressure gradient through pores. The viscous flow of moisture transport through macro-porous fabrics mainly depends on its porous structure. The relationship between the moisture resistance of the fabric and the fabric porosity and fabric thickness is shown in equation (2.17) [85].

$$R = \frac{L}{D_a P_{df}} \tag{2-17}$$

where
R is the moisture resistance of the fabric,
L is the fabric thickness,
P_{df} is the water vapour diffusivity of air,
D_a is the fabric porosity.

2.3.2 Thermal comfort properties of chemical protective clothing

Chemical protective clothing is widely made from an air-permeable porous fabric for use in a non-hazardous environment, and a thick-heavy impermeable fabric for use in extremely hazardous conditions. Therefore, the thermal comfort property of these types of chemical protective clothing varies based on their fabric structures. A study of a thick and tight woven chemical protective fabric with a high protection against pesticide but low air permeability showed that pore size and total volume of voids plays an important part in the transmission of moisture vapour [86]. Even though Tyvek fabric is a high air-permeability fabric, users also reported greater thermal discomfort and perceived higher thermal sensation [87].

In the case of the high protection level of chemical protective clothing, it was reported that workers wearing Gore®Chemical Splash Protection were able to work for at least 45 minute at 20°C, 85% RH [88]. Moreover, with respect to heat stress, it was found that among workers who wore encapsulated impermeable protective clothing working in life saving conditions at 21°C and 5°C, heat strain played a significant role during the warmer conditions; while in the cold conditions, heat strain was negligible but the difficulty came from the stiffness of the clothing [89]. It was also determined that in the case of the impermeable chemical protective fabric, heat stress became a serious problem for workers in moderate environmental conditions around 29.4°C, 45% RH [90].

2.3.3 Methods for characterisation of heat and moisture transfer through textile fabrics

There are various methods for characterising both thermal resistance and moisture transfer properties of textile fabric and barrier membranes. They include guarded hotplate methods for thermal resistance, sweating guarded hotplate methods for dry heat thermal resistance (R_{ct}) and moisture transfer resistance (R_{et}), dish methods for moisture vapour transmission rate, and other methods.

2.3.3.1 Guarded hot plate method

The guarded hotplate method is a conventional technique for determining the heat transfer ability through a sample in one dimension under steady state, and it is defined in standards ISO 8301:1991 [91], ISO 8302:1991[92], ASTM C177-13 [93], and ASTM C518-04 [94]. In this system, it is assumed that heat transfer only occurs in the direction perpendicular to the sample and the heat loss from the edge of the sample is neglected, since the cross-sectional surface area of the sample is much larger than the edge area of the sample. In a two-plate testing system such as Togmeter, one plate is heated and the other one is cooled until a constant state is reached. Thermal resistance and thermal conductivity of the sample is calculated from temperatures, thickness, and heat input using equation 2.16.

2.3.3.2 Thermal resistance (R_{ct}) - Sweating guarded hotplate method (SGHP) (ISO 11092:2014 [95])

The sweating guarded hotplate or the "skin model" testing is a standard test method to simulate the processes of heat and moisture transport from the body surface through the clothing system to the environment under steady state. The measurement of dry heat thermal resistance (R_{ct}) in ISO 11092:2014 is on a guarded hotplate surrounded by a guard that is heated to the same temperature in order to avoid any heat loss. The clothing sample is placed on a hotplate in a climatic chamber with a defined temperature, relative humidity, and air velocity parallel to the fabric surface. R_{ct} is determined by using the equation (2-18) below.

$$R_{ct} = A \cdot \frac{T_s - T_a}{Q_{steady}} - R_{ct0} \qquad (2\text{-}18)$$

where

R_{ct0} is the apparatus constant for measurement of thermal resistance

(m^2 K W^{-1}),

A is the area of the measuring surface (m^2),

Q_{steady} is the supplied steady state heating power (W),
T_s - T_a is the temperature difference between the air in the wind channel

(T_a = 20°C) and the skin model (T_s) (°C).

2.3.3.3 Water-vapour resistance (R_{et}) -Sweating guarded hotplate method (ISO 11092:2014)

For the determination of water-vapour resistance under isothermal conditions, an electrically heated porous test plate is covered by a cellophane membrane, which is water-vapour permeable and non-permeable to liquid-water. Water fed to the heated plate evaporates and passed through the membrane as vapour. The test specimen is placed on the membrane so that no liquid water contacts the test specimen. R_{et} is calculated by equation (2-19).

$$R_{et} = A \cdot \frac{p_s - p_a}{Q} - R_{et0} \qquad (2\text{-}19)$$

where
R_{et0} is the apparatus constant of water-vapour resistance of bare plate
(m^2 Pa W^{-1}),
p_s is the saturation water-vapour partial pressure at the surface of the measuring unit (Pa),
p_{air} is the saturation water-vapour partial pressure of the air in the test enclosure (Pa),
Q is the supplied steady state heating power (W).

The sweating guarded hotplate system is made from Measurement Technology Northwest Inc., USA, as shown in Figure 2.11. A simulation of the sweating guarded hotplate can be seen in Figure 2.12. It consists of three independently controlled heated zones: a test plate; a thermal guard ring which prevents lateral heat leakage from the edge of the sample; and a lower guard beneath the test section which prevents downward heat loss from the test plate.

Figure 2.11 The sweating guarded hotplate system

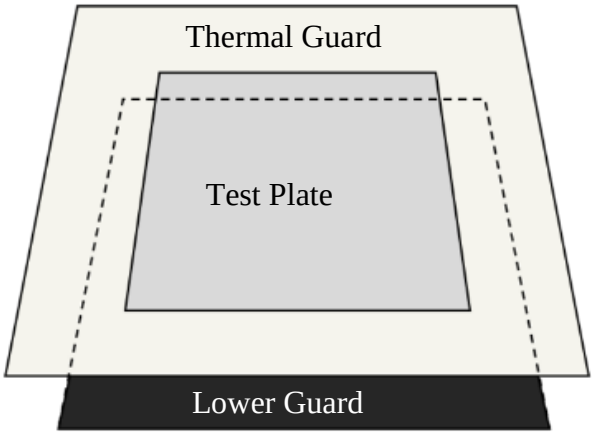

Figure 2.12 Schematic of the sweating guarded hotplate

2.3.1.1 Testing procedure

Three specimens of 30×30 cm are required for each of R_{ct} and R_{et} test. Measurement of R_{ct}: the sample is tested in the sweating guarded hotplate with the fabric surface normally facing the human body in contact with the hotplate. According to the EN 31092:2013, the temperature of the guard ring, test plate, lower guard, and the climate chamber are set as shown in Table 2.6 with a controlled air flow of 1 m s^{-1} over the fabric surface and 65% RH in the environmental chamber. When air temperature, relative humidity, temperature of hotplate, and the heating power reach their steady state, R_{ct} is calculated by using equation (2-18).

Table 2.6 EN 31092:2013 conditions requirement for R_{ct} and R_{et}

Test Methods / Conditions	R_{ct} (m^2 K W^{-1})	R_{et} (kPa m^2 W^{-1})
Test plate temperature (°C)	35	35
Climate chamber temperature (°C)	20	35
Relative humidity (%)	65	40
Air flow across parallel to its upper surface (m s^{-1})	1	1

Measurement of R_{et}: the test plate is covered by a cellophane membrane, which is water-vapour permeable and impermeable to liquid-water, and is fed with a flow of water via the diffusion mechanism. The heat of the hotplate is absorbed by the water contained in the wet cellophane membrane to evaporate it into water vapour. The sample is placed on top of the wet cellophane membrane without contact with any liquid water during the test. The testing conditions are also shown in Table 2.6. Each test takes approximately three hours until the measured quantities reach steady-state and R_{et} are calculated by using equation (2-19).

2.3.3.4 Water vapour transmission Rate (*WVTR*)

2.3.3.4.1 The upright cup method (ASTM E96 M-13 Method B [96] and BS 7209:1990 [97])

A cup containing a desiccant or distilled water is sealed by the test specimen and placed in a controlled atmosphere according to each standard method. The cup is weighed to calculate the water vapour transmission rate (*WVTR*) as per equation (2-20), before and after water vapour evaporation for a defined period of testing time.

$$WVTR = \left(\frac{G \times 24}{A \times t}\right) \tag{2-20}$$

where

WVTR is the water vapour transmission rate (g m^{-2} $24h^{-1}$),

G is the weight change (g),

t is the testing time duration (hour),

A is the cup opening area (m^2).

2.3.2.1 Testing procedure

Three specimens of 12×12 cm from the existing chemical protective fabrics are conditioned in a room at a temperature of 20±2°C and relative humidity of 65±2% RH for 24 hours before testing. A standard woven fabric is used as a reference fabric in similar conditions before testing.

In standard testing against BS 7209:1990, the specimens are placed on a turntable rotating at 1 m s^{-1} for 24 hours in an environment of 20±2°C and 65±2% RH. Standard glass cups filled with distilled water to give a layer of air at a depth of 10±1 mm between the surface of water and the specimen covering the opening of the cups are fitted with cover rings. The assembly cups are weighed one hour after the testing started to establish equilibrium of the water vapour gradient in the air gap inside the cup, then, each of the assembly cups is reweighed again after 8 hours. The *WVTR* of the tested fabrics is calculated using equation (2-20).

This method is easy to use and low cost, but it may take a few days to investigate the change of water vapour transmission rate for fabrics of low water vapour permeability. Also, the air layers on either side of the sample might dominate the total diffusion resistance which affects the accuracy of the water vapour transmission rate.

2.3.3.4.2 The desiccant invert cup method (BS EN ISO 15496: 2004 [98] and ASTM E96 M-13 Method A [96])

A measuring cup contains a certain amount of saturated potassium acetate solution, and a piece of waterproof and vapour permeable membrane is used to cover the measuring cup and sealed. A fabric specimen is covered by another piece of waterproof and vapour permeable membrane. The fabric specimen and the membrane are held without distortion using a rubber ring and inserted into a support frame. The support frame consisting of two plates is used to support a specimen holder in a distilled water bath. The specimen holder is immersed to a depth of 5 ± 2 mm in the water bath at 23ºC for 15 minutes prior to placing the measuring cup. The measuring cup is weighed before and after it is inverted and inserted into the specimen holder. The water vapour permeability of the fabric specimen is then calculated by the equation (2-21).

$$WVTR = \frac{96\times6(a_1-a_0)}{A} \quad \textbf{(}2\text{-}21\text{)}$$

where

a_1 is the weight of assembled cup after test (g),
a_0 is the weight of assembled cup before test (g)

It is noticed that the *WVTR* value from the desiccant invert cup method is highest in comparison with other methods [99].

2.3.3.4.3 The dynamic moisture permeation cell (DMPC) method and ASTM F2298-03 (2009)

A fabric specimen is mounted between two identical metal plates clamped tightly by two flow cells. Two nitrogen mass streams are passed through the duct of the flow cells. The relative humidity of the nitrogen stream is varied by merging dry and saturated streams in the duct of the flow cell. 95% RH and 5% RH are applied to the top and bottom nitrogen mass streams, respectively. The test is performed in a pure diffusion mode with no pressure gradient across the specimen. The DMPC was suggested because it could reduce the testing time compared to the previous testing method such as the cup method (ASTM E96) and the SGHP (ISO 11092:2014) [100]. *WVTR* is calculated by the equation (2-22).

$$WVTR = \frac{Q \times (C_2 - C_1)}{A} \times 1000 \times 3600 \times 24 \quad (2\text{-}22)$$

where

Q is the volumetric flow rate ($m^3\ s^{-1}$)

C_1 is the water vapour concentration of the bottom incoming stream ($kg\ m^{-3}$)

C_0 is the water vapour concentration of the bottom outgoing stream ($kg\ m^{-3}$)

It is noted that the water vapour transmission resistance results of the same fabric specimen obtained from different methods are not comparable. For example, theoretically the R_{et} from the SGHP method and the *WVTR* from the desiccant inverted cup method had a negative correlation [101].

The water vapour transport testing parameters are compared as indicated in Table 2.7.

Table 2.7 Parameter comparison of the water vapour transport testing method

Test Methods	ISO 11092:2014 (sweating guarded-hotplate)	Upright cup method		Invert cup method		ASTM F2298-03 (2009)
		BS 7209:1990	ASTM E96 M-13 (Method B)	BS EN ISO 15496: 2004 (desiccant invert cup method)	ASTM E96 M-13 (Method BW)	
Standard Title	Measurement of thermal and water-vapour resistance under steady-state conditions	Specification for water vapour permeable apparel fabrics	Standard test methods for water vapour transmission of materials	Measurement of water vapour permeability of textiles for the purpose of quality control	Standard test methods for water vapour transmission of materials	Standard test methods for water vapour diffusion resistance and air flow resistance of clothing materials using the dynamic moisture permeation cell **(**DMPC)
Property	Evaporative resistance	Water vapour transmission rate				Diffusion resistance of Water vapour transmission rate
Mode of transfer	Water on surface of hot plate to cellophane membrane to fabric to environment	Water inside upright cup to fabric to environment		Water inside tank to PTFE film to fabric to PTFE film inside desiccant inverted cup	Water inside inverted cup to fabric to environment	Atmosphere of high humidity to fabric to atmosphere of low humidity
Measuring Unit	M^2 Pa W^{-1}	g m^{-2} $24h^{-1}$		g m^2 Pa h	g m^{-2} $24h^{-1}$	g m^{-2} $24h^{-1}$

	Temperature (°C)	35°C chamber, 35°C hot plate	20°C chamber	23°C chamber			20°C chamber
	Relative Humidity (%)	40	65	50	23	50	95 and 5 in cell segments
	Air velocity (m s^{-1})	1	1	2.8	N/A	2.8	2 (gas flow rate)
Air layer		Boundary air layer, (subtracted out)	Air layers on either side of the fabric		No air layer	External air layer	Small air layers on either side of the fabric

2.4 Copolymerisation of thermo-sensitive PVDF-NIPAAM membrane

Both polyvinylidene fluoride (PVDF) and the thermosensitive monomer, N-isopropylacrylamide (NIPAAM), are used for making membranes of unique properties [102], [103]. It is envisaged that this thermosensitive NIPAAM-g-PVDF nonporous membrane might possibly be used in chemical protective clothing for the first time as its intelligent moisture management properties. Therefore, the properties of NIPAAM, PVDF polymer, and the copolymerisation of PVDF and NIPAAM are reviewed below.

2.4.1 NIPAAM and its application in smart textile applications

2.4.1.1 NIPAAM polymer

NIPAAM consists of both hydrophobic and hydrophilic groups and forms into gel in water; its chemical structure is shown in Figure 2.13 below.

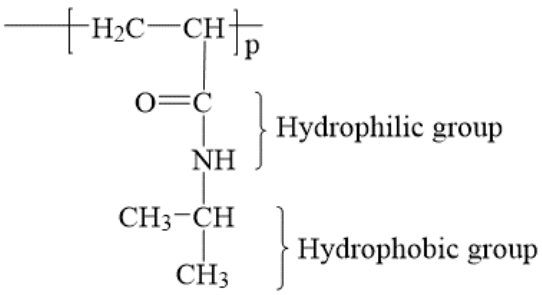

Figure 2.13 NIPAAM chemical structure [103]

NIPAAM is thermo-responsive material and it has a lower critical solution temperature (LCST) around 31-33°C in an aqueous environment [104]. Below the LCST, the polymer changes the conformation from hydrogen bonding with water molecules so the polymer has a random coil configuration. Above the LCST, a hydrogen bond is conformed internally within its molecule; the molecular chain is likely to take on a much more compact configuration by sudden dehydration and increased hydrophobic interaction between the polymer chains. When NIPAAM polymers dehydrate, they collapse in on themselves, exposing their hydrophobic backbone and showing the strong adhesion between NIPAAM molecules [105].

2.4.1.1 The application of NIPAAM in smart textiles

NIPAAM was used as the innovative smart textile material as pore-filling and a pore-gate system in bi-component fibre design [7]. NIPAAM and chitosan hydrogel was found to respond slowly, requiring a long time to respond [106]. The fast response hydrogel was made through the free-radical copolymerisation of NIPAAM with acrylonitrile [107]. The cross-linked copolymer of PU and NIPAAM in an AB block structure was found to have controllable swelling/de-swelling properties [108].

The plasma glow discharge of NIPAAM vapour prepared substrates and functionalised polymers [109]. NIPAAM was also grafted onto a nylon 6,6 membrane and a polystyrene membrane by free radical graft copolymerisation through atmospheric plasma treatment [110]. A NIPAAM monomer was grafted and polymerised onto argon plasma irradiated PP membrane [111],[112] and polycarbonate track-etched membrane through the plasma-induced graft polymerisation technique [113],[114]. The radiation-induced graft polymerisation of acrylic acid with NIPAAM on PET fabrics was also reported [115]. NIPAAM could blend with the poly(acrylic acid)-g-PVDF for a temperature sensitive microfiltration [116].

2.4.2 PVDF and its activation for copolymerisation

PVDF polymer has a repeated monomer unit of $CH_2=CF_2$ as shown in Figure 2.14.

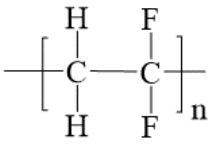

Figure 2.14 PVDF chemical structure

PVDF is a semi-crystalline polymer which shows an unusual polymorphism among polymers. PVDF normally consists of at least four polymorphs, α, β, γ, and δ; however, α-PVDF and β-PVDF are more commonly found. The mechanical properties of PVDF are reported as flexible, high mechanical resistance, dimensional stability, homogeneous piezoelectric activity within the film, high piezoelectric coefficients without any aging effect for temperatures up to 80°C, and a high dielectric constant [117]. It is known that PVDF is a hydrophobic material and the contact angle of pure PVDF film is approximately 88° [118].

It was reported that the α-PVDF has no local piezoelectric activity correspond to the nonpolarity of the macromolecule [119] while β-phase has the strongest piezoelectric and ferroelectric properties and spontaneous dipoles within its crystal structures. Therefore, the development of PVDF piezoelectric film based on the β-phase through the stretching process influenced by the degree of crystallinity of the polymer [120],[121] have been commercially introduced; however, this film is related to the strong coercive field. Recently, the ferroelectric materials with a weaker coercive field are designed on the basis of two copolymers, namely, the vinylidene fluoride–trifluoroethylene copolymer (VDF−TrFE) and the vinylidene fluoride–tetrafluoroethylene copolymer (VDF-TeFE) [122].

There are existing researches about the superhydrophobic of PVDF film; for example, the polyethylene glycol (PEG) and PVDF film showed a contact angle at 95° when mixing PVDF with PEG [123]. The nonsolvent induced phase separation can form a contact angle at about 135° [124]. Additionally, the chemical vapour deposition method can produce a contact angle of PVDF at 155° [125].

In contrast, there are existing researches about the hydrophilicity of PVDF; for example, irradiating PVDF film with argon ions and oxygen reduced the contact angle of the film to 31° [126]. The addition of TiO_2 to PVDF decreased the contact angle of the PVDF film to 55° [127]. Moreover, the graft polymerization of N-vinyl-2-pyrrolidinone under UV irradiation was used to treat the PVDF blended PES membrane and the contact angle of the film was reported at 32° [128]. PVDF membrane which is used in an immunological assay can be activated with ethanol and saturated with a wetting agent such as phosphate buffered saline (PBS) to produce a hydrophilic membrane [129].

PVDF is also used in the cosmetic and medical industries; for instance, the construction of vascular grafts and a sewing ring of prosthetic heart valves by a dip coating technique of PVDF on woven PET fabric, it was found to be uniform and no significant changes occurred on its physical and mechanical properties [130]. In additional, PVDF film was built into a wearable cardiorespiratory signal sensor device for monitoring sleep condition [131].

2.4.2.1 Activation of PVDF polymer via ozone oxidisation

PVDF is a hydrophobic and chemical resistant polymer: it hardly absorbs any water vapour and does not react with any other chemical agents without activation. Ozone oxidisation, plasma treatment, γ-irradiation [132], potassium hydroxide treatment

[133], and other methods to activate PVDF polymers for its copolymerisation with NIPAAM were reported. However, only ozone oxidisation and plasma treatment processes among those methods are environmentally friendly, low cost and commercially available technologies: they are reviewed in details below.

Ozone gas is a reactive substance able to degrade into an atom and a molecule of oxygen. Atomic oxygen is highly reactive due to the unpaired electrons in its last orbital allowing it to attack and etch most polymers [134]. The ozonisation of inert polymers, i.e. PVDF polymer, is to cut down its polymer molecular chains by adding new heat-sensitive groups such as peroxides and hydroperoxide groups (-COOH). This method is simple and quick by using the gas mixture of ozone and oxygen bubbled through the polymer solution, cooling it quickly and precipitating polymer in a non-solvent [135]. The adding of peroxide moieties to the backbone of the polymer can be seen in Figure 2.15 The peroxide moieties are either then reduced to hydroxyl groups that make the polymer reactive or serve as a thermal initiator to accept suitable free radical polymerizable moieties (i.e. $CHR_1=CR_2R_3$) onto the polymer [136].

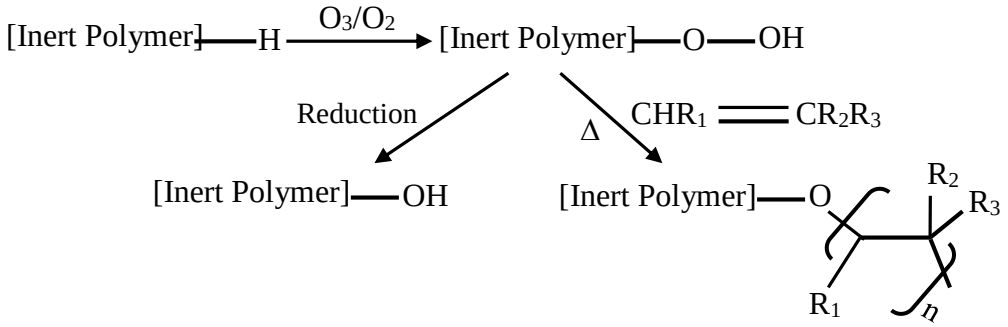

where R_1, R_2, R_3 are independent organic groups and *n* is a positive integer ranging from 1 to 100,000

Figure 2.15 The ozonolysis of the inert polymer [136]

The chemical bond between carbon and fluoride can be broken in an ozonalysis process [137]. The peroxy moieties attached to PVDF polymer chains might be reduced to hydroxy moieties as shown in Figure 2.16

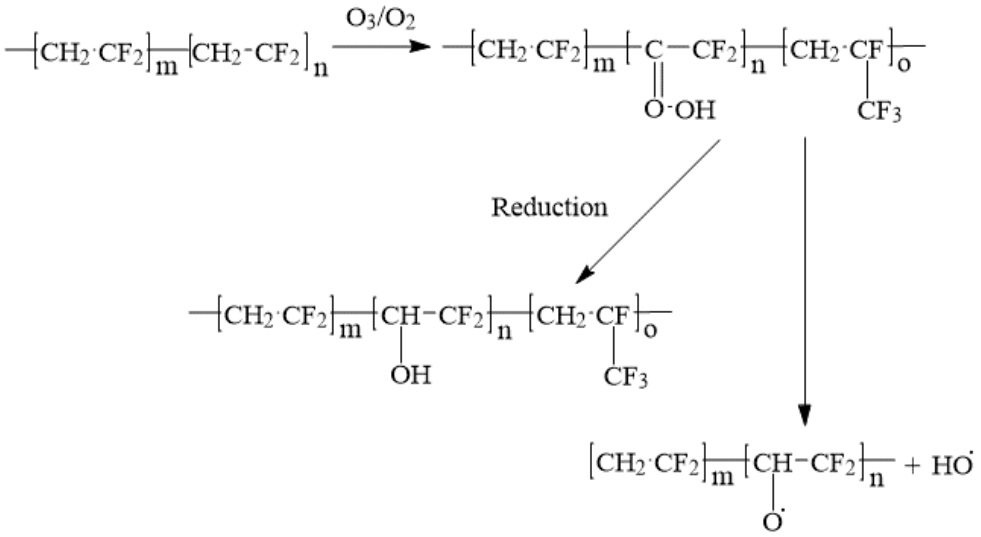

Figure 2.16 The ozonolysis of PVDF polymer [136]

2.4.2.2 Activation of PVDF polymer via plasma treatment

Plasma is a state of material in which all matter is ionized and it is composed of a mixture of negatively and positively charged particles, electrons, neutral atoms and molecules of an extreme high energy level [137]. Plasma energy is delivered into targeted objects in either low pressure or atmospheric pressure plasma treatment system [139].

There are three different modes reported; firstly, the plasma of non-polymerisable gases such as argon, helium, N_2, O_2, CO_2, NH_3 are widely used to give rise to the formation of free radicals on the polymer surface and further down the surface [140] in order to modify its surface properties. The porous polymer membrane treated with these non-polymerisable gases shows surface etching with an enlargement of pore dimensions. Functional groups such as hydroxyl, carboxyl, amine, imine, amide, or nitrile are added onto the membrane surface to enhance its polarity [141].

Secondly, the plasma of polymerisable vapours such as allyl alcohol, allylamine, and butylamine is used for the deposition of plasma thin film on the membrane surface. [139].

Lastly, the plasma generated radicals on polymer surface and thus induced grafting onto the polymer [142]. The plasma activated membrane was then exposed to oxygen or air and formed some peroxides and hydroperoxide groups on the membrane surface.

Plasma treatment of PVDF polymer with argon, oxygen, and the mixture of argon and oxygen plasma enhanced its hydrophilic property [143], [144]. It changes the surface polarity by adding C=O, hydroxyl, and carboxyl groups in the oxidation process [145]. The plasma induced copolymerisation of PVDF grafting with NIPAAM [146], [147] or styrene monomer [148] were achieved.

Both ozone oxidisation and plasma treatments of polymer membranes are environmentally friendly, fast, flexible, and versatile technologies [149]. However, plasma treatment has the drawback of low repeatability, scaling-up, and technical problems in continuous process [139].

2.4.3 Copolymerisation of PVDF-NIAAM polymer materials

Activated PVDF polymer can be copolymerised with various monomers including NIPAAM, styrene, acrylic acid and, glycidyl methacrylate [150]. However, this review focuses on the copolymerisation of PVDF and NIPAAM.

There are many NIPAAM and PVDF copolymerisation methods proposed. For example, atom transfers radical polymerisation by using copper(I)chloride (CuCl) as a catalyst with 4,4 dimethyl-2,2-dipyridyl as a ligand [151], [152], [153] was reported for the copolymerisation of PVDF and NIPAAM in an inert atmosphere; NIPAAM was grafted on PVDF polymer via surface-initiated atom transfer radical polymerization techniques using CuCl, and copper(II) chloride ($CuCl_2$) as the catalyst with hexamethyl tris (2-aminoethyl)-amine (Me6Tren) as the ligand [154]; NIPAAM hydrogel copolymerised with PVDF membrane by electron beam technique [155] was also reported. However, those methods require either longer copolymerisation time or a greater amount of NIPAAM than that in the thermally induced copolymerisation method.

Moreover, the other method for copolymerisation of NIPAAM on PVDF membrane is the γ-irradiation [132] or γ-rays from an extended Cobalt-60 source [156]. This method is fast processing because the radiation only involves the electron beam from electron accelerators. However, the reaction occurs at the molecular level and is not instantaneous, and it was performed in a small scale industry and requires equipment expertise [156].

Moreover, the copolymerisation of the NIPAAM and PVDF by thermally induced grafted copolymerisation was also proposed. PVDF polymer be activated by

ozonolysis before the copolymerisation. [157], [158], [159]. This method is quicker than the ATRP method and can be expanded to larger scale.

Lastly, in the copolymerisation of NIPAAM and PVDF by using plasma gas such as argon gas [105], [160] to activate the porous PVDF membrane, NIPAAM was copolymerised on the PVDF membrane in aqueous solution. However, there is not much research on the plasma induced copolymerisation of PVDF and NIPAAM by using the plasma induced copolymerisation. Therefore, the plasma treatment of other porous polymeric membranes such as PET, PP or polystyrene before grafting to NIPAAM by oxygen gas, atmospheric pressure gas [161], [162] or the mixture of the argon and oxygen [143] and a radio-frequency plasma [163] can be applied to treat the porous PVDF membrane before copolymerisation with NIPAAM.

2.4.4 Formation of copolymer membrane by phase inversion technique

Among all of the techniques available to produce polymeric membranes such as sintering, stretching, track-etching, and sol-gel processes, the phase inversion technique is used to produce membranes having all kinds of morphologies including porous and nonporous membranes of dense structures [164].

In the phase inversion process, the solidification of a polymer solution into a membrane is often initiated by the transition from one liquid state into two liquids (i.e., liquid-liquid demixing) and precipitation in a liquid solvent. The membrane precipitation is then induced by means of liquid-liquid de-mixing and/or crystallization. During demixing, one of the liquid phases (the high polymer concentration phase) will solidify so that a solid matrix is formed. The membrane morphology can be controlled by varying the initial stage of phase transition. During precipitation, the solvent evaporation, vapour phase, controlled evaporation, thermal precipitation, and immersion precipitation can be selected to prepare the membrane. The morphology of the membrane formed in the phase inversion process is influenced by the polymer concentration, composition, viscosity, and solvent when using the casting solution, the composition, and the temperature of the coagulation bath [131], [165], [166], [167].

2.4.5 Methods for the examination of membrane structure and properties

2.4.5.1 Methods for the examination of functional groups of membrane

2.4.5.1.1 Fourier Transform Infrared Spectroscopy (FTIR)

The FTIR technique has been used extensively for the determination of functional groups in polymer and copolymer materials. The presence of the new absorption bands in treated polymers is seen as evidence of new functional groups added to the untreated polymers. There are two types of FTIR analysis available that are frequently used: FTIR analysis of a mixture of polymer sample and potassium bromide (KBr) (KBr-FTIR); and FTIR analysis with attenuated total reflectance (ATR-FTIR). In KBr-FTIR, the targeted polymer samples are mixed with KBr which is transparent in the mid- infrared (IR) beam, so that the IR penetrates through the mixture of the polymer sample and KBr. This allows an infrared spectrum of the mixture to be collected; KBr-FTIR is thus used to determine the functional groups of the properties of the bulk polymer bulk materials. The infrared radiation in ATR-FTIR penetrates through the sample layer in the range of 0.5-3 μm [168] and it is thus used only for surface analysis.

2.4.5.1.2 Time-of-flight secondary ion mass spectrometry (ToF-SIMS), X-ray photoelectron spectroscopy (XPS) and Nuclear magnetic resonance spectroscopy (NMR)

Time-of-flight secondary ion mass spectrometry (ToF-SIMS) is a characterisation technique based on the mass spectrometric analysis of secondary ions which is generated by the interaction of a primary ion beam bombarding the sample surface in an ultra-high vacuum chamber. The principle is that the ions that have the same kinetic energy will have velocities proportional to their masses. In the ion source of a TOF instrument, ions of all masses are formed almost simultaneously using a very brief burst of energy and then are accelerated out of the ion source [169].

The resultant spectrum shows the intensity in counts per second as a function of mass ($m\ z^{-1}$). The ions of different $m\ z^{-1}$ values exhibit different speeds and the ions of different $m\ z^{-1}$ value reach the detector at the different times, and the proportional to the square root of their $m\ z^{-1}$ value [170]. This method provides a qualitative data by showing the presence of a compound composition at the surface in a range of parts per billions in the specific mass molecules.

X-ray photoelectron spectroscopy (XPS) is an analytical method for determining the species present at solid surfaces [171]. The method is based on an x-ray photoelectric effect to determine the molecular bonding environments present and elemental make up of a substrate; however, the depth of the x-ray is less than 10 nm, and so might not be representative of the composition of the whole samples.

Nuclear magnetic resonance spectroscopy (NMR) is another effective technique for obtaining physical, chemical, electronic, and structural information about molecules on the magnetic resonant frequencies of the nuclei present in polymer sample nuclei [172]. In principle, it is used to quantitatively determine the relative amount of molecular groups and to quantify the entire molecular structures in mixtures of a sample [173].

2.4.5.2 Methods for examination the porous structure of membrane

The structure and morphology of the porous membrane is examined by using various types of methods depending on the nature of pore geometry and pore sizes.

2.4.5.2.1 Scanning electron microscopy (SEM)

Scanning electron microscopy (SEM) is a tool used to obtain information on the surface morphology of a polymer membrane such as the pore structure or the surface roughness by applying a narrow beam of high energy electrons with a kinetic energy of around 1-25 kV onto the surface of polymer samples. The resultant images obtained from the reflected electrons and the electrons liberated from atoms in the polymer surface show the surface morphology of the sample. It has a high resolution of up to 300,000 in field emission SEM (FESEM).

2.4.5.2.2 Gas adsorption method

An inert gas such as nitrogen or argon is usually used as the adsorbed gas on the surface of the sample. Brunauer-Emmett-Teller (BET) isotherm is widely used for the gas adsorption.

In this method, the pore size and pore size distribution is measured by collecting the amount of adsorbed gases on the surface of a porous material, which depends on its microstructure, gas pressure, and a given temperature. The pore structure is assumed to resemble ink-bottle like cylindrical pores [14].

BET adsorption theory has been used to obtain the adsorption isotherms of gases adsorbed onto porous polymer materials; however, this theory is used based on three assumptions [174]. Firstly, gas molecules are physically absorbed into a solid polymer surface infinitely; secondly, there is no interaction between each absorption layer; and lastly the Langmuir theory of monolayer adsorption can be applied to each layer. The relationship between the volume of adsorbed gases and relative pressure is shown in equation (2-23) below [14].

$$\frac{P/P_0}{v(1-P/P_0)} = \frac{1}{v_m} + \frac{(c-1)}{cv_m} \cdot \frac{P}{P_0} \quad (2\text{-}23)$$

where

v is the volume of adsorbed gas (cm^3),

v_m is the volume of a monolayer of the gas (cm^3),

c is a constant related to the difference between the molar free energy of adsorption of the first layer and the liquefaction one,

$\frac{P}{P_0}$ is the gas pressure relative to its saturation pressure (Pa).

One limitation of the BET method is that it can only detect nanopores whose size is ranged from 1 to 300 nm, and it might also not be suitable for deformable polymer membrane.

2.4.5.2.3 Mercury Porosimetry

Mercury porosimetry is the characterisation method for measuring pore size, pore size distribution, specific surface area, pore volume, skeleton, and apparent density of the sample; however, the pores that were analysed are not the actual pore size but instead are the largest entrance to a pore [175]. The pore volume at a given pore size is assumed to equal to the volume of mercury introduced into the pores. The relationship between external pressure and pore size is described by using the Laplace equation as shown in equation (2-24) below [14].

$$r_p = -\frac{2\gamma\, cos\theta}{\Delta P} \quad (2\text{-}24)$$

where

r_p is the inner radius of a cylindrical pore (nm),

P is the external pressure applied on mercury flow (bar),

γ is the surface tension of mercury (0.48 N m^{-1}),

θ is the contact angle between mercury and the membrane specimen, it is often considered approximately 141.3°.

Mercury porosimetry is used to measure all kinds of pores including ink-bottle like cylinder pores and dead-end pores [164]. The pore size measured ranges from 2 nm to 100 µm. However, the pore structure measured under applied high pressure might be distorted and damaged during testing, and the method itself is expensive and requires expertise in handling the toxic mercury used in the testing.

2.4.5.3 Methods for the examination of the crystallinity of membrane

The crystallinity of a polymer membrane is not only related to its mechanical properties including yield stress, elastic modulus, and impact resistance [176], but also is an important factor influencing the vapour permeability of the membrane. While the amorphous phase of the polymer membrane has inter-chain space available for permeation [134], the crystalline phase of the membrane has little or no free space among its polymer chains for the passage of a permeant. It is thus normally considered impermeable to most fluid species. Therefore, it is necessary to characterise the polymer membrane for the evaluation of its fluid permeation properties. Infrared spectroscopy, Raman spectroscopy, NMR sprctroscopy, differential scanning calorimetry (DSC), thermal mechanical analysis, dynamical analysis, optical microscopy, transmission electron microscopy, XRD and neutron scattering are the characterisation techniques to investige the various structure of the polymer [177].

DSC might be the most widely used technique to determine the crystallinity even though it was the most misused method [176]; for example, this method defines the degree of crystallinity closed to the melting point of the polymer rather at room temperature as indicated in equation (2-25). However, the investigation of the crystallinity by DSC is used in this study in order to compare the difference of their crystallinity between the pristine PVDF polymer, the copolymer material and the copolymer membranes.

DSC analysis provides quantitative and qualitative information about physical and chemical changes that involve endothermic or exothermic processes and changes in heat capacity. The structure and crystallization of a polymer is sensitive to its thermal behaviour [178], especially the melting temperature and glass transition temperature of the polymer [179]. The influence of thermal history on the melting behaviour of a polymer is used to identify the polymer's polymorphs.

Enthalpy measurement is obtained from the area of the melting peak. The crystallinity of the polymer is obtained by quantifying the heat associated with its melting profile, and is presented as a percent crystallinity by normalizing the observed heat of fusion

to that of a 100 % crystalline sample of the same polymer as shown in equation (2-25) below [180].

$$\text{crystallinity } (\%) = \frac{(\Delta H_a - \Delta y)}{(\Delta H_a - \Delta H_c)} \times 100\% \quad (2\text{-}25)$$

where

ΔH is the enthalpy change of the unknown specimen,

ΔH_a is the enthalpy change of the pure amorphous standard (ΔH_a=0 for pure amorphous polymer),

ΔH_c is the enthalpy change of the pure crystalline standard.

2.4.5.4 Methods for examining water contact angle

Wetting is a thermodynamic process which depends on surface free energy and surface roughness. It is also used to describe the replacement of a solid-liquid or liquid-air interface with a liquid-liquid interface and a solid-air interface with a solid-solid interface. To determine the net effect of the three interfacial tensions, the water contact angle is proposed. When a liquid drop is placed on an ideal flat solid surface (smooth homogenous, impermeable, and non-deformable), the liquid drop comes to an equilibrium state corresponding to the minimization of interfacial free energy of the system. The forces involved in the equilibrium of wetting are given in Young's equation in equation (2-1). The water contact angle is used to determine the surface free energy of the solid membrane in order to compare the surface roughness during the membrane modification.

2.5 Problem identified, objectives and solutions

It is ideal for chemical protective clothing to have both excellent chemical barrier properties and better moisture management properties. It is found that, while the chemical barrier properties of existing impermeable and semipermeable chemical protective clothing are excellent (breakthrough time is at least greater than 480 minutes), the thermal comfort properties are not reported; however, it was reported that the maximum duration of 120 minutes wearing permeable protective clothing and a maximum of 30 minutes wearing impermeable clothing indicates that there is great

demand to improve the thermal comfort properties of existing chemical protective clothing.

Objectives of the research are summarised below:

1. To identify gaps between existing chemical protective clothing products in terms of the liquid chemical permeation property and the thermal comfort property.

2. To develop a new barrier membrane material for use as a protection layer in chemical protective clothing while improving the membrane's moisture management property in order to maintain the body temperature of the wearer when the environmental temperature is changed.

3. To study the mechanism of the liquid chemical permeation and water vapour permeation through the nanoporous membrane.

In this research, a thermo-responsive membrane is proposed to be used as a smart barrier membrane in chemical protective clothing in order to improve the water vapour transmission property of the chemical protective clothing while maintaining its excellent protection property.

NIPAAM is studied in this research as an alternative material by copolymerisation the thermo-responsive material with PVDF polymer for use as a semipermeable membrane in chemical protective clothing. Because the LCST of NIPAAM is around 31-33°C when responding to changes in the human body's temperature, the water vapour transmission property of the membrane may be improved. With the advantage of PVDF being a chemical resistant material, the developed copolymer membrane will maintain its excellent protection property for use as a barrier material in chemical protective clothing.

Chapter 3 Characteristics of structure and properties of the fabrics used in the commercially available protective clothing products

It was found in Chapter 2 that the thermophysiological comfort properties of commercially available chemical protective clothing products are not known, and that it is difficult to compare their chemical permeation properties as attested to by their manufacturers as the testing conditions were not known. The objective of this chapter is to characterise the structure, liquid chemical protection, and thermophysiological properties of barrier materials used in commercially available chemical protective clothing products. This is to identify ways of enhancing the thermophysiological properties of barrier membranes while maintaining their chemical permeation properties.

3.1 Characteristics of the porous structures of the commercially available chemical protective fabrics

No matter permeable or impermeable, the seven chemical protective clothing products examined in this chapter are made of porous textile fabrics. It is important, therefore, to understand how the fabrics' porous structures affect the chemical permeation and thermal comfort properties of the protective clothing.

The characteristics of the porous structures of the fabrics used in the seven commercially available chemical protective clothing products described in Section 2.1.2 in Chapter 2 are examined and discussed in this chapter. Two aspects of the fabric's porous structures are examined in this section: fabric porosity and their porous morphology.

3.1.1 Porosities of the fabric structures

Fabric porosity is determined as the ratio of bulk density to the true density of the fabric materials in the equation below [181].

$$\varepsilon = \left(1 - \frac{\rho}{\rho_s}\right) \times 100 \qquad (3\text{-}1)$$

where
ε is the porosity (%),
ρ is the bulk density of the fabric (kg m^{-3}),
ρ_s is the true density of the fabric (kg m^{-3}).

True density is the density of a solid material excluding any void contained within it, whereas in contrast bulk density is the average density of the material including voids, in a specific volume [182]. The true density of the fabrics was measured by using AccuPyc 1330 pycnometry based on the standard ISO 12154:2014 [183]. Before the measurement, the sample was dried at 60°C in an oven over 24 hours to remove their moisture contents. The average of five measurements of each specimen was obtained as the true density of the fabrics.

Bulk density is defined as the mass per unit area divided by fabric thickness as shown in the equation (3-2) below.

$$\text{Bulk density} = \frac{\text{Mass per unit area}}{\text{Fabric thickness}} \quad (3\text{-}2)$$

The fabric thickness was measured in Progage thickness tester (Thwing-Albert Company) by applying pressure at 0.5 kPa on the surface according to the standard ISO 4593:1993 [184]. The fabric's mass per unit area was measured based on the standard BS 2471:2005 [185], and its mass was obtained on an Ohaus Adventurer™ balance. The fabrics were conditioned in a conditioned room at 23±2°C and 65±5 % RH for at least 24 hours before testing their mass and thickness.

The fabric porosity of the seven commercially available chemical protective fabrics, together with their thickness, mass per unit area, bulk density and true density, are shown in Table 3.1.

It is found in Table 3.1 that Tyvek is a flashspun thermobonded polyethylene nonwoven fabric with the smallest thickness; Tychem F is a laminated fabric that has a comparably small thickness. The fabrics from the other commercially available chemical protective clothing products are laminated nonwoven fabrics of many layers including membrane materials having greater thickness.

The porosity of the fabrics, whether permeable or impermeable, ranges from 66.8% to 86.9%. Tyvek is a permeable fabric designed to prevent the penetration of solid particulates, and has the smallest mass per unit area of 45 g m^{-2} and highest porosity of 86.9% among the fabrics. Microgard 2500 and Microchem 3000 consists of multiple layers of polypropylene spunbond nonwovens laminated with barrier membrane, and have the medium mass per unit area around 72~86 g m^{-2} and high porosities around 82%. Microchem 4000, Tychem F and Tychem F2 consist of multiple layers of coated nonwoven fabrics laminated with multiple-layers of barrier

membrane: they have the greatest mass per unit area and smallest porosities between 66.8% and 78.8%. Tychem C2 also consists of multiple layers of coated nonwoven fabrics laminated with a barrier membrane, but it has medium mass per unit area of 120 g m^{-2} and greater porosity around 82%.

Therefore, whether the fabric is permeable or not, the barrier fabrics could be made in a different range of fabric porosities and fabric mass per unit area. This is engineering design of various fabric structures is expected to achieve different fabric thermal resistance and moisture management performance, which determines the thermophysiological performance of chemical protective clothing made from those fabrics.

Table 3.1 Density and porosity of the fabrics used in the chemical protective clothing

Sample	**Average thickness (mm)**	**Mass per unit area (g m^{-2})**	**Bulk density (kg m^{-3})**	**True density (kg m^{-3})**	**Porosity (%)**
Tyvek	0.38	45	118.4	904.80	86.9
Tychem C2	0.76	125	164.5	925.20	82.2
Microgard 2500	0.44	72	163.6	910.80	82.0
Microchem 3000	0.57	86	150.9	887.30	83.0
Tychem F	0.39	122	312.8	941.80	66.8
Tychem F2	0.79	155	196.2	925.80	78.8
Microchem 4000	0.52	102	196.2	869.10	77.4

3.1.2 Microstructure of commercially available chemical protective fabrics

The morphology of the fabrics used in the seven commercially available chemical protective clothing products are examined by using SEM as shown in Figure 3.1. The examples of the cross section of the porous structure of Tyvek and Tychem F2 shown in Figure 3.2 and Figure 3.3, respectively.

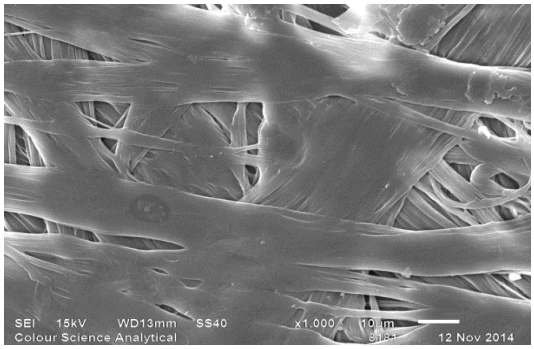

(a) Tyvek

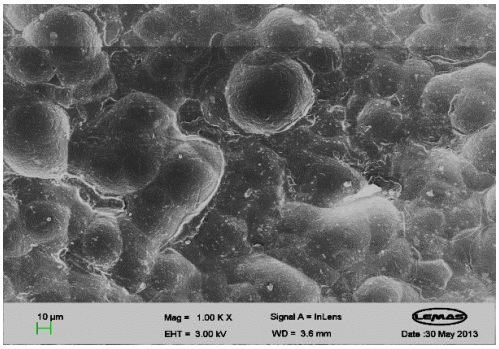

(b) Tychem C2

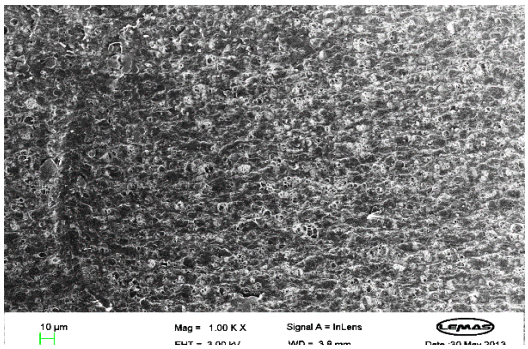

(c) Microgard 2500

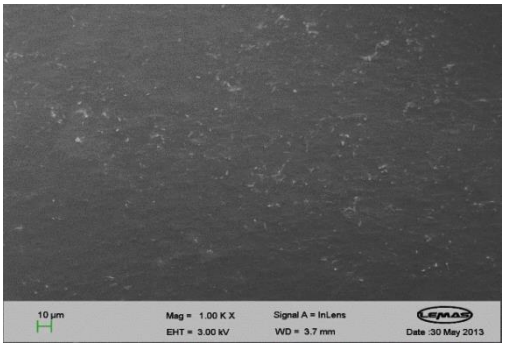

(d) Microgard 3000

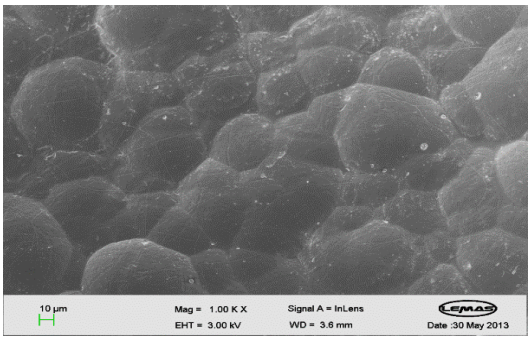

(e) Tychem F

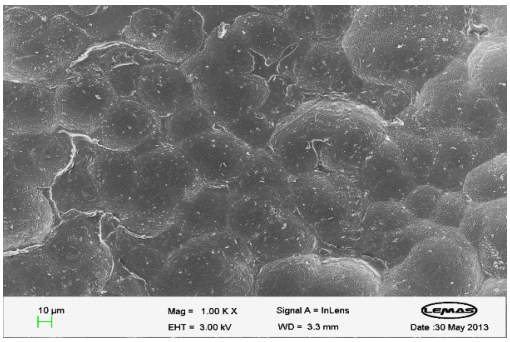

(f) Tychem F2

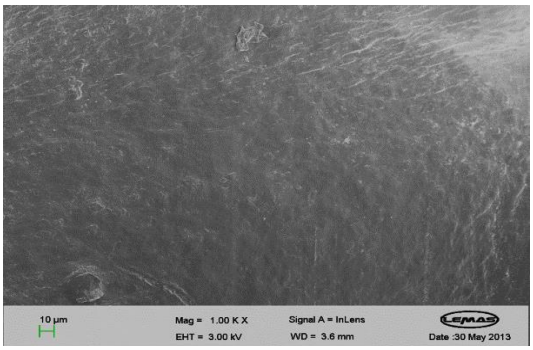

(g) Microgard 4000

Figure 3.1 The surface morphology of the fabrics used in the seven commercially available chemical protective clothing products (magnification: 1000)

It is found in Figure 3.1(a) that Tyvek has much more pores than the other six fabrics because it is an uncoated spunbond polyethylene nonwoven fabric. Both Microgard

2500 and Microchem 3000 are also uncoated fabrics and have much smaller pores on the polymeric laminated layer on the fabric surface as seen in Figure 3.1 (c) and (d), respectively. Fabrics of Tychem C2, Tychem F, Tychem F2 and Microchem 4000 are all fabrics coated with continuous barrier layer without apparent pores appeared as shown in Figure 3.1 (e), (f) and (g), respectively.

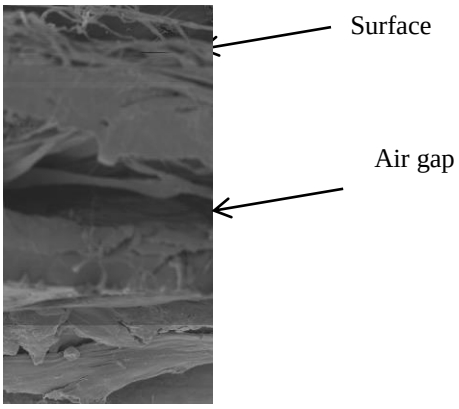

Figure 3.2 The cross section of Tyvek (magnification: 100)

It is found in the cross-section of Tyvek nonwoven fabric in Figure 3.2 that, while the Tyvek fabric has the smallest thickness as shown in Table 3.1, it still contains two layers of nonwoven fabric with an apparent air gap in between.

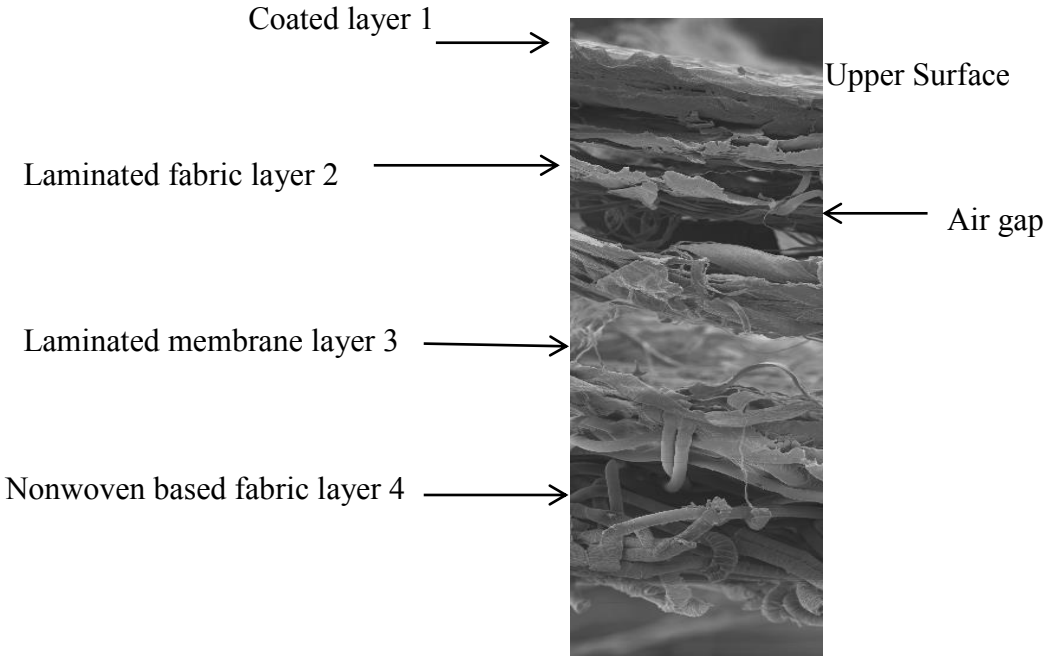

Figure 3.3 Tychem F2 Cross section (magnification: 80)

Tychem F2 is a typical impermeable coated fabric: its cross-section structure is shown in Figure 3.3. There are four layers in this laminated fabric: one coating layer; two layers of nonwoven fabric and one layer of membrane laminated together. There are air gaps or air pockets found between these laminated structures. The layer of the laminated membrane between the spunbonded nonwoven fabric is expected to act as a resistant layer to resist chemical permeation through the laminated chemical barrier fabric.

In summary, all of the seven protective fabrics contain multiple layers of porous nonwoven fabric. This characteristic of their porous structure is envisaged to influence the thermal properties of the fabrics and thermal comfort performance of their clothing. It is also found that some of the fabrics are coated fabrics and some contain coated fabrics together with laminated continuous membrane. Therefore, the seven protective fabrics are characterised based on the air permeability through their fabrics as can be seen in Table 3.2.

Table 3.2 The classification of commercially available chemical protective clothing

Fabrics	**Types**
Tyvek	Permeable fabric
Microgard 2500	
Tychem C2	Semi-permeable fabric
Microchem 3000	
Tychem F	Impermeable fabric
Tychem F2	
Microchem 4000	

It is expected that the coated polymeric layer and the continuous membrane included act as the main barrier layer to resist the chemicals permeation through the protective fabrics. The characteristics of liquid chemicals permeation through the seven fabrics are examined in Section 3.2 below.

3.2 Chemical permeation properties of commercially available chemical protective fabrics

The selection of challenge chemical agent is the first vital factor to be considered in the design of proper method to characterise the permeation properties of protective fabrics.

As indicated in the literature review in Chapter 2, the liquid chemical permeation and water vapour transmission properties of NIPAAM-g-PVDF copolymer membranes are the main interests of the project. It is envisaged that a challenge solvent which could dissolve NIPAAM and have a smaller molecular size might have greater permeation rate in NIPAAM-g-PVDF copolymer membranes. A permeation test using such a solvent could thus better represent the more harsh chemical attack situations in chemical protective clothing.

It is noticed that NIPAAM is dissolved in n-hexane (C_6H_{14}), which is a strongly non-polar, aprotic solvent and have smaller molecular size. N-hexane is thus used to challenge the permeation performance of NIPAAM-g-PVDF copolymer membrane, in order to compare the permeation performance of NIPAAM-g-PVDF copolymer membrane and the fabrics from commercially available chemical protective clothing. The solvent used to challenge the fabrics used in the seven commercially available chemical protective clothing products is n-hexane as well.

However, the permeation properties of four fabrics of the seven commercially available chemical protective clothing products using n-hexane are not available (see Table 2.3). It is necessary, therefore, to characterise the permeation properties including dynamic permeation rate and breakthrough time of the seven commercially available chemical protective fabrics using n-hexane.

3.2.1 Modified method for characterisation of liquid permeation through barrier fabrics

An open loop system for measuring the dynamic permeation of liquid chemicals through protective fabrics is designed and developed for operating in ambient temperature in the range of 20°C to 27°C as defined in BS ISO 6529:2013.

3.2.1.1 Characteristics of the liquid chemical permeation measurement system

This system consists of a liquid permeation cell from Pesce Lab Sales Ltd, USA, and a multifunction Photo Ionization Detector (PID) gas detector, iBrid MX6, from Scientific Instrument Inc. USA. The liquid chemical permeation system is shown in Figure 3.4.

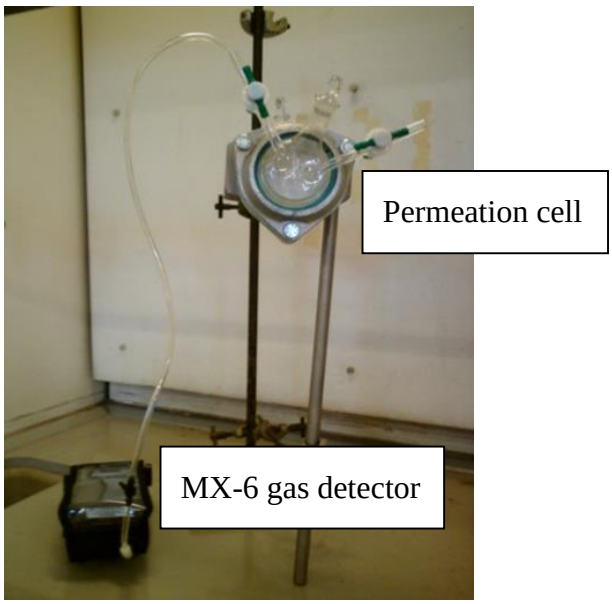

Figure 3.4 Schematic of the chemical permeation measurement system

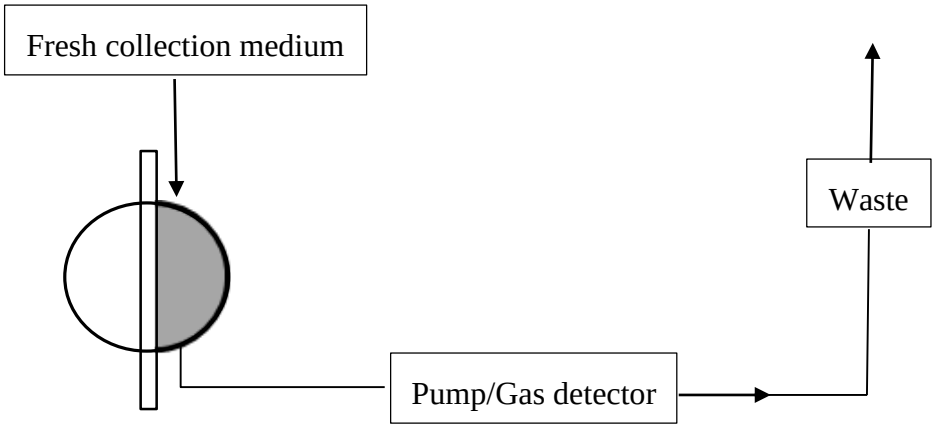

Figure 3.5 Schematic of the experiment setup of open-loop permeation measurement system

The liquid permeation cell consists of two chambers: challenge chamber and collection chamber. The cell is constructed from two end-fitting sections of straight glass pipe, each nominally sized to 51 mm diameter with the inlet and the outlet ports with appropriate stopcock valves added to each glass section. When assembled, the two glass sections are joined horizontally by flanges and a gasket is used at the joint.

The two chambers are separated by the fabric to be tested; the challenge chamber is filled with the chemical challenge agents and the collection chamber is filled with collection medium. The schematic of the assembly of the permeation testing system is illustrated in Figure 3.5.

Ambient air is used as the collection medium with a flow rate of 250 cm^3 min^{-1}. The real-time dynamic change of the concentration of the challenge chemicals permeation through the fabric sample is monitored and recorded by using an MX-6 PID gas detector. These data can be downloaded into computer for further data processing and analysis. The dynamic permeation rate of the challenge chemicals' permeation through a fabric is calculated by using the equation (3-3) below [42].

$$\varphi_i = \frac{c_i q_v}{A} \tag{3-3}$$

where

φ_i is the dynamic permeation rate at time t_i, (µg cm^{-2} min^{-1}),

i is an indexing number to indicate the specific concentration c_i that was measured at time t_i,

t_i is the time elapsed beginning with the initial chemical contact and end with the measurement of concentration c_i (minutes),

c_i is the concentration of test chemical in collection medium (µg dm^{-3}),

q_v is the flow rate of fresh collection medium through the cell (dm^3 min^{-1}),

A is the area of the fabric specimen contacted with chemical challenge agent (cm^2).

A comparison of the testing conditions used in ASTM 739-99a, EN ISO 6529:2013 standards, and the new system designed in this research is shown in Table 3.3. The common requirements defined in both ASTM F 739-99a and EN ISO 6529:2013 standards are that they both allow the diameter of permeation cell to be 51mm; dry air to be the collection medium; and the detection limit to be 0.1 µg cm^{-2} min^{-1}. However, the flow rate of the collection medium defined in the two systems varies widely each system. Because the flow rate of the collection medium has a great influence on the permeation rate measured, and thus a greater flow rate leads to a greater permeation rate, in this study, the new system is established to have a greater flow rate of collection medium to ensure that the challenge chemical agent is able to permeate

both the commercially available protective fabrics and the newly-developed membranes at a later stage in this research. Therefore, the new system is designed against the EN ISO 6529:2013 standard testing method while also considering the ASTM standard 739-99a: the diameter of the permeation cell is 51 mm, the collection medium is dry air, and the detection limit is 1 μg cm^{-2} min^{-1}. However, the flow rate of the collection medium is set as 250 cm^3 min^{-1}, which is greater than any of the flow rates defined in the two standards. This is a designated advantage of the new system for making sure chemical liquids are able to permeate through the testing fabrics.

Table 3.3 Comparison of the testing conditions used in ASTM 739-99a, EN ISO 6529:2013 standards and the new system designed in this research

Test method	**Diameter of permeation cell (mm)**	**Flow rate of collection medium (cm^3 min^{-1})**	**Detection Limit (μg $cm^{-2}min^{-1}$)**	**Collection Medium**
ASTM F 739-99a	51	50-150	0.1	- Dry air - Nitrogen gas - Helium gas - Distilled water
EN ISO 6529:2013	25 or 51	Five volume changes of collection chamber per minute	0.1 or 1	- Dry air - Dry, non-flammable inert gas - Distilled water - Other liquid not influence the resistance of the permeation
New system	51	250	1	Air

N-hexane, one of the hazardous chemical agent listed in NFPA 1991 and shown in Table 2.3, is selected in this research as the challenging chemical agent as discussed above. All of the tests conducted on each specimen should reach a steady-state condition as defined in both of the standards.

3.2.1.2 Calibration of the permeation measurement system

The new testing system need to be calibrated in a regular period of time. A standard reference material (neoprene sheet, 16 mm thickness) provided by Pesce Lab Sales Ltd, USA, is used as the inter-laboratory calibration for permeation resistance against acetone following the standard ASTM 739-99a. It is expected that the reference material should have a permeation breakthrough time about 12 minutes at 0.1 μg cm^{-}

^{2} min^{-1}, and the average permeation rate is around 245±54 µg cm^{-2} min^{-1} when the flow rate of collection medium defined in the standard is used [20].

A greater flow rate of 250 cm^{3} min^{-1} in this system leads to a greater permeation rate and a smaller breakthrough time, the expected permeation rate of the reference material is tested in the new system against acetone to compare with standard permeation rate provided.

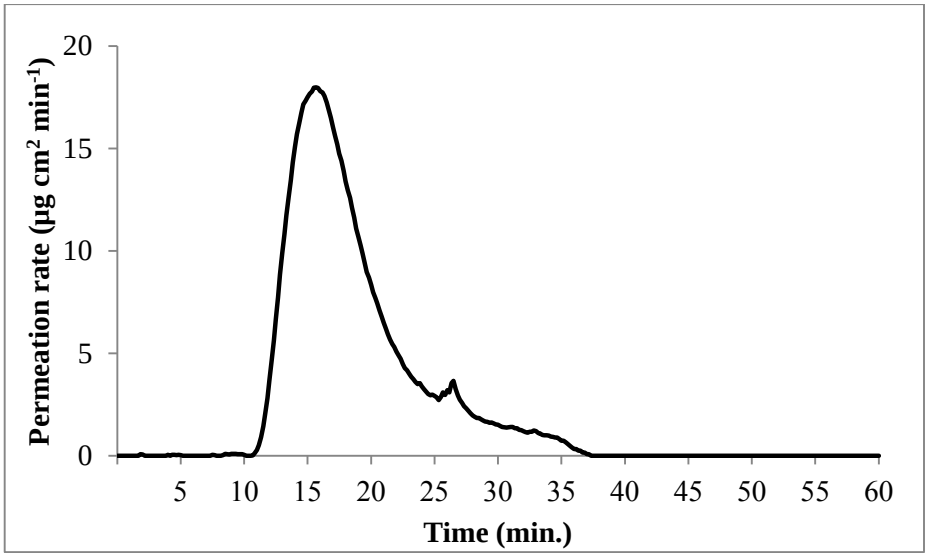

Figure 3.6 The permeation behaviour of standard reference material under flow rate of 250 cm^{3} min^{-1}

The standard reference material is prepared similar to the method as discussed in 3.2.1.2. The average of dynamic permeation rate of acetone through the standard reference barrier material is presented in Figure 3.6. It is found the breakthrough time of the standard reference barrier material is about at 10 minutes in comparison with 12 minutes for standard testing conditions when the permeation rate reaches 0.1 µg cm^{-2} min^{-1} according to the ASTM 739-99a Procedure A, which is lower than the standard requirement at 12 minutes. Therefore, it is estimated that the tested fabrics in the new system are about 17% quicker to breakthrough than they are in the standard system.

It is thus concluded that the newly established testing system in this study can be used to investigate the liquid chemical permeation behaviour of protective fabrics in this research.

3.2.1.3 Procedures of permeation test

Three specimens are taken randomly from the commercially available chemical protective clothing, the size of each specimen is approximately 50×50 mm. The specimens are conditioned at 21±5°C, 65±10% RH for at least 24 hours before testing.

The testing sample is placed into the liquid permeation cell as a partition between challenge chamber and collection chamber, so that the normal outside surface of the samples is in contact with the liquid chemical in the challenge chamber as shown in Figure 3.7. The collection chamber of the testing system is connected to the gas detector, iBrid MX6. The test is started when the challenge chemical is put into the challenge chamber and it is terminated when the steady-state permeation rate is reached and then proceeds at an ever increasing rate, when a maximum rate is reached, or when a pre-specified time has passed [42]. Therefore, the liquid permeation test is terminated when the permeation rate reach 1 μg cm^{-2} min^{-1} according to the requirement of the international standard.

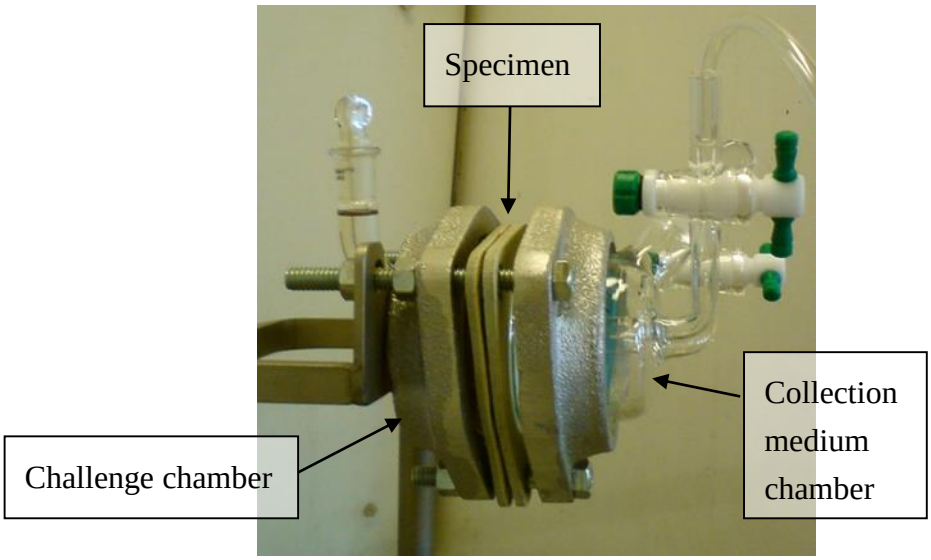

Figure 3.7 Assembly of the testing fabric specimen in the permeation cell

3.2.2 The liquid chemical permeation properties of the commercially available chemical protective fabrics

The liquid chemical permeation properties of the seven commercially available chemical protective fabrics were tested in the new system according to the testing procedures described in Section 3.2.1.3. It was found that the liquid chemical permeation properties of porous Tyvek fabric, classified as Type 2 of EN 943-1:2002,

cannot be tested in this new system as the liquids leak through the fabric immediately when it comes into contact with chemical challenge agent, n-hexane.
The chemical permeation properties of the other six chemical protective clothing fabrics are shown in Figure 3.8 to Figure 3.13, respectively.

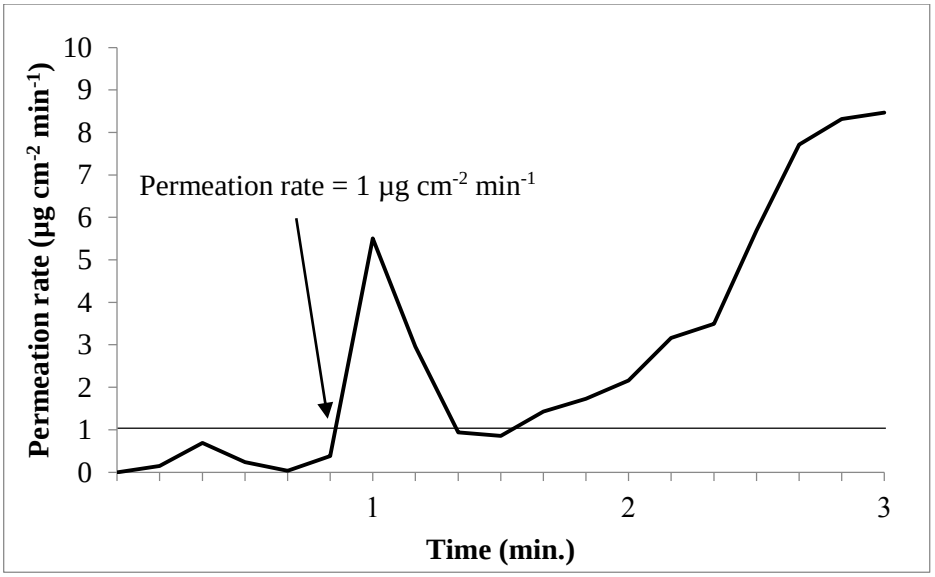

Figure 3.8 The dynamic chemical permeation rate of Tychem C2 fabric

The breakthrough time of Tychem C2 at the permeation rate of 1 µg cm^{-2} min^{-1} is approximately 50 seconds (see Figure 3.8) in this test. It is noticed in Table 2.3 that n-hexane permeates through the fabric immediately and there is no permeation data available for Tychem C2 in its datasheet summarised. It is not surprising that this fabric does not resist the permeation of n-hexane. It is also interesting to note that, while there is a polymeric coating layer on the fabric surface, as shown in Figure 3.1(b), the liquid chemical permeation property of Tychem C2 suggests the fabric and its polymeric coating to be porous structures.

The breakthrough time of both Microgard 2500 (see Figure 3.9) and Microchem 3000 (Figure 3.10) are around 10 seconds at the permeation rate of 1 µg cm^{-2} min^{-1}, which is much shorter than the breakthrough time of the polymeric coated fabric, Tychem C2. As with Tychem C2, there is no data available for the n-hexane permeation through the two fabrics in Table 2.3. This corresponds to the microporous structure found on the fabric surface as shown in Figure 3.1 (c) and (d) respectively.

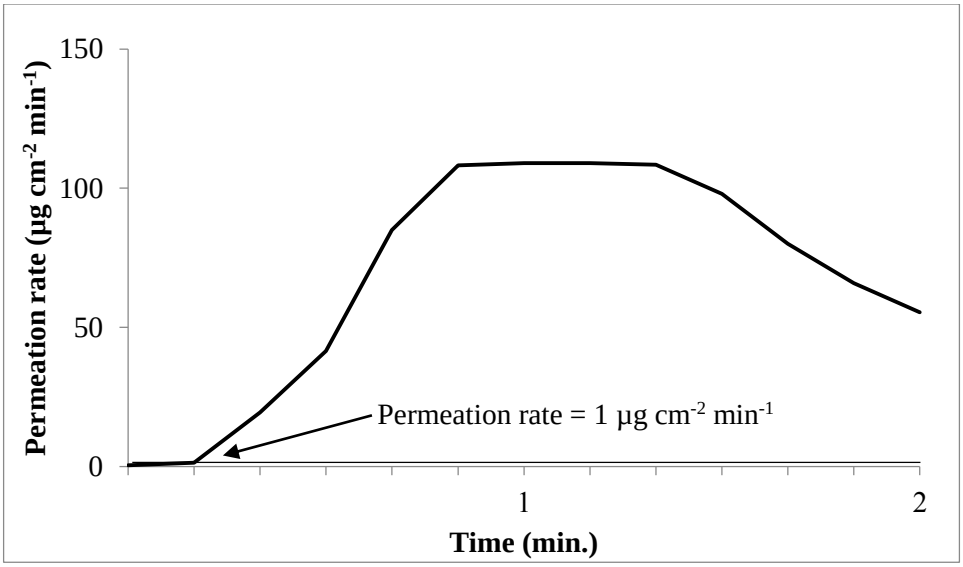

Figure 3.9 The dynamic chemical permeation rate of Microgard 2500 fabric

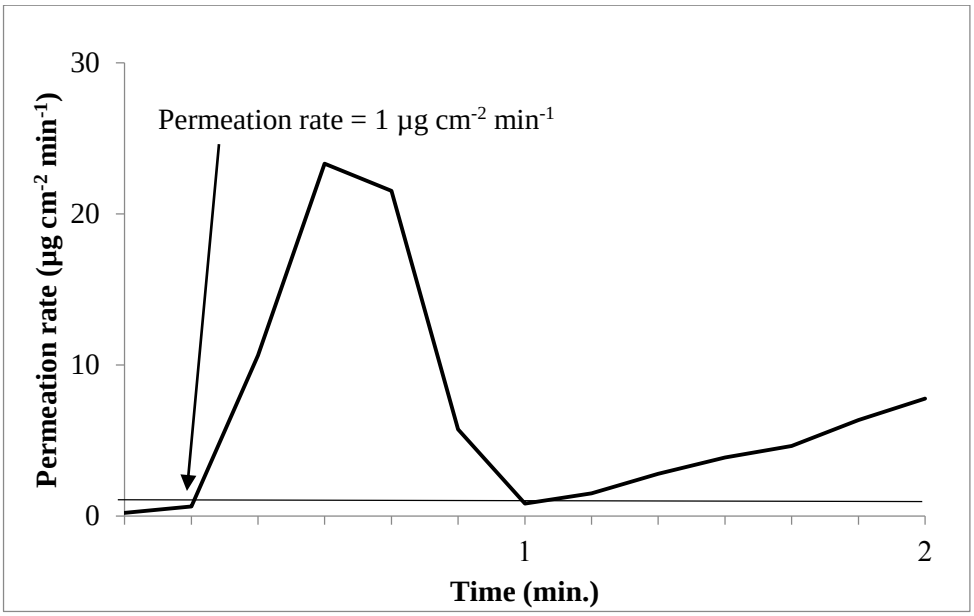

Figure 3.10 The dynamic chemical permeation rate of Microchem 3000 fabric

The breakthrough time of the fabric Tychem F (see Figure 3.11) is 47 minutes at the permeation rate of 1 µg cm^{-2} min^{-1}, which does not correspond to the breakthrough time of more than 480 minutes provided in Table 2.3. Moreover, when considering the surface morphology of Tychem F, it is found in Figure 3.1(e) that Tychem F is a thin, polymeric coated fabric with a similar mass per unit area as Tychem C2. It is suspected that the shorter breakthrough time might be due to either defects or pores existed in its polymeric coating layer.

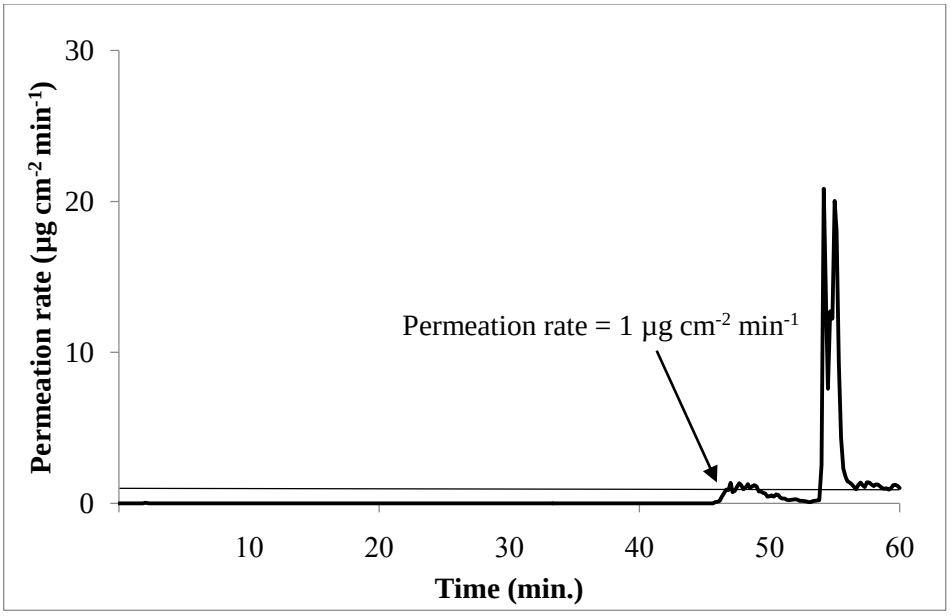

Figure 3.11 The dynamic permeation rate of Tychem F fabric

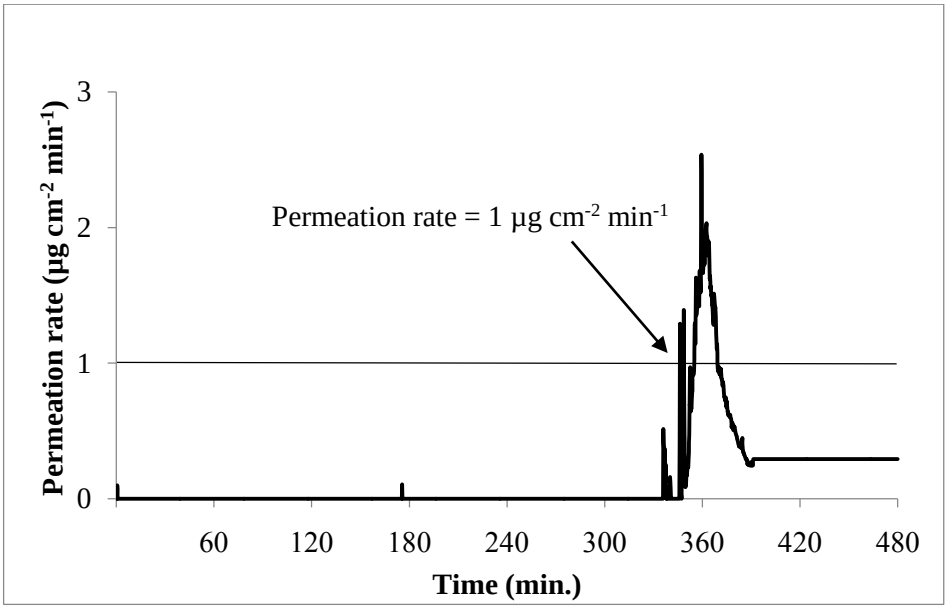

Figure 3.12 The dynamic chemical permeation rate of Tychem F2 fabric

The breakthrough time of Tychem F2 (Figure 3.12) and Microchem 4000 (Figure 3.13) are 330 minutes and 480 minutes respectively. The breakthrough time of Tychem F2 (Figure 3.12) tested is about 31% shorter than the breakthrough time of 480 minutes reported in Table 2.3. This is understandable as the flow rate of the collection medium is 250 cm^{-3} min^{-1}, and so the permeation rate measured should be about 17% less that that tested in standard conditions as discussed in Section 3.2.1. It is known from Figure 3.1(f) that both Tychem F2 and Microchem 4000 are coated

and laminated fabrics containing a continuous membrane. This multiple layered membrane structure corresponds well with the excellent liquid permeation property these fabrics have.

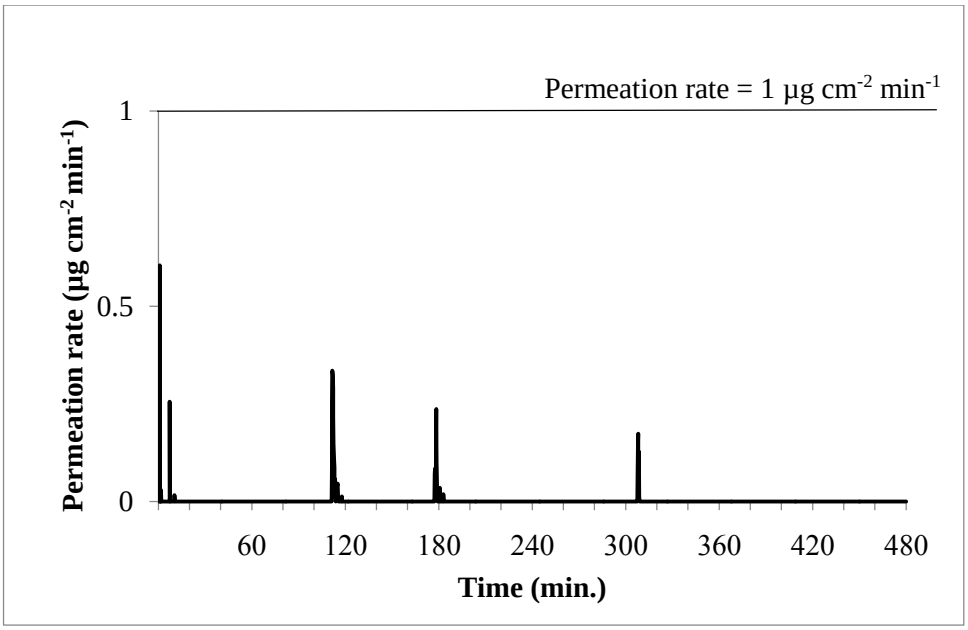

Figure 3.13 The dynamic chemical permeation rate of Microchem 4000 fabric

3.2.3 Section summary

A summary of the breakthrough time of the liquid n-hexane permeation through commercially available chemical protective fabrics is shown in Table 3.4.

It is found in Table 3.4 that these seven commercially available chemical protective fabrics can be generally grouped into three types according to their n-hexane permeation property. Firstly, Tyvek is an open and porous structure and has no liquid barrier property at all. Tychem C2, Microgard 2500 and Microchem 3000 can only resist permeation of n-hexane for less than 30 seconds and are thus grouped as poor barrier fabric which is corresponds to the classification of the fabric as mentioned in Table 3.2. Thirdly, Tychem F, Tychem F2 and Microchem 4000 can resist the permeation of n-hexane through the fabrics for 47 minutes, 330 minutes and 480 minutes, respectively, these three fabrics thus have a high level of chemical protection performance against n-hexane. Therefore, Tychem F, Tychem F2 and Microchem 4000 are classified as the excellent n-hexane resistant fabrics.

Table 3.4 Performance of the commercially available chemical protective clothing products

Samples	**Breakthrough time at permeation rate of 1 µgcm^{-2}min^{-1}(minutes)**
Tyvek	N/A
Tychem C2	0.3
Microgard 2500	0.2
Microchem 3000	0.2
Tychem F	47
Tychem F2	330
Microchem4000	480

N/A = Not Applicable

3.3 Thermal and moisture management properties of commercially available chemical protective fabrics

The thermal resistance and moisture transmission properties of the commercially available protective fabrics are examined in this section. There are two methods used to characterise the thermal and moisture transmission properties of the seven commercially available chemical protective fabrics: sweating guard hotplate (SGHP) method based on EN 31092:2013 for measuring thermal resistance (R_{ct}) and water vapour resistance (R_{et}) and a modified upright cup method based on BS 7209:1990 for measuring water vapour transmission rate (*WVTR*).

3.3.1 R_{ct} and R_{et} measured in sweating guarded hotplate method

R_{ct} of the commercially available chemical protective fabrics are shown in Table 3.5.

Table 3.5 R_{ct} of commercially available chemical protective fabrics

Samples	**R_{ct} (m^2 K W^{-1})**				**S.D.**
	1	**2**	**3**	**Average**	
Tyvek	0.078	0.074	0.069	0.074	0.004
Tychem C2	0.103	0.096	0.117	0.105	0.010
Microgard 2500	0.129	0.127	0.133	0.130	0.003
Microchem 3000	0.145	0.118	0.133	0.132	0.014
Tychem F	0.132	0.138	0.123	0.131	0.008
Tychem F2	0.113	0.109	0.120	0.114	0.005
Microchem 4000	0.137	0.150	0.142	0.143	0.006

It is found in Table 3.5 that Tyvek has the smallest R_{ct} at 0.074 m^2 K W^{-1} because of its porous structure and smallest thickness (see Table 3.2). Microchem 4000 shows the greatest R_{ct} of 0.143 m^2 K W^{-1} which corresponds to its five-layer lamination and coating on polypropylene nonwoven (see Figure 2.2).

Microgard 2500, Microchem 3000 and Tychem F have a similar R_{ct} of 0.130 m^2 K W^{-1}, 0.132 m^2 K W^{-1} and 0.131 m^2 K W^{-1}, respectively, which also corresponds to previous research [186].

Two coated fabrics, Tychem C2 and Tychem F2 have a similar R_{ct} of 0.105 m^2 K W^{-1} and 0.114 m^2 K W^{-1}, respectively, which is smaller than that of Microgard 2500, Microchem 3000 and Tychem F.

It is concluded that the multiple-layer laminated and coated fabric, Microchem 4000, has the greatest thermal resistance and uncoated porous, thin nonwoven fabric. Tyvek has the smallest thermal resistance, while the other fabrics have similar level of thermal resistance without apparent differences. Therefore, laminated and coated fabric could be engineered to have different permeation performance but with similar thermal resistance properties.

The R_{et} of the commercially available chemical protective fabrics are shown in Table 3.6.

Table 3.6 R_{et} of the commercially available chemical protective fabrics

Samples	R_{et} (kPa m^2 W^{-1})				S.D.
	1	2	3	Average	
Tyvek	16.8	21.0	21.2	19.6	2.5
Tychem C2	Infinity	Infinity	Infinity	Infinity	N/C
Microgard 2500	36.8	31.6	33.0	33.8	2.7
Microchem 3000	Infinity	Infinity	Infinity	Infinity	N/C
Tychem F	Infinity	Infinity	Infinity	Infinity	N/C
Tychem F2	Infinity	Infinity	Infinity	Infinity	N/C
Microchem 4000	Infinity	Infinity	Infinity	Infinity	N/C

N/C =Not calculation because other values are infinity

As a permeable, spunbond nonwoven fabric without any coating, Tyvek is open to water vapour that can transfer through its porous structure. Tychem C2 is a coated fabric and its R_{et} is much greater than Tyvek and the other two porous fabrics, Microgard 2500.

The R_{et} of Microchem 3000, Tychem F, Tychem F2 and Microchem 4000 are not significantly different. This is because they all included a continuous membrane in their multiple layer laminated nonwoven structure, which obstructs the transport of water vapour through the fabrics. Therefore, the R_{et} of the impermeable chemical protective fabrics is higher than that of the permeable protective fabrics.

3.3.2 *WVTR* by a modified upright cup method

The *WVTR* of the commercially available chemical protective clothing products is examined by a modified upright cup method according to BS 7209:1990 at two temperatures, 20°C and 40°C. The testing procedure is exactly the same as the standard test method defined in BS7209:1990 except the following conditions:

(1) Instead of testing the fabrics in a turning table, the experiment is carried out in an environmental chamber in which air flow are self-circulated at a velocity of 0.2 m s^{-1} to avoid the formation of a still air layer above the cups;

(2) The testing could be done at both 20°C and 40°C; when the testing is carried out at 40°C, distilled water is heated to 40°C before being filled in the cups;

(3) The water cup is placed in a hotplate, the temperature of which is heated to the temperature of water at either 20°C or 40°C;

(4) The assembly cups are placed into the controlled chamber for 30 minutes to establish equilibrium of the water vapour gradient before being weighed.

The *WVTR* of Tyvek and the standard reference fabrics being tested in standard turntable method and environmental chamber at 20°C are shown in Table 3.7.

Table 3.7 Comparison of *WVTR* (g m^{-2} $24h^{-1}$) of the reference fabric and Tyvek fabrics tested in the standard turntable method and environmental chamber at 20°C

Methods / **Samples**	**Turntable**	**Environmental chamber**
Reference fabric	674.4	781.3
Tyvek	482.0	462.4

It is found from Table 3.7 that there is a difference of less than 5% in the *WVTR* between the turntable method and the environmental chamber at 20°C when adjusting the air velocity at 0.2 m s^{-1}. Therefore, the environmental chamber method in which the air velocity is adjusted at 0.2 m s^{-1} is used for the investigation of *WVTR* of the commercially available chemical protective fabrics at both 20°C and 40°C.

The *WVTR* of the commercially available chemical protective fabrics at 20°C and 40°C is compared in Figure 3.14 and Figure 3.15. The ratio of the *WVTRs* at two different temperatures (R_{WVTR}) is compared as shown in Table 3.7

The ratio of the *WVTR* at 20°C and 40°C is calculated by using the equation (3-4) below.

$$R_{WVTR} = \frac{WVTR_{at\ 40°C}}{WVTR_{at\ 20°C}} \tag{3-4}$$

Table 3.8 *WVTR* of the commercially available chemical protective fabrics at 20°C and 40°C

Samples	***WVTR* (g m^{-2} 24h^{-1})**		**S.D.**		**R_{WVTR}**
	20°C	**40°C**	**20°C**	**40°C**	
Tyvek	477.3	1663.6	17.0	186.5	3.9
Tychem C2	21.2	81.5	0.9	63.1	3.8
Microgard 2500	432.2	1465.0	56.8	3.5	3.4
Microchem 3000	22.2	41.6	5.7	2.6	1.9
Tychem F	16.9	55.2	3.3	46.2	3.3
Tychem F2	23.2	46.5	2.0	8.7	2.0
Microchem 4000	16.7	34.5	2.0	4.9	2.1

It is found in Table 3.8 that *WVTR* of uncoated porous Tyvek fabric and porous coating Microgard 2500 fabric are the greatest among the seven fabrics at both of the two temperatures. This might be due to water vapour diffusion along the fibres itself, through the air space between the fibres and the porous coating membrane layer structure which depends on the porosity of the fabrics [187]; however, the standard deviation of *WVTR* of those two fabrics are also very high, which is common in nonwoven fabrics, and usually because of the uniformity of the fabrics and coatings (if any) making water vapour transport through their local areas in different rates.

It is also found that *WVTR* of all the fabrics at 40°C is greater than that in 20°C. This is because higher temperature induces greater mobility of water molecules in moisture and leads to greater water vapour pressure. For example, the saturation pressure of water vapour at 40°C and at 20°C are 7.37 kPa and 2.33 kPa, respectively [188]; and it is known that the greater water vapour pressure in higher temperature leads to the greater water vapour transmission through fabrics [189], [190].

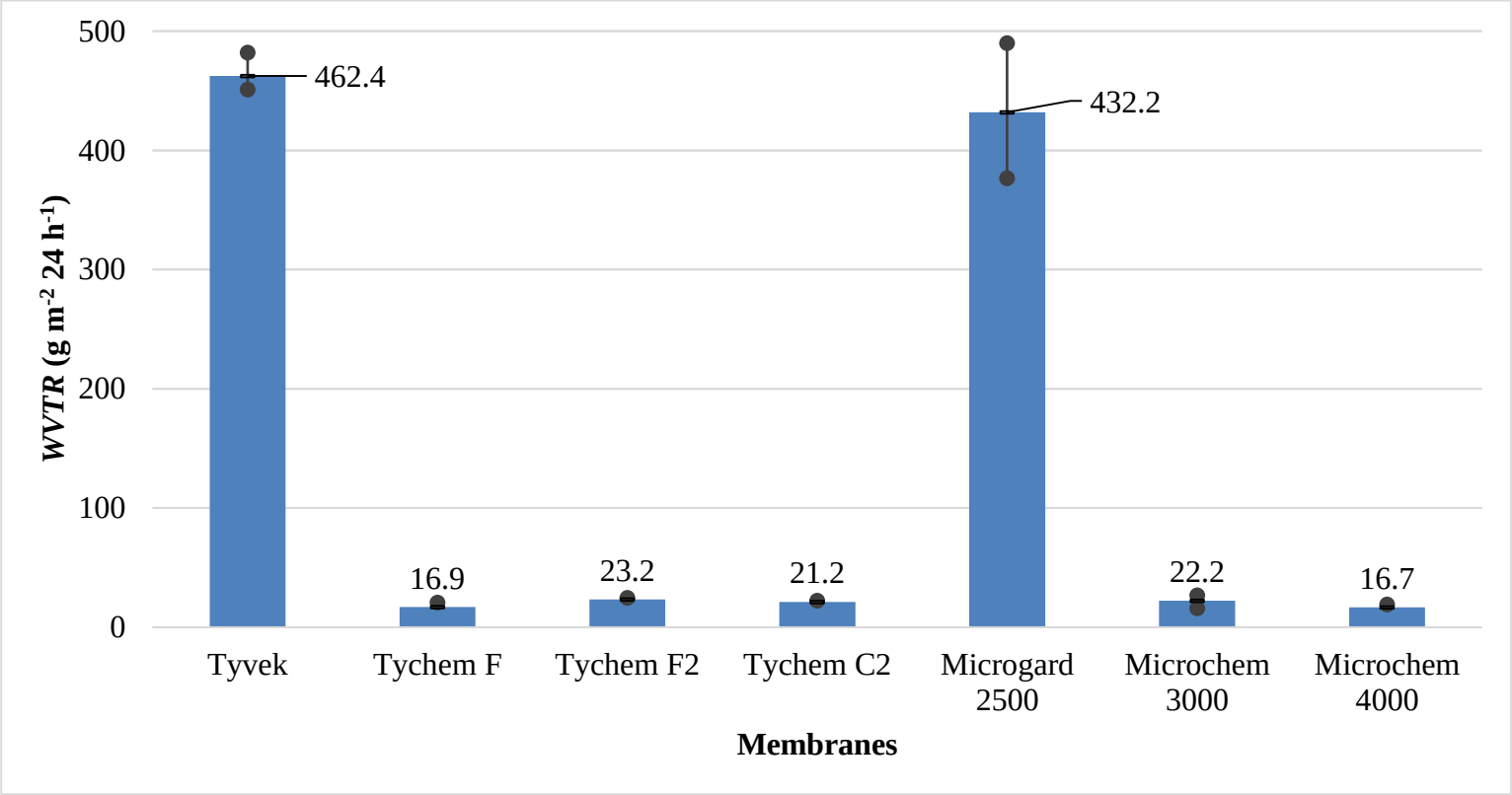

Figure 3.14 The water vapour transmission rate of the seven commercially available chemical protective fabrics at 20°C

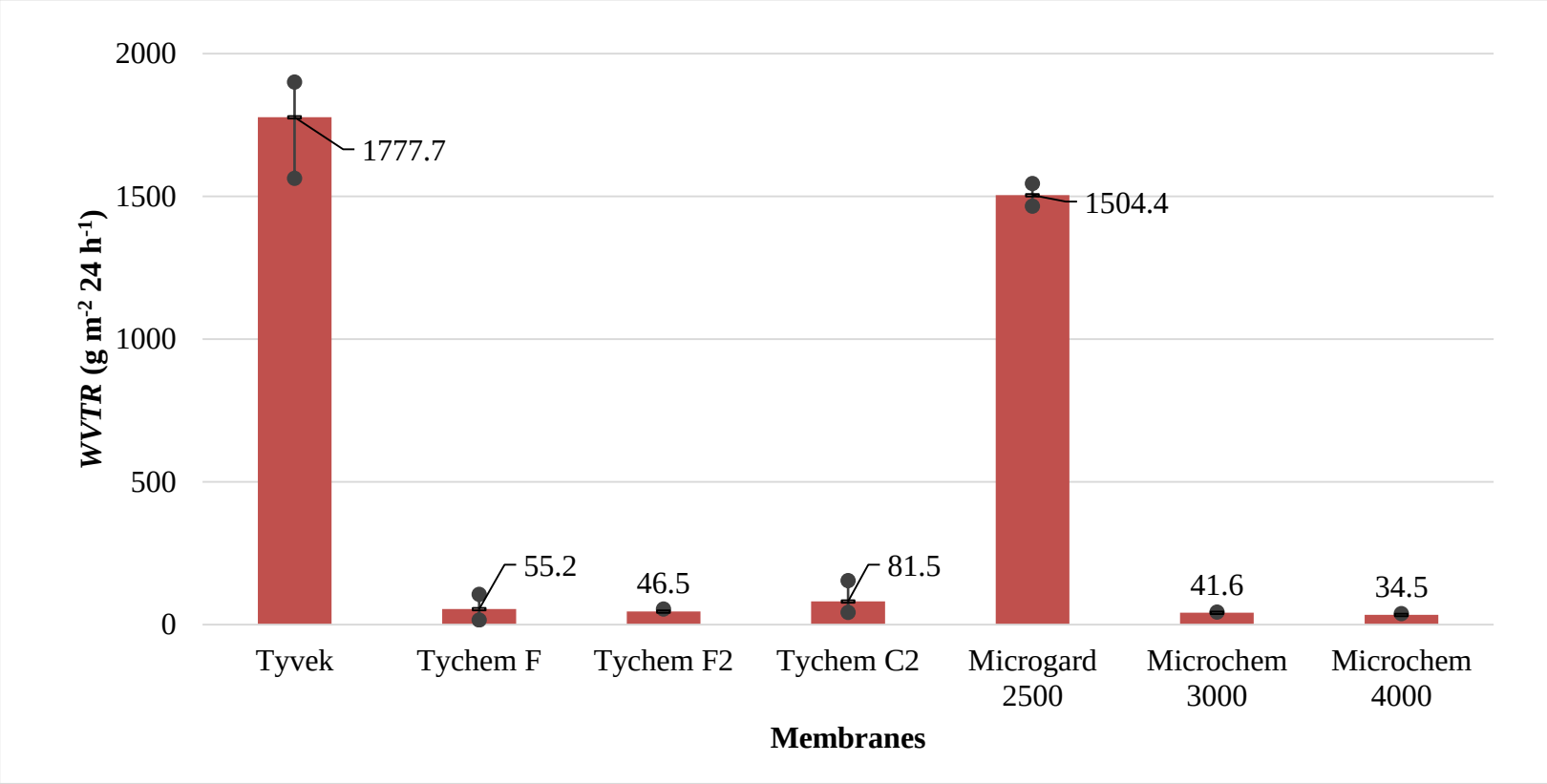

Figure 3.15 The water vapour transmission rate of the seven commercially available chemical protective fabrics at 40°C

It was also found in Table 3.8 that *WVTR* of Tychem F and Microchem 4000 at 20°C is lower than that of Tychem F2. This is probably because Tychem F2 has the greatest thickness and the smallest density among these three fabrics (see Table 3.1). The water vapour transport through the porous fabric structures is described by Darcy's law in equation (3-5) below,

$$Q_s = -\frac{k}{\eta}\frac{dP}{L} \tag{3-5}$$

where

Q_s is volumetric flow rate of the fluid flow through a unit cross-section area in the porous structure ($m^3\ s^{-1}$),

K is specific permeability (m^2),

η is viscosity of the water vapour (Pa s),

dP is differential pressure along the conduit length (Pa),

L is fabric thickness (m).

As can be seen in equation (3-5), the fabric thickness is inversely proportional to the flow rate, and this might explain why *WVTR* of Tychem F2 is greater than that of Tychem F and Microchem 4000 fabrics at 20°C.

Based on Darcy's law shown in equation (3-5), for water vapour transport through porous fabrics, *WVTR* is proportional to the fabrics' pressure gradient at different temperatures. Thus, the theoretical ratio of the volumetric flow rate of the water vapour transmission through a unit cross-section area of the same fabric at 20°C and at 40°C is shown as the equation (3-6) below;

$$\frac{Q_{40}}{Q_{20}} = \frac{\Delta P_{40}}{\Delta P_{20}} \tag{3-6}$$

Considering that of the saturated water vapour pressure at 40°C and at 20°C are 7.37 kPa and 2.33 kPa, respectively, the difference in water vapour pressure at 40°C, 65%RH and 20°C, 65%RH are $\Delta P_{40} = 0.35 \times 7.37$ kPa and $\Delta P_{20} = 0.35 \times 2.33$ kPa, respectively. Therefore, the ratio of the volumetric flow rate of the water vapour transmission through a unit cross-section area of the same fabric at 20°C and at 40°C are shown as the equation (3-7) below;

$$\frac{Q_{40}}{Q_{20}} = \frac{\Delta P_{40}}{\Delta P_{20}} = \frac{0.35 \times 7.37}{0.35 \times 2.33} = 3.16 \quad (3\text{-}7)$$

Moreover, from equation (3-5) and equation (3-7), the specific permeability (K_{20} and K_{40}) of the commercially available chemical protective clothing at 20°C and at 40°C are calculated and shown in Table 3.9. The viscosity of water vapour at 20°C and at 40°C is 1.002 Pa s and 0.653 Pa s, respectively [191].

Table 3.9 The specific permeability of the commercially available chemical protective clothing

Samples	K_{20} **(m^2)**	K_{40} **(m^2)**
Tyvek	5.1×10^{-12}	3.9×10^{-12}
Tychem C2	3.4×10^{-13}	1.5×10^{-13}
Microgard 2500	4.7×10^{-12}	3.4×10^{-12}
Microchem 3000	4.9×10^{-13}	1.9×10^{-13}
Tychem F	3.6×10^{-13}	6.4×10^{-13}
Tychem F2	2.9×10^{-13}	2.1×10^{-13}
Microchem 4000	2.4×10^{-13}	2.4×10^{-13}

The specific permeability of each commercially available chemical protective clothing at 20°C and at 40°C are not significantly difference. It is described that the volumetric flow of water vapour through the commercially available chemical protective clothing that Tyvek and Microgard 2500 have a high level of specific permeability at both 20°C and at 40°C so the water vapour can transport through easily.

On the other hand, the other commercially available chemical protective clothing have the lower specific permeability. It is probably because of the multilayer structure of the laminated fabric which obstructs the transport of the water vapour through the fabrics.

In Henry's law shown in equation (2-4) for water vapour permeation through coated and laminated fabrics, permeability is proportional to diffusion flux and solubility of

water vapour in the fabric materials. In diffusion equation (2.3), it is assumed that water vapour concentration gradient is proportional to the water vapour pressure gradient [192]. We thus have:

$$\frac{\Delta c_{40}}{\Delta c_{20}} = a \times \frac{\Delta P_{40}}{\Delta P_{20}} \quad (3\text{-}8)$$

It is also known that solubility of liquids in a polymer changes with temperature and varies from polymer to polymer [193]; therefore, the theoretical ratio of volumetric flow rate of the water vapour permeation through a unit cross-section area of the same fabric at 20°C and at 40°C is shown as the equation (3-10) below.

$$\frac{Q_{40}}{Q_{20}} = a \times \frac{\Delta P_{40}}{\Delta P_{20}} \times \frac{S_{40}}{S_{20}} \quad (3\text{-}9)$$

The ratio of measured flow rate is shown in Table 3.8. In comparison with the theoretical ratio of volumetric flow rate of the water vapour transport through fabrics based on Darcy's law (i.e., 3.16), only the ratio of measured flow rate of the fabric Tychem F (i.e., 3.27) is more or less the same as the theoretical ratio (3.16). This might be an indication that this fabric has pores or holes (no matter fabric pores or defect holes). It is noticed that the ratio of measured flow rate of the three porous fabrics, Tyvek, Tychem C2, and Microgard 2500, is much greater (3.48 ~3.85) than the theoretical ratio based on Darcy's law (3.16). This might be an indication that, besides the moisture transfer through porous fabrics depending on Darcy's law, there are either additional mechanism (e.g. an additional diffusion or the solubility) involved to promote the moisture transfer at 40°C or additional mechanism (e.g. condensation) resistant to moisture transfer involved at 20°C.

The ratio of measured flow rate (1.87 ~ 2.07) of the three coated and laminated fabrics, Microchem 3000, Tychem F2 and Microchem 4000, is much smaller than the theoretical ratio based on Darcy's law (3.16). This is a clear indication that the water vapour transfer through the fabrics does not pass through their fabric pores/holes: they work on a permeation mechanism instead.

3.4 Conclusions

A modified liquid chemical permeation testing system has been established to investigate the liquid chemical resistance of the commercially available chemical protective fabrics, the structure of the barrier membrane materials used in

commercially available chemical protective clothing is categorised into three groups according to the characteristics of their n-hexane permeation properties: the open and porous material, the limited barrier material and the chemical resistance fabric material.

Additionally, their thermal comfort properties were characterised by using R_{ct}, R_{et} and water vapour transmission rate. It is found that the water vapour flowing through conventional porous barrier membranes obeys Darcy's Law and mainly transport through pores in the membrane. It was found the thin, permeable nonwoven fabrics have smaller thermal resistance and a greater water vapour transmission rate, and the ratio of water vapour transmission rate between 40°C and 20°C which indicates either greater water vapour condensation in the fabric pores at 20°C or additional diffusion mechanism promoting the moisture transfer at 40°C. In contrast, the multiple-layer laminated and coated barrier fabrics have greater thermal resistance and greater water vapour resistance simultaneously. While an indication the ratio of water vapour transmission rate between 40°C and 20°C shows the water vapour transfer through these types of fabrics might depends on diffusion and permeation process rather than following Darcy's law in macroposous.

It was thus concluded that the fabric structures such as the multiple-layered and laminated architecture, fabric thickness, and porous membrane structures influence both liquid chemical protection and thermophysiological properties of the membranes. Therefore, the influence of the microstructural structure of the smart copolymer barrier membrane to be developed on their permeation and thermophysiological properties needs to be investigated.

Chapter 4 NIPAAM-g-PVDF copolymerisation by thermally induced graft copolymerisation

In Chapter 2, two methods were identified for the copolymerisation of poly(vinylidene fluoride) (PVDF) and N-isopropylacrylamide (NIPAAM); one was the thermally induced copolymerisation and the other one was plasma induced copolymerisation. This chapter investigates the copolymerisation of PVDF and NIPAAM by thermally induced graft copolymerisation and the characterisation of samples were done by using Fourier Transform Infrared Spectroscopy (FTIR) spectroscopy, Time-of-Flight Secondary Ion Mass Spectrometry (ToF-SIMS), and Differential scanning calorimetry (DSC).

4.1Chemicals and equipment

4.1.1 Chemicals

PVDF Hylar® 301 powder was obtained from Solvay & Solexis Company. NIPAAM (99% purity) was purchased from Fisher Scientific and recrystallined in n-hexane before use (10 g of NIPAAM in 100 cm^3 of n-hexane at 40°C for 1 hour and leave to room temperature overnight [194]). N-methyl-2-pyrrolidone (NMP) (99% purity) was purchased from VWR International. 2,2-diphenyl-1-picrylhydrazyl (DPPH) was obtained from Sigma Company. Ethanol and isopropanol were purchased from Fisher Scientific Ltd.

4.1.2 Ozone generator

The ozone generator model TCB-Y913GA2C from Trump XP Company, China was placed in a container with a pump. A silicone tube was used to connect the ozone generator to the three-neck flask as shown in Figure 4.1. A gas flow rate of 8 g dm^{-3} gives an ozone concentration about 3 g h^{-1}.

Figure 4.1 The ozone generator

4.1.3 Copolymerisation device

The copolymerisation of PVDF and NIPAAM was carried out in a three-necked round-bottom flask equipped with a thermometer, a condenser, and a gas line connected with nitrogen gas as shown in Figure 4.2. The water bath was placed over the thermostat hotplate magnetic stirrer in order to control the temperature throughout the copolymerisation process.

Figure 4.2 The copolymerisation device

4.2 NIPAAM-g-PVDF copolymerisation

PVDF and NIPAAM were copolymerised by using the thermally induced grafted copolymerisation method. PVDF Hylar® 301 powders was activated via ozone oxidisation in NMP solutions; then the activated PVDF polymer was thermally copolymerised with NIPAAM in an NMP solution as shown schematically in Figure 4.3.

As it is expected the activated PVDF polymers contained the hydroperoxide group (–CO-OH) and peroxide groups (-O-O-) as side groups which were reacted with NIPAAM to form copolymers [137]; therefore, PVDF molecules will be acted as a backbone of the NIPAAM-g-PVDF copolymer chain and NIPAAM were added to the backbone as branches as indicated in Figure 4.3.

The copolymerisation reaction of ozone activated PVDF and NIPAAM was carried out under nitrogen atmosphere at 60°C for 6 hours. There are two polymerisation routes for the thermally induced copolymerisation of NIPAAM and the ozone activated PVDF, they were described in the Section 4.2.2.

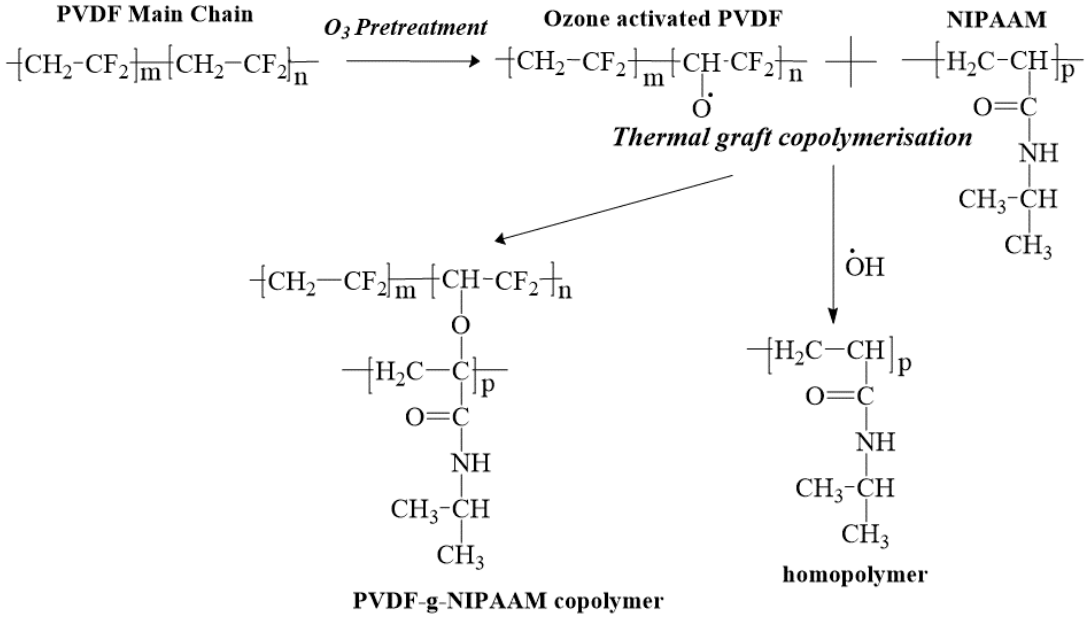

Figure 4.3 Schematic illustration of the thermally induced graft copolymerisation process (Improved from [150], [157])

4.2.1 PVDF ozone activation process

PVDF does not have any active group to react with NIPAAM, the introduction of active group onto the surface of PVDF polymer via ozone oxidisation is the first step

of copolymerisation between PVDF and NIPAAM. Previous research suggests that the amount of peroxide content in the ozone activated PVDF polymer could be controlled by varying process parameters such as the treatment temperature, the ozone concentration, and the treatment time [135]. In this research, the treatment temperature was kept at room temperature (25°C). The procedure of ozonolysis of PVDF was carried out according to the process described in previous research [157]. However, before the copolymerisation process, the ozone activated PVDF (in NMP) was precipitated in excess ethanol and dried either by pumping under reduced pressure at room temperature or by using supercritical CO_2 to remove the solvent; the effect of treatment time and the efficiency of drying processes were characterised by using the process described below.

A 75 g dm^{-3} of PVDF particulates in NMP solution was prepared and then 100 cm^3 of this solution was bubbled in a round-bottom flask by passing a continuous stream of O_2/O_3 with a flow rate of 3 g h^{-1} (See Figure 4.1). The duration of the activation time was varied at 4, 8, 24 and 48 hours. After the ozone activation, the reaction flask was placed in an ice bath for 30 minutes and the ozone activated PVDF was precipitated in 100 cm^3 of ethanol for 45 minutes. After that, the ozone activated PVDF material was dried by using two different types of drying methods; the filter-oven drying method and the supercritical CO_2 drying method. The peroxide contents of ozone treated PVDF samples were determined by using DPPH assay as shown in Section 4.3.1.

4.2.2 NIPAAM-g-PVDF copolymerisation process

There are two possible routes to copolymerise the ozone activated PVDF with the NIPAAM together. The first route is that the ozone activated PVDF was precipitated in ethanol solution and then dissolved in NMP solution again to copolymerise with NIPAAM. The second route is that the activated PVDF polymer in the NMP solution without any further processing was copolymerised with the NIPAAM polymer directly. The two thermal induced copolymerisation processes are described below respectively.

Route 1: the activated PVDF polymer in NMP solution was firstly precipitated in ethanol solution and dried to obtain dried activated PVDF polymer, which was dissolved in NMP solution again to copolymerise with NIPAAM monomers [157]. The schematic of Route 2 is shown in Figure 4.4.

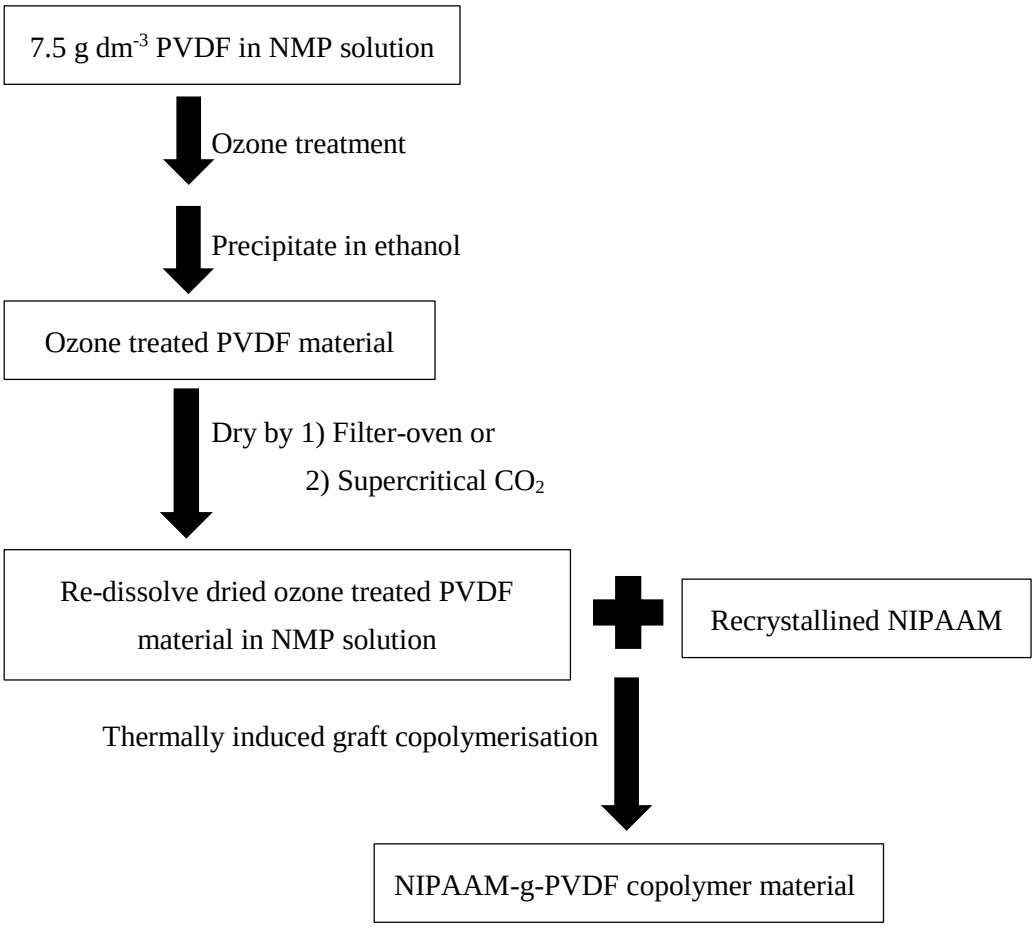

Figure 4.4 Schematic of thermally induced graft copolymerisation of PVDF and NIPAAM (Route 1)

The ozone activated PVDF material could be dried by using two different types of drying methods; the filter-oven drying method and the supercritical CO_2 drying method. It was found that the weight of the activated PVDF increased after the ozone activation and to prevent the contaminating of ethanol in the copolymerisation process. Therefore, NMP and ethanol need to be removed from the ozone activated PVDF. These two types of drying method are discussed below:

(1) Glass Buchner filtering funnel was connected to the pump under vacuum is used in the filter-oven drying method. The ozone activated PVDF was placed into the funnel for at least one hour until no more ethanol could be filtered. Then, the activated PVDF was dried in an oven at 40°C for 24 hours.

(2) To the best of author's knowledge, there is no literature that relates to the removal of ethanol from PVDF by using supercritical CO_2 method. However, the supercritical CO_2 method is frequently used to remove ethanol in sol-gel process

to make aerogel materials [195] and there are some literatures which relates to the removal of NMP and/or DMF from PVDF membrane by using supercritical CO_2. A summary is given in Table 4.1.

Table 4.1 The removal of solvent from PVDF by using supercritical CO_2

Conditions	**Pressure (MPa)**	**Temperature (°C)**	**Time (hours)**
PVDF-HFP membrane drying in NMP [196]	13.5	35	2
Remove NMP from electrode film which containing PVDF as a binder [197]	30	40	2
PVDF in DMF membrane drying [198]	15	40	4

In this study, supercritical CO_2 method was used to facilitate the removal of ethanol from the ozone activated PVDF by using the following process parameters;

Flow rate of supercritical CO_2: 5 g min^{-1}
Time: 6 hours
Pressure: 20 MPa
Temperature: 60°C

The experimental design to study of the effect of the ozone activation process to PVDF polymer is indicated in Table 4.2.

Table 4.2 Experimental plan for the ozone activation process of PVDF

Samples	**Drying methods**	**Treatment time (Hours)**
O1	-	-
O2	Filter-oven	4
O3		8
O4		24
O5		48
O6	Supercritical CO_2	24

Later the copolymerisation was carried out after the drying method, in Route 1; the filter-oven drying method was used. 2 g of dried ozone activated PVDF was dissolved in 25 cm^3 of NMP again for 30 minutes, the PVDF solution and the recrystallined NIPAAM were introduced into a three-necked round-bottom flask in a reflux was adjusted at 40 cm^3 of the final volume which sit in a water bath of 60°C. NIPAAM concentration is varied from 0.8 g to 2 g as indicated in
The experimental design to study of the thermally induced graft copolymerisation process by using Route 1 and Route 2 is shown in Table 4.3. However, it is important to bear in mind that PVDF in Route 1 in Table 4.3 is the dried activated PVDF after the filter-oven drying method and PVDF in Route 2 is the initiated weight of PVDF before the ozone activation process.

Table 4.3. After the PVDF was dissolved with stirring with NIPAAM under nitrogen gas and the reaction was maintained at 60°C for 6 hours.

The reaction yield (NIPAAM-g-PVDF copolymer) was precipitated in excess distilled water for 48 hours in order to remove any uncopolymerised NIPAAM (homopolymer in Figure 4.3) from NIPAAM-g-PVDF material because of NIPAAM dissolves in water while both the unreacted activated PVDF and the resultant NIPAAM-g-PVDF copolymer does not. The grafted NIPAAM-g-PVDF copolymer was then dried by using the filter-oven drying method at 40ºC for 24 hours.

Route 2: In this method, NIPAAM was added to 20 cm^3 of activated PVDF in NMP solutions directly after the ozone activation process, rather than going through the ozone activated PVDF precipitation process and the drying process. NIPAAM was recrystallined in n-hexane (see Section 4.1.1) and the NIPAAM concentration is varied from 0.02 g to 2 g as indicated in
The experimental design to study of the thermally induced graft copolymerisation process by using Route 1 and Route 2 is shown in Table 4.3. However, it is important to bear in mind that PVDF in Route 1 in Table 4.3 is the dried activated PVDF after the filter-oven drying method and PVDF in Route 2 is the initiated weight of PVDF before the ozone activation process.

Table 4.3. However, the precipitation of NIPAAM-g-PVDF copolymer was similar to the process in Route 1. The schematic of Route 2 is shown in Figure 4.5.

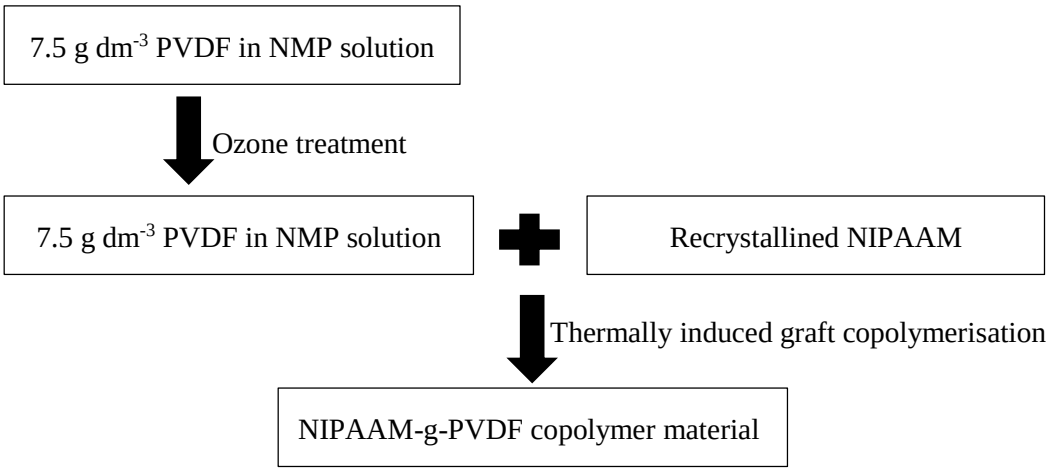

Figure 4.5 Schematic of thermally induced graft copolymerisation of PVDF and NIPAAM (Route 2)

The experimental design to study of the thermally induced graft copolymerisation process by using Route 1 and Route 2 is shown in Table 4.3. However, it is important to bear in mind that PVDF in Route 1 in Table 4.3 is the dried activated PVDF after the filter-oven drying method and PVDF in Route 2 is the initiated weight of PVDF before the ozone activation process.

Table 4.3 Experimental plan for the copolymerisation of NIPAAM and PVDF

Samples	**Copolymerisation Methods**	**NIPAAM (g)**	**PVDF (g)**	**Weight ratio (NIPAAM:PVDF)**
D1	Route 1	0.08	2	1:25
D2		0.4	2	1:5
D3		2	2	1:1
D4		4	2	2:1
D5	Route 2	2	2	1:1
D6		0.2	2	1:10
D7		0.02	2	1:100

4.2 Methods for the characterisation of NIPAAM-g-PVDF

4.2.1 Ultraviolet–visible spectroscopy (UV-Vis)

UV-Vis Spectroscopy was employed to characterise the DPPH concentration in a solution in order to determine the amount of the hydroxide existed in the ozone activated PVDF polymers. In order to establish the calibration curve for the determination of peroxide content in the activated PVDF material, the DPPH concentration was examined by using the UV-Vis Spectrophotometer model V-630 from JASCO analytical instrument with the quartz cuvette. The mixture of NMP and isopropanol at 16:1 ratio was used as the reference solvent.

4.2.2 Differential scanning calorimetry (DSC)

The thermal property of PVDF, NIPAAM, ozone-treated PVDF, and NIPAAM-g-PVDF copolymer were investigated using a Perkin Elmer Jade differential scanning calorimetry.

Zinc and Indium (melting points 156°C and 419°C, respectively) were used for calibration reference. About 25 mg of the sample were prepared in a stainless steel pan and covered with the stainless steel cover, both supplied by Perkin Elmer. The sample assembly was placed in the DSC along with the reference sample and heated to 440°C at a rate of 20°C min^{-1} under nitrogen atmosphere. The crystallinity and the change of temperature profile were obtained according to equation (2-25).

4.2.3 Attenuated total reflectance- Fourier transform infrared spectroscopy (ATR-FTIR) and KBr-FTIR

The ozone activated PVDF, NIPAAM, and NIPAAM-g-PVDF copolymer were subjected to FTIR spectroscopy using a Perkin-Elmer Spectrum BX spectrophotometer with diamond ATR attachment.

ATR-FTIR was used to characterise activated PVDF and the NIPAAM-g-PVDF copolymer. Scanning was conducted from 4000 to 500 cm^{-1} with 64 repetitious scans averaged, resolution was 16 cm^{-1} and interval scanning was 2 cm^{-1} for each spectrum.

KBr-FTIR (with KBr disc) was used to characterise NIPAAM-g-PVDF copolymer obtained in Route 2. Before testing, KBr powder was dried in an oven at 100°C at least 24 hours, 1.5 mg of NIPAAM-g-PVDF material was ground with 150 mg of KBr by using an agate mortar and pestle. A mixture of KBr and NIPAAM-g-PVDF

material was poured in an assembly of dies and pressed by a hydraulic press for 3 minutes in order to form into the KBr disc. Scanning was conducted from 4000 to 500 cm^{-1} with 64 repetitious scans averaged for each spectrum. Resolution was 16 cm^{-1} and interval scanning was 2 cm^{-1}.

4.2.4 Time-of-Flight Secondary Ion Mass Spectrometry (ToF-SIMS)

ToF-SIMS was used to analyse the surface chemical compositions of PVDF and the synthesised copolymers. The testing was performed at the Intertek Wilton Laboratory, UK. The powder sample was prepared by placing the powder onto a small piece of silicone-free double-sided sellotape. Any excess powder was shaken off and the surface was given a gentle air dusting with ambient air in order to remove any loose particles. The positive and negative ion spectra were recorded with 200x200 mm analysis areas by Static Secondary Ion Mass Spectrometry using the IoN-Tof 'TOFSIMS IV' instrument. The total ion dose for each acquisition was ca. 1 x 10^{12} ions cm^{-2}.

4.3 Oxidisation of PVDF polymer by using ozone activation method

PVDF got superior chemical resist and therefore it is important to modify PVDF before the copolymerisation. The ozone treatment is a simple and rapid method to functionalise PVDF [136] and was used in this study. The effect of ozone treatment time on the peroxide content of the activated PVDF polymer and the influence of the drying method after the ozone activation were studied.

4.3.1 Methods for the determination of peroxide concentration

Ozone activation of PVDF should add peroxide moieties to the backbone of the PVDF, the level of oxidation of PVDF could thus be represented by using the concentration of peroxide in the activated PVDF [137]. DPPH assay was done to determine the amount of peroxide and hydroperoxide in the ozonized polymers [199]. The reaction of DPPH and the ozone activated PVDF is shown in Figure 4.6. As a result of this reaction, the colour of the DPPH solution changes from deep violate to yellow-orange and this results in a decrease in the absorption peak at 520 nm.

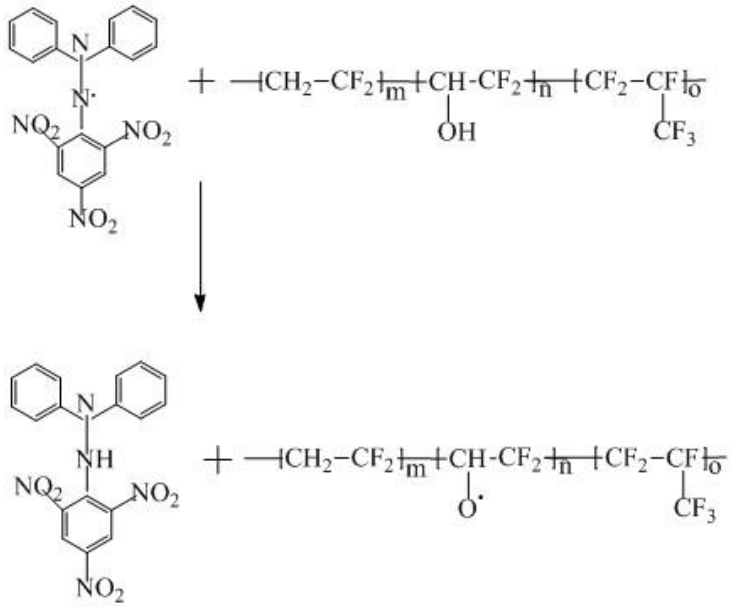

Figure 4.6 The reaction of DPPH and activated PVDF [136],[199]

4.3.1.1 Calibration curve for DPPH

Base on previous research [137], 6 g dm^{-3} DPPH in NMP solution was prepared and diluted to different concentration by using a NMP: isopropanol (1:16) mixture as shown in Table 4.4.

The absorption spectra (from 400-700 nm) of the DPPH solutions were determined by using UV-vis spectroscopy (Figure 4.7).

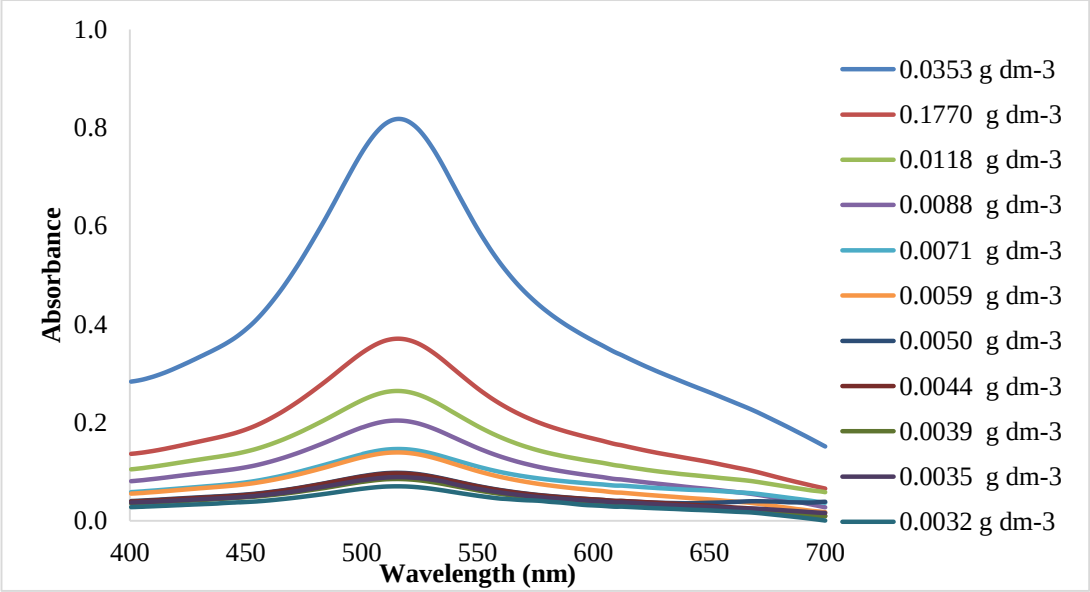

Figure 4.7 The absorbance spectrum of different DPPH solutions

Table 4.4 The concentrations of DPPH to produce the calibration curve

6 g dm^{-3} DPPH in NMP (cm^3)	The mixture of NMP and isopropanol = 1:16(cm^3)	The residual DPPH concentration (g dm^{-3})
1	0	3.53×10^{-2}
1	1	1.77×10^{-2}
1	2	1.18×10^{-2}
1	3	8.80×10^{-3}
1	4	7.10×10^{-3}
1	5	5.90×10^{-3}
1	6	5.00×10^{-3}
1	7	4.40×10^{-3}
1	8	3.90×10^{-3}
1	9	3.50×10^{-3}
1	10	3.20×10^{-3}

The concentration of the unknown DPPH solutions was calculated using equation (4-1) which was generated from the calibration curve.

$$y_1 = 22.623x_1 \quad (4\text{-}1)$$

where

y_1 is the absorbance at 516 nm,

x_1 is the concentration of DPPH in solution (g dm^{-3}).

It can be seen from Figure 4.7 that the peaks of the spectrums are at 516 nm; therefore, the absorbance at 516 nm was selected to produce the calibration curve as shown in Figure 4.8.

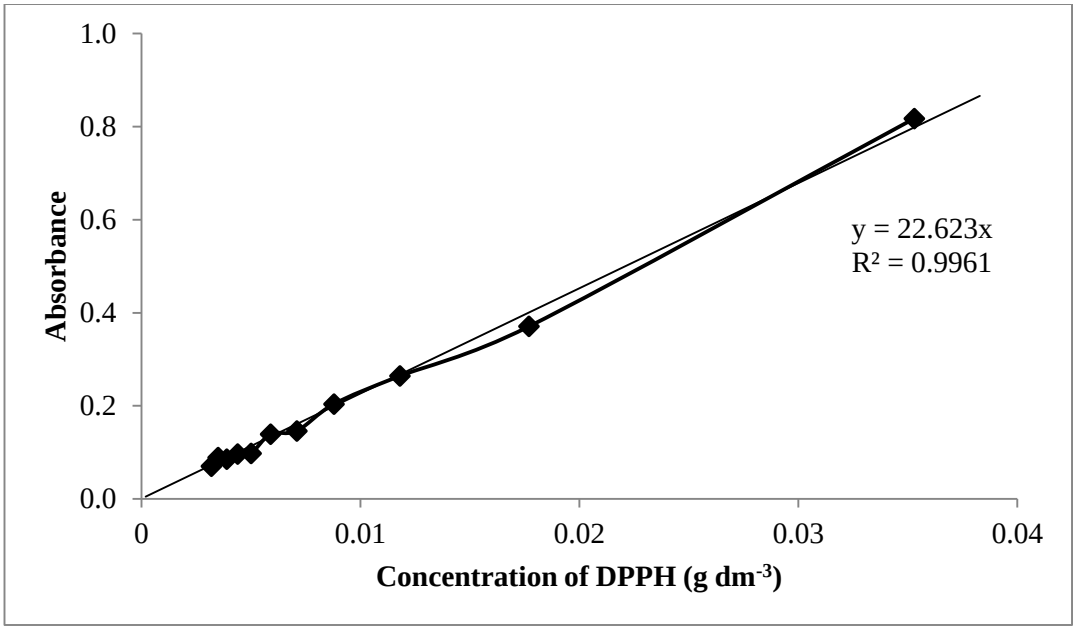

Figure 4.8 The calibration curve of DPPH

4.3.1.2 The measurement of peroxide concentration

The measurement of peroxide concentration in the ozone activated PVDF polymer material for the ozone activated PVDF polymer which were dried by both the filter-oven drying method and the supercritical CO_2 method was carried out based on the procedure reported in previous research and as described below [137].

100 mg of ozone-treated PVDF was dissolved in 10 cm^3 of 6 g dm^{-3} DPPH in NMP. 10 cm^3 of the solution was saturated in the round-bottom flask which connected with a thermometer, a condenser, and a helium gas line. The resultant solution was bubbled in the helium gas for 45 minutes; then, the reaction flask was placed on a silicone oil bath at 110°C for 10 minutes and cooled in an ice bath for another 10 minutes. After that, the ozone-treated PVDF polymer was precipitated in 160 cm^3 of isopropanol in the conical flask and left without shaking for 30 minutes. The DPPH solution was then filtered by the glass Buchner filtering funnel which connected to the pump under vacuum. The absorption spectrum of the liquor was determined using UV-Vis spectroscopy at 516 nm. The concentration of residual DPPH in the solution was calculated by using the equation (4-1). The number of moles of peroxides per gram of the ozone-treated PVDF (T) was determined by equation (4-2) [201].

$$T = \frac{(x_0 - x) \times 180}{(2000 \times 394.33 \times m)} \qquad (4\text{-}2)$$

where

T is the content of initiator brought about by a gram of ozone activated PVDF (mole of peroxide per gram of ozonized polymer),

x_0 is the initial DPPH concentration (g dm^{-3}),

x is the final DPPH concentration (g dm^{-3}),

m is the weight of effective PVDF (g).

4.3.2 Peroxide content of ozone activated PVDF polymer

4.3.2.1 Effect of treatment time on peroxide content in the activated PVDF polymer by using the filter drying

In the section, the effect of the treatment time on peroxide content in the activated PVDF polymer obtained by the filter-oven drying method is studied in order to optimise the duration of the treatment time during the ozone activation process.

The ozone activation process was carried out at room temperature in different treatment time: 4, 8, 24 and 48 hours and compared with PVDF Hylar® 301 as indicated the experimental plan in Table 4.5. The peroxide content of PVDF and activated PVDF polymer were investigated by using DPPH assay. The changes in peroxide and hydroperoxide groups were also examined by ATR-FTIR. Moreover, ToF-SIMS spectrum of the PVDF and the ozone activated PVDF were investigated.

4.3.2.1.1 DPPH

The peroxide content of PVDF Hylar® 301 powder and activated PVDF samples were investigated using DPPH assay to determine the effect of treatment time. The results are shown in Table 4.5.

It is found in Table 4.5 the presence of peroxide content in the untreated PVDF polymer (sample O1); however, it was assumed that it is not the result of peroxide content because of the colour of PVDF solution in NMP is yellow which affected to the colour of DPPH solution. When the DPPH solution changed from deep violate to yellow-orange colour, the yellow colour from the PVDF solution was mixed with the DPPH solution and showed the absorption peak at 520 nm.

The peroxide contents in ozone-treated PVDF polymers increase with the increase in treatment time. However, after 24 hours of treatment (sample O4), there is not much

improvement in peroxide content. Therefore, 24 hours of treatment was considered optimistic condition and this condition will be used for further experiment.

Table 4.5 Peroxide content of PVDF and activated PVDF: effect of treatment time

Samples	**Treatment Time (hours)**	**Peroxide content (mole of peroxide per gram of ozone activated PVDF)**
O1	0	2.84×10^{-5}
O2	4	3.11×10^{-5}
O3	8	4.19×10^{-5}
O4	24	7.41×10^{-5}
O5	48	7.52×10^{-5}

4.3.2.1.2 ATR-FTIR

The ozone treated PVDF samples (O1-O5) were subjected to ATR-FTIR analysis to study the functional changes as shown in Figure 4.9.

It is expected that the infrared spectrum of ozone treated PVDF should have carboxylic acid group (-COOH) which could be identified by the C=O stretching at 1760-1670 cm^{-1}.

It is found in Figure 4.9 that the ozone treated PVDF samples where the treatment times were 4, 8, 24 and 48 hours (O2-O5) show the absorption peak at 1760-1670 cm^{-1} which represented to the carboxylic acid group added by the ozone activation process. However, the IR spectrum of PVDF Hylar® 301 powder (O1) does not show any characteristic peak that relates to ozone treated PVDF. The C=O stretching could be seen for the ozone activated PVDF samples.

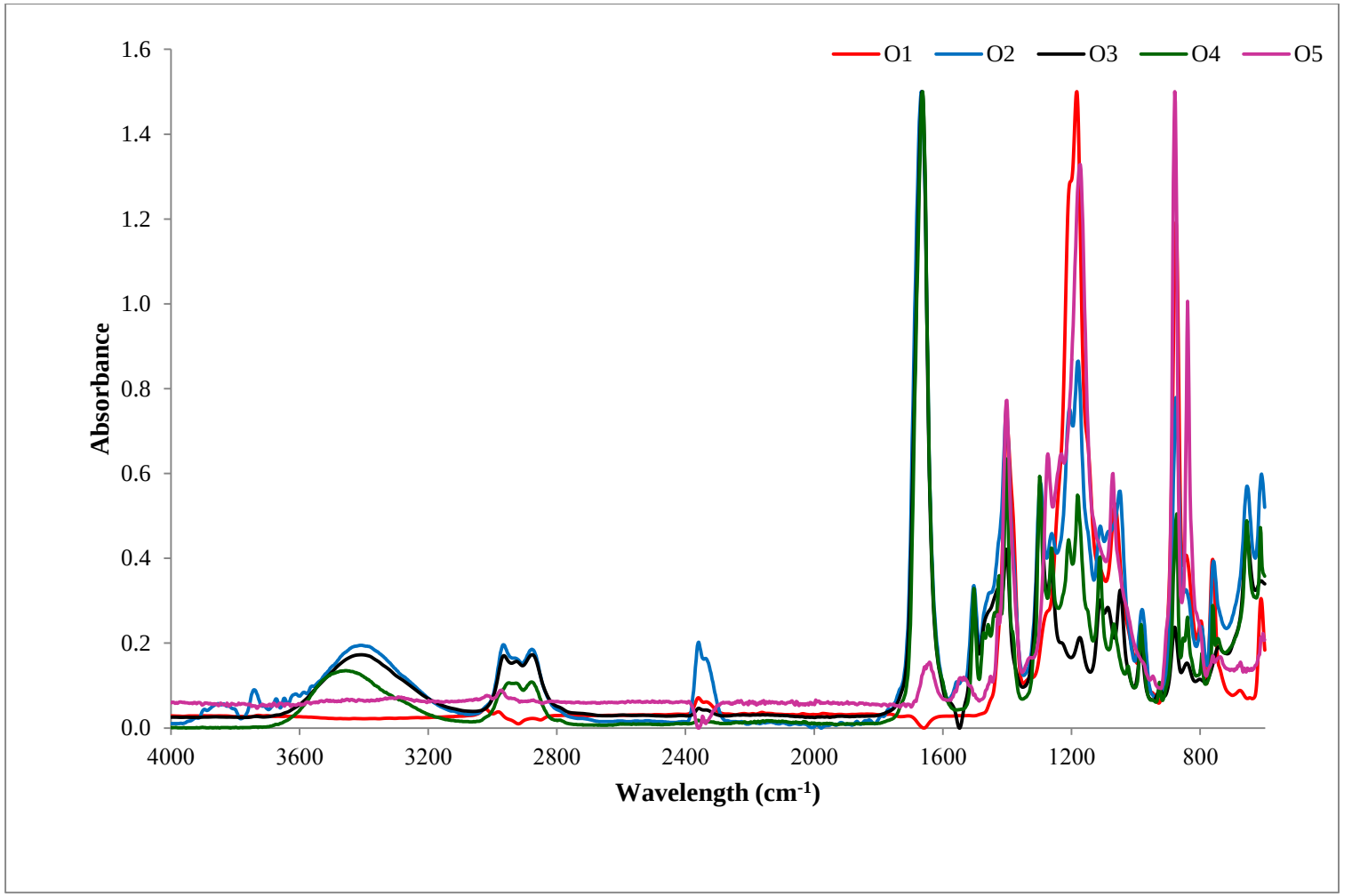

Figure 4.9 ATR-FTIR spectra of untreated PVDF and ozone activated PVDF (O1-O5)

4.3.2.2 Efficiency of the different drying methods

This section is to investigate the method which will be efficiently used to remove the NMP solvent and ethanol from activated PVDF polymer between the filter-oven drying method and the supercritical CO_2 method before the copolymerisation. The peroxide content in the ozone activated PVDF samples after drying from both drying methods were investigated by using DPPH assay (Table 4.7). ATR-FTIR spectrum of the ozone activated PVDF from two different drying methods were investigated and compared. DSC thermogram of the ozone activated PVDF from two different drying methods were also examined.

4.3.2.2.1 DPPH

Effect of different drying methods on the peroxide content of ozone treated PVDF polymer at room temperature for 24 hours are indicated in Table 4.6 with the investigation of the weight change of activated PVDF polymer after drying. The peroxide content in the ozone treated PVDF polymer was investigated by using the DPPH assay as indicated in Table 4.7.

Table 4.6 The comparison of ozone activated PVDF weight after drying

Samples	**Drying method**	**Weight (g)**	
		before ozone activation	**after ozone activation and drying**
O4	Filter-oven	7.5	29.1
O6	Supercritical CO_2		39.6

It can be seen from Table 4.6 that for both the methods, there is an increase in weight of the samples after the treatment. The weight of samples dried by supercritical CO_2 (O6) is increased approximately 5.3 times higher than to the untreated sample while the samples dried by filter-oven method (O4) is increased approximately 3.9 times. It could be concluded that these two drying methods cannot remove the NMP solvent and ethanol from the activated PVDF completely. However, these results shows that there are some solvents remaining in the activated PVDF. Therefore, the effective weight of activated PVDF was used for peroxide content measurements instead of the actual weight. The effective weight of the samples were calculated by dividing the actual weight with 5.3 for the supercritical CO_2 dried samples and with 3.9 for the filter-oven dried samples.

Table 4.7 The peroxide content in activated PVDF drying in different drying methods

Samples	**Actual weight (mg)**	**Effective PVDF weight (mg)**	**Peroxide content (mole of peroxide per gram of ozonized polymer)**
O4	100	25.6	7.41×10^{-5}
O6	100	18.9	2.72×10^{-4}

It can be seen from Table 4.7 that the supercritical CO_2 drying method shows superior peroxide content compared to the filter-oven drying method. Ethanol [200] and NMP [202] are miscible with supercritical CO_2 and they also have shown excellent solubility. Therefore, ethanol and NMP were removed from the ozone activated PVDF material easier than they were removed from the filter-oven drying method. Therefore, the supercritical CO_2 drying method could be an alternative novel drying method to dry the ozone activated PVDF polymers. In addition, the drying time is shorter for supercritical CO_2 drying.

4.3.2.2.2 ATR-FTIR

The ATR-FTIR spectra of the ozone activated PVDF polymers (O6 and O7) obtained from two different drying methods are shown in Figure 4.10. The absorption peak at 1665 cm^{-1} belongs to C=O stretching and are present in both activated PVDF samples, implying successful functionalisation.

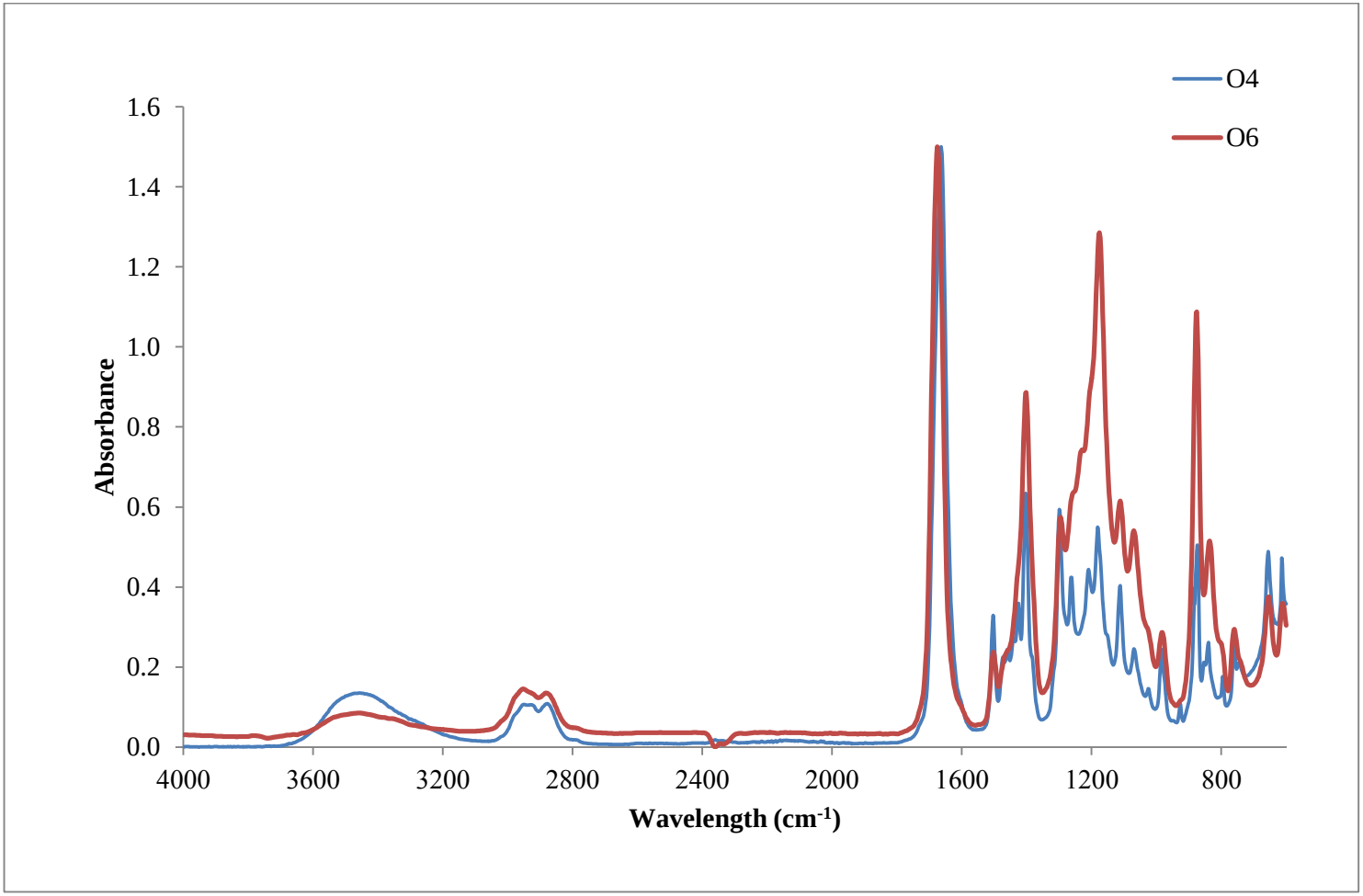

Figure 4.10 ATR-FTIR spectra of the ozone activated PVDF obtained from different drying methods (O4 and O6)

4.3.2.2.3 DSC

The ozone treated PVDF samples (O4 and O6) were analysed using DSC; this is to quantify the effect of drying processes on the melting temperature and the enthalpy change. DSC spectrum of PVDF Hylar®301, the ozone activated PVDF dried by the supercritical CO_2 method and the ozone activated PVDF dried by the filter-oven drying method are shown in Figure 4.11, Figure 4.12, and Figure 4.13, respectively. Moreover, the degree of crystallinity of the ozone activated PVDF from two different drying methods were compared to PVDF Hylar® 301; the results are shown in Table 4.8.

Table 4.8 The comparison of enthalpy (ΔH), melting temperature and the degree of crystallinity of the pristine PVDF powder and the ozone activated PVDF polymers dried using different drying methods

Samples	**Tm (°C)**	**Crystallinity (%)**	**ΔH**
O1 (PVDF Hylar®)	157.3	32.56	34.0
O4 (Filter-oven drying)	141.5	35.38	37.0
O6 (Supercritical CO_2 drying)	125.5	59.20	61.9

It is found in Figure 4.11 that PVDF Hylar® shows the partially crystalline polymer with the broad melting curve. However, there was a melting with the composition in the activated PVDF material from the filter-oven drying (O4) (see Figure 4.12). However, there was evaporation occurred during the DSC characterisation of the activated PVDF material from the supercritical CO_2 drying (O6) because the peak of DSC is very broad and the onset temperature started at 84.1°C which are earlier than the others samples as indicated in Figure 4.13.

Therefore, it can be seen from Table 4.8 that the melting temperature of PVDF Hylar® 301, the activated PVDF from filter-oven drying method, and the activated PVDF from supercritical CO_2 drying method are 157.3°C, 141.5°C, and 125.5°C respectively. The melting temperature of O4 and O6 are lower than PVDF Hylar® polymer because there were some solvent and impurities contained in the sample. Therefore, when the solvents started to evaporate, it effects the thermal properties of the activated PVDF samples.

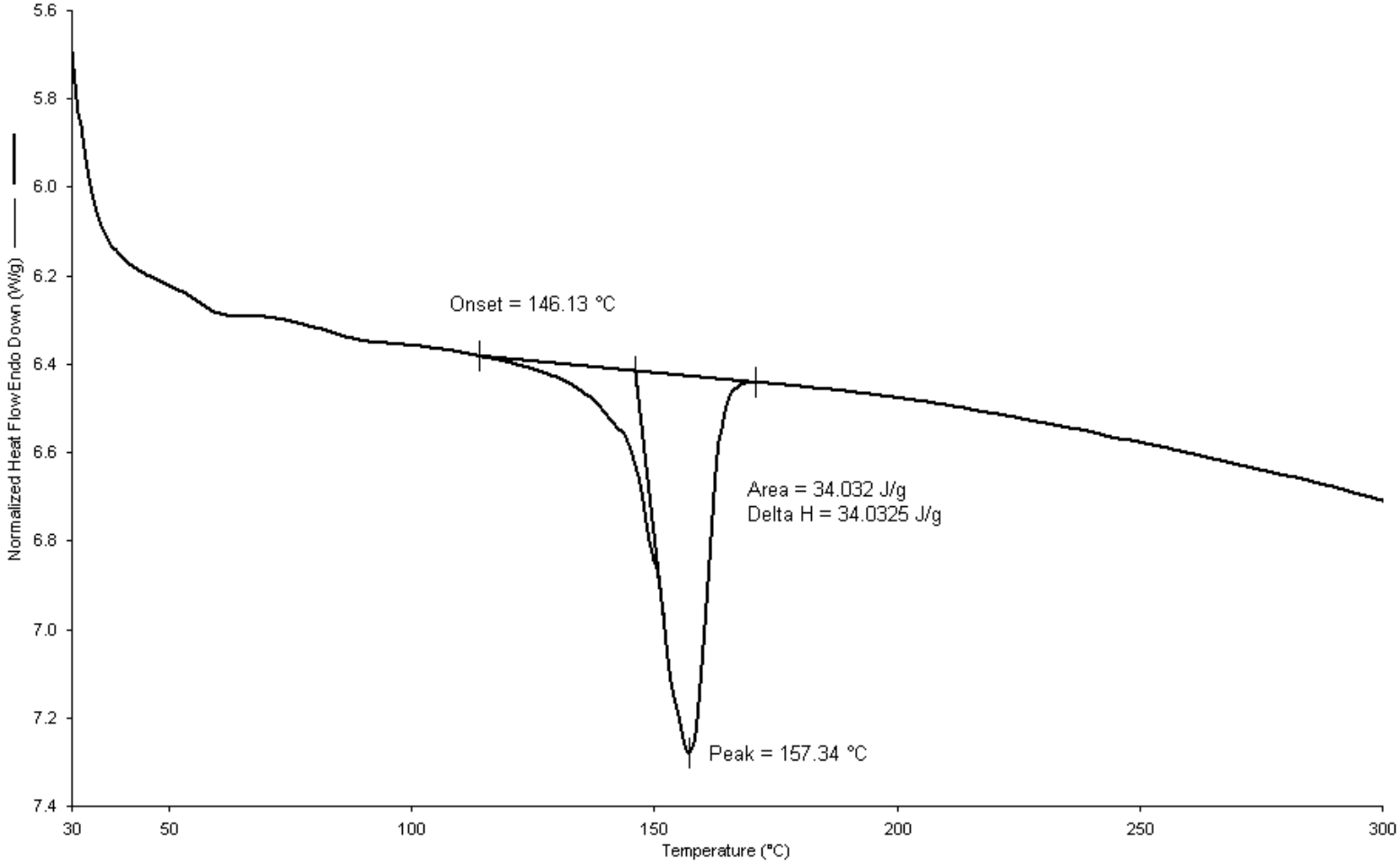

Figure 4.11 DSC spectrum of the PVDF Hylar® 301 (O1)

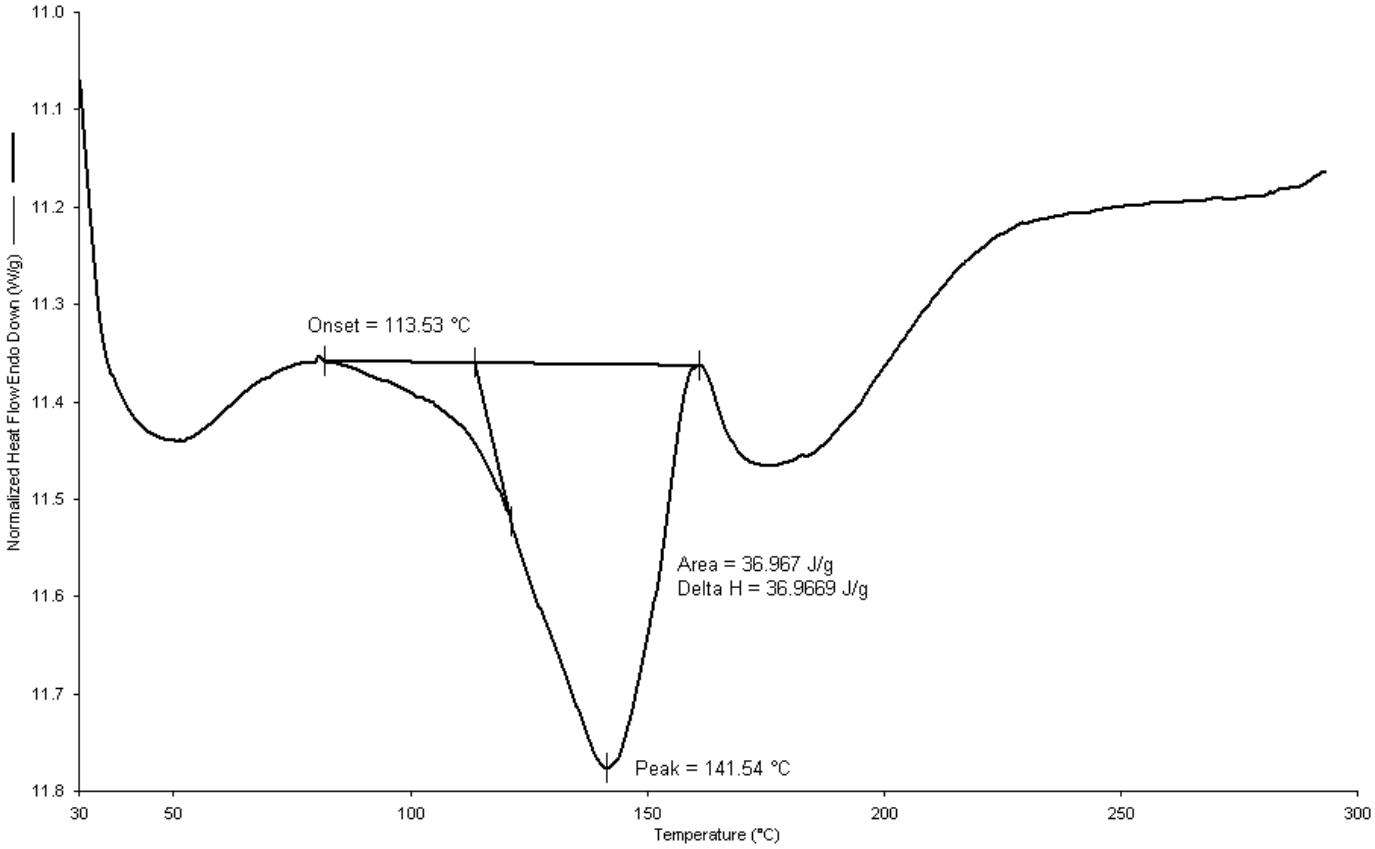

Figure 4.12 DSC of the ozone activated PVDF drying by using the filter-oven drying method (O4)

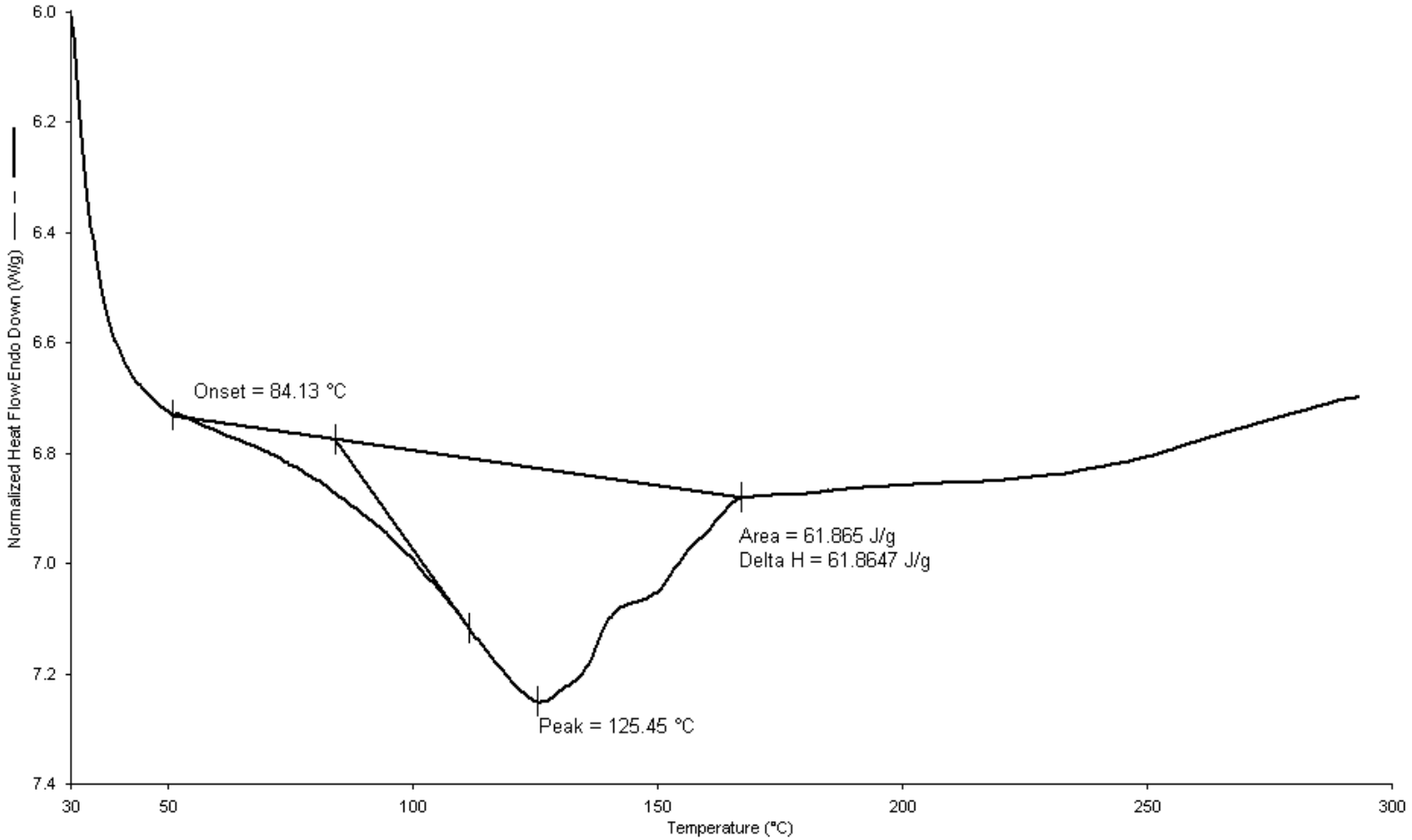

Figure 4.13 DSC of the ozone activated PVDF drying by using the supercritical carbon dioxide method (O6)

Moreover, the degree of crystallinity of the materials was measured as the ratio between the melting enthalpy (ΔH) of material and the melting enthalpy of absolute crystalline material (ΔH_0=104.5 J g^{-1} for PVDF) as shown in equation (2-25). The melting enthalpy of the activated PVDF from supercritical CO_2 drying process is higher than that of both PVDF Hylar® 301 and the activated PVDF from the filter-oven drying process. However, it could not be concluded that the degree of crystallinity of the activated PVDF from supercritical CO_2 drying process is the highest among the untreated PVDF and the activated PVDF from the filter-oven drying. This is due to the shape of the DSC curve of these three samples are different so the degree of crystallinity are incomparable.

4.4 PVDF-NIPAAM copolymerisation by thermally induced methods

In the study of the structure of the NIPAAM-g-PVDF copolymer materials, ATR-FTIR is used to analyse the structure of the NIPAAM-g-PVDF obtained by Route 1; in contrast, KBr-FTIR is used to analyse the structure obtained by Route 2. However, the result from KBr-FTIR and ATR-FTIR are not comparable according to the approaches of the methods. Therefore the comparison of the resultant NIPAAAM-g-PVDF made from Route 1 and Route 2 at the same concentration of NIPAAM is investigated in Section 4.4.2.2.

4.4.1 The structure of NIPAAM-g-PVDF copolymer obtained from Route 1 copolymerisation process by ATR-FTIR

The NIPAAM-g-PVDF copolymer materials obtained using Route 1 were analysed using ATR-FTIR. The difference among the samples is in the different proportion of NIPAAM used in the copolymerisation reactions. Table 4.9 is the referencing table for the qualitative characterise peak of NIPAAM in PVD-g-NIPAAM material.

According to the chemical structure of NIPAAM, amide I, amide II and amide III are considered. The absorbance at 1646 cm^{-1} represents the C=O stretching vibration with minor contributions from the out-of-phase CN stretching vibration and the absorbance at 1680 cm^{-1} represents CCN deformation and the NH in-plane bend. Moreover, the absorbance at 1546 cm^{-1} and 1280 cm^{-1} are considered as amide II and amide III [204]. Amide II is the out-of-phase combination of the NH in-plane bend and the CN stretching vibration with smaller contributions from the CO in-plane bend and the CC and CN stretching vibrations. While amide III is the in-phase combination of the NH

bending and the CN stretching vibration with small contributions from the CO in-plane bending and the CC stretching vibration [205]. In this study, the characteristic peak from NIPAAM is focused on the amide III peak at 1280 cm^{-1}.

Table 4.9 Peaks wavenumber of IR absorption bands and the interpretation of both NIPAAM and PVDF polymers

Polymers	**Wavenumber (cm^{-1})**	**Assignment**	**Interpretation**	**References**
NIPAAM	3435-3350	N-H	N-H stretching of secondary amide carbonyl group	[154], [203]
	1680-1642	C=O	Stretching of secondary amide carbonyl group	[116], [148], [154], [204],
	1629	N–H	N–H stretching of carbonyl amide group	[206]
	1550-1538	N-H and C-N	N–H stretching of the CONH groups amide II	[116], [133] [147],
	1280	C-N	Amide III	[205]
	1245	C=O	Amide III	
PVDF	3016	CH_2	Symmetric stretching	[207]
	2978	CH_2	Asymmetric stretching	
	1453	CH_2	In-plain bending or scissoring	
	1335	CH_2	Out-of-plane bending	
	1175-1290	CF_2		[158]
	884	CH_2	Alkene	
	840	CH_2 and CF_2	CH_2 rocking and CF_2 asymmetric stretching	[200]
	763	CH_2	In plane bending or rocking	
	745	CH_2	In plane bending or rocking	

In the case of PVDF, the absorption peak of 1175-1290 cm^{-1} represents the CF_2 functional groups of PVDF and the absorption peak at 884 cm^{-1} and 840 cm^{-1} were assigned to the CH_2 rocking and CF_2 asymmetric stretching [207].

To investigate the presence of NIPAAM in the NIPAAM-g-PVDF copolymers synthesised using Route 1, the ATR-FTIR was used to analyse the copolymers (D1-D4) as shown in Figure 4.14. It could be seen from Figure 4.14 that the amide III peak at 1280 cm^{-1} was introduced to the PVDF polymer after the copolymerisation processes (samples D1 to D4) using Route 1 suggesting a successful polymerisation reactions.

Table 4.10 The intensity of ATR-FTIR absorption peaks

Wavenumber (cm^{-1})	Interpretation	Intensity (Maximum high peak)				
		O1	D1	D2	D3	D4
1280	amide III (NH)	0.2861	0.4683	0.4832	0.5470	0.5340
880	alkene	1.1330	1.2747	1.3275	1.3625	1.2713

Table 4.11 Ratio of intensity of ATR-FTIR peaks of the NIPAAM-g-PVDF obtained from the conventional copolymerisation method

Samples	Ratio of amide III: alkene
O1	0.25
D1	0.37
D2	0.36
D3	0.42
D4	0.40

The intensity of the of ATR-FTIR absorption peak of amide III to alkene of PVDF Hylar® 301 in comparison with to the NIPAAM-g-PVDF copolymer material with produced by the different weight of NIPAAM (D1-D4) are indicated in Table 4.10 and then ratio of the intensity of amide III peak to alkene was indicated in Table 4.11. It is found the increasing of the weight ratio of NIPAAM in the initiated polymer from 1:25 to 1:1 (see D1 and D3) was effected to the amount of grafted copolymerisation

as the ratio of amide III to alkene increased from 0.37 to 0.42. However, the increasing of the weight ratio of NIPAAM in the initiated polymer was from 1:1 to 2:1 (see D3 and D4), the ratio of the amide III to alkene was decreased from 0.42 to 0.40.

Therefore, it is concluded in this study that the weight of NIPAAM in PVDF/NIPAAM solution is important parameter during the copolymerisation process using a small amount of NIPAAM did not achieve the NIPAAM-g-PVDF copolymerisation material; however, using a large amount of NIPAAM was not an ideal as well according to the ATR-FITR result did not show the larger ratio of the amide III to alkene peak. Therefore, the weight ratio of NIPAAM to PVDF at 1:1 (D3) is used in further experiment in order to compare the structure of NIPAAM-g-PVDF obtained between Route 1 and Route 2.

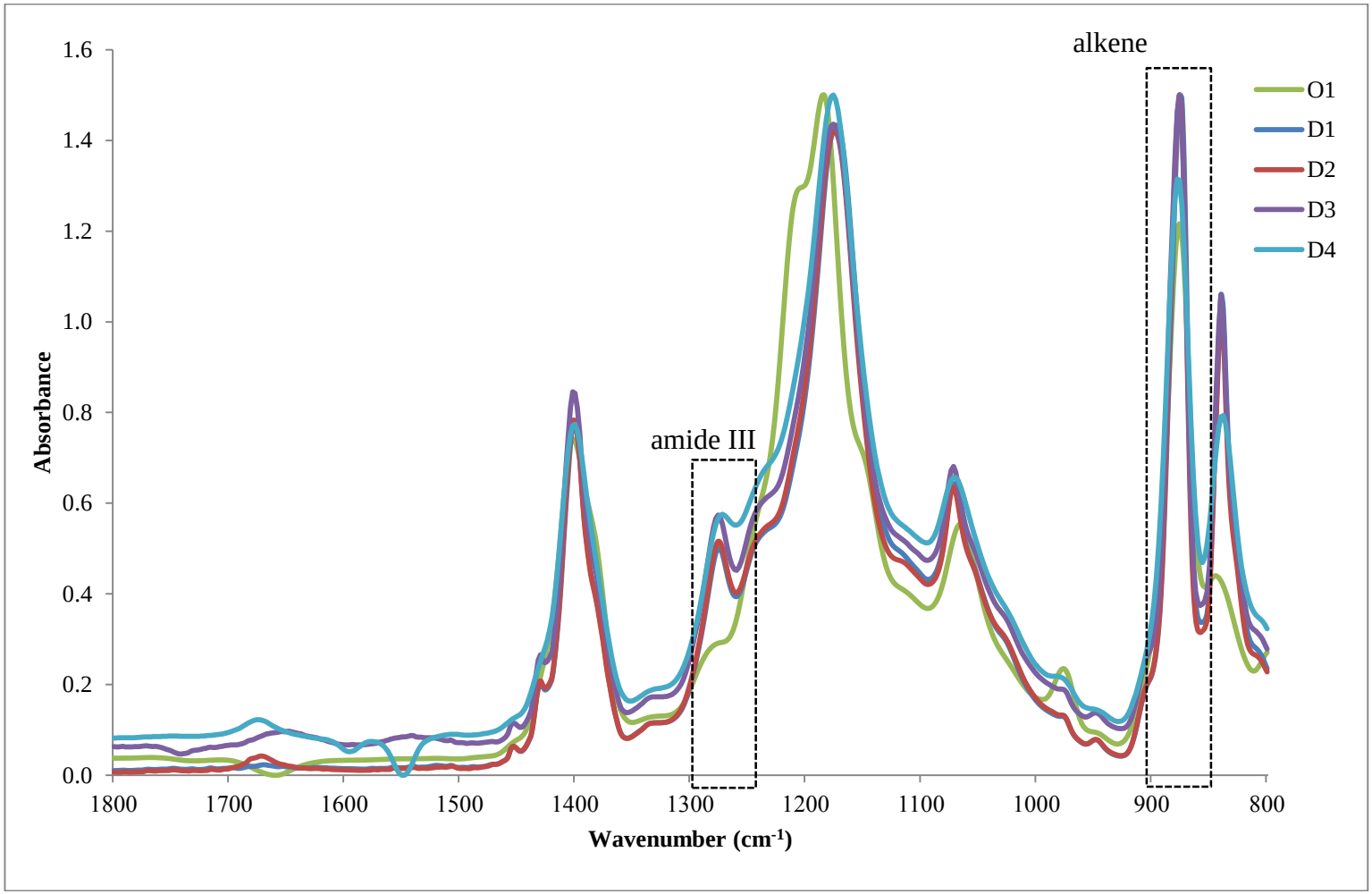

Figure 4.14 ATR-FTIR spectra PVDF Hylar® 301 (O1, D1, D2, D3 and D4)

4.4.2 The structure of NIPAAM-g-PVDF copolymer obtained from Route 2 copolymerisation process

Route 2 of the copolymerisation reaction was proposed to shorten the processing time and to retain the peroxide content in the ozone activated PVDF material. In this section, NIPAAM-g-PVDF copolymer obtained from Route 2 was analysed using different analytical techniques to investigate the presence of NIPAAM in the copolymer.

4.4.2.1 Time-of-Flight Secondary Ion Mass Spectrometry (ToF-SIMS) analysis

NIPAAM-g-PVDF copolymer (D5) was chosen to compare ToF-SIMS spectrum with the pristine PVDF Hylar®301 (O1) (See Figure 4.16). It is expected the copolymerisation reaction would be substantiated by the presence of isopropyl fragments ($C_3H_8N^+$) at 58 m z^{-1} as the expecting chemical structure of NIPAAM-g-PVDF indicated in Figure 4.15. The positive ion ToF-SIMS spectrum of NIPAAM-g-PVDF (sample D5) is shown in Figure 4.17. The signal of fragments peaks at 18, 44 and 58 m z^{-1} are attributed to NH_4, C_3HO^+ and $C_3H_8N^+$ fragments from NIPAAM [208].

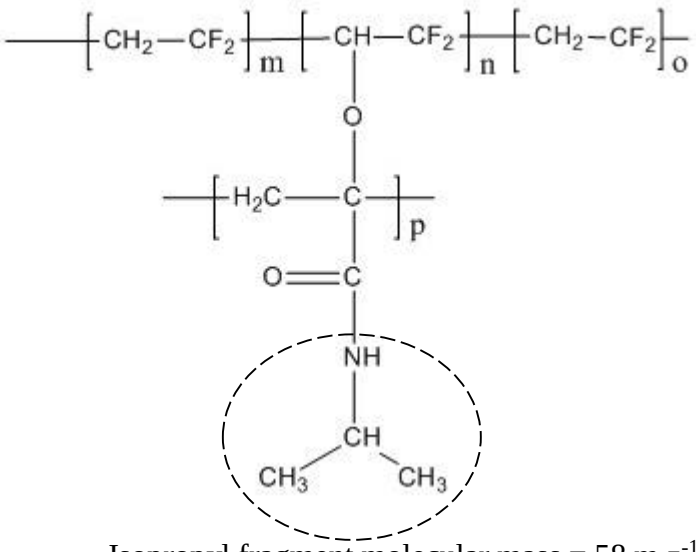

Isopropyl fragment molecular mass = 58 m z^{-1}

Figure 4.15 The expecting NIPAAM-g-PVDF copolymer chemical structure

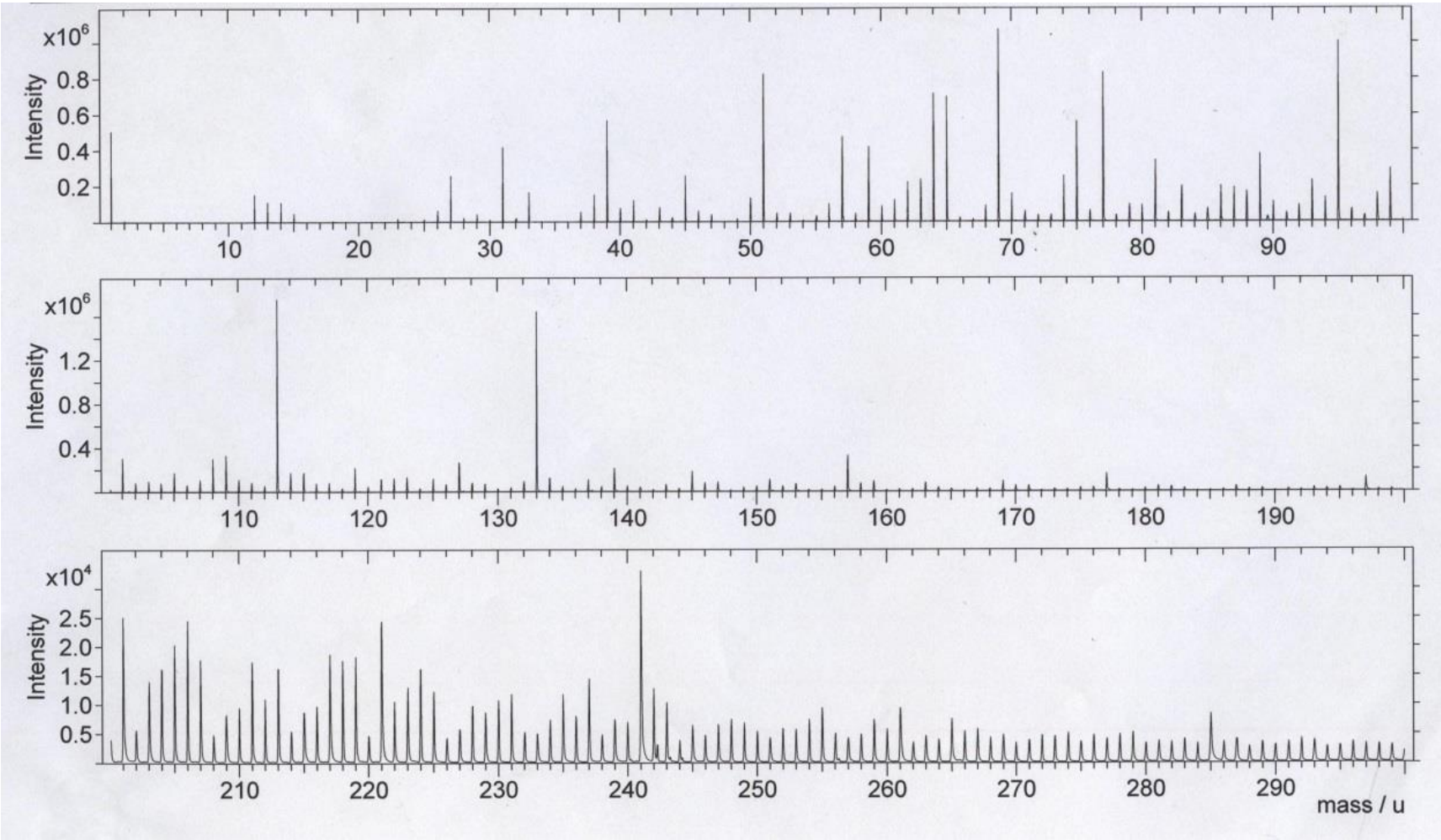

Figure 4.16 Positive ion ToF-SIMS spectra ($0 \leq m\ z^{-1} \leq 300$) of PVDF Hylar® powder

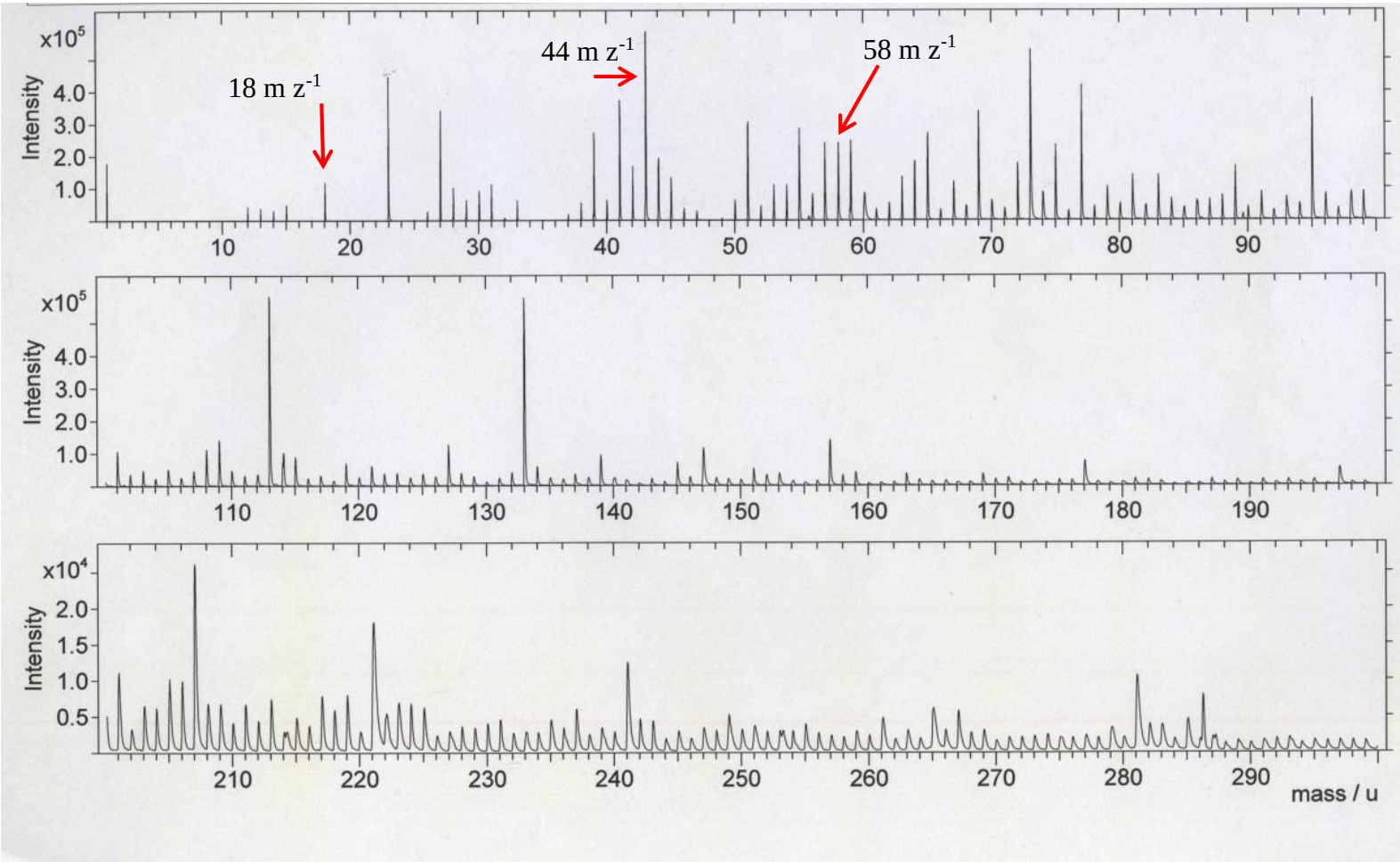

Figure 4.17 Positive ion ToF-SIMS spectra ($0 \leq m\ z^{-1} \leq 300$) of NIPAAM-g-PVDF (D5)

4.4.2.2 Fourier transform infrared spectroscopy (KBr-FTIR) analysis

FTIR (KBr disc method) was used to analyse the NIPAAM-g-PVDF copolymer synthesised using Route 2 (sample D5) to investigate the presence of NIPAAM in the copolymer (Figure 4.18). It could be seen in Figure 4.18 that the absorption peak of amide III at 1280 cm^{-1} was introduced to the PVDF polymer after the copolymerisation processes using Route 2 suggesting a successful polymerisation reaction. To compare the structure of NIPAAM-g-PVDF copolymer obtained from Route 2 to the NIPAAM-g-PVDF polymer material obtained from Route 1, the KBr-FTIR is investigated as indicated in Figure 4.18. Moreover, the intensity of the amide III and alkene peak was examined in Table 4.12. Then, the ratio of amide III peak to alkene and the ratio of amide II peak to alkene are used as the indicator in order to compare the grafted copolymerisation between two different route of copolymerisation as indicated in Table 4.13.

Table 4.12 The intensity of IR absorption bands

Wavenumber (cm^{-1})	**Interpretation**	**Intensity (Maximum high peak)**	
		D3	**D5**
1280	amide III	1.2130	1.2797
880	alkene	1.1380	1.1915

Table 4.13 The ratio of intensity of KBr-FTIR peak of D3 and D5

Samples	**Ratio of amide III : alkene**
D3 (Route 1)	1.07
D5 (Route 2)	1.07

It is found in Table 4.13 that the ratio of both amide III to alkene of the NIPAAM-g-PVDF copolymer material which produced by the Route 1 and Route 2 are similar. However, it is found the ratio of the amide III to alkene of D3 investigated by the ATR-FTIR which reported at 0.42 (see Table 4.11). Therefore, KBr-FTIR is more effective method because of ATR-FTIR is the characterisation technique to detect the functional group only on the surface of the material. Moreover, as it reported in Table 4.11, the ratio of the amide III to alkene of D3 is the greatest among the sample, it is thus concluded that even though using ATR-FTIR or KBr-FTIR to investigate the

structure of the resultant NIPAAM-g-PVDF material, the comparison of the presence of NIPAAM in the structure is validated.

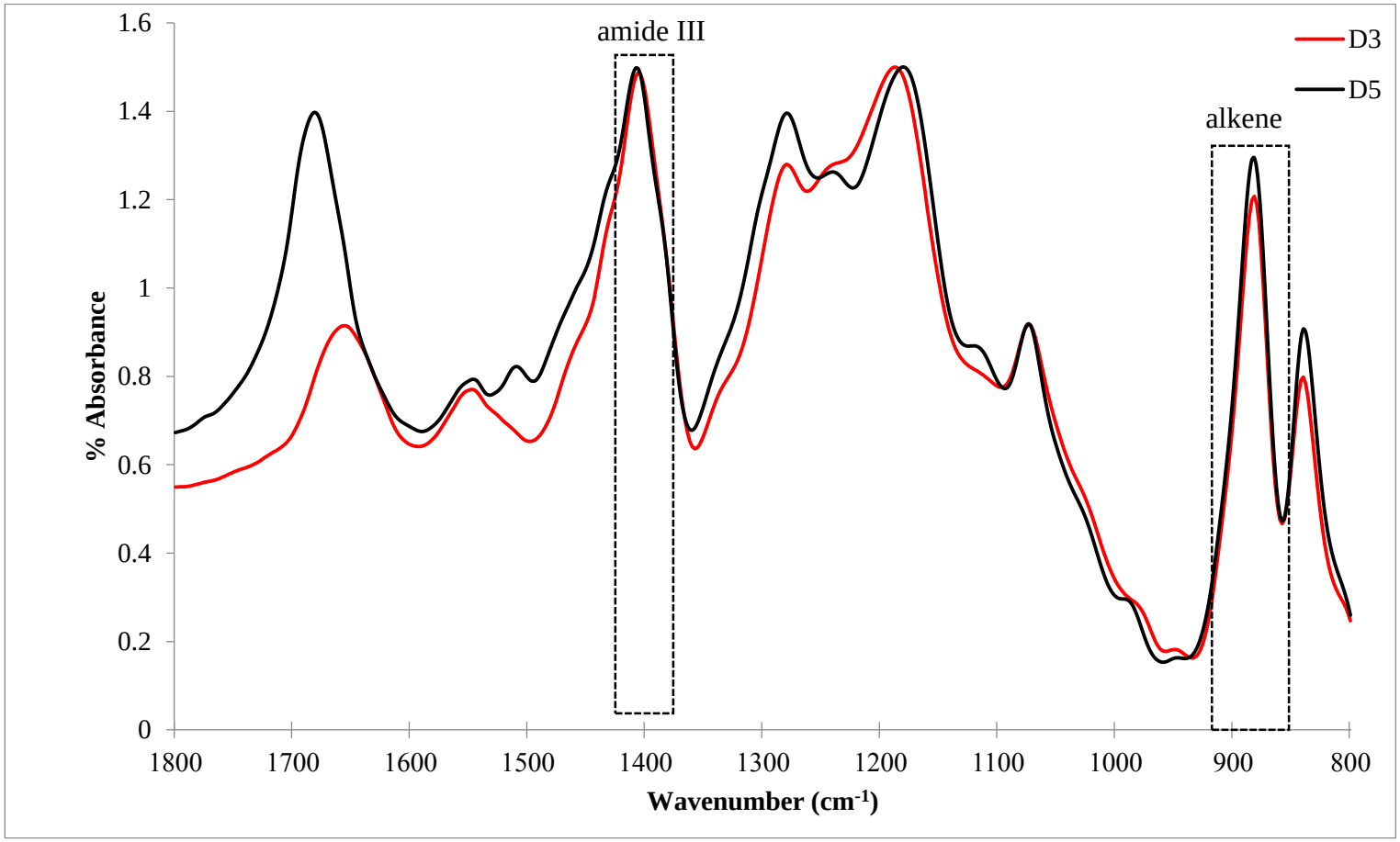

Figure 4.18 The comparion of KBr-FTIR spectra in the range of 1800–800 cm^{-1} between the traditional Route and the direct route (D3 and D5)

4.4.3 The difference in thermal properties between copolymers obtained from Route 1 and Route 2

In this section, the thermal properties of the NIPAAM-g-PVDF copolymers obtained from the Route 1 (sample D4) and Route 2 (sample D5) of the copolymerisation processes are characterised using DSC to analyse the enthalpy, the melting temperature, and the degree of crystallinity of the copolymers. The weight ratio of NIPAAM to PVDF is kept the same (1:1) for comparison.

DSC thermogram of the recrystallined NIPAAM polymer and NIPAAM-g-PVDF copolymers are shown in Figure 4.19, Figure 4.20, and Figure 4.21, respectively. The comparison of enthalpy, the melting temperature and the degree of crystallinity of the PVDF-NIPAAM copolymers from two different routes are shown in Table 4.14.

Table 4.14 Comparisons of enthalpy (ΔH), melting temperature and the degree of crystallinity of the PVDF-NIPAAM copolymers synthesised using Route 1 and Route 2

Sample	ΔH	Crystallinity (%)	Tm (°C)
D3 (Route 1)	48.9	46.83	154.1
D5 (Route 2)	52.5	31.16	156.1

The melting point of recrystallined NIPAAM polymer is 60-63°C [32]; however, DSC thermogram of NIPAAM is examined in this study as indicated in Figure 4.19. It is found that the melting point is at 66°C and showed an amorphous polymer.

It is found in Table 4.14 that the melting temperature of PVDF Hylar®301 (157.4°C) is different from the melting temperature of the NIPAAM-g-PVDF copolymer material suggesting that a structural change due to the copolymerisation reaction. It can be seen from Table 4.14 that the melting temperature of both the NIPAAM-g-PVDF copolymer materials (154.1°C and 156.1°C) are lower than the PVDF Hylar®301 because it is presumed that the NIPAAM in the NIPAM-g-PVDF copolymer material remains as clusters and immobilizes some of the PVDF [209]; therefore, NIPAAM prevents the crystallization and reduces the degree of crystallinity.

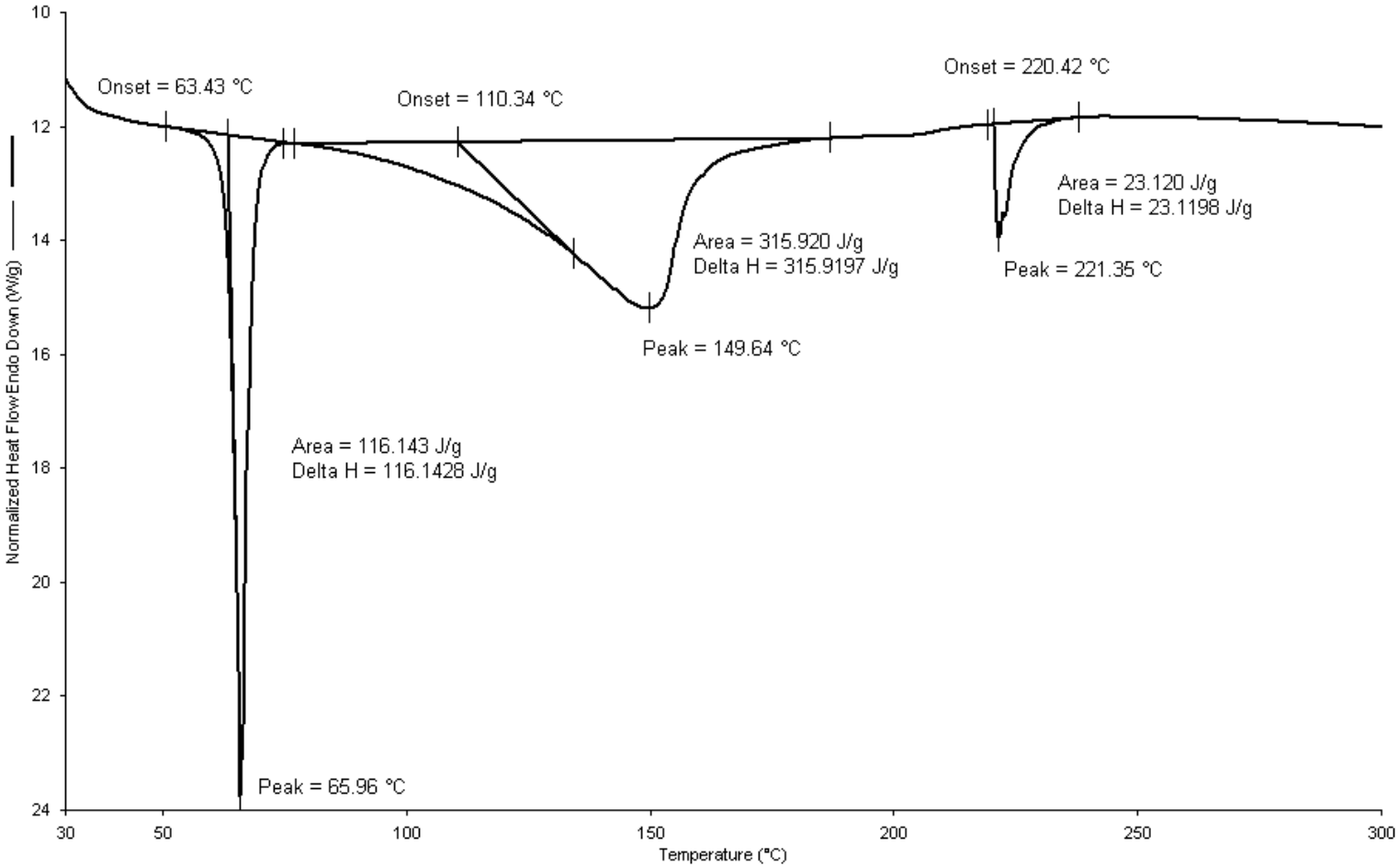

Figure 4.19 DSC of recrystallined NIPAAM

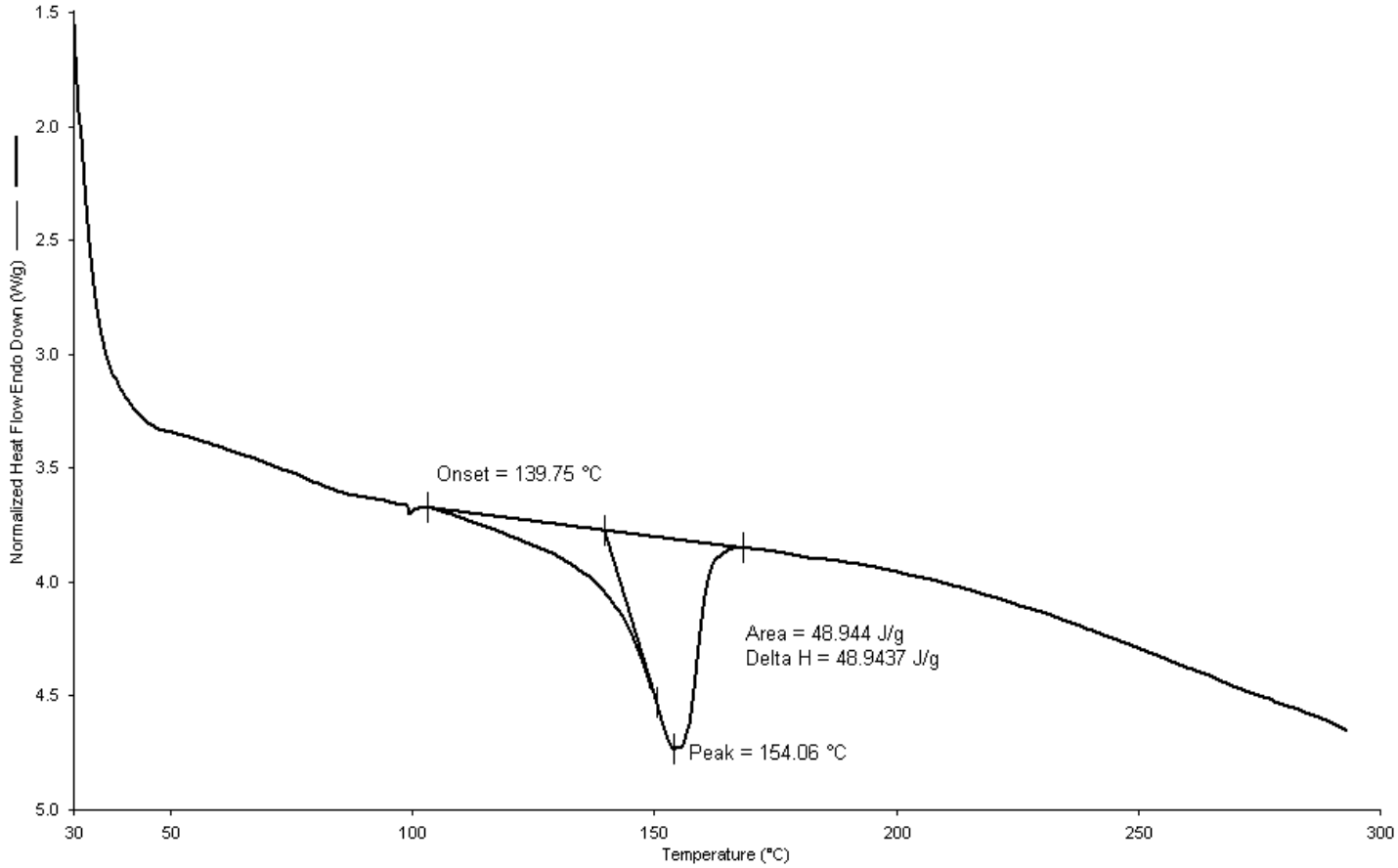

Figure 4.20 DSC of the NIPAAM-g-PVDF copolymer synthesised using Route 1 (Sample D3)

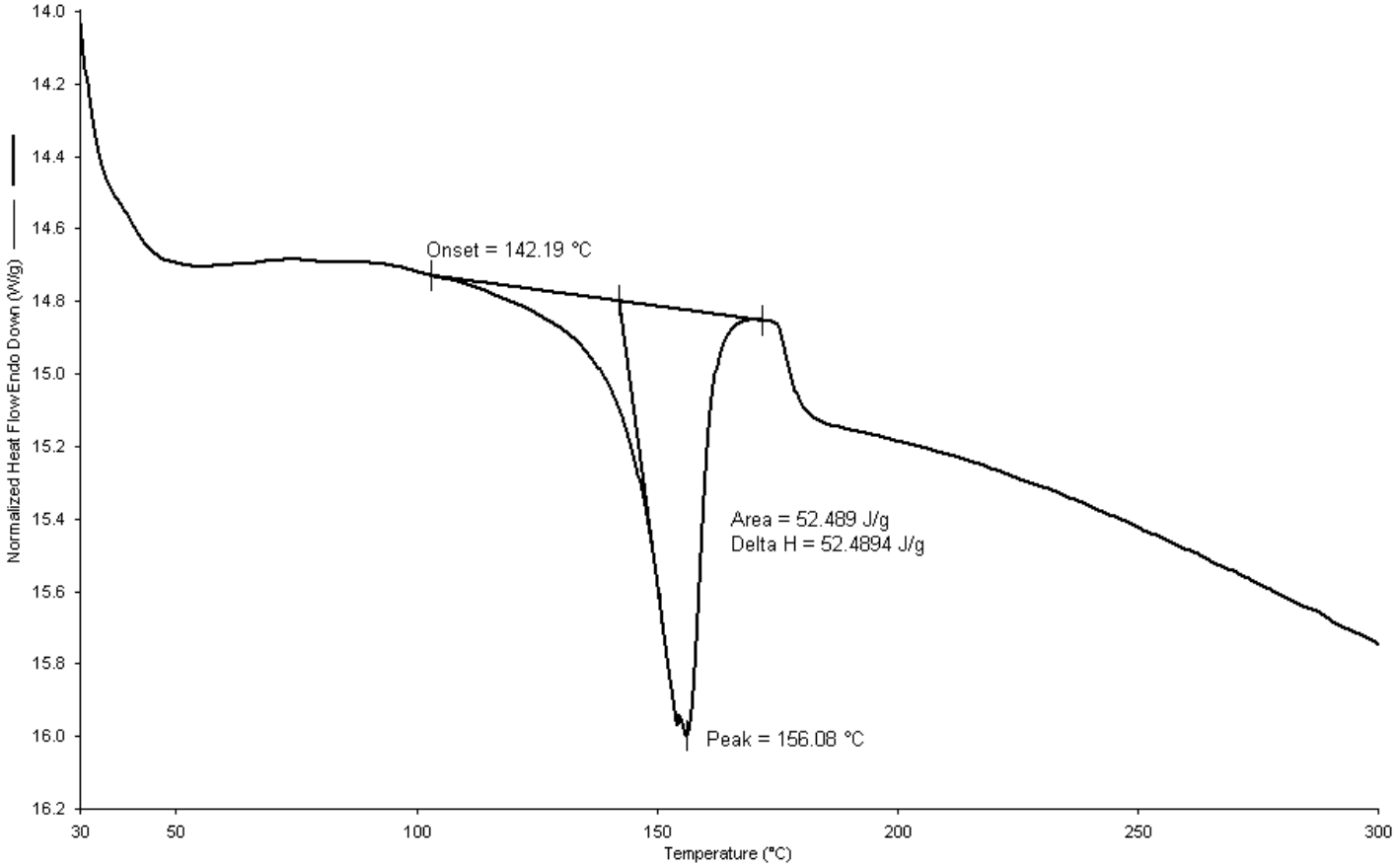

Figure 4.21 DSC of the NIPAAM-g-PVDF copolymer synthesised using Route 2 (Sample D5)

After the grafted copolymerisation with activated PVDF material, the structural symmetry of PVDF is partially destroyed resulting in the decrease of the melting temperature from 157.4°C to 155.0 °C as can be seen in Table 4.15. It is found that the degree of crystallinity of NIPAAM-g-PVDF copolymer materials is greater than the pristine PVDF (32.6%).

Figure 4.21, Figure 4.22, and Figure 4.23 showed the thermal analysis of the different weight ratio of NIPAAM copolymerised with the 24 hours activated PVDF material. However, the peak at 190ºC appeared in the NIPAAM-g-PVDF copolymer material at D5 and D6 thermogram but this peak was not appeared in D7. This may be due to the endothermic of the copolymer material has been changed. As discussed above, NIPAAM content in the NIPAAM-g-PVDF material may reduce the degree of crystallinity; therefore, the samples contained higher NIPAAM have a lower of degree crystallinity as indicated in sample D5 and D6. However, sample D7 which contains the lowest proportion of NIPAAM having the higher crystallinity than sample D6 as indicated in Table 4.15.

Table 4.15 The comparison of enthalpy (ΔH), melting temperature and the degree of crystallinity of the pristine PVDF powder and the NIPAAM-g-PVDF copolymer material

Samples	**ΔH**	**Crystallinity (%)**	**Tm (°C)**
D5	52.5	31.16	156.1
D6	62.3	59.62	155.7
D7	57.5	50.02	158.3

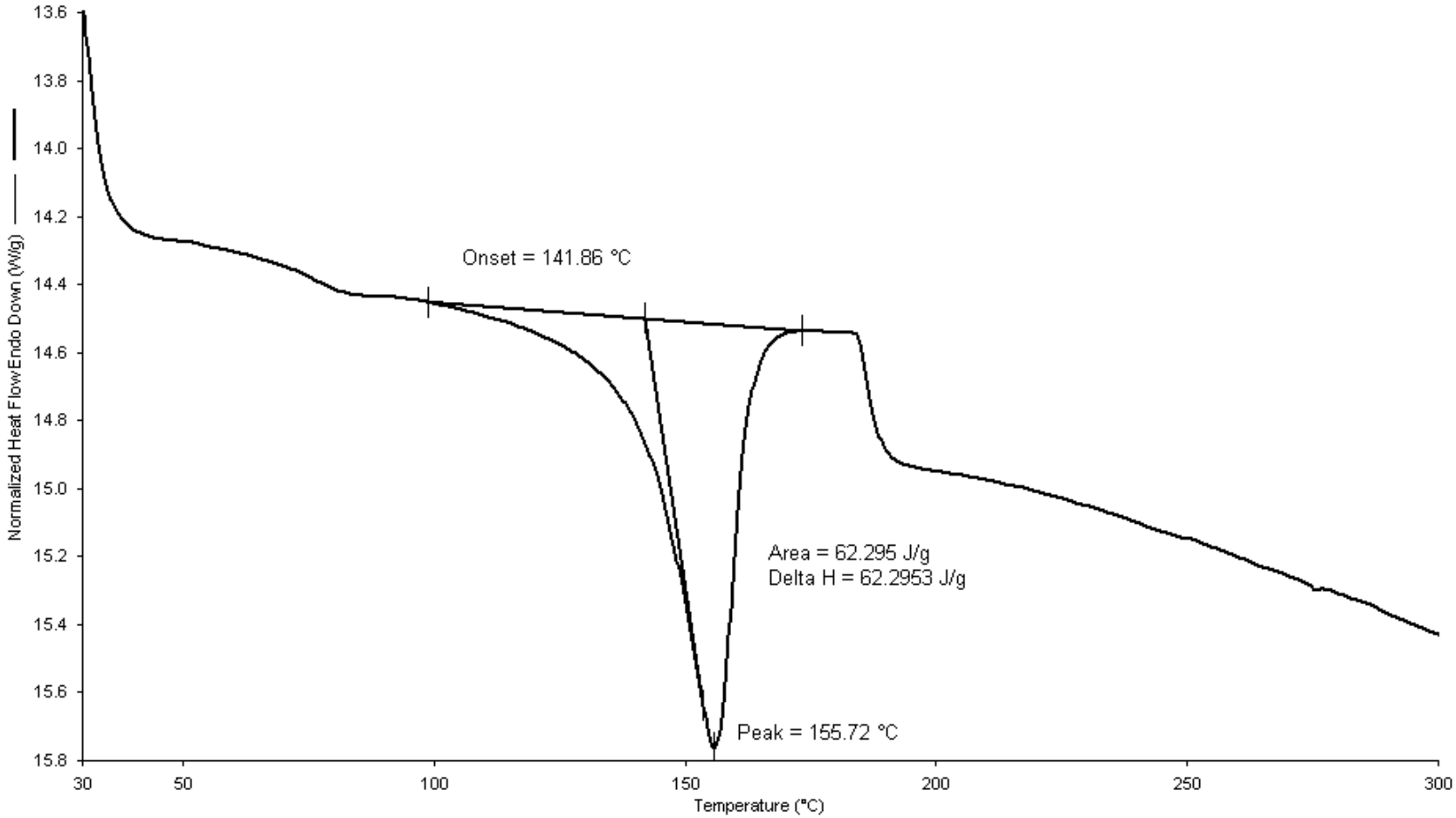

Figure 4.22 DSC curve of D6 (weight ratio = 1:10)

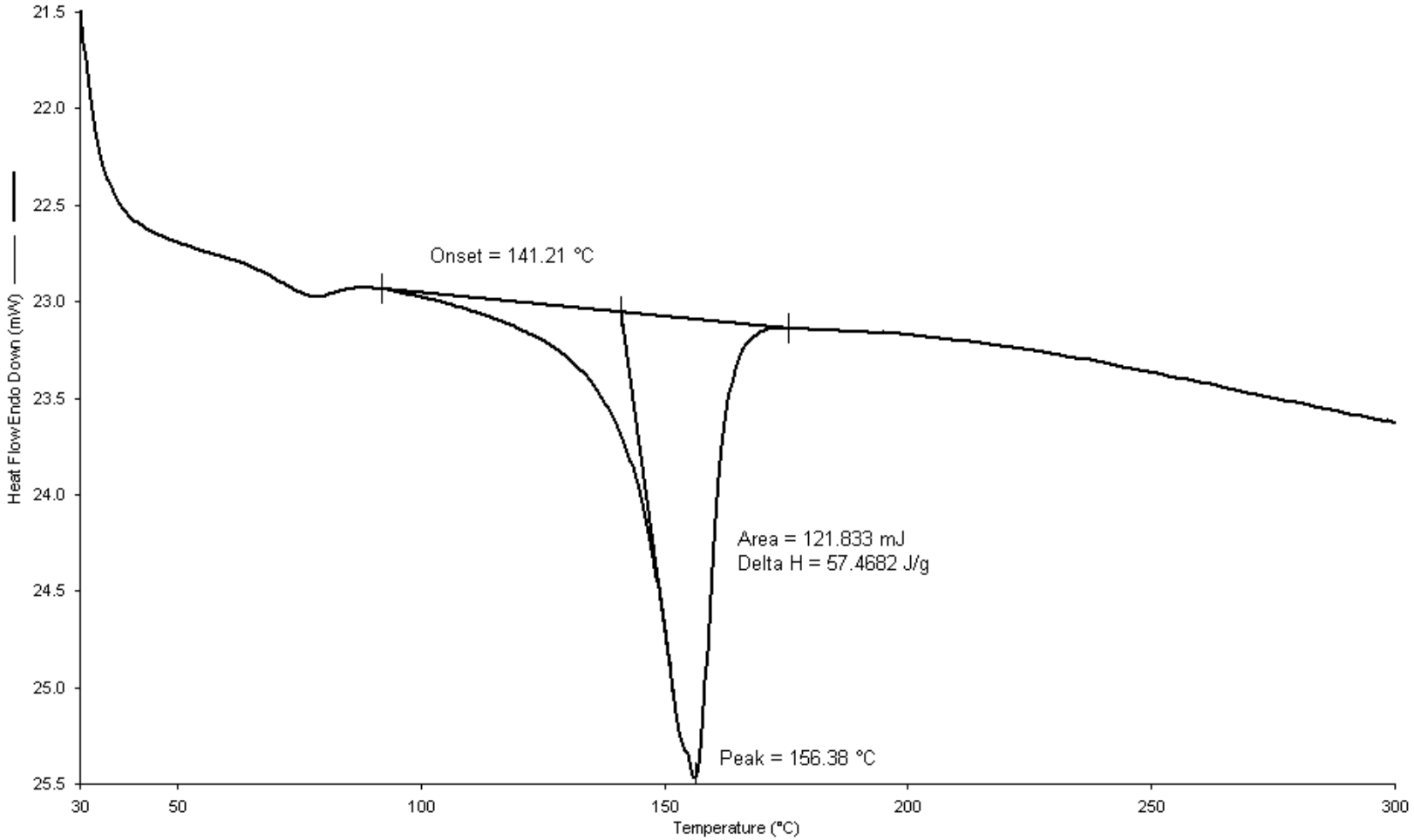

Figure 4.23 DSC curve of D7 (weight ratio = 1:100)

4.4.4 Estimated proportion of NIPAAM in the NIPAAM-g-PVDF copolymers obtained in the Route 2

In this study, NIPAAM polymer at three different concentrations in NMP solution including 0.5, 5 and 50 g dm^{-1} was used to copolymerise with the 24 hours ozone activated PVDF material. According to this copolymerisation procedure, the NIPAAM monomers that did not copolymerised with the activated PVDF was supposed to be dissolved in distilled water during the precipitation step. It means the NIPAAM homopolymer was remained in the mixture of NMP and distilled water rather than remained in the copolymers obtained. So the final NIPAAM-g-PVDF material after washing by water and drying at 40°C can be assumed as the purely grafted copolymer materials. Therefore, the actual amount of NIPAAM reacted with activated PVDF and the actual proportion of NIPAAM contained in the resultant NIPAAM-g-PVDF copolymers is unknown. Two methods are used to estimate the actual proportions of the NIPAAM in the resultant NIPAAM-g-PVDF copolymers.

4.4.4.1 Estimated proportion of NIPAAM contained in the resultant NIPAAM-g-PVDF copolymers by using masses consumed in the reactions

The mass of the raw materials of NIPAAM, activated PVDF and the dried resultant copolymer products are shown in Table 4.16, it is found that there are mass loss of both PVDF and NIPAAM during the reaction process, and the proportion of NIPAAM contained in the resultant NIPAAM-g-PVDF copolymers can be estimated by using masses consumed in the reactions explained below.

Table 4.16 The final copolymer material products

Samples	**NIPAAM (g)**	**PVDF (g)**	**NIPAAM-g-PVDF Copolymer materials (g)**	**Proportion of NIPAAM in the final NIPAAM-g-PVDF obtained (wt%)**
D5	2	2	2.2	14.5
D6	0.2	2	2.0	6
D7	0.02	2	1.9	1

If we assume that the 0.02 g of NIPAAM was completely bonded to the activated PVDF in sample D7, there is 1.88 g of PVDF in the 1.9 g of NIPAAM-g-PVDF

copolymers obtained; this means that there is a mass loss of 0.12 g of activated PVDF for every 2 g of activated PVDF added in the reaction process. Based on this assumption, the activated PVDF contained in samples D5 and D6 are 1.88 g as well. Therefore, the mass of NIPAAM in the 2.2 g (sample D5) and 2.0 g (sample D6) of NIPAAM-g-PVDF copolymers obtained are 0.32 g (sample D5) and 0.12 g (sample D6), respectively. Therefore the proportions of the NIPAAM in the samples D5, D6 and D7 are 14.5%, 6% and 1% respectively.

4.4.4.2 Estimated proportion of NIPAAM contained in the resultant NIPAAM-g-PVDF copolymers by using the intensity of amide III and alkene groups shown in the KBr-FTIR spectra

The characteristics of the KBr-FTIR spectra of the three NIPAAM-g-PVDF copolymer materials are shown in Figure 4.24. The absorption band in region of 1120 to 1280 cm^{-1} which is contributed as the CF_2 functional groups of PVDF. It also is obviously seen the absorption peak at 1645 cm^{-1}, 1546 cm^{-1} and 1280 cm^{-1} in of the NIPAAM-g-PVDF copolymer materials as they are referred to amide I, amide II and amide III from NIPAAM respectively.

Then, the amount of grafted polymer for samples prepared with the difference of NIPAAM concentration (sample D5-D7) is investigated by the ratio of the intensity of absorption peaks of amide III to alkene. The wavenumber between 1280 cm^{-1} to 880 cm^{-1} are chosen respectively as indicated in Table 4.17. Moreover, the ratio of amide III to alkene is indicated in Table 4.18.

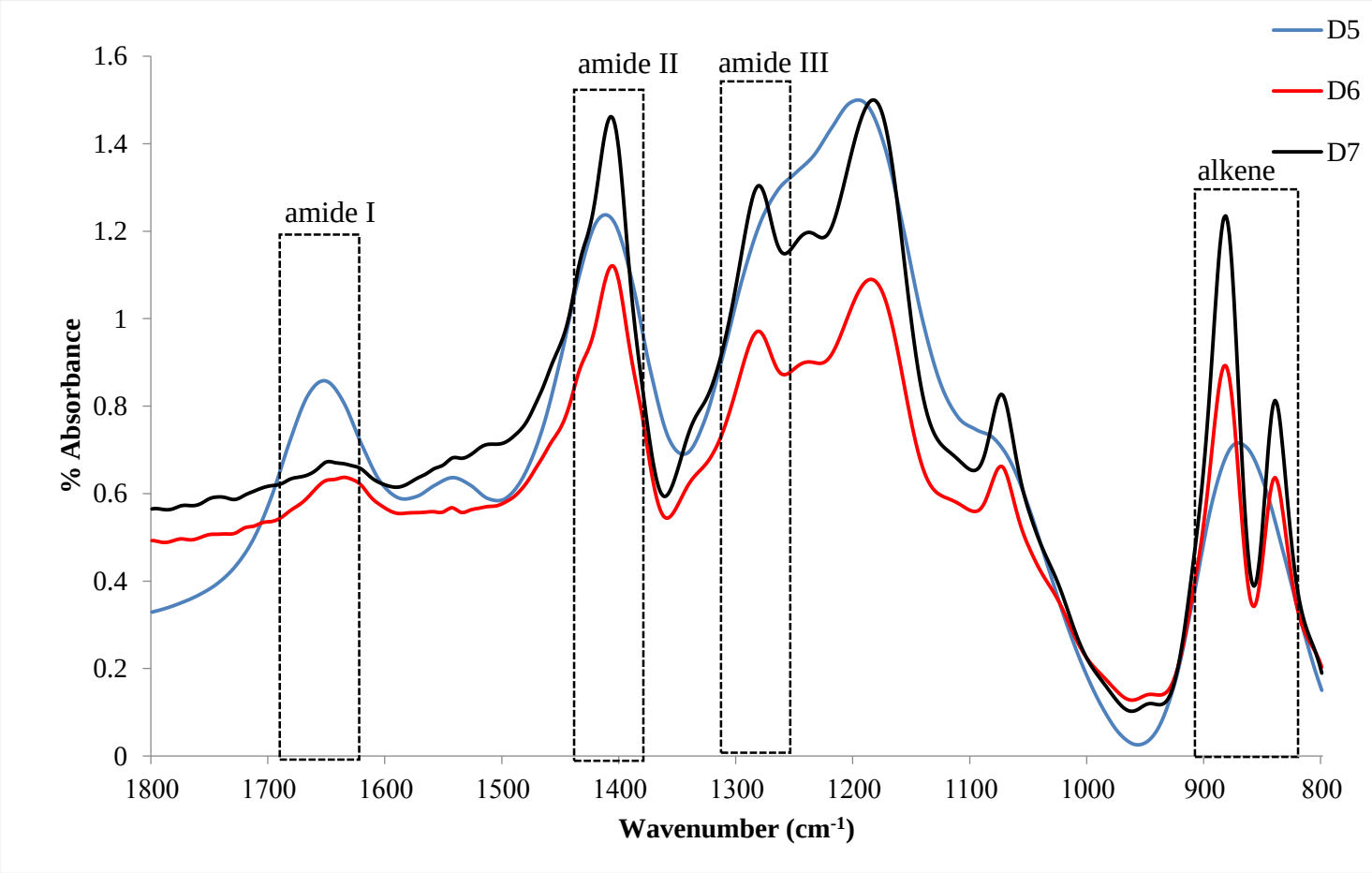

Figure 4.24 The comparison of KBr-FTIR spectrum of the NIPAAM-g-PVDF copolymer materials

Table 4.17 Intensity of KBr-FTIR absorption peaks of NIPAAM-g-PVDF material (Route 2)

Wavenumber (cm^{-1})	**Interpretation**	**Intensity (Maximum high peak)**		
		D5	**D6**	**D7**
1280	amide III (NH)	1.2196	0.9699	1.3030
880	alkene	0.6949	0.8777	1.2134

Table 4.18 Ratio of intensity of KBr-FTIR peaks of the NIPAAM-g-PVDF materials (Route 2)

Samples	**Ratio of amide III: alkene**
D5	1.76
D6	1.11
D7	1.07

It is found in Table 4.18 that the increasing of NIPAAM polymer in the initiated substance before the copolymerisation, the amount of grafted copolymer increases. Even though it was found that NIPAAM-g-PVDF copolymer materials at weight ratio 1:1 (sample D5) was vanished during the copolymerisation more than 40%. The presence of amide III in the weight ratio are still higher than the NIPAAM-g-PVDF grafted copolymer material at 1:10 and 1:100 weight ratios.

4.5 Conclusions

NIPAAM-g-PVDF copolymers were synthesised by using thermally induced graft copolymerisation method from ozone activated PVDF polymer. It was found that the ozone treatment time and the drying method influenced the peroxide content in the ozone activated PVDF polymer. The supercritical carbon dioxide drying method was proposed to be used as an alternative method to dry the ozone activated PVDF polymer. However, NIPAAM-g-PVDF copolymer materials are obtained by adding NIPAAM monomer solution into ozone activated PVDF solution in NMP (Route 2) makes the drying process of activated PVDF unnecessary. Moreover, it was also proved to be efficient; it is a quicker process and the resultant NIPAAM-g-PVDF

copolymer obtained was not significantly different from the polymers obtained from Route 1. Therefore, the novel route of thermally induced grafted copolymerisation will be used in the subsequent studies.

Chapter 5 NIPAAM-g-PVDF copolymers produced by using plasma-induced graft copolymerisation method

In this chapter, the copolymerisation of PVDF polymer with NIPAAM monomers by using plasma-induced graft copolymerisation method is investigated. There are two types of PVDF membrane involved in the research, a commercially available nonporous PVDF membrane (Polyflon®) and a porous PVDF membrane which produced by the phase inversion method. The resultant NIPAAM-g-PVDF copolymers are characterised by using Time-of-Flight Secondary Ion Mass Spectrometry (ToF-SIMS) and Scanning Electron Microscope (SEM).

As illustrated in Figure 5.1, the procedure of the copolymerisation of PVDF with NIPAAM by using the plasma-induced graft copolymerisation method is to begin with the preparation of a PVDF porous membrane by using phase inversion method. The obtained porous PVDF membranes are oxidised in an oxygen plasma treatment process in different conditions to produce various functional groups on the membrane surface. During the plasma treatment, the nonporous PVDF Polyflon® membrane is used to optimise the plasma treatment process. The plasma activated PVDF membranes are copolymerised with NIPAAM monomer in DMF aqueous solution.

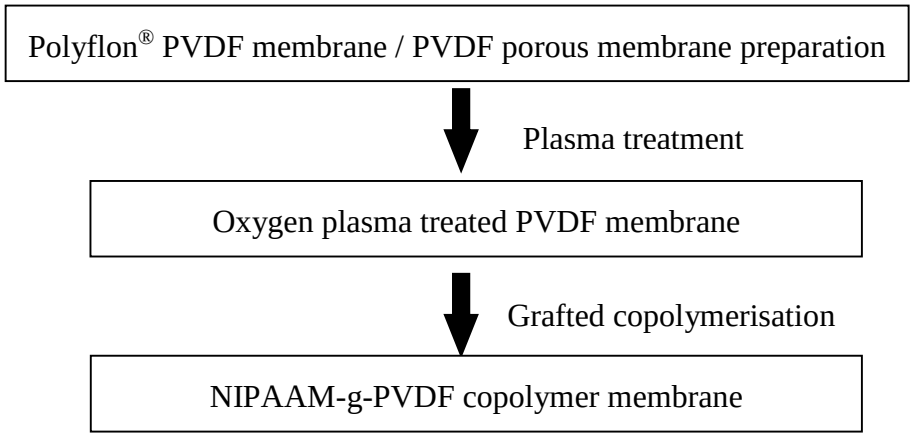

Figure 5.1 NIPAAM-g-PVDF plasma induced copolymerisation procedure

5.1 Materials and equipment

5.1.1 Materials

Nonporous Polyflon® PVDF membranes was obtained from Polyflon® Technology Limited, its thickness is 0.13 mm.

N,N-dimethylformamide (DMF) from Sigma was used in the preparation of the membrane for dissolving PVDF. 95% of ethanol from Fisher Scientific Ltd. was used as washing solvent to clean the Polyflon® before the plasma treatment process. Distilled water from the chemistry laboratory, School of Design, was used during the copolymerisation process.

5.1.2 Equipment

5.1.2.1 Knife coating device

The knife coating (K-Bar) device consists of a series of stainless steel rods and a 30×30 cm glass plate. In this study, a 300-μm gap casting knife and 500-μm gap coating knife are used in order to obtain resultant porous PVDF membrane of different thickness as it is expected that the porous membrane prepared by smaller gap casting knife may have smaller mass per unit area, thickness and bulk density. Both K-bar and glass plates are washed by acetone and leave them dry at room temperature before being used for the production of porous membranes.

During membrane casting process, certain amount of PVDF solution is placed at one edge of the glass plate and spread onto the glass plate evenly with controlled membrane thicknesses.

5.1.2.2 Plasma treatment machine

A low pressure plasma generator, Pico Type 6 from Diener Electronic, Germany, is used in this study. The frequency of the plasma generator is 40 kHz with the power is adjustable from 0 to 1000 Watts. PVDF membranes are placed horizontally onto an aluminium plate in the plasma chamber filled with oxygen gas at room temperature around 20 to 25°C. Then, the PVDF polymer is treated in continuously discharged plasma power with a controlled oxygen flow rate and pressure.

5.1.2.3 Copolymerisation system

The copolymerisation of NIPAAM monomer with PVDF polymer membrane is carried out in a water bath of controlled temperature, Model OLS200, from Grant, UK. Oxygen plasma treated PVDF membrane is immersed in a beaker containing NIPAAM aqueous solution. Then, the beaker covered with Parafilm® to protect the evaporation of the water is placed in a shaking water bath of controlled temperature at 20°C and the shaking strokes at 50 rounds per minute. The copolymerisation device is shown in Figure 5.2.

Figure 5.2 NIPAAM-g-PVDF copolymerisation carried out in a beaker immersed in a shaking water bath

5.2 Methods for the characterisation of PVDF porous membrane and NIPAAM-g-PVDF membrane

5.2.1 Bulk density

The mass per unit area, the thickness and the bulk density of the porous PVDF membrane are characterised using the same methods described in the Section 3.1.1.

5.2.2 Porous structure and porosity

The classification of the pore diameter was proposed based on their sizes as the following [209]:

(i) Macropore: the pores with diameter exceeding 50 nm;
(ii) Micropore: the pores with diameter not exceeding about 2 nm;
(iii) Mesopore: the pores with diameter of intermediate size which indicated by the pore diameter between 2 to 50 nm.

Membrane porous structures including specific surface area, average pore diameter and total pore volume are investigated by using Brunauer-Emmett-Teller (BET) method according to BS ISO 9277:2010 [210]. The resultant membranes are dried in an oven at 60°C over 24 hours for the removal of moisture before the BET measurement in a Micromeritics TriStar 3000 in the Institute of Particle Science and Engineering Laboratory, University of Leeds.

5.2.3 Water contact angle

Water contact angle of the resultant PVDF porous membranes might vary with roughness and porous surface of the membranes; it might be affected by both the coagulation bath in the PVDF porous membrane production process and the oxygen plasma treatment process.

The surface modification is examined by using the change of water contact angle before and after the plasma treatment according to BS EN 828:2013 [211]. A drop of distilled water of 10 μm^3 in volume is dropped on the membrane surface using a micro pipette in a vertical distance of 10 cm between the pipette tip and the membrane surface. The photos of the water drop sitting on the membrane surface immediately after the dropping were captured by using a JVC camera KYF550E and analysed using ImagePro software. The contact angle is a tangent to the drop contour going through one of the triple point where the solid, the liquid and the gas phases coincide with each other.

5.2.4 Surface morphology

The surface morphology of the NIPAAM-g-PVDF membranes is examined by using a Leica Cambridge Instruments' S 360 scanning electron microscope (SEM). The element analysis of the NIPAAM-g-PVDF membranes is examined in an LEO 1530: Gemini FEGSEM with Oxford Instruments' AZtecEnergy EDX system with 80mm X-Max SDD detector in the Leeds Electron Microscopy and Spectroscopy Centre (LEMAS), University of Leeds.

5.3 Production of the porous PVDF membrane

5.3.1 PVDF porous membrane production procedure

Several studies investigated the formation of the PVDF membranes by using two successive non-solvent baths, the first bath initiated the formation of a dense top layer and the second bath gave the actual polymer precipitation [212]. Different solvents were used in the coagulation baths, for example, alcohols such as methanol, ethanol, n-propanol and n-butanol was used as the first bath and distilled water was used as the second bath to prepare hydrophobic PVDF membranes (the water contact angle is over 140°) [213]. Additionally, the influences of other processing parameters such as the polymer concentration [212],[214], the casted solvent used [214], and the

temperature of the casting solution, the composition and the temperature of the coagulation bath [215], on the polymer precipitation and morphology of the membrane were also studied.

The porous PVDF membranes are produced using phase inversion technology with two different coagulation bath methods: single coagulation bath and dual coagulation bath. In the single coagulation bath, the distilled water at 40℃ is used as the coagulation solvent [213]; in the dual coagulation bath, ethanol is used as the first coagulation bath and the distilled water is used as the second coagulation bath, respectively.

Firstly, 237.17 grams of PVDF membrane, Hylar® 301, is dissolved in one litre of DMF solvent solution [216] at 60°C for 360 minutes, and then left at room temperature for 12 hours to degas. Then PVDF membranes of various thicknesses are produced by casting PVDF solution on a glass plate by using a 300-μm gap casting knife and 500-μm gap casting knife respectively.

Subsequently, the casted PVDF membrane on the glass plate is immersed in a coagulation bath (single or double bath) for solidification. Lastly, the membrane is dried in an oven at 40°C for 12 hours ready for the further experiment.

The effect of the solvents used in the immersion baths on the water contact angle and the bulk density of the porous membrane, the effect of the solvents used in the immersion bath, the coagulation time in the first bath of the dual coagulation bath were studied in order to produce porous membranes of higher bulk density and higher mass per unit area. The influences of using single or dual coagulation bath, the coagulation time, the gap of the knife coating on the structure of resultant membranes (e.g., the mass per unit area, the thickness, the bulk density and the water contact angle) are investigated as shown in the experimental plan in Table 5.1.

Bulk density, porous structure and the water contact angle of the resultant PVDF porous membranes are characterised in Section 5.3.2.

Table 5.1 The experimental plan for the production of porous PVDF membranes

Samples	K-Bar (µm)	1st bath			2nd bath		
		Solvent	Temperature (°C)	Time (min)	Solvent	Temperature(°C)	Time (min)
S1	300	Distilled water	40	2	Not applicable		
S2				10			
S3	500			2			
S4				10			
S5	300	Ethanol	RT	1	Distilled water	RT	10
S6				10			
S7				30			
S8	500			1			
S9				10			
S10				30			

5.3.2 Characteristics of PVDF porous membranes

5.3.2.1 Bulk structure

The bulk structure including mass per unit area, membrane thickness and bulk density. The porous PVDF membranes obtained from both single coagulation bath method and dual coagulation baths method are shown in Table 5.2.

Table 5.2 Bulk density of porous PVDF membranes

Samples	**Mass per unit area (g m^{-2})**	**Thickness (mm)**	**Bulk density (kg m^{-3})**
S1	181	0.23	0. 8
S2	176	0.31	0. 6
S3	182	0.65	0.3
S4	127	0.34	0.1
S5	113	0.76	0.1
S6	141	0.52	0.3
S7	130	0.76	0.2
S8	211	1.00	0.2
S9	245	0.98	0.3
S10	220	1.06	0.2

Effect of the coagulation time in the single coagulation method on the physical property of the porous PVDF membranes (S1-S4) is examined as indicated in Table 5.2. It is found that the PVDF porous membrane made from the single coagulation bath method (S1-S4), membranes made from longer period in coagulation (S2 and S4) have much smaller bulk density than the membranes made from shorter period of coagulation (S1 and S3). When the coagulation time is fixed (e.g., S2 and S4), the bulk density of the membrane (S4) made using the higher gap casting knife (500-μm gap coating knife) is much smaller (0.1 kg m^{-3}).

The effect of the dual coagulation bath processing parameters on the bulk density of the membrane is also examined. Fixed duration of 10 minutes in coagulation bath time

duration of 10mins and the room temperature distilled water were used in the second bath in order to eliminate the effect of the second coagulation bath. It is found in Table 5.2 that the membrane produced using the high gap knife casting (S8, S9 and S10) have greater mass per unit area, greater thickness and greater bulk density.

In the dual coagulation bath process, when the coagulation time duration is increased from 1 minute to 10 minutes, the mass per unit area, the thickness and the bulk density of these membranes also increase. However, when the coagulation time is increased from 10 to 30 minutes, the mass per unit area increase and the thickness decrease. Interestingly, it is found that the bulk densities of these PVDF porous membranes made from the dual coagulation method do not change as significantly as those made from the single coagulation bath method.

It is concluded that the coagulation time is one of the most important processing parameters for the production of porous PVDF membranes.

5.3.2.2 Porous structure

The porous structure including pore size distribution of the representative of the PVDF porous membranes made from both single coagulation bath (sample S3) and dual coagulation baths (sample S9) are illustrated in Figure 5.3 and Figure 5.4, respectively. Their true density, BET surface area, average pore diameters, and the total pore volume ranging from 0 to 170 nm are summarised in Table 5.3.

It is found in Figure 5.3 that the pore size distribution of the PVDF porous membranes (e.g., S3) obtained in the single coagulation bath process is bimodal. One peak is in the range of mesopores and the other peak is in the range of macropores. The pore volume of the macropores in the peak pore size is much greater than that of the mesopores in the peak pore size.

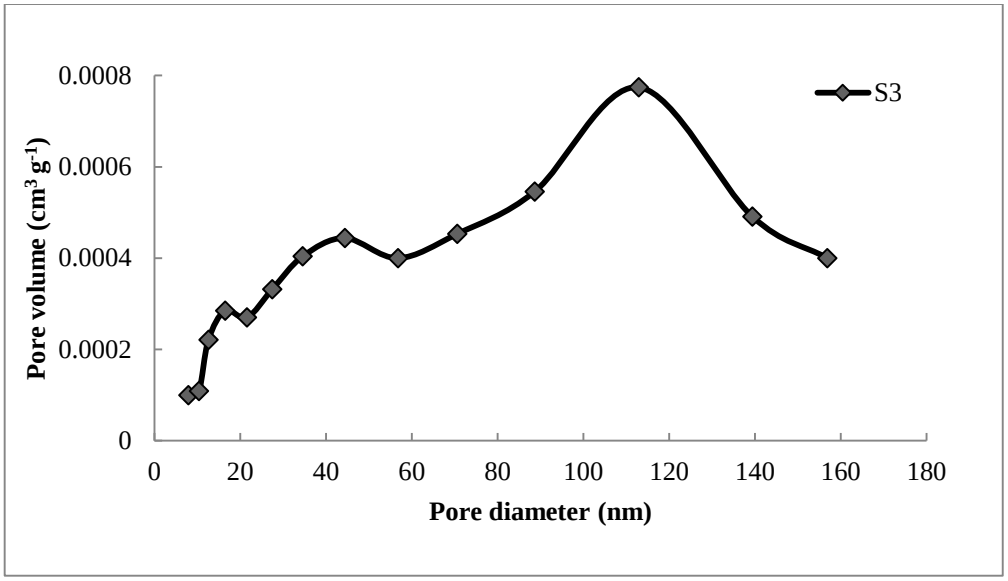

Figure 5.3 Representative pore size distribution of the porous PVDF membranes (e.g., S3) made from the single coagulation bath method

It is found in Figure 5.4 that the pore size distribution of the PVDF porous membranes (e.g., S9) obtained by dual coagulation bath method has multiple peaks. The volume of the macropores in the peak pore size is more or less similar to that of the mesopores in the peak pore size. As shown in Figure 5.4, the total pore volume of the mesopores in the range of pore size between 2 and 50 nm is approximately 49.1% while the total pore volumes of the macopores in the range of pore size between 50 and 170 nm is approximately 50.9%.

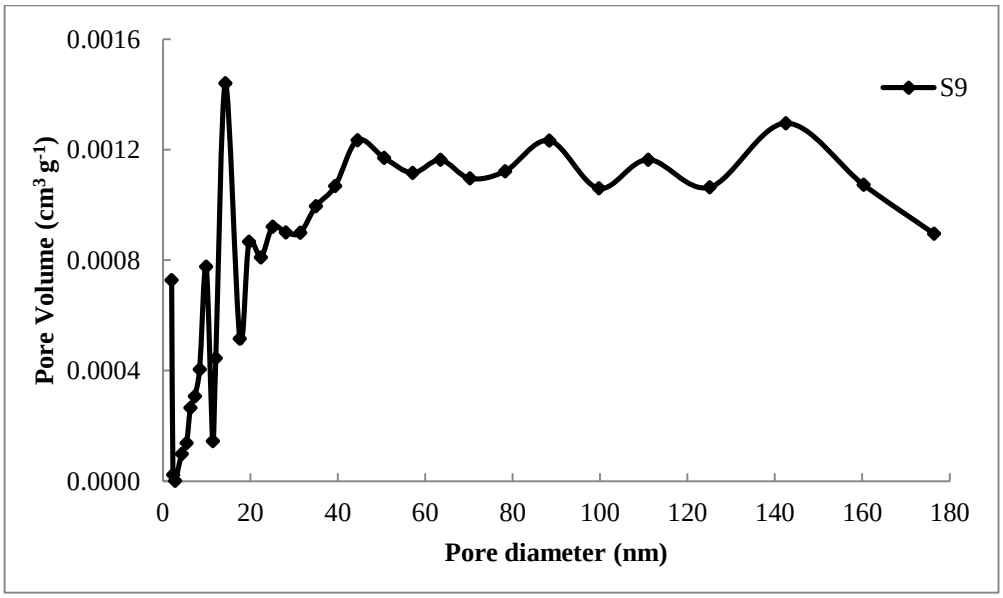

Figure 5.4 Representative pore size distribution of the porous PVDF membranes (e.g., S9) made from dual coagulation bath method

Table 5.3 Characteristics of porous structure of two PVDF porous membranes obtained from different coagulation methods

Property		**Single coagulation bath (S3)**	**Dual coagulation bath (S9)**
Porosity (%)		99.0	98.8
True density (g cm^{-3})		2.38	2.40
BET surface area ($m^2 g^{-1}$)		2.2	32.0
Average pore diameter (nm)		7.4	12.9
Mesopores	Pores volume ($cm^3 g^{-1}$)	0.002	0.013
	Percentage (%)	41.4	49.1
Macropores	Pores volume ($cm^3 g^{-1}$)	0.003	0.013
	Percentage (%)	58.6	50.9

The other characteristic of the porous structure of the PVDF porous membranes obtained by the two different coagulation methods are also summarised in Table 5.3. It is found that the average pore diameter of the porous PVDF membrane made from the single coagulation method (S3) is 7.4 nm while the average pore diameter of the porous PVDF membrane made from the dual coagulation method (S9) is 12.9 nm, which is much greater than that of the membranes obtained from the single coagulation method (S3).

Interestingly, it is noted that the PVDF porous membrane made from the dual coagulation method (S9) has significantly larger surface area (32.0 $m^2 g^{-1}$) in comparison with that of the PVDF porous membrane made from the single coagulation method (S3) (2.2 $m^2 g^{-1}$).

There is little difference between the porosity and the true density of these two samples. Their porosities are 99.0% and 98.8% and their true densities are 2.38 g cm^{-3} and 2.40 g cm^{-3} respectively for the PVDF porous membranes made from single coagulation bath method (S3) and dual coagulation baths method (S9).

It is concluded that the PVDF porous membranes made from the dual coagulation method have higher surface area and larger average pores; however the porosity and

true density of the PVDF porous membranes made from different methods hardly differ from each other.

5.3.2.3 Water contact angle

Water contact angle of the PVDF porous membrane made from both single coagulation bath method and dual coagulation baths method are summarised in Table 5.4.

Table 5.4 Water contact angle of the porous PVDF membranes

Samples	**Water contact angle (°)**
S1	52.6
S2	50.2
S3	67.0
S4	68.0
S5	123.7
S6	63.6
S7	51.8
S8	121.0
S9	107.3
S10	82.7

It is found in Table 5.4 that the PVDF porous membranes made from the higher gap casting knife (S3 and S4) have greater water contact angle (67.0° and 68.0°) in the single coagulation method; and the coagulation time duration has hardly any effect on the water contact angle of these membranes (S1 vs S2 and S3 vs S4) .

In the case of the dual coagulation method, it is found the water contact angle of the membranes decreases (123.7° to 63.6° and 121.0° to 107.3°) with the increases of the coagulation time in ethanol from 1 to 10 minutes (S5 vs S6 and S8 vs S9); when the coagulation time further increases from 10 to 30 minutes (S6 vs S7 and S9 vs S10), the water contact angle further decreases (63.6° to 51.8° and 107.3° to 82.7).

Therefore, the longer coagulation time leads to greater hydrophilicity of the PVDF porous membrane which is in agreement with the previous research that the hydrophilic PVDF membrane were produced by placing the casted PVDF membrane in the first bath for a longer period of time in the dual coagulation method [217].

Therefore, it is concluded that the coagulation time influences the bulk density of the resultant PVDF porous membranes in the single coagulation method and determines their hydrophilicity in the dual coagulation bath method.

Therefore, the PVDF porous membranes are produced in the dual coagulation bath system (they are immersed in the first ethanol bath for 10 minutes and the second distilled water bath for 10 minutes at room temperature is used as a substrate in the plasma treatment and copolymerised with NIPAAM) and use the 500-μm gap coating knife to cast the PVDF solution on a glass plate.

5.4 Plasma treatment of PVDF membranes

5.4.1 Plasma treatment procedure

Both nonporous Polyflon® PVDF membrane and porous PVDF membrane were cut into 10×10 cm and immersed in ethanol for 5 minutes in order to remove any potential impurities (e.g., greases and dirt contaminations) on the membrane surface. Then, the membranes were dried in the oven at 50°C for 1 hour before plasma treatment.

Oxygen gas applying to the chamber was varied at 2, 5, 10 and 20 standard cubic centimetres per minute (sccm). Plasma power was set at 250 and 500 Watts.

To determine the effect of plasma treatment on the surface of PVDF Polyflon® membrane, the experiment plan is indicated in Table 5.5. Based on the optimistic condition of the oxygen plasma treatment on PVDF Polyflon® nonporous membrane, the PVDF nonporous membrane shows the lowest water contact angle and this optimistic condition is selected to treat on the porous PVDF membrane.

Table 5.5 Experimental plan for oxygen plasma treated PVDF nonporous membrane (Polyflon®)

Samples	**Flow rate of oxygen gas (sccm)**	**Plasma power (Watt)**	**Time (min)**
P1	-	-	-
P2	5	250	1
P3			5
P4			10
P5		500	1
P6			5
P7			10
P8		750	1
P9			5
P10			10
P11	10	250	1
P12			5
P13			10
P14		500	1
P15			5
P16			10
P17		750	1
P18			5
P19			10
P20	20	250	1
P21			5

P22			10
P23		500	1
P24			5
P25			10
P26		750	1
P27			5
P28			10

5.4.2 Water contact angle of the plasma treated PVDF membranes

In order to indicate the effect of plasma treatment on the surface property (e.g., water contact angle) of PVDF polymers, a commercially available nonporous PVDF membrane, Polyflon®, is used as a reference substrate for plasma treatment. It was expected that the functional groups such as peroxide groups and hydrogen peroxide groups are introduced on the surface of the nonporous PVDF membranes and the surface area is increased after the oxygen plasma treatment process, so the plasma treated PVDF membranes could be used to form chemical bonds with the other chemicals (e.g., NIPAAM) during subsequent copolymerisation process. Water contact angle is used as an indication of the changes of specific surface area and surface roughness after plasma treatment. The water contact angle of both plasma treated PVDF Polyflon® nonporous membrane and plasma treated porous PVDF membranes are compared with untreated PVDF membranes in this section.

The oxygen pressure and temperature used in the plasma chamber cannot be adjusted by the instrument controller; they are recorded and reported in Table 5.6 with corresponding water contact angles of the membranes.

Table 5.6 The water contact angle of the plasma treated nonporous PVDF membrane (Polyflon®)

Samples	**Pressure (Pa)**	**Average Chamber Temperature (°C)**	**Contact angle (°)**
P1	-	-	82.0
P2	36	25	28.2
P3	36	25	25.8
P4	36	25	29.6
P5	36	21	25.4
P6	36	21	37.1
P7	36	25	29.3
P8	36	23	35.6
P9	36	23	37.4
P10	38	25	38.1
P11	48	25	33.1
P12	48	24	29.8
P13	48	25	32.5
P14	48	23	36.2
P15	48	24	24.2
P16	48	24	32.9
P17	48	24	28.6
P18	48	25	30.0
P19	48	25	31.5
P20	64	24	27.6
P21	64	24	28.3

P22	64	24	26.4
P23	65	23	29.0
P24	65	25	31.9
P25	65	23	30.5
P26	65	25	30.7
P27	64	25	31.8
P28	65	25	40.1

It is shown in Table 5.6 that the oxygen pressure increased with the increase of the flow rate of oxygen gases. It is noticed that the water contact angle of the plasma treated PVDF nonporous membranes decreased in comparison with untreated PVDF nonporous membranes. It means the hydrophilicity of the nonporous PVDF membrane was improved after treated with the oxygen plasma.

As sample P15 which was treated by the oxygen gas flow rate at 10 sccm, 500 watts plasma power for 5 minutes shows the lowest water contact angle, this condition is used as the generic condition to treat porous PVDF membranes in the rest of this research.

It is expected the change of water contact angle of both the PVDF porous membrane and PVDF Polyflon® membrane represents the change of surface property such as the surface roughness and the surface area of PVDF nonporous membrane. Water contact angle of the plasma treated PVDF Polyflon® membrane is shown in Figure 5.5.

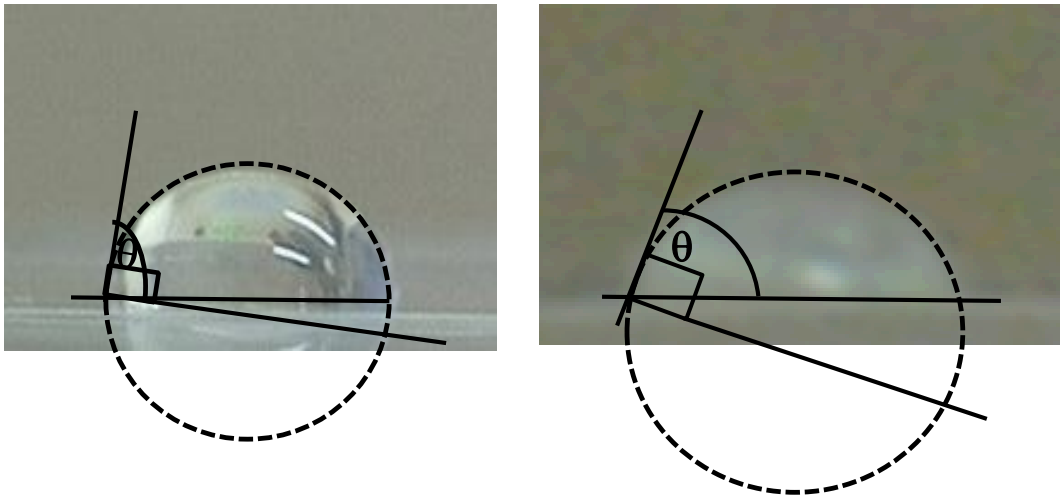

a) Before plasma treatment (P1) b) After plasma treatment (P15)

Figure 5.5 The water contact angles of a PVDF nonporous membrane before and after oxygen plasma treatment (oxygen gas flow rate at 10 sccm, 500 watts plasma power for 5 minutes).

Figure 5.5 shows the water contact angles of an untreated PVDF nonporous membrane and a plasma treated PVDF nonporous membrane by using oxygen gas flow rate at 10 sccm, 500 watts plasma power for 5 minutes, it is found that the water contact angle of the plasma treated PVDF nonporous membrane is 24.3° which is much smaller than the untreated PVDF nonporous membrane (82.0°).

Similar to the PVDF Polyflon® nonporous membrane, the plasma pressure, the average temperature of the chamber during the plasma treatment of the PVDF porous membrane were recorded and the water contact angle of the plasma treated PVDF porous membrane is shown in Figure 5.6.

It is found that the water contact angle of the plasma treated PVDF nonporous membrane is 42.3° which is also much smaller than the untreated PVDF nonporous membrane (78.0°). This means that oxygen plasma treatment significantly changes the hydrophilicity of the PVDF membranes, most likely due to the introduction of hydrophilic active groups onto the surface of PVDF membrane surface.

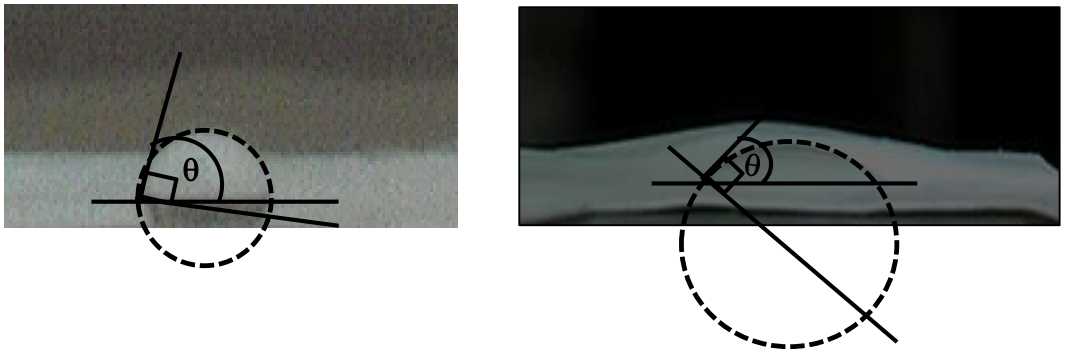

a) Before plasma treatment b) After plasma treatment

Figure 5.6 The water contact angles of a porous PVDF membrane before and after plasma treatment (oxygen gas flow rate at 10 sccm, 500 watts plasma power for 5 minutes).

5.5 Copolymerisation of NIPAAM-g-PVDF

5.5.1 NIPAAM-g-PVDF copolymerisation procedure

The plasma-induced pore-filling copolymerisation method [146] is studied in this section. The effect of the porous structure of the PVDF porous membranes, the NIPAAM aqueous solution temperature and the plasma treatment time on the structure and properties of the resultant NIPAAM-g-PVDF are studied.

In this study, only porous PVDF membranes made from the dual coagulation bath method (S9) (see Section 5.3) are used as the substrate in the plasma induced graft copolymerisation process to copolymerise with NIPAAM monomers. These membranes are treated by the oxygen plasma at 10 sccm, 500 watts plasma power for 5 minutes, and copolymerised with the NIPAAM in the aqueous solution at 30°C which is carried out below LCST of NIPAAM (33°C).

5.5.2 Characteristics of NIPAAM-g-PVDF membranes

The presence of NIPAAM in the NIPAAM-g-PVDF copolymerised membranes is examined by using ToF-SIMS; and the mass increase of the masses of NIPAAM-g-PVDF membranes before and after the copolymerisation process is used to estimate the presence of NIPAAM on the porous PVDF membrane which is defined as the grafting yield. The porous structure of the NIPAAM-g-PVDF copolymer membrane is examined by using SEM and characterised by using BET method in order to indicate the degree of grafted copolymer [114].

5.5.2.1 ToF-SIMS

PVDF membrane plays the role of backbone structure while NIPAAM is grafted on the PVDF surface and filled in the porous structure. The expected chemical structure of the NIPAAM copolymerised with PVDF porous structure [151] is illustrated in Figure 5.7. The positive ion spectrum (m z^{-1} = 0 to 300) of the NIPAAM-g-PVDF copolymer porous membrane is illustrated in Figure 5.7.

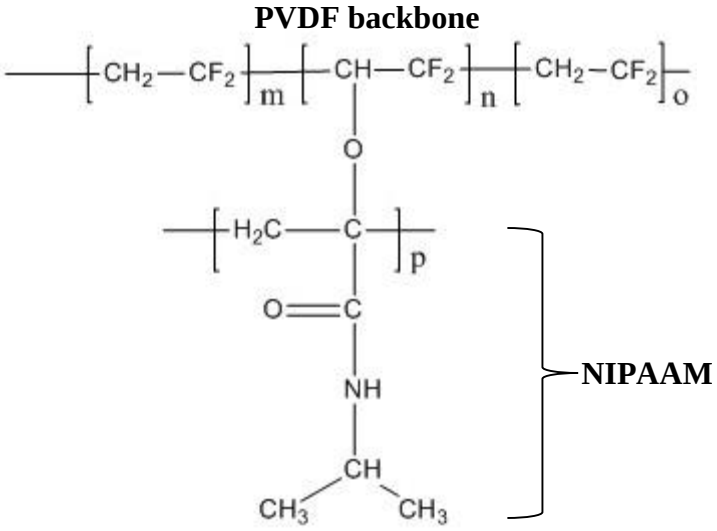

Figure 5.7 The expecting NIPAAM-g-PVDF copolymer chemical structure [151]

m z^{-1} = 58+ m z^{-1} = 114+

Figure 5.8 The structure of the protonated dimethylamine and fragments

In Figure 5.9, the prominent signal characteristics of the NIPAAM are observed at m z^{-1} value of 58 m z^{-1} which is referred to the protonated dimethylamine ($(CH_3)_2NH_2$) [218] as expected. The high intensity peaks of monomer fragments ($C_6H_{12}NO^+$) at 114 m z^{-1} is an indication of the NIPAAM structural units of the NIPAAM polymer [207] as chemical structures are indicated in Figure 5.8. Also, a signal of the peak at 286 m

z^{-1} as the indication of a new bond formed in the NIPAAM-g-PVDF membrane is shown.

It is thus concluded NIPAAM-g-PVDF new copolymer is formed in this plasma-induced graft copolymerisation method; this is evident in the ToF-SIMS spectrum.

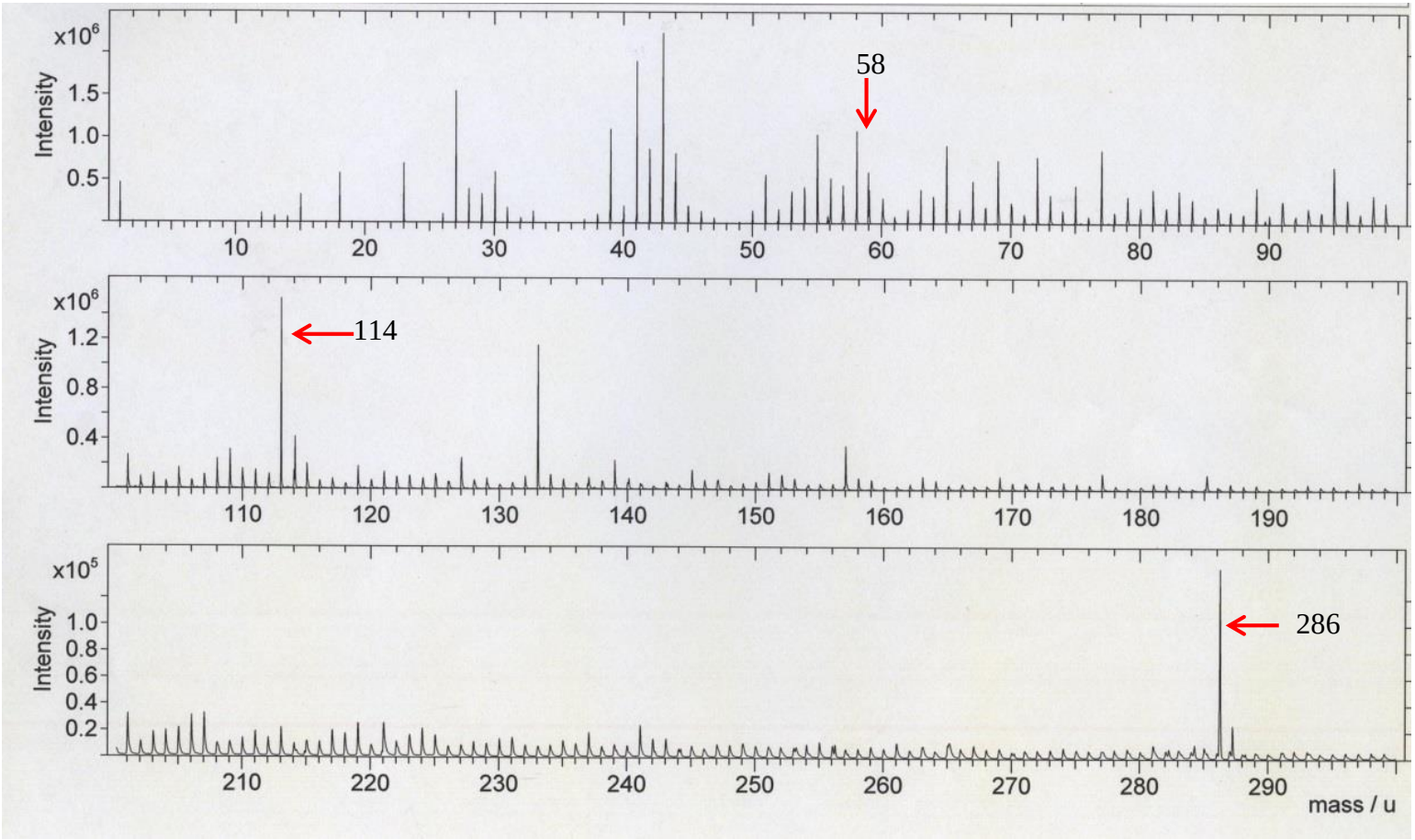

Figure 5.9 Positive ion ToF-SIMS spectra ($0 \leq m\ z^{-1} \leq 300$) of NIPAAM-g-PVDF membrane (S9C)

5.5.2.2 Grafting yield

The grafting yield is expected to give an indication whether there is any amount of NIPAAM polymers is formed and added on the surface of PVDF membrane during the NIPAAM-g-PVDF copolymerisation process. The grafting yield of the NIPAAM-g-PVDF membrane is defined as the mass increase of the PVDF membrane before and after the grafting copolymerisation process and is calculated by the following equation (5-1) [146]:

$$Y_g = \frac{W_g - W_0}{W_0} \times 100\% \quad (5\text{-}1)$$

where
Y_g is the grafting yield (%),
W_g is the mass of the membrane after grafting (g),
W_0 is the mass of the membrane before grafting (g).

The mass changes of the porous PVDF membrane after the plasma treatment and after the copolymerisation are indicated in Table 5.7 respectively.

Table 5.7 Masses of the porous PVDF membranes (S9 and S9C) before/after the plasma treatment and the copolymerisation processes

Mass (g)			**Mass change (%)**	
Before plasma treatment	After plasma treatment	After copolymerisation	After plasma treatment	After copolymerisation
1.382	1.382	1.383	0.00	0.07

In a previous research, the grafting yield of the NIPAAM-g-PVDF membrane produced from a porous PVDF membrane which was plasma treated with the argon plasma (10 Pa plasma pressure, 30 Watts plasma flow rate, the NIPAAM grafting temperature at 30°C) [146] showed higher grafting yield from 0.79%-16.61% when the plasma treatment time is increased from 1 to 7 minutes. However, in this study, it is found in Table 5.7 that the mass of the NIPAAM-g-PVDF membrane hardly changes (only 0.07%).

5.5.2.3 Porous structure

It is expected that some of NIPAAM polymers grafted on the surface of PVDF membrane by adding the NIPAAM chains to the activated groups of the plasma treated PVDF membrane and some of NIPAAM polymer particles may fill into the pores of the porous PVDF membrane. Therefore, the porous structure may play important role in the copolymerisation process. The pore-filling ratio [114], as shown in equation (5-2), was proposed to represent the degree of grafted membranes.

$$F = \frac{V_g}{V_0} = 1 - \left(\frac{d_g}{d_0}\right) \quad (5\text{-}2)$$

where
F is the pore filling ratio,
V_g is the volume of grafted PNIPAAM polymer in the pore (cm^3),
V_0 is the volume of pore before grafting NIPAAM (cm^3),
d_0 and d_g is the average pore diameters before and after grafting NIPAAM.

Pore size distribution of the resultant NIPAAM-g-PVDF porous membrane is shown in Figure 5.10 and its porosity, true density, BET surface area and average pore diameter of NIPAAM-g-PVDF are summarised in Table 5.8. Then, the pore-filling ratio is also calculated according to equation (5-2).

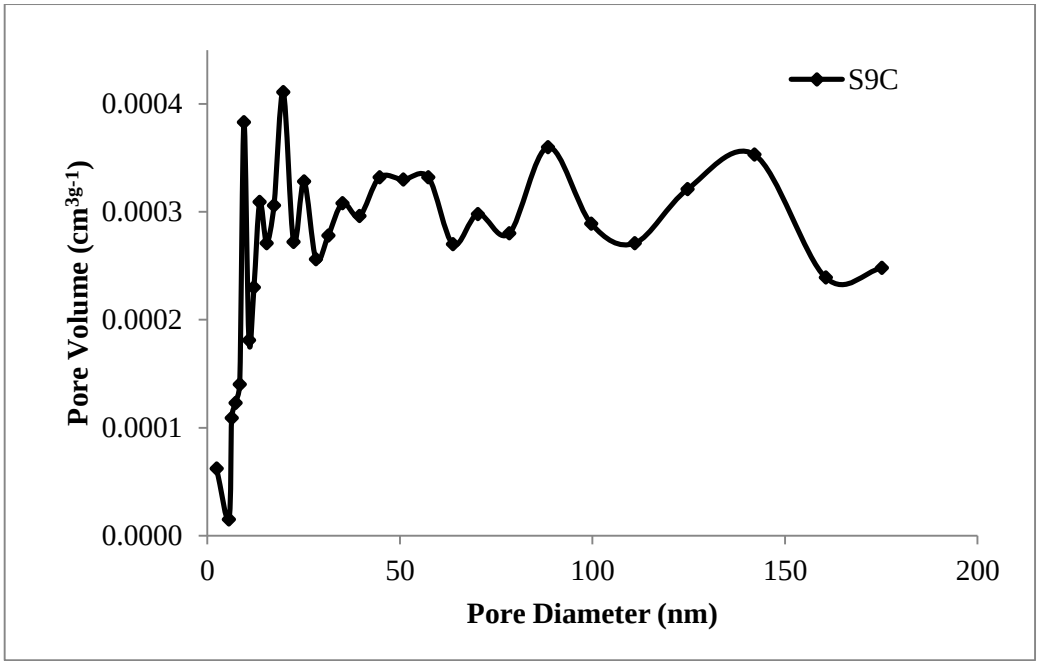

Figure 5.10 Pore size distribution of the NIPAAM-g-PVDF copolymerised membrane (S9C)

Table 5.8 The comparison of characteristics of porous structure of the pristine PVDF porous membrane and corresponding resultant NIPAAM-g-PVDF membrane

Property		**S9**	**S9C**
Porosity (%)		98.8	99.1
True density (g cm^{-3})		2.40	2.78
BET Surface area (m^2 g^{-1})		32.0	2.49
Average pore diameter (nm)		12.9	11.2
Mesopores	Pores volume (cm^3 g^{-1})	0.013	0.005
	Percentage (%)	49.1	57.7
Macropores	Pores volume (cm^3 g^{-1})	0.013	0.004
	Percentage (%)	50.9	42.3

It is found in Figure 5.10 that the pore size of the NIPAAM-g-PVDF membrane is distributed in both mesopore and macropore ranges. The pore volume of the macropores (the pores with diameter exceeding 50 nm) in its peak pore size is significantly greater than that of the mesopores (2-50nm) in its peak pore size. As shown in Table 5.8, the total pore volume for the mesopores is approximately 57.7% while the total pore volume for the macropores is approximately 42.3%. The surface area of the NIPAAM-g-PVDF copolymer membrane is significantly decreased from 32.0 m^2 g^{-1} to 2.49 m^2 g^{-1} after copolymerisation.

However, the porosity of the PVDF porous membrane, in comparison with the resultant NIPAAM-g-PVDF copolymer membranes (98.8% and 99.1%) hardly changes after the copolymerisation. While the true density of the NIPAAM-g-PVDF copolymer membrane is slightly increased from 2.40 g cm^{-3} to 2.78 g cm^{-3} (15.8%).

The average of pore diameter is slightly decreased from 12.9 nm to 11.2 nm after the copolymerisation, and the pore-filling ratio, as defined in equation (5-2) and a representative of the degree of grafted membrane, is therefore approximately 0.13.

5.5.2.4 Surface morphology

The surface morphology of the pristine PVDF porous membrane (S9) and the NIPAAM-g-PVDF copolymer membrane (S9C) are shown in the SEM images detected by using FEGSEM tool as shown in Figure 5.12.

Because nitrogen and oxygen are the two elements contained only in NIPAAM monomer molecules and not presented in PVDF polymers, they are detected in the EDX element analysis associated with FEGSEM. In the NIPAAM-g-PVDF copolymer membranes as indicated in Figure 5.11.

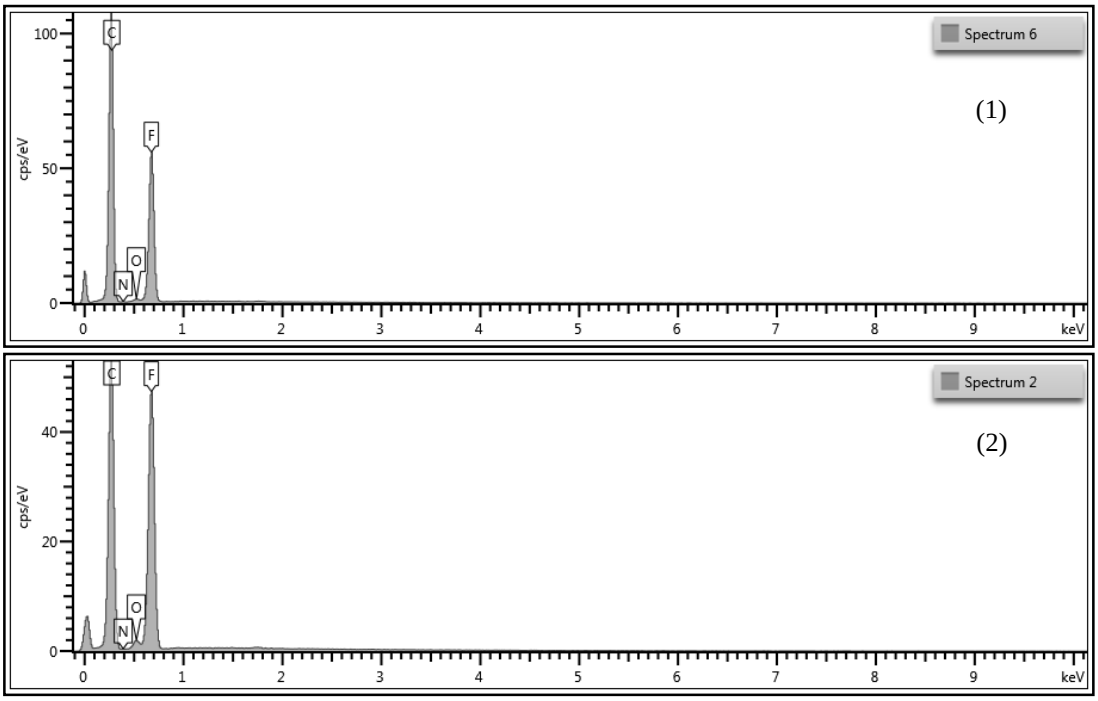

Figure 5.11 Spectrum of the detected elements in (1) PVDF porous membrane (S9) and (2) NIPAAM-g-PVDF porous membrane (S9C)

The atomic weight percentage of each element contained in both the pristine PVDF and NIPAAM-g-PVDF copolymer membranes is compared in Table 5.9.

It is found in Table 5.9 that the percentage of the nitrogen atom in the porous PVDF membrane is zero while the nitrogen containing in the NIPAAM-g-PVDF copolymer membrane is around 0.2%. Similarly the oxygen element contained in the NIPAAM-g-PVDF membrane markedly increased from 0.5% to 1.5%. This indicates that there is a significant amount of NIPAAM presented onto the NIPAAM-g-PVDF membrane.

Table 5.9 The comparison of element containing in the porous membrane

Elements	PVDF porous membrane (S9) (Atomic %)	NIPAAM-g-PVDF porous membrane (S9C) (Atomic %)
C	80.7	65.6
N	0.0	0.2
O	0.5	1.5
F	18.8	32.7
Total:	100.0	100.0

It is found in Figure 5.12 (a) and (b) that the small pores scattering on the NIPAAM-g-PVDF copolymer porous membrane (S9C) but not in the PVDF membrane (S9), this indicates that these small pores/holes may be created during the plasma treatment process before the copolymerisation.

(a) PVDF porous membrane (S9)

(b) plasma treated PVDF membrane

(c) NIPAAM-g-PVDF porous membrane (S9C)

Figure 5.12 Surface morphology of the porous PVDF membrane before and after copolymerisation (magnification: 10k)

5.6 Conclusions

Porous PVDF membrane of greater surface area is made from the phase inversion method in order to produce a porous PVDF substrate for grafting with NIPAAM polymer by using the plasma-induced graft copolymerisation method. It is found that the surface properties (e.g., water contact angle) of PVDF membranes are markedly changed after oxygen plasma treatment process. NIPAAM molecules are found to be both filled in the pores and grafted on the surface of the plasma treated PVDF membrane to form NIPAAM-g-PVDF copolymer membranes.

Chapter 6 The influence of heat-press processing parameters on the nanoporous structure and permeation properties of PVDF membranes

In Chapter 5, the micro-porous poly(vinylidene fluoride) (PVDF) membrane was obtained by using the phase inversion method; however, it is necessary to minimise the liquid chemical passage and the water vapour transfer through the pores in the membrane, as it is indicated in Chapter 3 that the fluid permeation through such porous membrane structures obeys Darcy's law. Such porous structure in NIPAAM-g-PVDF membrane might impose difficulties for us to evaluate the role of the thermosensitive, N-isopropylacrylamide, (NIPAAM) components in the copolymer membrane on its water vapour transmission rate (*WVTR*) in different temperatures. Therefore, heat-press processing is used to produce the nanoporous membrane. The influences of the heat-press processing parameters (e.g. temperature, pressure and press time duration) on the nanoporous structure are studied. Furthermore, the influences of the nanoporous structures on the liquid chemical permeation properties (e.g. breakthrough time and the permeation rate) of the nanoporous PVDF membrane are investigated.

6.1 Experimental plan for producing heat-pressed PVDF membranes

PVDF porous membranes produced in a single coagulation bath using phase inversion method (see Section 5.3.1) are heat-pressed to achieve nanoporous membranes. The heat press system (made by Stewart-Buchanan, Glasgow, UK) used in this project is shown in Figure 6.1. The porous PVDF membrane is placed between two stainless steel hotplates of the heat press system during the heat-press process.

The experimental plan for studying the effect of heat-press processing parameters, which includes the temperature of the hotplates, pressure, duration time of heat-press processing and number of membrane layers pressed together, on the structures of resultant membranes are shown in Table 6.1.

Figure 6.1 The heat-press processing system

The crystallinity of membranes might be changed depending on the number of layers of porous pristine PVDF membrane after heat-press processing.

Table 6.1 The experimental plan for producing heat-pressed membranes

Membranes	**Pressure (kPa)**	**Temperature (°C)**	**Time (min)**	**Layers of pressed together**
U0	Original porous pristine PVDF membrane			
U1	98	170	20	1
U2	98	150	20	1
U3	147	150	40	1
U4	147	150	60	1
U5	147	150	60	2

The temperature of the heat-press processing might affect the crystallinity of the membranes, especially when it is greater or smaller than the melting point of the polymers processed [219]. In Table 6.1, the effect of two levels of temperature of the heated plates, 150°C and 170°C, are studied. 170°C is the melting point of PVDF polymer as shown in the DSC thermogram of PVDF polymer in Figure 4.10. 150°C is below the melting point of PVDF polymers. It is noted that, when the pristine PVDF membrane is melted during the heat-press processing at 170°C, it needs a period of

time to form into a new microstructure. Therefore, the heating temperature below the melting point of PVDF is adopted (150°C) in order to let the porous membrane soften rather than melt. When temperature is at 150°C, longer time duration (20, 40 and 60 minutes) for the heat-press processing is thus chosen. It is hoped that this might decrease the number of pores in the resultant membrane.

Pressure has a significant effect on the structure of heat-pressed membranes. Greater pressure could help achieve a nonporous PVDF membrane, which was obtained by applying a pressure of 1.5×10^7 Pa on a porous PVDF membrane for 10 minutes at 150°C [218]. However, the maximum pressure that could be applied on this heat press system is only approximately 30 tonnes m^{-2} (~294 kPa) due to the limitation of the system, so the membranes produced in the study are bound to be membranes of smaller pores rather than nonporous pores. The effect of two pressure levels between 98 kPa and 147 kPa (10 and 15 tonnes m^{-2}) are studied as shown in Table 6.1.

6.2 The characteristics of the microstructure of heat-pressed PVDF membranes

In this section, the influence of the heat-press processing parameters including temperature, pressure and processing time of heat-press processing on the porous structure of heat-pressed PVDF membranes are studied. PVDF microporous membranes produced in a single coagulation bath using their phase inversion method (see Section 5.3.1) are heat-pressed to achieve nanoporous membranes. The porous structures including surface morphologies and chemical permeation properties including breakthrough time of the membranes obtained under various heat-press processing parameters are compared, and processing conditions to achieve less porous structures are identified.

The surface morphology and element analysis of the nanoporous membranes are examined by using Scanning Electron Microscope (SEM). All the membranes are gold sputter coated in a Q150RS sputter coater, the porous pristine PVDF membrane (U0) and its single layer heat-pressed PVDF membrane (U4) are examined by using a Leica Cambridge Instruments S 360 SEM while the double layer heat-pressed PVDF membranes (U5) are examined by using a Jeol JSM-6610LV SEM coupled with an Oxford Instruments INCA X-max 80 EDS system. The test is carried out in the Colour Science Analytical Laboratory, School of Chemistry, University of Leeds.

The porous structure is examined by using both a BET method and a mercury porosimeter. The average pore diameters and pore size distribution of the heat-pressed PVDF membrane is determined by using a Micromeritics TriStar 3000 BET system as described in Section 5.2.2. The cumulative surface area, pore volume, average pore diameters and pore size distribution of the PVDF membranes including both porous and their corresponding heat-pressed PVDF membranes are determined according to BS ISO 15901-1:2005 standard [220] by using Micromeritics Hg-injection porosimeters (Micromeritics Instrument Corporation). The test is carried out in the Wolfson Multiphase Flow Laboratory, School of Environment, University of Leeds.

6.2.1 Bulk density and surface morphology

The microstructure, bulk density and thickness of the heat-pressed PVDF membranes are summarised in Table 6.2.

Table 6.2 Bulk density of the heat-pressed PVDF membranes

Membranes	**Mass per unit area ($g\ m^{-2}$)**	**Average thickness (mm)**	**Bulk density ($kg\ m^{-3}$)**
U0	203	0.49	431.9
U1	171	0.38	449.3
U2	167	0.31	539.9
U3	169	0.52	325.6
U4	184	0.57	322.9
U5	263	0.64	410.5

However, it is found there are two different areas, translucent area and transparent area, distributed across the surface of the heat-pressed membranes of the double layer heat-pressed PVDF membrane as indicated in Figure 6.2.

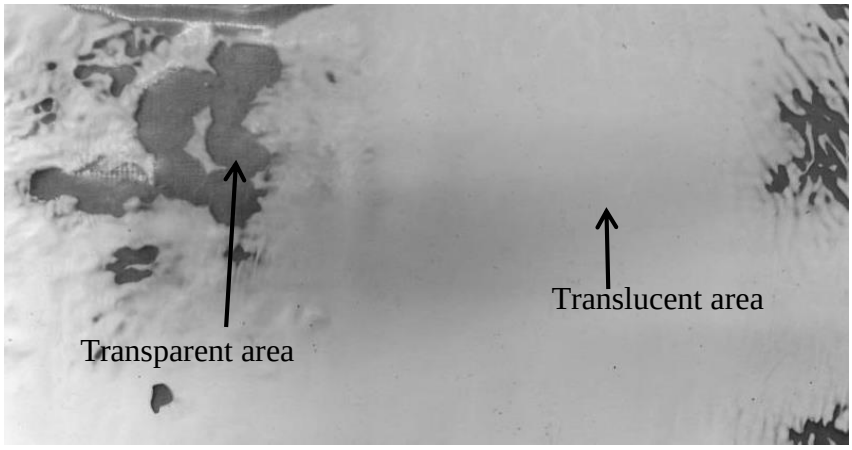

Figure 6.2 Translucent and transparent areas in a heat-pressed membrane

A comparison of the surface morphology of the porous pristine PVDF membrane (U0), its single layer heat-pressed PVDF membrane (U4) and its double layer heat-pressed PVDF membrane at 147 kPa, 170°C for 60 minutes (U5) are shown in Figure 6.3.

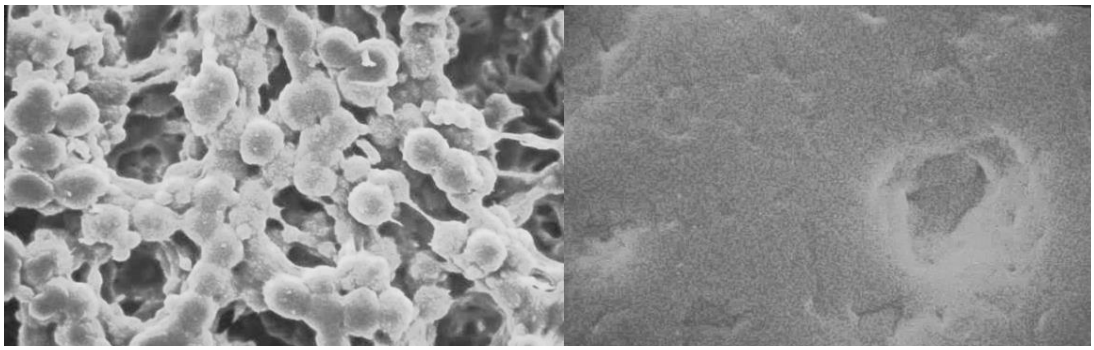

(a) U0 (b) U4

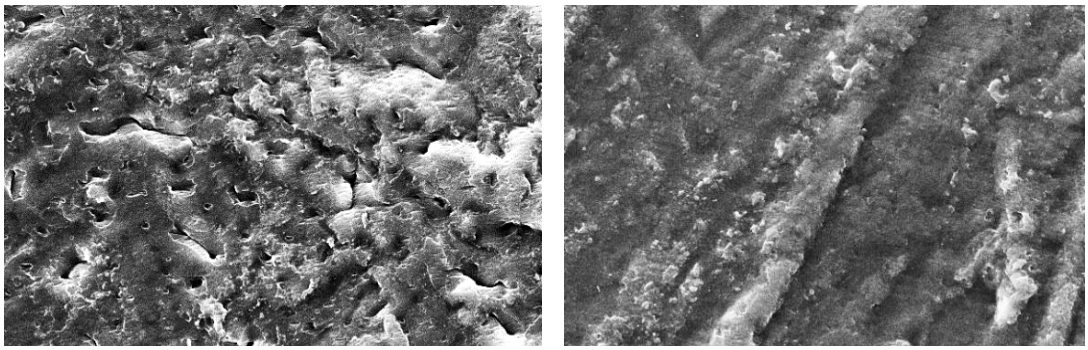

(c) U5 (translucent) (d) U5 (transparent)

Figure 6.3 The surface morphologies of PVDF membranes before and after heat-press processing (magnification: 2000)

It is found in Figure 6.3 that a great amount of large pores is evident on the surface of the pristine PVDF membrane (see Figure 6.3 (a)) and that there are fewer pores on the

surface of the heat-pressed pristine PVDF membrane (see Figure 6.3 (b)). This means that pores of micrometres in size in the original pristine PVDF membranes are apparently reduced after the heat-press processing. The porous structures of the PVDF membrane before and after the heat-press processing are quantified in Section 6.2.2. Moreover, the translucent area is a porous structure and the transparent area is a less porous, dense structure. This might be also linked with their crystallinity and this will be discussed in Section 6.2.3.

6.2.2 Porous structure characteristics

The pore size distribution of the heat-pressed pristine PVDF membrane (U4) is examined by BET as indicated in Figure 6.4.

It is found in Figure 6.4 that only two points of the average pore diameter at 69.7 nm and 90.6 nm were reported and both are in macropores range. However, it is obviously seen the existence of the macro-scale pores in the membranes as shown in SEM pictures (see Figure 6.3 (b)), BET method is not suitable for examining the porous structure of the PVDF membranes; therefore, the mercury porosimeter is used in this research as an alternative method for the examination of the membrane porous structure.

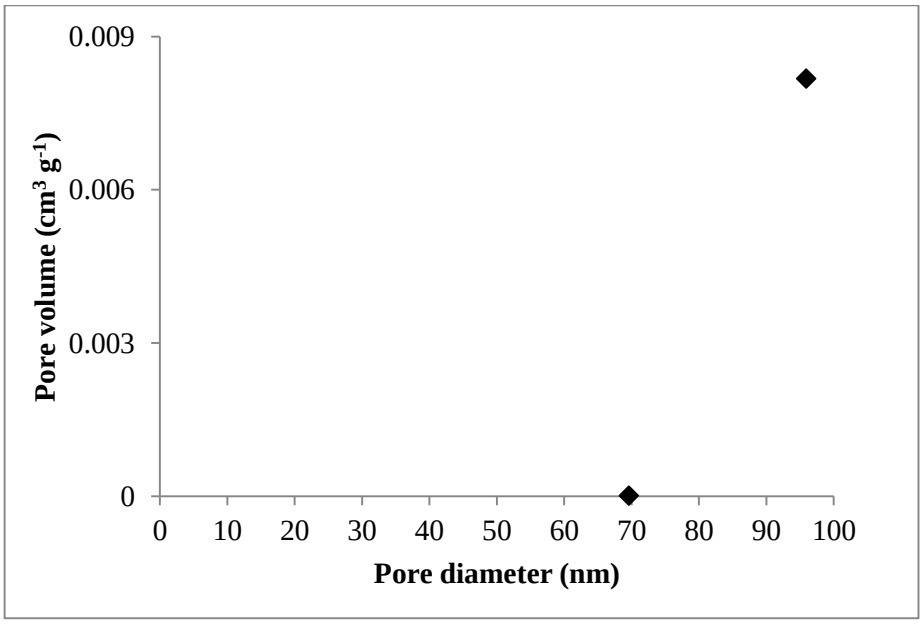

Figure 6.4 Pore size distribution of the heat-pressed pristine PVDF membrane (U4)

The pore size distribution of the porous PVDF membrane (U0) and its single layer (U4) and double layer (U5) heat-pressed membranes are shown in Figure 6.5. Their bulk density, skeletal density, cumulative surface area and average pore diameters are

summarised in Table 6.3. The porosity of the membranes is calculated by the equation (6-2) below:

$$\epsilon = \left(1 - \frac{\rho_b}{\rho_a}\right) \times 100 \qquad (6\text{-}1)$$

where

ε is the porosity (%),

ρ_b is the bulk density at 10.27 kPa (g cm^{-3}),

ρ_a is the apparent skeletal density at 10.27 kPa (g cm^{-3}).

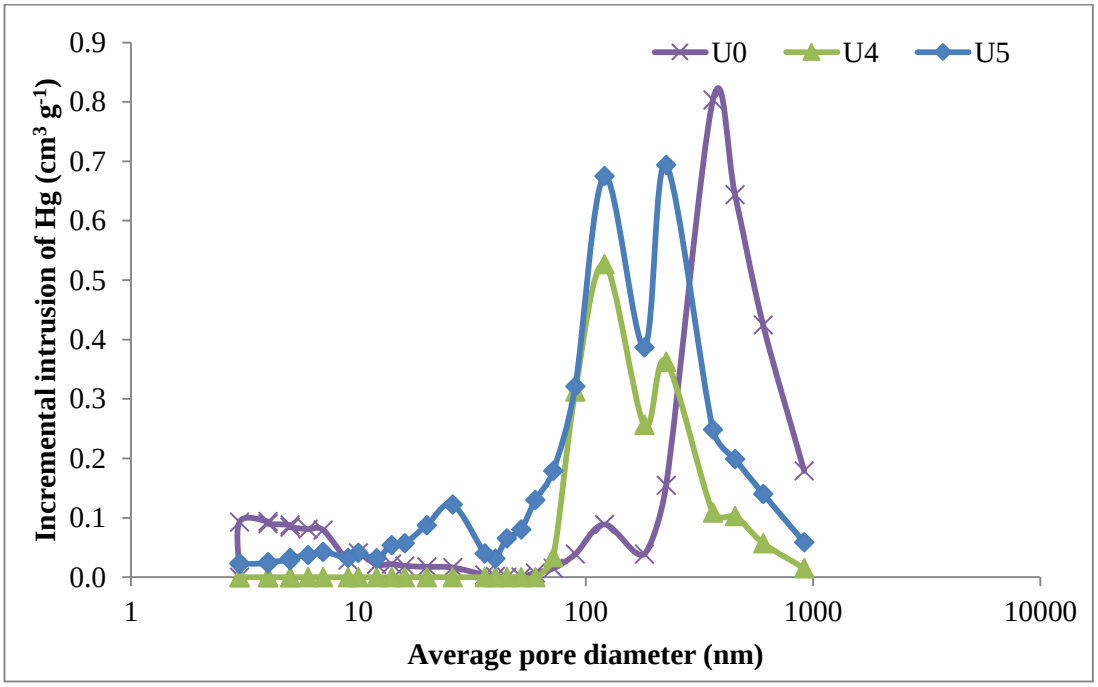

Figure 6.5 The pore size distribution of the porous PVDF membrane (U0) and its single layer heat-pressed PVDF membranes (U4) and double layer heat-pressed PVDF membranes (U5)

It is found in Figure 6.5 that, for the porous PVDF membrane U0, the pore volume in the range of macropores (50-900 nm) are significantly greater (2.39 cm^3 g^{-1} or 75.4%) than the pore volumes (0.78 cm^3 g^{-1}, or 24.6%) in the range of mesopores (between 2 to 50 nm). Similar trend also appears in the pore size distribution for double layer heat-pressed membrane U5 in Figure 6.5, in which the pore volume heat-pressed in the range of mesopores (between 2 to 50 nm) is approximately 0.80 cm^3 g^{-1}, or 20.4% and the pore volumes for the macropores (50 to 900 nm) is approximately 3.11 cm^3 g^{-1}, or 79.6% (also see Table 6.3).

The volumetric pore size distribution of the single layer heat pressed PVDF membrane (U4) is 1.78 $cm^3 g^{-1}$ in the range of macropores (50-900 nm) only (see Table 6.3) but there is no peak in the range of mesopores and micropores (2-50 nm).

Table 6.3 The characteristics of the porous structure of a porous and its double layer heat-pressed PVDF membranes (U5)

Porous structure		Porous membrane (U0)	Single layer heat- pressed membrane (U4)	Double layer heat- pressed membrane (U5)
Bulk density at 10.27 kPa (g cm^{-3})		1.09	0.96	1.21
Apparent skeletal density at 10.27 kPa (g cm^{-3})		1.21	1.59	1.87
Porosity (%)		9.92	35.29	35.29
Cumulative pore area ($m^2 g^{-1}$)		34.23	34.23	34.23
Average pore diameter (nm)		61.6	61.6	48.2
Micropores and Mesopores	Pores volume ($cm^3 g^{-1}$)	0.78	0	0.80
	Percentage (%)	24.6	0	20.4
Macropores	Pores volume ($cm^3 g^{-1}$)	2.39	1.78	3.11
	Percentage (%)	75.4	100	79.6
Total pore volume ($cm^3 g^{-1}$)		3.17	1.78	3.91

It is found in Table 6.3 that the porosity of the porous PVDF membrane (U0) before the heat-press process is 9.92% while the single layer heat-pressed PVDF membrane and the double layer heat-pressed PVDF membranes have the porosity of 63.52% and 35.29%, respectively. This means that the effect of heat press on the porous structure of the membranes depends on the heat-press processing parameters including the layers of membranes.

The cumulative pore area of these three samples is similar around 34.23 $m^2 g^{-1}$. It is found the average pore diameter of the porous PVDF membrane (U0) and the single

layer heat-pressed PVDF membrane showed (U4) had a similar value of 61.6 nm while the double layer heat-pressed PVDF membrane (U5) showed a lower result of 48.2 nm. This means the heat-pressed membrane from two layers of porous PVDF membrane has smaller pore diameter when these two membranes were melt together, However, its pore volume increased only a small proportion (from 4.10 cm^3 g^{-1} in porous membrane to 3.91 cm^3 g^{-1} in double layer heat-pressed membrane), and this indicates that most of the polymer in the double layer structure unable to be molten and reformed into new structures at 150°C and 147 kPa.

In contrast, the total pore volume of the heat-pressed single layer porous membrane is massively decreased to only 1.78 cm^3 g^{-1}; however, its average pore diameter is still 61.6 nm, this means that there is still some small amount of large macropores remained in the membrane but most of the micropores, mesopores and macropores in the original single layer porous membrane have been diminished during the heat-press process at 150°C and 147 kPa. These parameters could thus be useful in producing NIPAAM-g-PVDF membranes with less pore. Pores become accessible after the membrane re-formation during the heat press process.

6.2.3 Crystallinity

The melting temperature, melting enthalpy, and degree of crystallinity of both porous (U0) and single layer heat-pressed PVDF membranes (U4), are studied using a DSC method, as shown in Figure 6.6 and Figure 6.7, respectively. As the double layer heat-pressed PVDF membrane (U5) has translucent and transparent areas distributed across the surface, the DSC thermogram of the two areas in the double layer heat-pressed PVDF membranes is studied in Figure 6.8 and Figure 6.9, respectively. The thermal properties of these three membranes are summarised in Table 6.4.

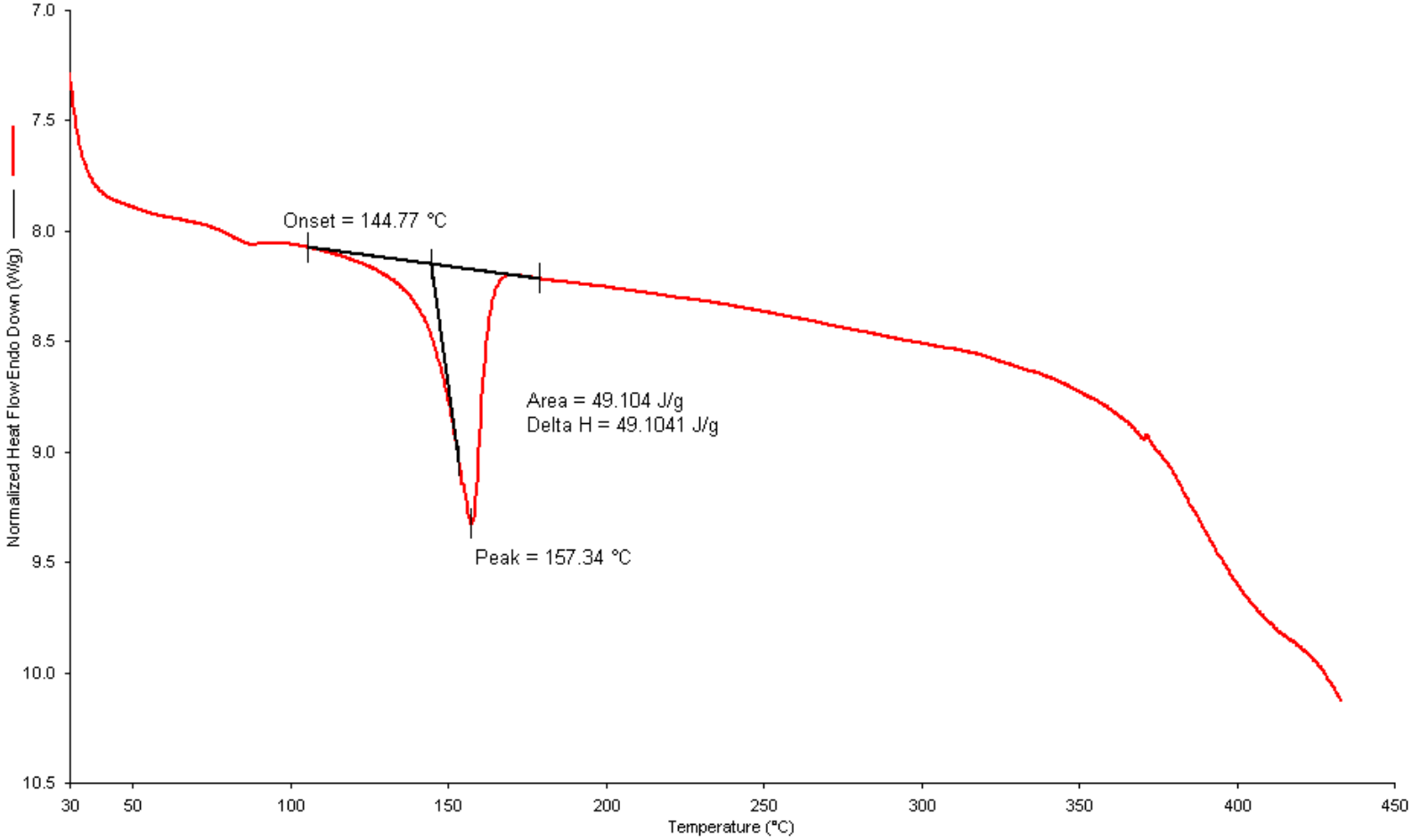

Figure 6.6 DSC of the porous pristine PVDF membrane (U0)

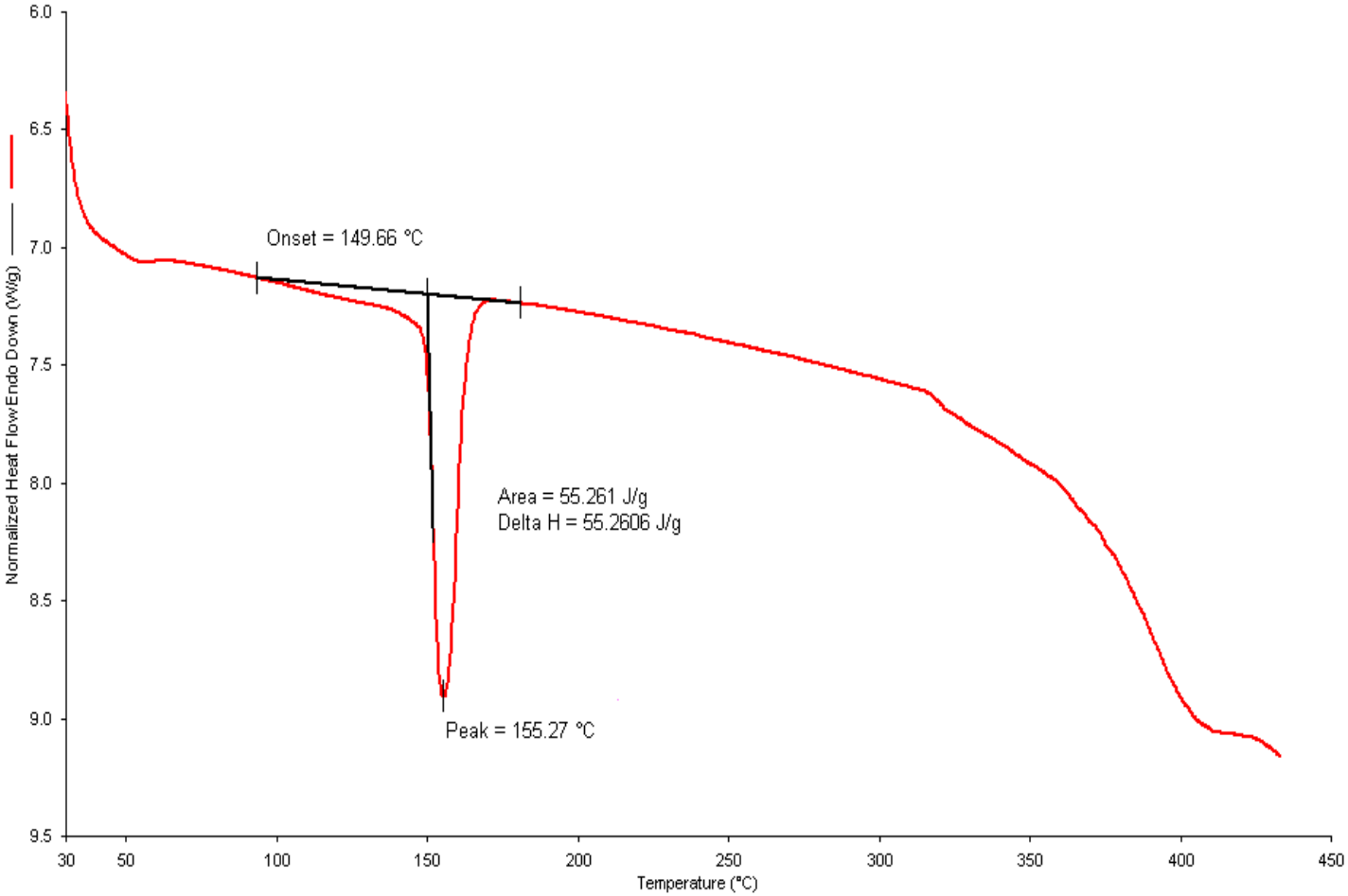

Figure 6.7 DSC of the single layer heat-pressed PVDF membrane (U4)

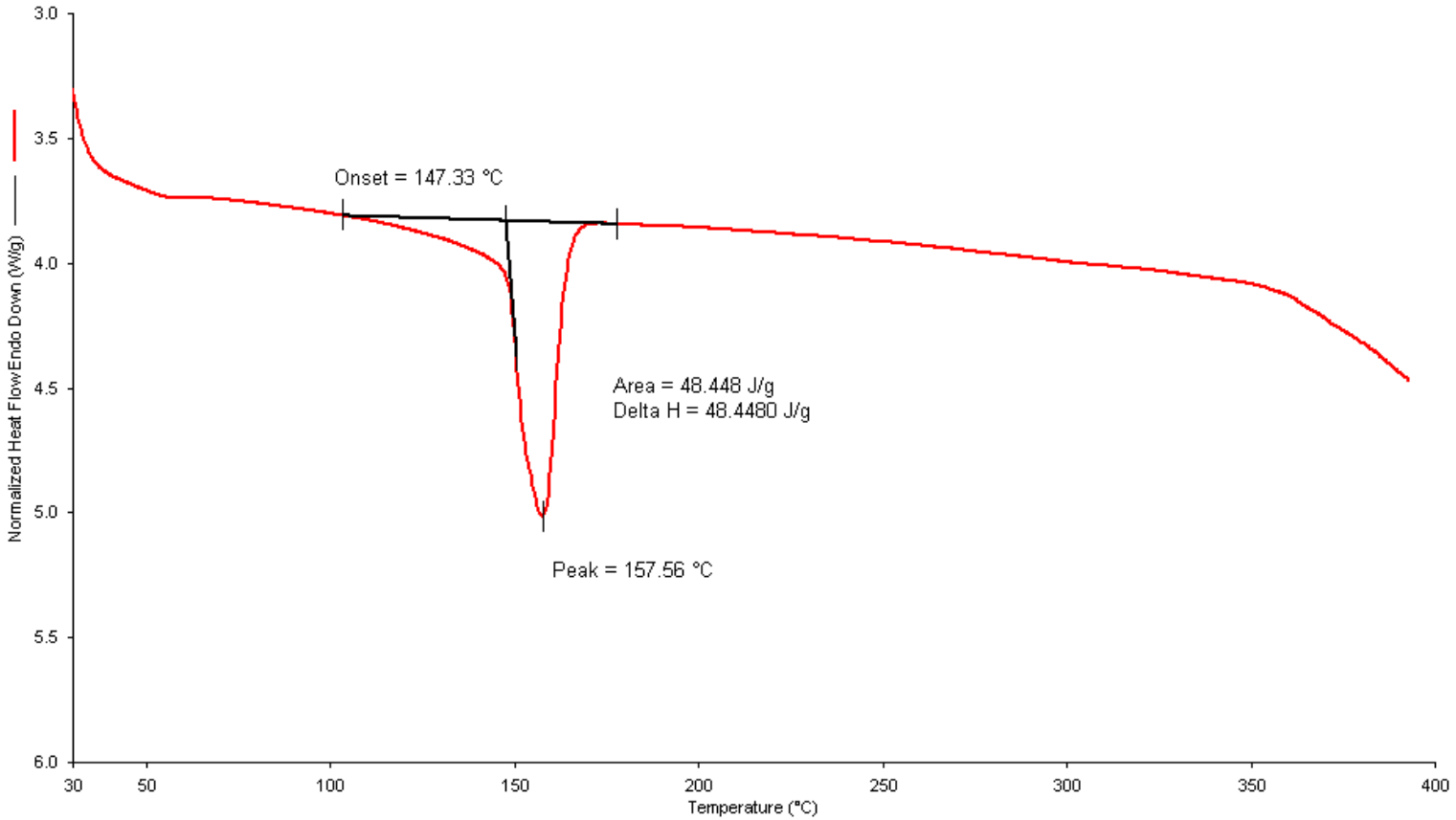

Figure 6.8 DSC of the transparent area (or porous structure) in the double layer heat-pressed pristine PVDF membrane (U5)

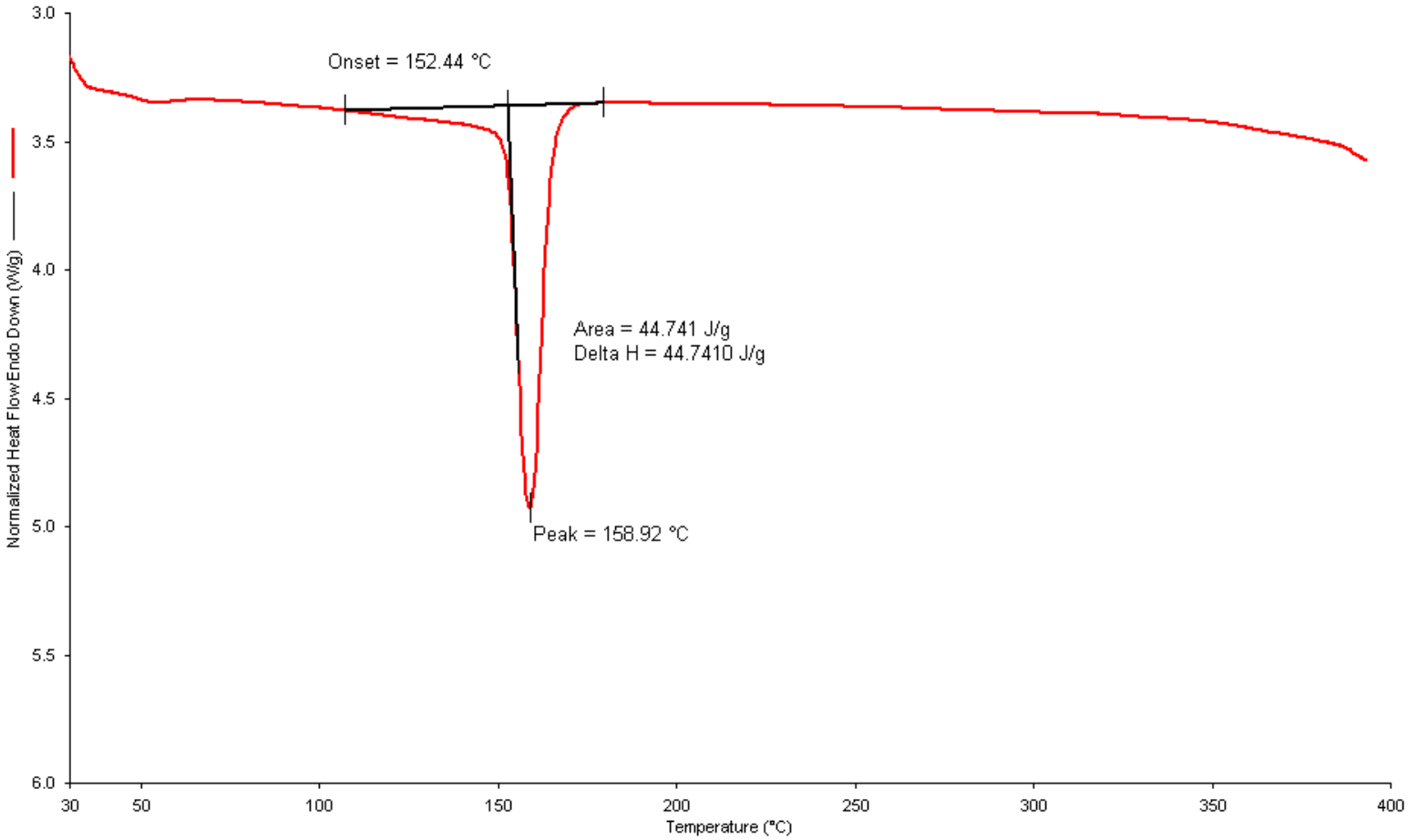

Figure 6.9 DSC of the translucent area (or dense area) in the double layer heat-pressed pristine PVDF membrane (U5)

Table 6.4 Crystallinity of the porous PVDF membrane and its heat-pressed membranes

Membrane	ΔHm (J g^{-1})	Crystallinity (%)	Tm (°C)
U0	49.10	47.0	157.3
U4	55.26	52.9	155.3
U5 (Transparent)	48.44	46.4	157.6
U5 (Translucent)	44.74	42.8	158.9

It is indicated in Table 6.4 that the crystallinity of the single layer heat-pressed PVDF membrane (U4) is greater than both its original porous membrane (U0) and its double layer heat-pressed membranes (U5). The crystallinity decreases as a result of the destruction of the crystalline structure based on previous studies [206]. It is thus concluded that new crystalline regions are formed in the porous PVDF membranes during the single layer heat-press process, while the crystalline regions of the porous PVDF membranes are deconstructed during the double layer heat-press processing. The reason for such difference is unclear.

6.3 The chemical permeation properties of the resultant heat-pressed PVDF membranes

The liquid chemical permeation properties are studied in this section in order to investigate the chemical resistance property of the PVDF membrane after heat-press processing. The modified chemical permeation test using n-hexane as permeant and its testing conditions have been described in section 3.2.1. The breakthrough time at the permeation rate of 1 µg cm^{-2} min^{-1} is determined to characterise the liquid barrier properties of the resultant heat-pressed PVDF membranes. However, since the size of the heat-pressed PVDF membrane specimen produced in this research is smaller than 50 mm which is the size required by EN ISO 6529:2013, a new gasket of 30 mm in diameter was made from a polyvinylchloride (PVC) polymer sheet (0.3 mm thickness) which has good resistance to n-hexane [221] to fit the membrane prototype in the system. The chemical permeation properties including breakthrough time of the PVDF membranes obtained under various heat-press processing parameters are compared, and processing conditions to achieve less porous structures are identified.

The dynamic permeation rate of the Polyflon® commercial PVDF membrane is used as a reference material as shown in Figure 6.10. It is clearly shown that this membrane is a nonporous impermeable membrane. The breakthrough time of the commercial PVDF Polyflon® nonporous membrane is approximately 480 minutes (or 8 hours) and the steady state permeation rate is still zero, this reaches the minimum breakthrough time required by the commercial chemical protective clothing as shown in Chapter 3. As indicated in Chapter 5, the membrane has a smooth continuous structure without any porous structure appeared on the surface.

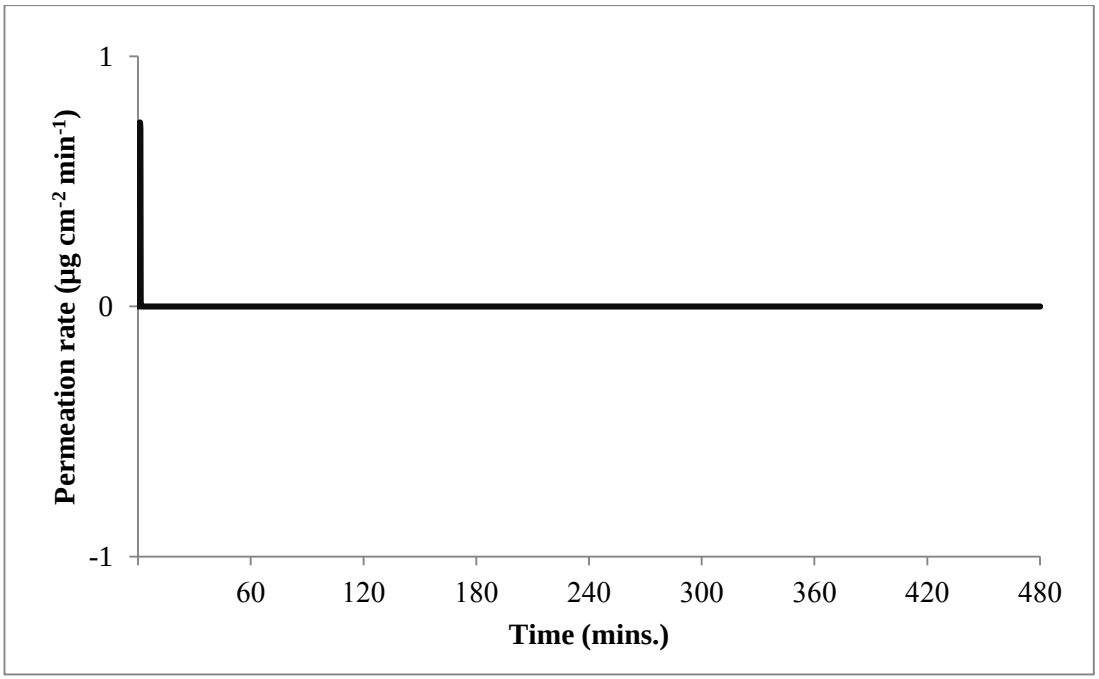

Figure 6.10 The dynamic permeation rate of the Polyflon® nonporous PVDF membrane

The dynamic permeation rates of the heat-pressed PVDF membrane (U0) and the heat-pressed PVDF membrane (U1) at 170°C, 98 kPa for 20 minutes are compared in Figure 6.11.

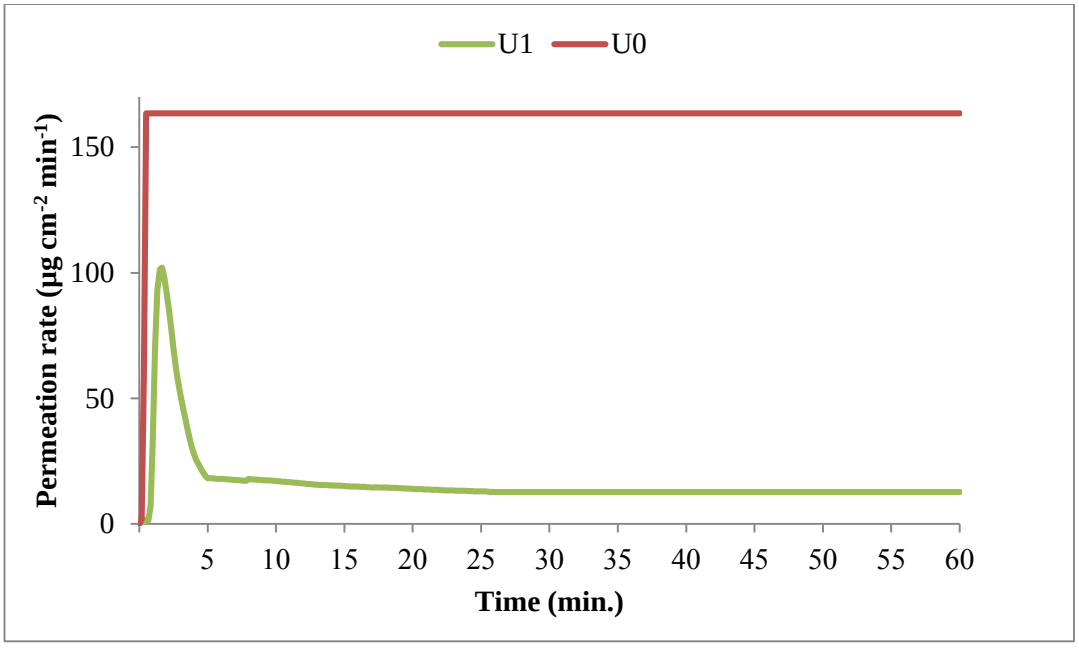

Figure 6.11 The dynamic permeation rate of the porous PVDF membrane (U0) and the heat-pressed PVDF membrane (U1)

It is found in Figure 6.11 that the breakthrough time of the porous PVDF membrane (U0) is 10 seconds and its peak permeation rate is 160 µg cm^{-2} min^{-1} immediately after the membrane is broken through in 10 seconds, while the breakthrough time of the heat-pressed PVDF membrane (U1) is 40 seconds and its peak permeation rate reaches 102 µg cm^{-2} min^{-1} in 100 seconds, which is much smaller than the porous PVDF membrane.

The dynamic permeation rates of the resultant heat-pressed membranes (U2, U3 and U4) which were heat-pressed at 150°C for 20, 40 and 60 minutes at 147 kPa are compared in Figure 6.12.

It is found in Figure 6.12 that the heat-pressed PVDF membranes which were pressed for 20 and 40 minutes (U4 and U2) have the breakthrough time of around 20 and 100 seconds respectively, while the heat-pressed PVDF membrane which was pressed for 60 minutes (U3) is around 13 minutes. Even though the breakthrough time of the heat-pressed PVDF membrane heat-pressed for 60 minutes is not comparable to the breakthrough time of the commercial PVDF Polyflon® membrane as indicated in Figure 6.10, the result showed that the longer time duration of the heat-press processing, the longer breakthrough time of the resultant membranes.

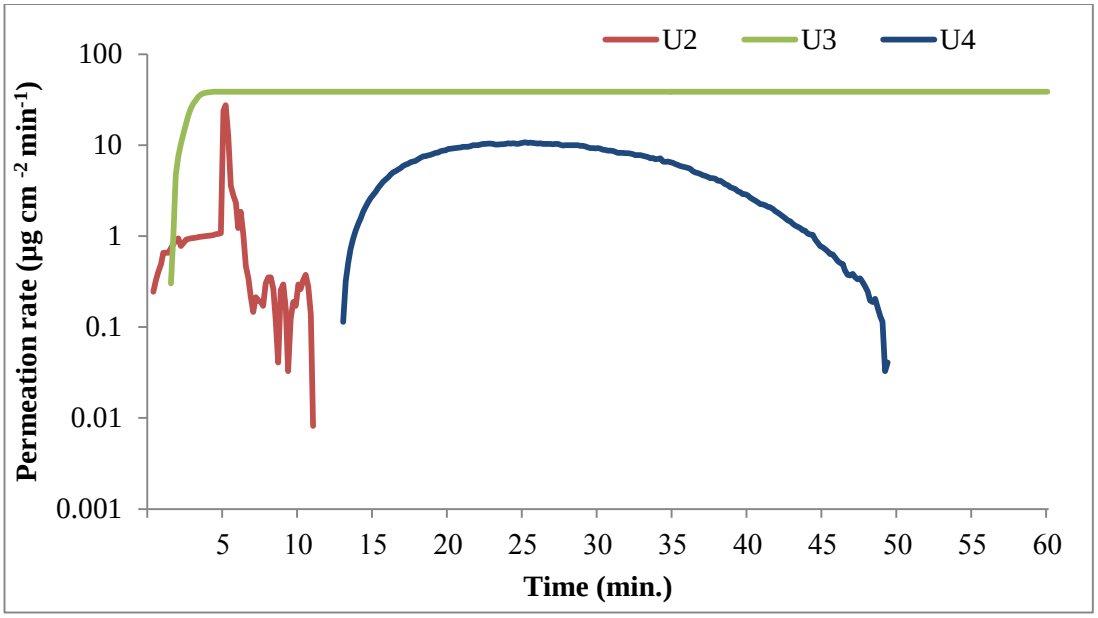

Figure 6.12 The dynamic permeation rate of liquid chemicals permeation through heat-pressed PVDF membranes (U2, U3 and U4) at 150°C, 147 kPa for 20, 40 and 60 minutes

The comparison of the dynamic permeation rates of the double layer heat-pressed pristine PVDF membrane (U5) and the single layer heat-pressed pristine PVDF membrane (U4) is shown in Figure 6.13.

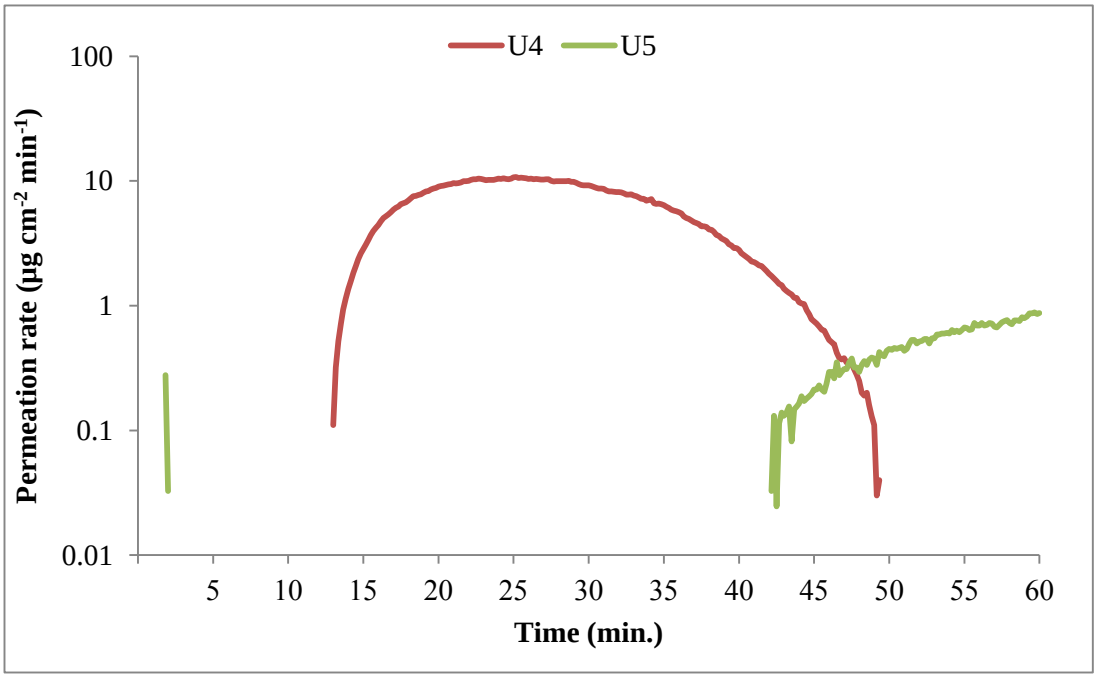

Figure 6.13 The dynamic permeation rates of the single layer (U4) and the double layer heat-pressed PVDF membranes (U5)

It is found in Figure 6.13 that the breakthrough time of the double layer heat-pressed pristine PVDF membrane (U5) is approximately 65 minutes, which is nearly 5 times greater than the single layer heat-pressed pristine PVDF membrane (U4). Therefore, the heat-pressed double layer porous PVDF membranes will effectively reduce their permeation rate and increase breakthrough time.

6.4 The relationship between the microstructure and the liquid permeation properties

6.4.1 The influence of membrane thickness on breakthrough time

The relationship between the thickness of the PVDF heat-pressed membrane and the breakthrough time at the permeation rate is shown in Figure 6.14.

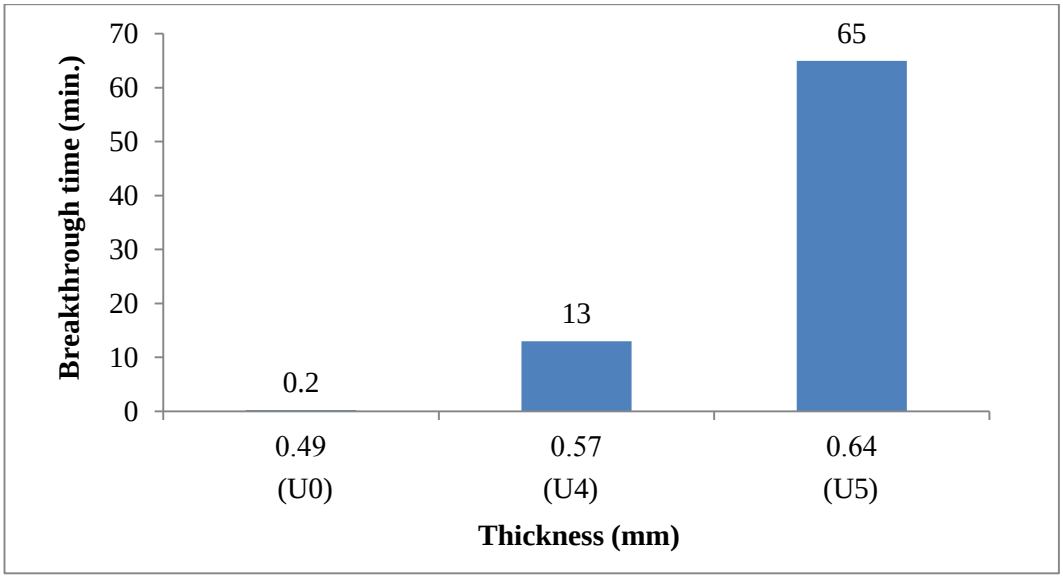

Figure 6.14 Breakthrough time of PVDF membranes vs its thickness

It is found in Figure 6.14 that the single layer heat-pressed PVDF membrane (0.57 mm) is thicker than the porous heat-pressed PVDF membrane (0.49 mm) and its breakthrough time is greater (13 minutes) than that (0.2 minutes) of the porous membrane. Similarly, the double layer heat-pressed PVDF membrane (0.64 mm) is thicker and its breakthrough time is longer (65 minutes) than that (0.57 mm and 13 minutes) of the single layer heat-pressed PVDF membrane. Therefore, it is concluded that the breakthrough time of the heat-pressed PVDF membranes are influenced by their membrane thickness and this is in agreement with Henry's law shown in equation (2-7).

6.4.2 The influence of membrane porous structures on breakthrough time

As indicated in Figure 6.3 porous PVDF membranes have a large amount of pores on their surfaces, while both single layer and double layer heat-pressed pristine PVDF membranes show smoother surface morphology and have a smaller amount of pores. Therefore, the influences of the porous structural parameters (e.g. the total pore volume, the cumulative pore area and the average pore diameters) on the dynamic rate of the liquid chemical permeation through the membranes are discussed in this section.

6.4.2.1 Breakthrough time vs Total pore volume

The total pore volume might influence the breakthrough time; however, the three membranes have a different membrane thickness whose influence was studies in the Section 6.4.1. Therefore the influence of the combined effect of membrane thickness and the average pore diameters of these membranes are shown in in Figure 6.15.

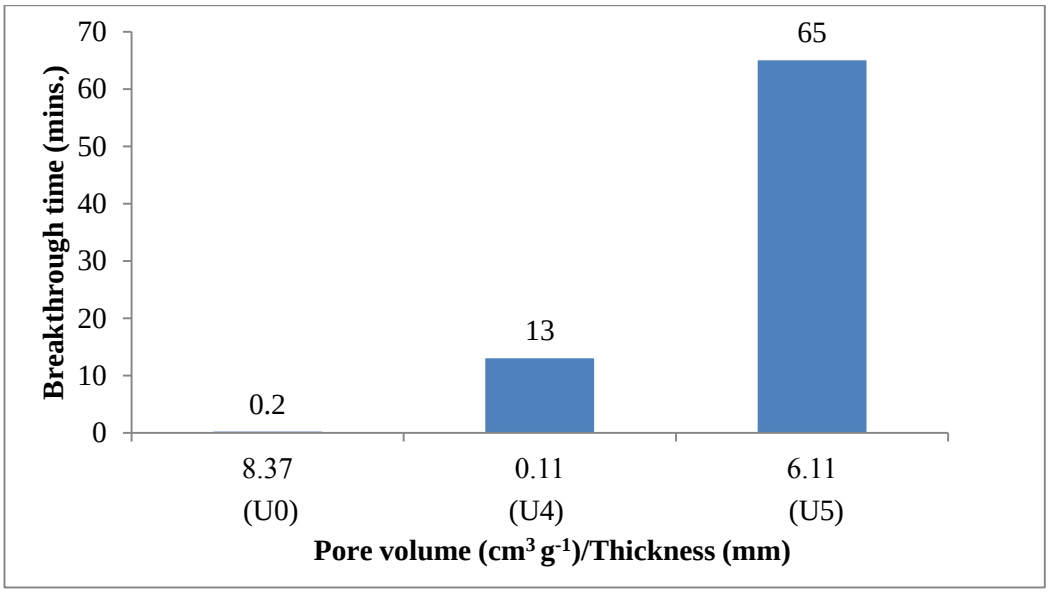

Figure 6.15 Breakthrough time vs the ratio of total pore volumes to thickness of heat-pressed PVDF membranes

It is found in Figure 6.15 that the breakthrough time is linked to the ratio between the total pore volumes to thickness of the heat-pressed PVDF membranes. The breakthrough time of these three membranes happen regardless of their total pore volumes to thickness. The reasons for such relationship might be complicated, but one of the possible reasons might be that the amount of pores having two different geometry shapes (i.e., through pores and non-through pores) inside the membranes

plays an important role in liquid permeation and diffusion. It is noticed that the total pore volume is obtained by using the mercury porosimetry method, and the volume of the pores measured includes both through-pores as well as open and non-through pores. It is known that the non-through pores might not contribute significantly to the liquid diffusion process, thus a membrane having a large volume of open- through pores might have a greater total pore volume but might not have a promote liquid permeation and diffusion, thus the total pore volume measured is not directly linked to the liquid permeation rate and breakthrough time.

6.4.2.2 Breakthrough time vs Average pore diameters

Similar to Section 6.4.2.1, the thickness of the membrane are influenced to the average pore diameters. Therefore the influence of the combined effect of membrane thickness and the average pore diameters of these membranes are shown in Figure 6.16. It is clearly shown in the Figure 6.16 that breakthrough time increase with the increase of the ratio of pore diameter over membrane thickness; this means that the combined effect of membrane thickness and pore diameter is one important factor influencing the liquid permeation through the membranes.

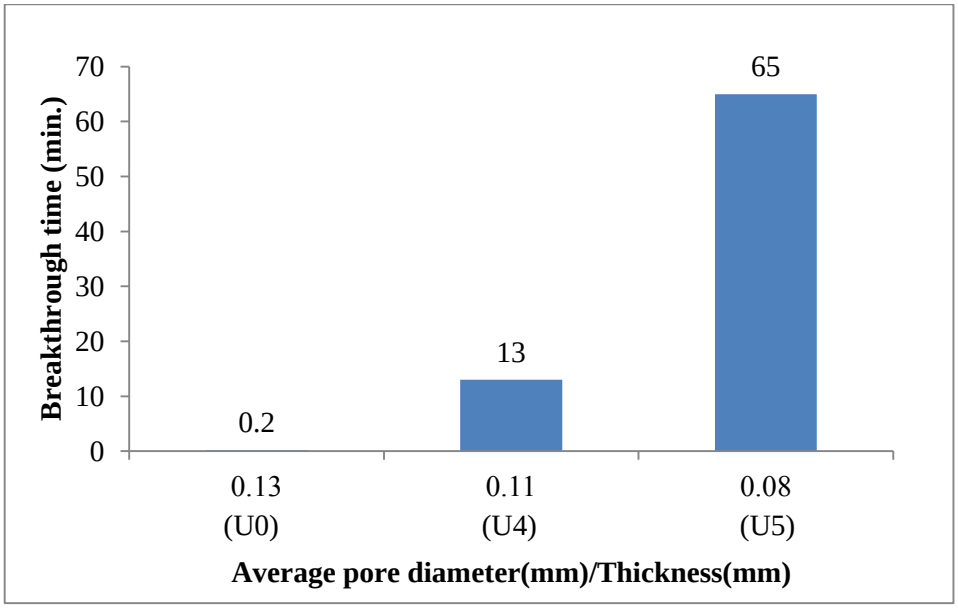

Figure 6.16 Breakthrough time vs the ratio of average pore diameter to thickness of heat-pressed PVDF membranes

6.4.3 The influence of membrane crystallinity on breakthrough time

Considering that the membranes have different membrane thickness as indicated in Section 6.4.1, this might indicate that the effect of crystallinity of membranes on its

liquid permeation property might be masked by the effect of membrane thickness, thus, the combined effect of both membrane thickness and crystallinity on the breakthrough time is investigated, and this is represented as the influence of the ratio of crystallinity over membrane thickness on the breakthrough time as indicated in Figure 6.17.

It is clearly shown that the breakthrough time increases with the decreases with the ratio of crystallinity over membrane thickness (see Figure 6.19). It is worth to point out that the crystallinity varies in a small range of 18.6% (i.e., the crystallinity of 52.9% is 18.6% greater than the crystallinity of 44.6%) while the thickness varies in a larger range of 30.6% (i.e., 0.64 mm is 30.6% greater than 0.49 mm). Therefore, we are still not certain whether this means smaller crystallinity leading to less porous structure and thus greater breakthrough time, or this is because the membrane thickness plays a greater role over crystallinity and has masked the effect of crystallinity on breakthrough time.

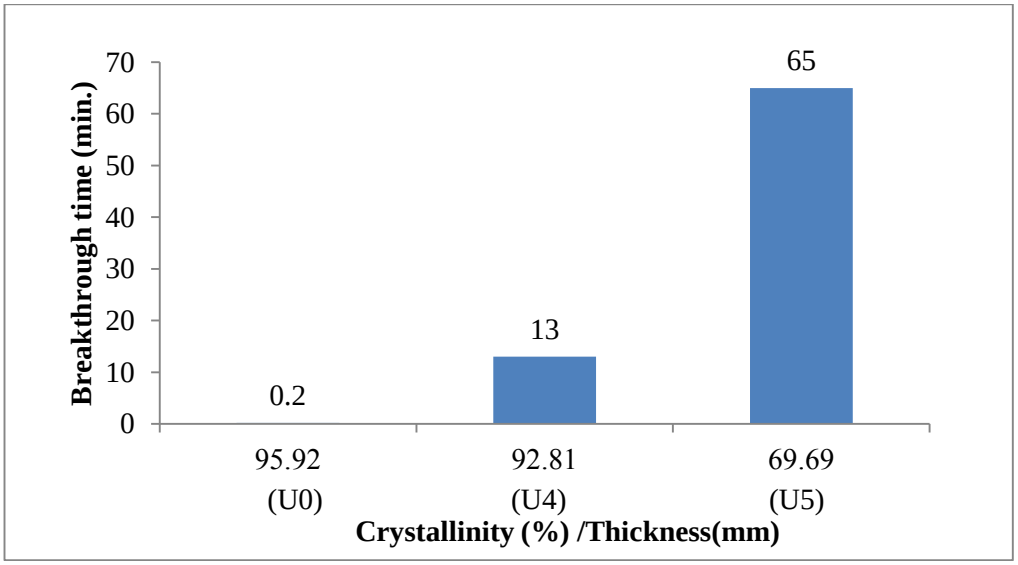

Figure 6.17 Breakthrough time vs the ratio of crystallinity over thickness of the heat-pressed PVDF membranes

6.5 Conclusions

PVDF heat-pressed membranes are obtained by the heat-press process in order to minimise the liquid chemical passage and the water vapour transfer through their pores. It is found temperature of the hotplates, the time of heat-press processing and the number of layer of the membranes influence their nanoporous structures and their liquid chemical permeation properties. It is found that the breakthrough time and the

permeation rate of the heat-pressed PVDF membranes are influenced by their thickness, their average pore diameter and their crystallinity. Therefore, the heat-press processing parameters which are used to produce the double layer heat-pressed PVDF membrane will be applied to produce the less porous NIPAAM-g-PVDF membrane in the following study.

Chapter 7 The influence of nanoporous structure to water vapour permeation properties and liquid chemical permeation properties of NIPAAM-g-PVDF barrier membranes

In Chapters 4 and 5, poly(vinylidene fluoride) grafted N-isopropylacrylamide (NIPAAM-g-PVDF) copolymer membranes obtained by using two different technical routes- plasma induced copolymerisation and thermally induced copolymerisation- are porous. Similar to the porous PVDF membrane, the porous structure in the NIPAAM-g-PVDF copolymer membranes needs to be minimised to resist the passage of liquid chemicals through the pores in the membranes.

In order to determine and characterise the thermal sensitive component in the copolymer membranes, heat-press processing was used to produce nonporous PVDF membranes, and is thus used in this research to convert the micro-scale porous NIPAAM-g-PVDF copolymer membranes into nano-scale porous membranes. In order to achieve better nanoporous membrane structures, the influence of heat-press processing parameters on the porous structure of NIPAAM-g-PVDF copolymer membranes is investigated.

However, the contents of NIPAAM in NIPAAM-g-PVDF copolymer membranes might complicate the effect of the heat-press processing parameters on the resultant porous structures. In this chapter, the influence of heat-press processing parameters on the porous structure and permeation properties of the resultant nanoporous PVDF polymer membranes subjected to heat-press processing has studied in Chapter 6, and the results will be used to heat press NIPAAM-g-PVDF copolymer membranes.

Water vapour transport through the porous membrane structures as determined by Darcy's law is not the only factor that determines fluid permeation through the membrane. In addition, the role of NIPAAM components and the water vapour transmission property of NIPAAM-g-PVDF copolymer membrane must also be considered, and the two parameters are determined and discussed in this chapter.

7.1 The characteristics of the microstructure of heat-pressed NIPAAM-g-PVDF membranes

The NIPAAM-g-PVDF copolymers were synthesised by using both thermally grafted induced copolymerisation and plasma induced copolymerisation methods described in Chapters 4 and 5 respectively, and their nanoporous membranes were produced using heat-press processing method (147 kPa, 150°C, 60 minutes) as described in the

Section 6.2. The conditions were used to produce the heat-pressed PVDF membrane showed the better chemical permeation property, the membranes used in this study and their bulk density, true density and porosity are summarised in Table 7.1.

Table 7.1 Bulk density of the NIAAM-g-PVDF membrane produced by plasma induced copolymerisation before and after heat press process

Membranes		**Mass per unit area ($g\ m^{-2}$)**	**Average thickness (mm)**	**Bulk density ($kg\ m^{-3}$)**	**True density* ($g\ cm^{-3}$)**	**Porosity* (%)**
A1	Double layer heat-pressed thermally induced copolymerised membrane	322	1.47	219.8	1.75	30.29
A2		307	0.78	393.6	1.84	28.80
A3		380	0.92	413.0	1.87	19.79
J1	Single layer heat-pressed plasma induced copolymerised membrane	188	0.71	264.4	1.85	35.14
J2		164	0.36	456.5	1.85	35.14
U4	Single layer heat-pressed pristine PVDF membrane	184	0.57	322.9	1.21	3.33

*True density and porosity were investigated by the mercury intrusion method

The surface morphology, porous structure and crystallinity of the membranes are examined by using scanning electron microscope (SEM), mercury porosimetry and DSC techniques respectively. It is found in Table 7.1 that the porosity of the two heat-pressed NIPAAM-g-PVDF membranes made from plasma induced copolymerisation were not significantly different while the lower concentration of NIPAAM in the heat-pressed NIPAAM-g-PVDF membranes made from the thermally induced copolymerisation has the lowest porosity among the membranes made from the same route.

It was found in Table 7.1 that A1, A2 and A3 are the membrane made from the sample D5, D6 and D7, respectively (see Chapter 4). Each NIPAAM-g-PVDF copolymer material was re-dissolved in DMF at 60°C for 6 hours. The solution was left at room temperature for another 12 hour to degas. Then, it was casted on glass plate by 500-µm gap casting knife and immediately immersed in the distilled water bath at 40°C for 2 minutes. After that the NIPAAM-g-PVDF copolymer membranes were immersed in distilled water for 24 hours to get rid of the excess solvent, and then they

were dried in an oven at 40°C for 24 hours. The amount of NIPAAM in the NIPAAM-g-PVDF copolymer membrane is estimated based on the knowledge as same as it was proposed in Table 5.2.

In the case of NIPAAM-g-PVDF membrane made from the plasma induced copolymerisation, J1 and J2 membrane were produced by different plasma treatment time in order to obtain the difference the amount of NIPAAM on the NIPAAM-g-PVDF membrane. The estimated proportions of NIPAAM on the NIPAAM-g-PVDF membrane are indicated in Table 7.2.

Table 7.2 The mass increase of the porous PVDF membrane before/after the plasma treatment and the copolymerisation

Membranes	**Plasma treatment time (min)**	**Weight (g)**			**Proportion of NIPAAM in the final NIPAAM-g-PVDF obtained (wt%)**
		BP	**AP**	**AC**	
J1	2	1.351	1.351	1.353	0.15
J2	5	1.382	1.382	1.383	0.07

*BP = Before plasma treatment

**AP = After plasma treatment

***AC = After copolymerisation

7.1.1 Amount of grafted copolymer

Because of the amount of the NIPAAM contained in the NIPAAM-g-PVDF copolymer membrane cannot be directly measured, the areas under the amide II and alkene peaks are calculated by using ATR-FTIR for each spectrum between 1701-1589 cm^{-1} and 930-823 cm^{-1}, respectively to compare the presence of NIPAAM in the heat-pressed NIPAAM-g-PVDF membranes. ATR-FTIR spectrum of the NIPAAM-g-PVDF membranes as indicated in Figure 7.1. Then, the amount of grafted copolymer of the NIPAAM-g-PVDF membranes is indicated in Table 7.3.

It is found in Table 7.3 that the heat-pressed NIPAAM-g-PVDF membrane made from the thermally induced grafted copolymerisation method which contained a greatest NIPAAM mass ratio (1:1) to PVDF (A1) show the greatest amount of grafted copolymer which corresponds to membrane A2 and A3 which contained the lower amount of NIPAAM in the membrane (1:10 and 1:100). Similar to the heat-pressed

NIPAAM-g-PVDF membranes made from the plasma induced copolymerisation method, sample J1 contained higher NIPAAM show the higher amount of grafted copolymer than the other sample.

Therefore, it is concluded that the amount of NIPAAM contents in the NIPAAM-g-PVDF membranes are estimated by the proportion of NIPAAM polymer in the NIPAAM-g-PVDF copolymer material after the copolymerisation processes.

Table 7.3 Amount of grafted copolymer of the heat-pressed NIPAAM-g-PVDF membrane

Membranes	**Total Area (A.cm^{-1})**		**Amount of grafted NIPAAM**	**Proportion of NIPAAM in the final NIPAAM-g-PVDF obtained (wt%)**
	1701-1589 cm^{-1}	**930-823 cm^{-1}**		
A1	5.0186	52.8648	0.09	14.55
A2	0.8513	37.4561	0.02	6.00
A3	1.2245	43.7556	0.03	1.05
J1	4.6550	50.1596	0.09	0.15
J2	0.3709	41.8273	0.01	0.07
U4	0.0000	56.7967	0.00	0.00

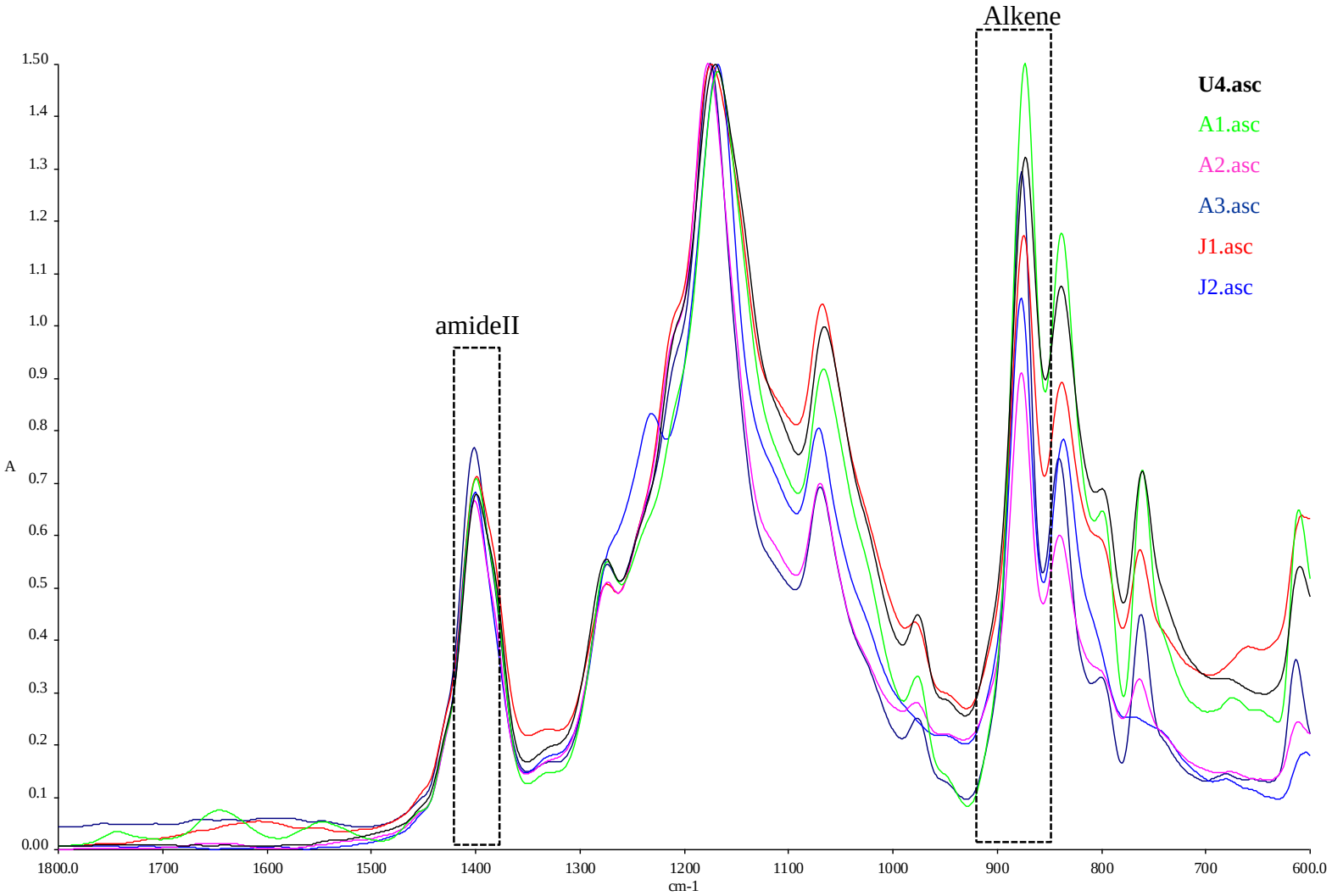

Figure 7.1 ATR-FTIR spectra of the NIPAAM-g-PVDF membranes

7.1.2 Surface morphology

SEM images of the heat-pressed NIPAAM-g-PVDF membranes which were produced by thermally induced copolymerisation contain two areas: the translucent area and the transparent area throughout the membrane. However, both areas are scattered and practically cannot be separated from each other, similar to the heat-pressed PVDF membranes (see Figure 6.2). SEM images of the two areas with three different NIPAAM concentrations the NIPAAM-g-PVDF copolymer membranes at a magnification of 2k were examined and shown in Figure 7.2. SEM images of the heat-pressed NIPAAM-g-PVDF membranes which were produced by a plasma induced copolymerisation method; however, are shown only translucent across the membranes.

The surface composition of the heat-pressed NIPAAM-g-PVDF membranes was characterised by using EDX, to compare percentage of atomic with the element level in the heat-pressed pristine PVDF membrane, the results are shown in Table 7.4.

It is shown in Figure 7.2 (a), (c), and (e) that the translucent areas are porous structures; in contrast, the transparent areas are likely to be smoother and show nano-scale porous structures (see Figure 7.2 (b), (d), and (f)). It is also found that the translucent area of A1 appears to be smoother than the other two heat-pressed NIPAAM-g-PVDF membranes. This is due to the melting point of NIPAAM being lower than PVDF. When applying heat over the melting point of NIPAAM, NIPAAM was melted and formed the new formation with the PVDF backbone and covered the pores of the NIPAAM-g-PVDF copolymer membrane. However, the resultant heat-pressed NIPAAM-g-PVDF membranes obtained from the plasma induced copolymerisation method show more porous structures than the heat-pressed NIPAAM-g-PVDF membranes obtained by the thermally grafted copolymerisation method, because they were produced using the single layer heat-press processing method.

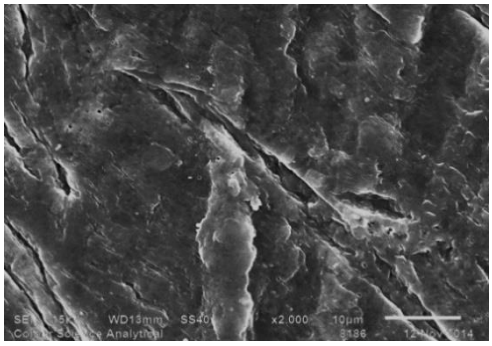

(a) A1 (Translucent area)

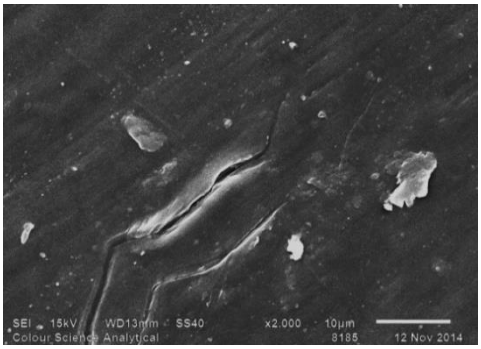

(b) A1 (Transparent area)

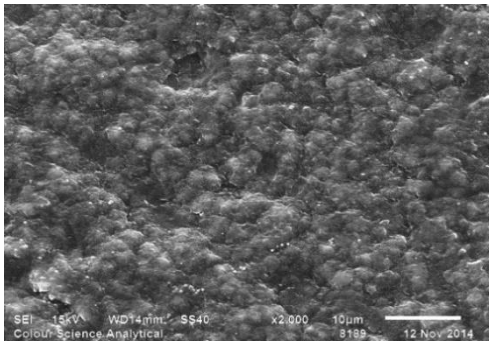

(c) A2 (Translucent area)

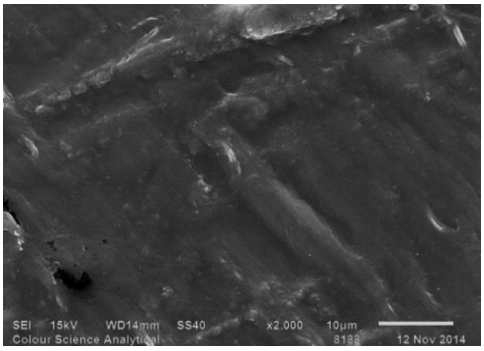

(d) A2 (Transparent area)

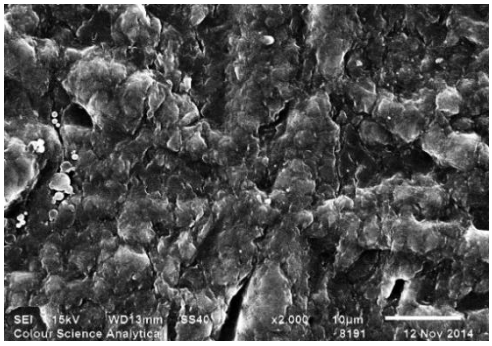

(e) A3 (Translucent area)

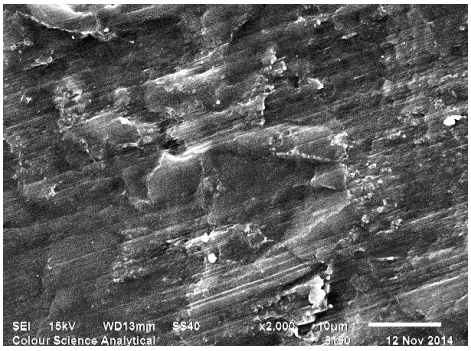

(f) A3 (Transparent area)

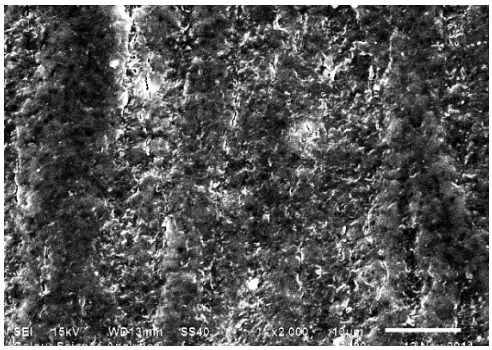

(g) J1

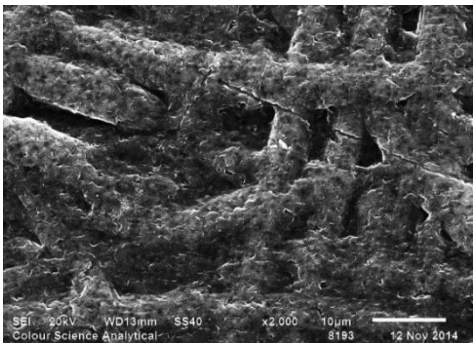

(h) J2

Figure 7.2 SEM photographs of the translucent area and the transparent area of the heat-pressed membranes: (a, b) A1, (c, d) A2 (e, f) A3 (g) J1 and (h) J2 (magnification: 2000)

Table 7.4 The element level of pristine PVDF membrane and NIPAAM-g-PVDF membrane surface by EDX analysis

Membranes		**C (%atomic)**	**F (%atomic)**	**O (%atomic)**
A1	Transparent	45.4	53.2	1.4
	Translucent	46.0	54.0	0.0
A2	Transparent	45.0	55.0	0.0
	Translucent	43.7	56.3	0.0
A3	Transparent	43.9	56.1	0.0
	Translucent	43.8	56.2	0.0
J1		45.8	54.2	0.0
J2		43.7	56.3	0.0
U3		44.7	55.3	0.0

The element level of the heat-pressed pristine PVDF membrane (U3) and the heat-pressed NIPAAM-g-PVDF membranes from both translucent area and transparent area was reported in Table 7.4. Elemental oxygen was expected to be present in the heat-pressed NIPAAM-g-PVDF membranes because oxygen is one of the elements in NIPAAM. Elemental oxygen was found only on the surface of the transparent area of A1 membrane because this sample contained the largest amount of NIPAAM among the other samples while the other areas in the others samples were not able to detect any elemental oxygen.

It is concluded from the surface morphology study that the heat-pressed NIPAAM-g-PVDF membranes presented both porous and nanoporous structures on the surface and the oxygen level which presented in only one sample of NIPAAM-g-PVDF membrane can also confirm that the NIPAAM still contained in the heat-pressed NIPAAM-g-PVDF membranes.

7.1.2 Pore size distribution

The characteristics of pore size distribution of NIPAAM-g-PVDF membranes that produced by the thermally and the plasma induced copolymerisation were examined

and indicated in Figure 7.3. The porosity, the cumulative pore area, the average pore diameters and the pore volume are shown in Table 7.5.

It is shown in Figure 7.3 that the volumetric pore size distributions of the three NIPAAM-g-PVDF heat-pressed membranes made from different NIPAAM concentrations are in the range of 2-900 nm, and most of the pores in terms of the pore volumes were macropores, being larger than 50 nm in diameters as indicated in Table 7.5 at 2.97, 2.81, 2.87 and 2.94 $cm^3 g^{-1}$ in membranes A1, A2, J1 and J2 respectively. There was also a smaller proportion of mesopores, which are pores between 20nm~50nm. However, the volumetric of mesopores of membrane A3 was 46.5 $cm^3 g^{-1}$ which was higher than the other sample.

Table 7.5 The characteristics of porous structure of NIPAAM-g-PVDF membrane

Property		**A1**	**A2**	**A3**	**J1**	**J2**
Cumulative pore area ($m^2 g^{-1}$)		34.23	34.23	34.23	34.27	34.23
Average pore diameters (nm)		38.2	32.2	25.4	47.2	44.6
Mesopores	Pores volume ($cm^3 g^{-1}$)	1.27	1.67	1.65	1.09	0.96
	Percentage (%)	29.94	37.35	46.50	27.55	24.61
Macropores	Pores volume ($cm^3 g^{-1}$)	2.97	2.81	1.90	2.87	2.94
	Percentage (%)	70.06	62.65	53.50	72.45	75.39
Total pore volume ($cm^3 g^{-1}$)		4.24	4.48	3.56	3.97	3.89

The other porous properties of the heat-pressed NIPAAM-g-PVDF copolymer membranes were compared in Table 7.5. It is found the average pore diameter of the heat-pressed NIPAAM-g-PVDF membranes decreased when the concentration of NIPAAM in the membrane decreased in the membranes for both copolymerisation methods. However, the NIPAAM-g-PVDF heat-pressed membranes from the plasma induced copolymerisation showed the larger average pore diameter because these membranes are single heat-pressed membranes which correspond to the results in Chapter 6.

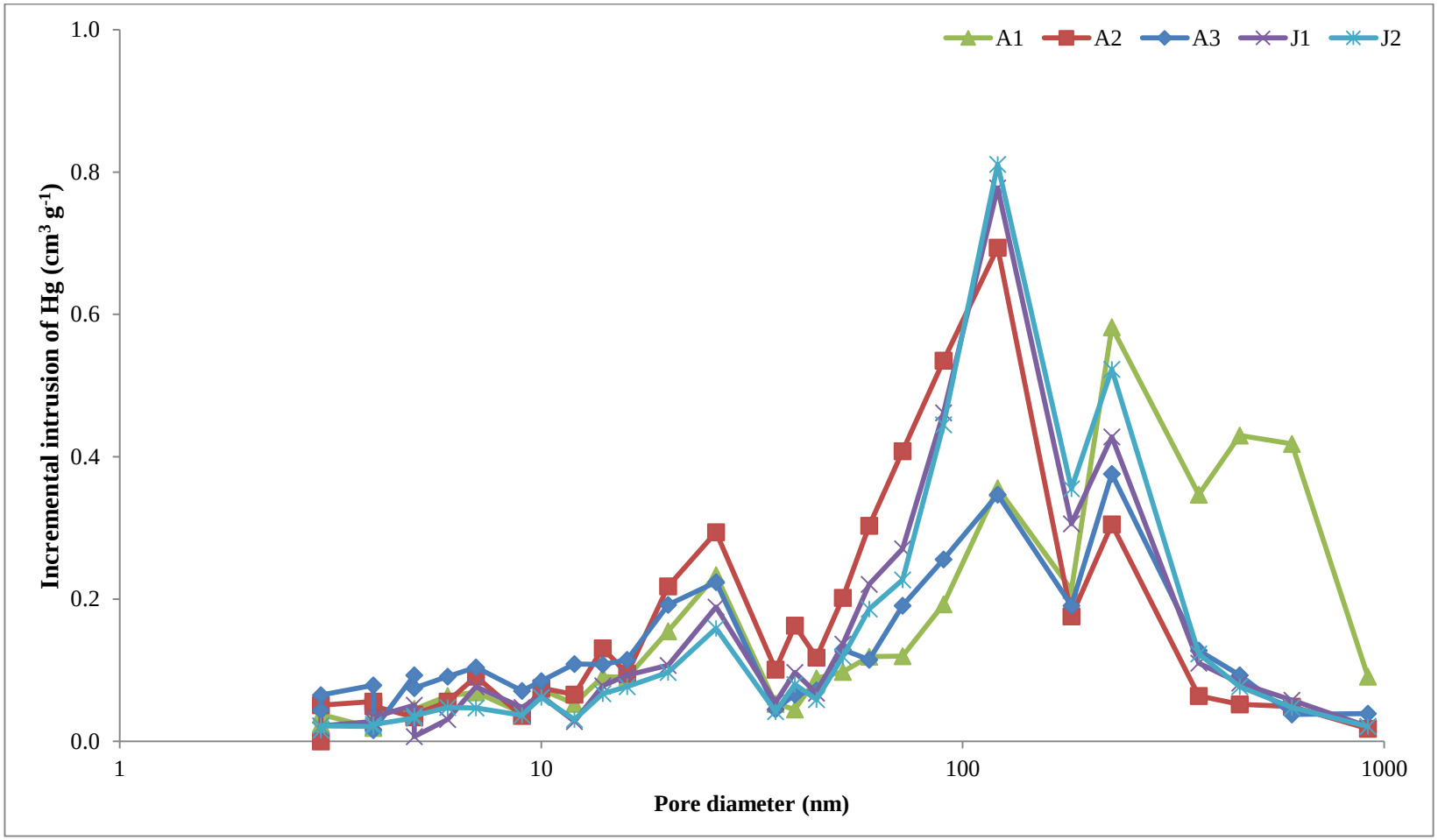

Figure 7.3 The pore size distribution of the NIPAAM-g-PVDF copolymerised membrane

In this section, it is found that the difference in NIPAAM concentration in the NIPAAM-g-PVDF heat-pressed membranes made from the thermally grafted copolymerisation affected the porosity, the average pore diameter and the pore volume. However, the different NIPAAM concentrations in the NIPAAM-g-PVDF heat-pressed membranes made from the plasma induced copolymerisation did not significantly change in porosity, pore area and total pore volumes. This is because of the amount of NIPAAM in the membrane is very small compared to the amount of NIPAAM in the NIPAAM-g-PVDF heat-pressed membranes made from the thermally grafted copolymerisation.

7.1.4 Crystallinity

The surface morphology study in the previous section showed two different kinds of area distributed across the NIPAAM-g-PVDF heat-pressed membranes made from the thermally induced copolymerisation: translucent and transparent areas. For example, the transparent area mostly showed a smoother surface morphology; in contrast, the translucent area mainly showed a porous surface. Therefore, a DSC study of heat-pressed NIPAAM-g-PVDF membranes produced by thermally induced copolymerisation (A1, A2 and A3) from both transparent area and translucent area was carried out and results are shown in Figure 7.4 to Figure 7.9. Additionally, the DSC of the heat-pressed NIPAAM-g-PVDF membranes made from plasma induced copolymerisation (J1 and J2) which showed only transparent areas across the membranes is also investigated and results are shown in Figure 7.10 and Figure 7.11.

The average of the crystallinity and the melting temperature between two different areas in the heat-pressed NIPAAM-g-PVDF membrane are summarised in Table 7.6.

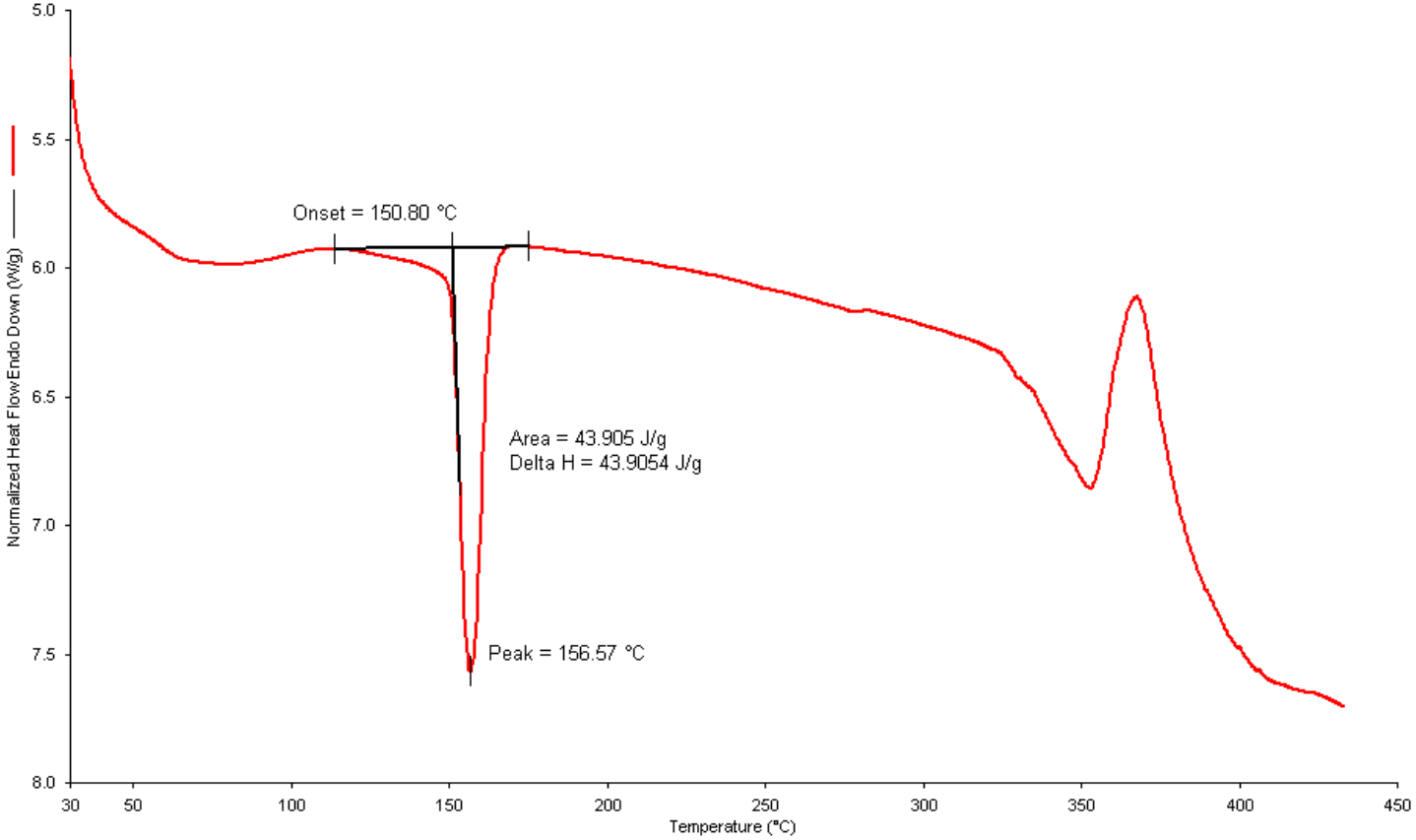

Figure 7.4 DSC of A1 (Transparent)

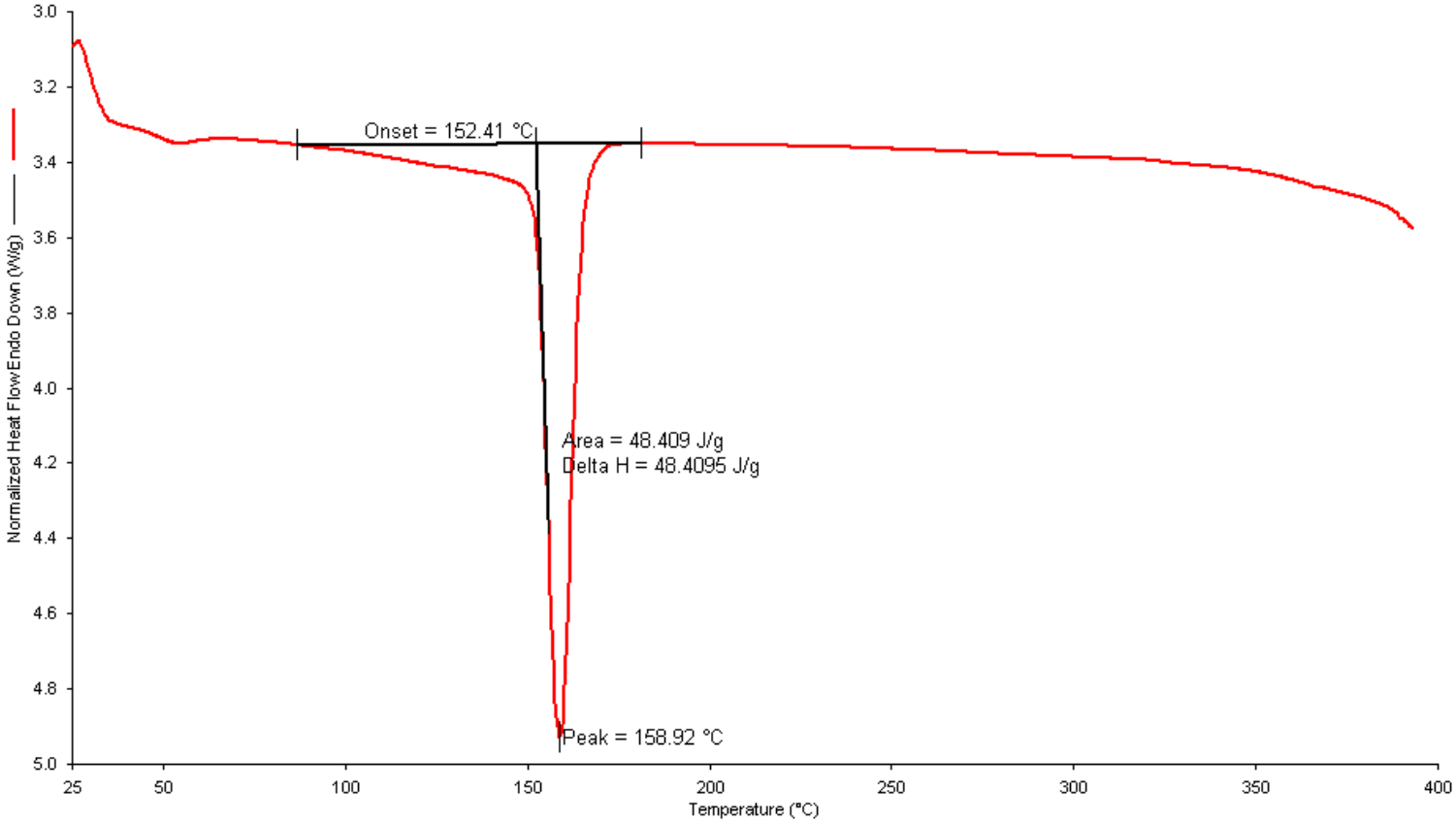

Figure 7.5 DSC of A1 (Translucent)

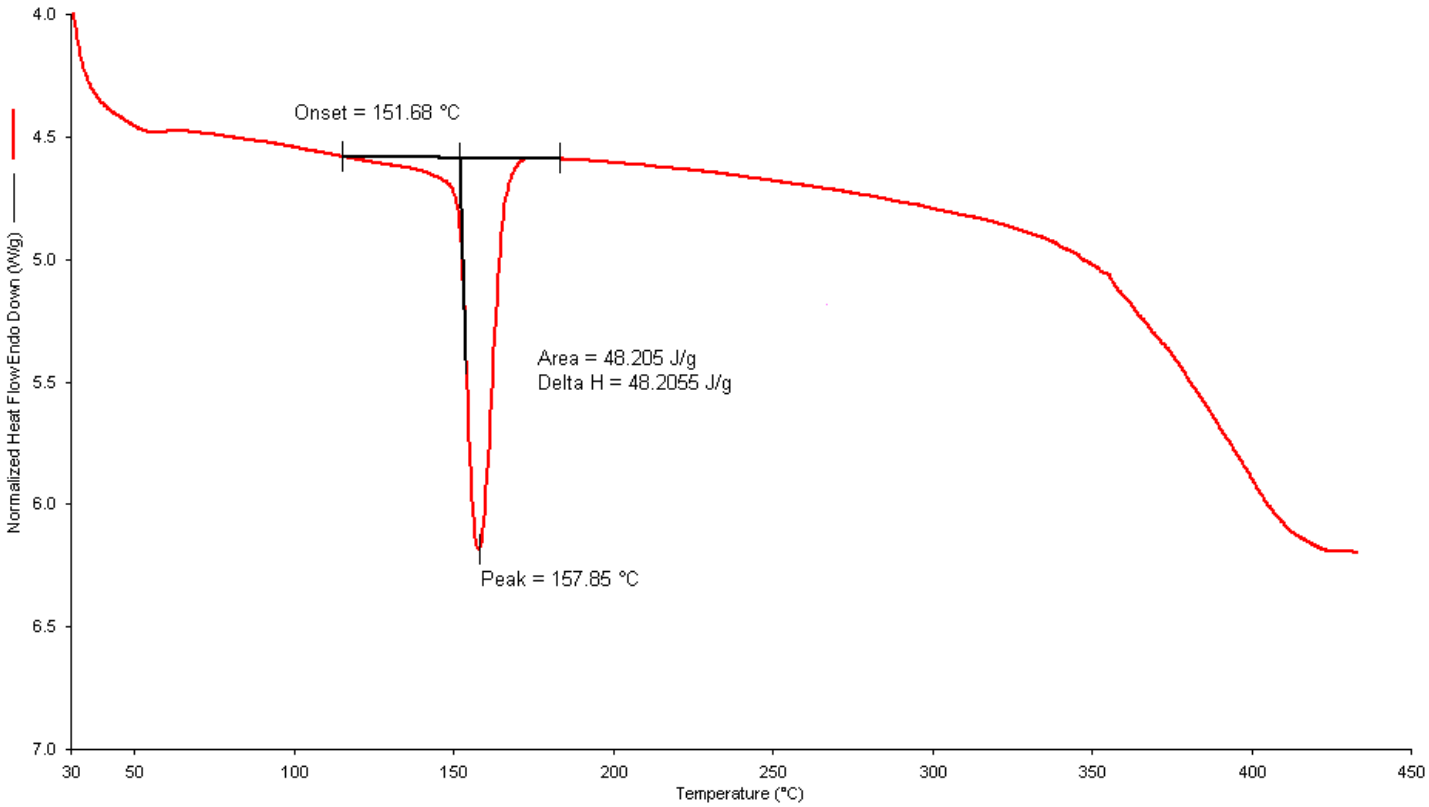

Figure 7.6 DSC of A2 (Transparent)

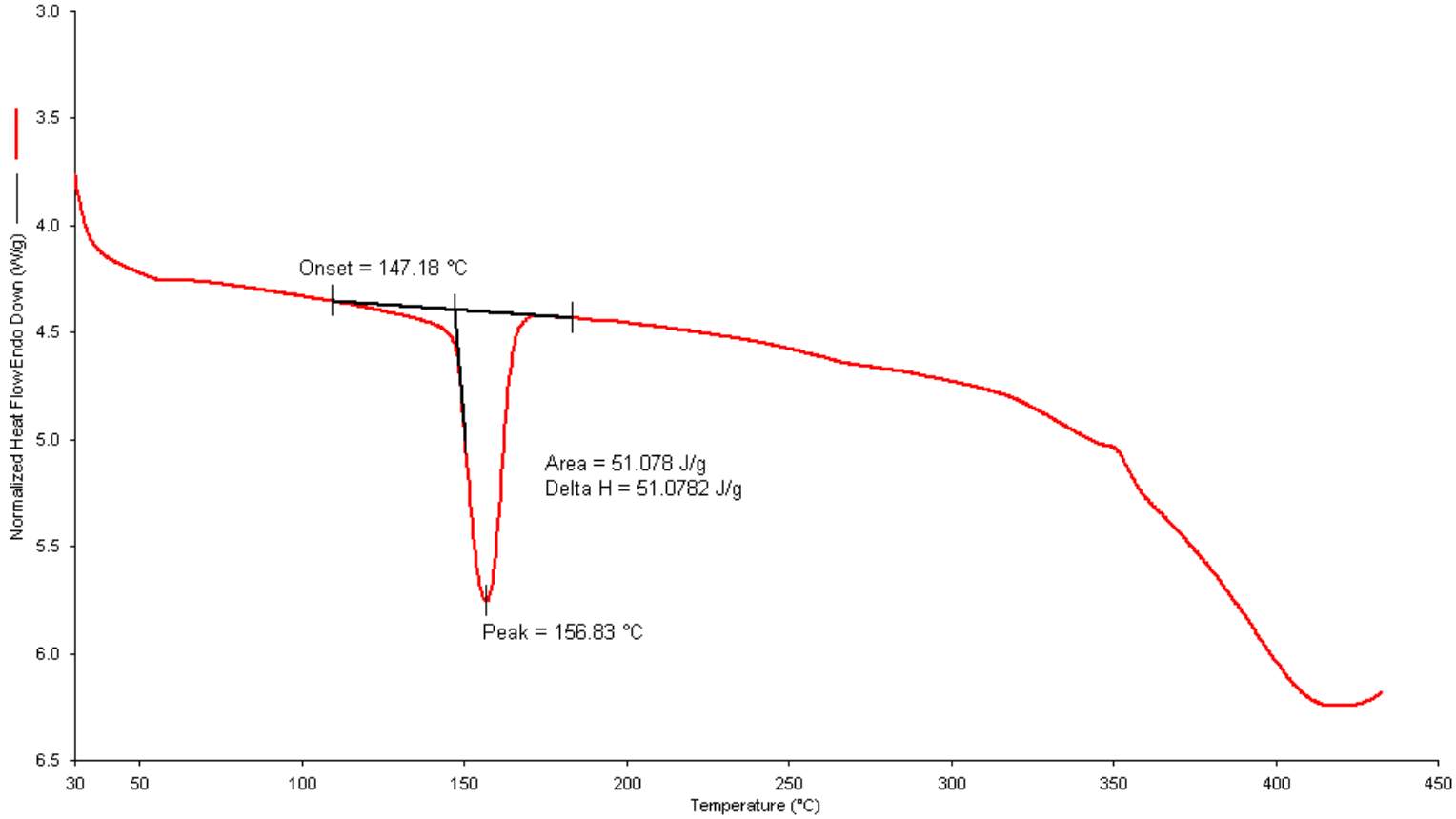

Figure 7.7 DSC of A2 (Translucent)

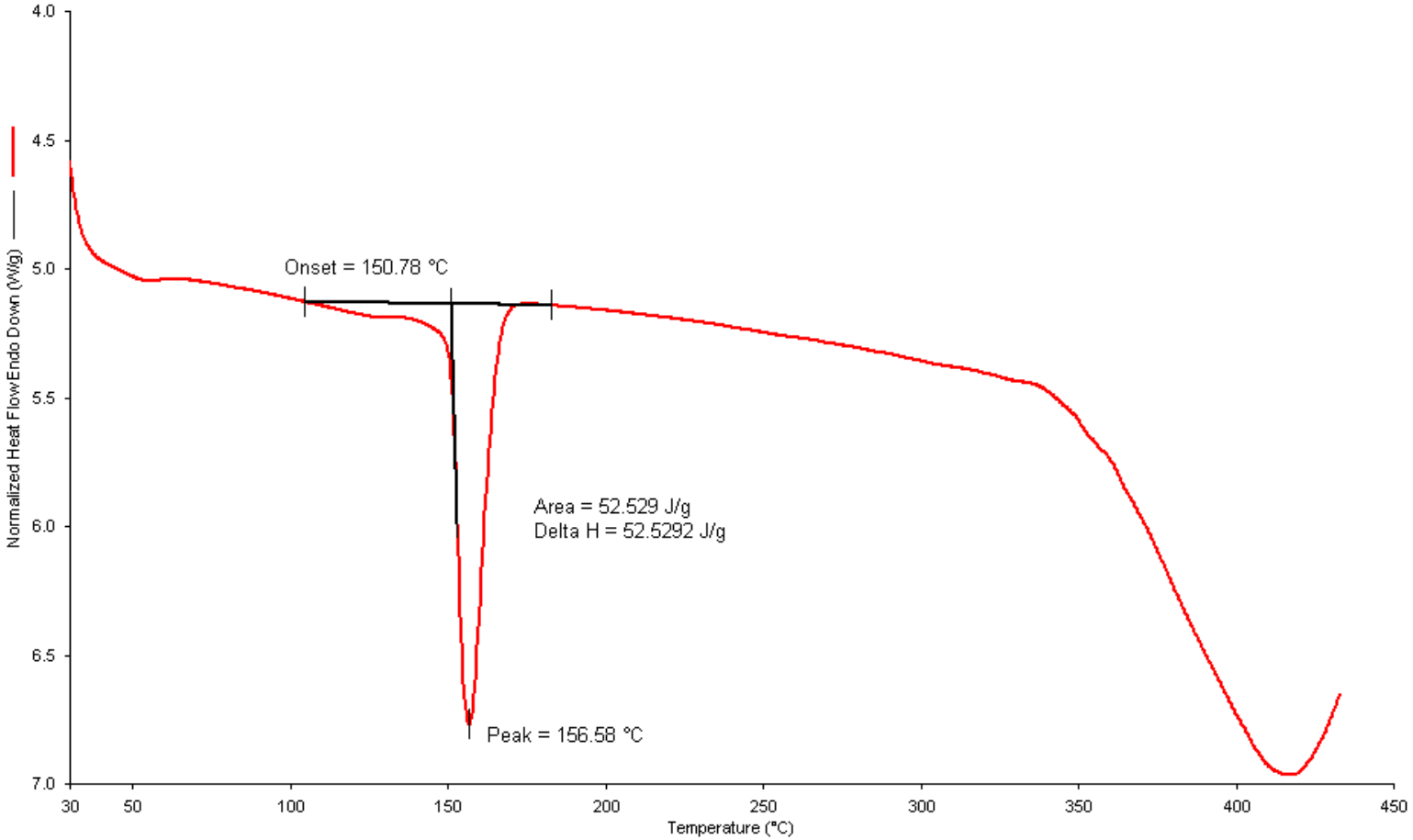

Figure 7.8 DSC of A3 (Transparent)

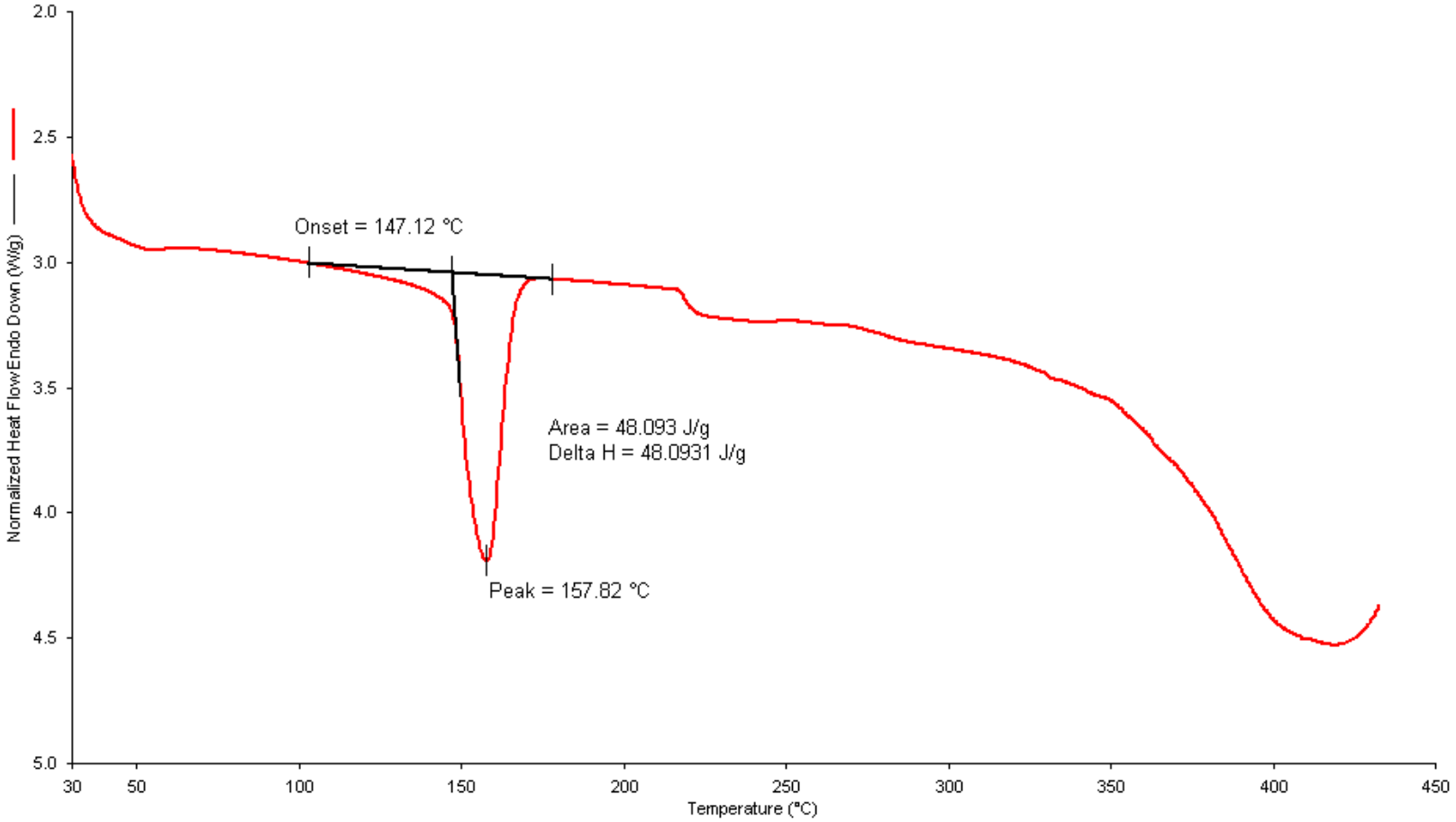

Figure 7.9 DSC of A3 (Translucent)

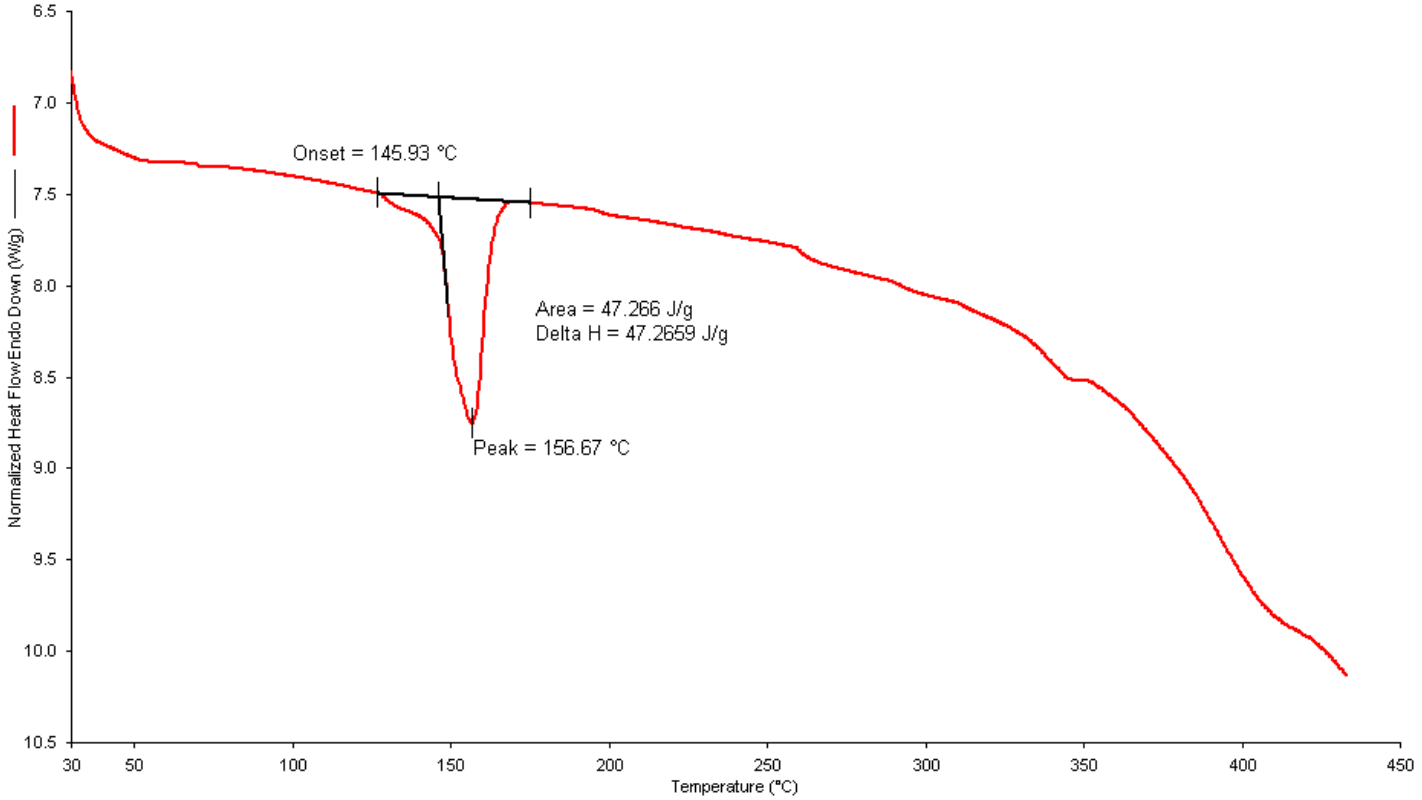

Figure 7.10 DSC of J1

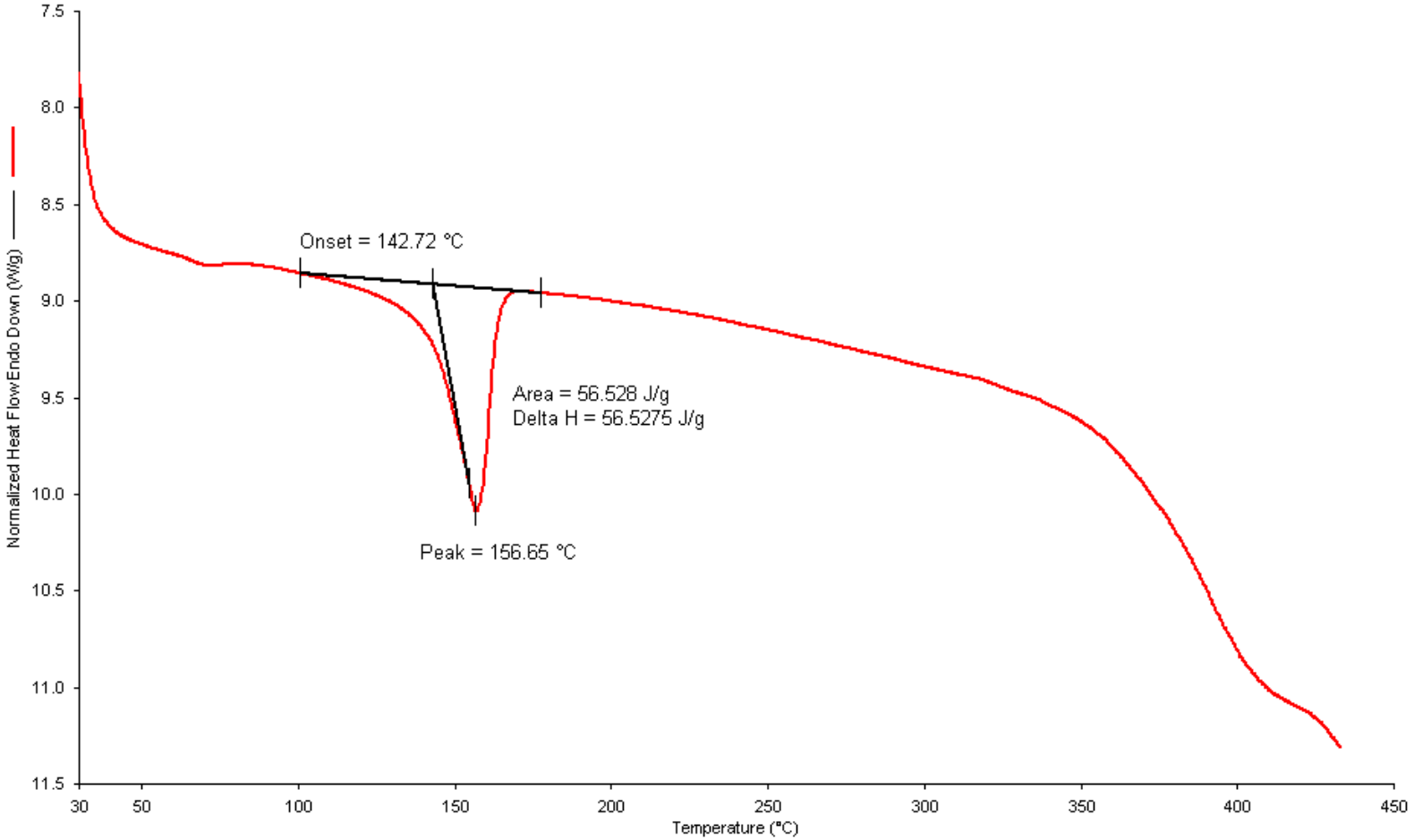

Figure 7.11 DSC of J2

Table 7.6 The crystallinity of the heat-pressed NIPAAM-g-PVDF copolymer membranes

Membranes		**ΔHm (J g^{-1})**	**Crystallinity (%)**	**Tm (°C)**
A1	Transparent	43.91	42.0	156.6
	Translucent	60.91	58.3	157.2
average		52.41	50.2	156.9
A2	Transparent	48.21	46.1	157.9
	Translucent	51.08	48.9	156.8
average		49.65	47.5	157.4
A3	Transparent	52.53	50.3	156.6
	Translucent	48.09	46.0	157.8
average		50.31	48.2	157.2
J1		47.27	45.2	156.7
J2		56.53	54.1	156.7

According to the previous study of the heat-pressed PVDF membrane, the crystallinity in the transparent area was higher than the crystallinity of the translucent area. This finding is consistent with the lower amount of NIPAAM content in the heat-pressed NIPAAM-g-PVDF membrane (1:100). Thus, the amount of NIPAAM content in copolymerised NIPAAM-g-PVDF membrane was higher (1:1 and 1:10), the degree of crystallinity of the translucent areas was also higher.

However, the crystallinity of the heat-pressed NIPAAM-g-PVDF membranes made from the plasma induced copolymerisation are significantly different, especially, the crystallinity of J2 is higher than J1 which corresponds to the result from the pristine PVDF heat-pressed membrane that indicated the crystallinity of the single layer heat-pressed PVDF membrane (U4) is greater than both its original porous membrane (U0) and its double layer heat-pressed membranes (U5).

The melting temperature of both the heat-pressed NIPAAM-g-PVDF membranes made from the both the thermally and the plasma induced copolymerisation was not

significantly different. However, it was lower than the heat-pressed pristine PVDF membrane in Table 6.4. In this case, the structural symmetry of the PVDF membrane was partially changed because of the graft copolymerisation of NIPAAM polymer on the PVDF membrane resulting in an increase of the melting point from 155.0°C to 156.7°C.

7.2 Moisture vapour absorbency (MVA) and water vapour transmission rate (*WVTR*) of NIPAAM-g-PVDF copolymer membranes

7.2.1 Moisture Vapour Absorbency (*MVA*)

The effect of NIPAAM components on moisture vapour absorption in the NIPAAM-g-PVDF copolymer membrane is investigated. The heat-pressed NIPAAM-g-PVDF membranes were dried in an oven at 60°C for 24 hours, and their weight were checked every 6 hours to verify if there was no further change in mass to ensure the membranes dried completely. Then, the membranes were conditioned at 20°C, 65% RH for 24 hours. The membranes before and after being conditioning were weighed and the MVA at 20°C, 65% RH is obtained by using the equation (7-1) below:

$$MVA(\%) = \frac{(M_1 - M_0)}{M_0} \, x \, 100\% \qquad (7\text{-}1)$$

where
M_0 is the mass of the membrane before conditioning,
M_1 is the mass of the membrane after conditioning.

The moisture vapour absorbency of the heat-pressed pristine PVDF membrane and the heat-pressed NIPAAM-g-PVDF membranes is shown in Table 7.7 below.

NIPAAM shows the hydrophilic property at a temperature below the LCST in an aqueous environment and the hydrophobic property above its LCST [148]. It is found in Table 7.7 that the NIPAAM components in two of the NIPAAM-g-PVDF copolymer membranes at the temperature below LCST (20°C) also show the hydrophilic property in atmosphere, and they absorbed moisture vapour from the environment at a temperature at 20°C. However, the moisture absorbency of both A1 and J1 membranes is very low and only 0.14% and 0.13%, respectively. In addition, there is no apparent moisture absorption shown in the other membranes.

Table 7.7 Moisture vapour absorbency of heat-pressed NIPAAM-g-PVDF membranes and heat-pressed PVDF membrane

Membranes	**M_0 (g)**	**M_1(g)**	**MVA (%)**
A1	0.672	0.673	0.14
A2	0.452	0.452	0.00
A3	0.506	0.506	0.00
J1	0.767	0.768	0.13
J2	0.550	0.550	0.00
U4 (reference PVDF membrane)	0.900	0.900	0.00

There are two possible explanations for the small *MVA* of the membranes. Firstly, there might be a small amount of NIPAAM components in the heat-pressed NIPAAM-g-PVDF copolymer membranes to absorb water vapour from the atmosphere. Secondly, most of the NIPAAM components in the copolymer membranes might be enclosed by hydrophobic and non-absorbent PVDF polymer and thus it cannot access moisture vapour in the atmosphere. Nevertheless, we can conclude that the moisture vapour in the atmosphere has little effect on the water vapour absorbency of the membranes, and it thus has little effect on the water vapour transmission property of the membranes which is discussed in the section below.

7.2.2 *WVTR* of the copolymer membranes at the temperatures below and above LCSTs

WVTR of the heat-pressed NIPAAM-g-PVDF membranes are examined at two different temperatures, below and above the LCST of NIPAAM (around 33°C [32]). The *WVTR* results at 20°C and 40°C are shown in Figure 7.12 and Figure 7.13, respectively. It is difficult to identify the influence of the amount of the NIPAAM contents on their *WVTR* at different temperatures through direct comparison of their *WVTR* values because the membranes have different porous structure from each other; therefore the ratios of the *WVTR* of the heat-pressed NIPAAM-g-PVDF membranes at 40°C and 20°C, which was defined in equation (3-4), are summarised in Table 7.8 in order to elucidate the effect of the temperature changes on the *WVTR* of the NIPAAM-g-PVDF membranes.

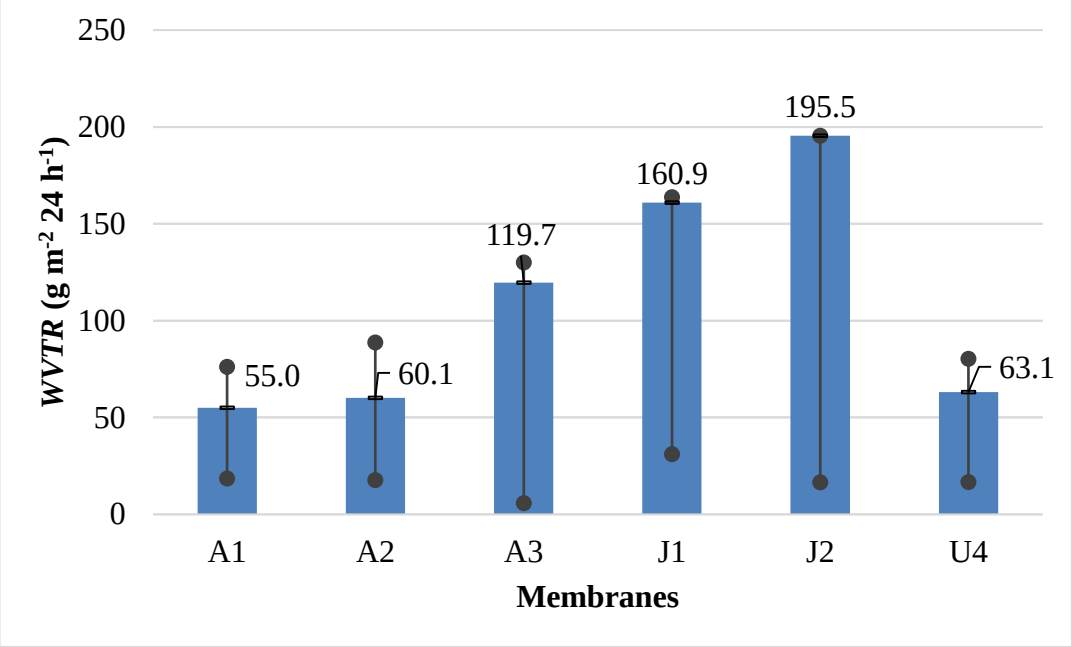

Figure 7.12 *WVTR* of the heat-pressed NIPAAM-g-PVDF membranes and the heat-pressed PVDF membranes at 20°C and 40°C

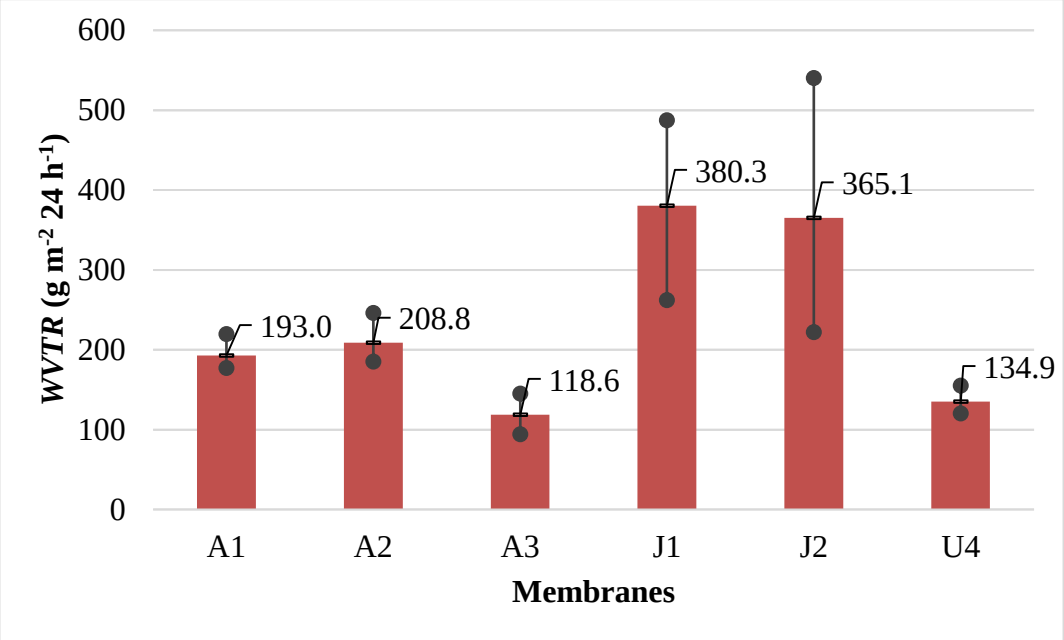

Figure 7.13 *WVTR* of the heat-pressed NIPAAM-g-PVDF membranes and the heat-pressed PVDF membranes at 40°C

It is found in Figure 7.12 and Figure 7.13 that the *WVTR* at 40°C is greater than that at 20°C for all of the membranes, including both the five heat-pressed NIPAAM-g-PVDF membranes and the heat-pressed pristine PVDF membrane (U4).

It is also found that among the three heat-pressed NIPAAM-g-PVDF membranes made from the thermally induced grafted copolymerisation method (A1, A2 and A3), the two membranes having higher concentrations of NIPAAM (A1 and A2) and a much greater *WVTR* at 40°C than that at 20°C in comparison with the *WVTR*s changes at 40°C and 20°C of both membranes that have smaller NIPAAM concentrations (A3) and the heat-pressed pristine PVDF membrane (U4).

Moreover, the *WVTR*s of the heat-pressed NIPAAM-g-PVDF membranes made from the plasma grafted copolymerisation method (J1 and J2) at 40°C are also greater than their *WVTR* at 20°C even though it is found the amount of NIPAAM contained in the two heat-pressed NIPAAM-g-PVDF membranes is quite similar.

As indicated in Section 3.3.2, the theoretical ratio of the volumetric flow rate of water vapour transmission through a unit cross-section area of a porous area at 40°C and 20°C (R_{WVTR}) is 3.16 as shown in equation (3-8) based on Darcy's Law when the porous structure of the membrane keeps identical at the two temperatures. The water vapour flow through the membrane would be a diffusion flow if a *WVTR* ratio is less than 3.16, and the water vapour flow through the membrane could involve an extra diffusion mechanism alongside a diffusion flow if a *WVTR* ratio is greater than 3.16.

Table 7.8 *WVTR*s of the heat-pressed PVDF and NIPAAM-g-PVDF membranes at 20°C and 40°C

Membranes	***WVTR* (g m^{-2} 24h^{-1})**		R_{WVTR}
	20°C	**40°C**	
A1	55.0	193.0	3.5
A2	60.1	208.8	3.5
A3	119.7	118.6	1.0
J1	160.9	380.4	2.4
J2	195.5	365.1	1.9
U4 (reference PVDF membrane)	63.1	134.9	2.2

It is found in Table 7.8 that the ratio of the *WVTR* of the heat-pressed NIPAAM-g-PVDF membranes (A1 and A2) between 40°C and 20°C (~3.5) is greater than the

theoretical ratio (3.16). This might indicate that the water vapour transferring through the porous membrane follows not only the Darcy's Law but also some other additional mechanisms (e.g. additional diffusion actions through NIPAAM polymers and meso-/micro- pores during water vapour transmission at 40°C). However, the *WVTR* ratios between 40°C and 20°C of other membranes containing either no or a smaller proportion of NIPAAM (U3, A3, J1 and J2) is smaller than this theoretical value (3.16). This is an indication that the water vapour transport through these membranes does not occur through the pores/holes but via the permeation and diffusion mechanism, we might conclude that NIPAAM components in the NIPAAM-g-PVDF copolymer membranes might neither act nor insufficient amount to act at 40°C to form pores in the copolymer membranes.

7.2.3 Relationship between *WVTR* and the structure of NIPAAM-g-PVDF membranes

As indicated in Section 6.3, there are three parameters are related to the liquid chemical permeation property through the heat-pressed PVDF membranes: thickness, porous structure and crystallinity. However, the relationship between the water vapour transmission property to the structure of the NIPAAM-g-PVDF membranes is still unknown. This section will study the volumetric flow rate of water vapour permeation through a unit cross-section area (J_{total}).

The volumetric flow rate of fluid flow through a unit cross-section area of a porous material is described by Darcy's law in equation (3-5) and the permeation rate of fluid flow permeation through a nonporous membrane or microporous membrane is described by Henry's law as shown in equation (2-7). Based on equations (3-5) and (2-7), the permeability coefficient J_{total} ($cm^3\ cm^{-2}\ s^{-1}\ (Pa/cm)^{-1}$), of the water vapour flow through a membrane is thus described in equation (7-2) below (also see equation 2-6);

$$J_{total} = WVTR \times \frac{1}{24 \times 3600 \times 10^6 \times \rho_{wv}} \times \frac{L}{\Delta P_{wv}} \qquad (7\text{-}2)$$

where

J_{total} is the permeation coefficient of water vapour permeation through of membrane ($cm^3\ cm^{-2}\ s^{-1}\ (Pa/cm)^{-1}$),

$WVTR$ is the water vapour transmission rate of the membranes ($g\ m^{-2}\ (24h)^{-1}$) defined in equation (2-20),

ρ_{wv} is the density of water vapour (g cm^{-3}); at 20°C, ρ_{wv}= 1.73×10^{-5} g cm^{-3}, at 40°C, ρ_{wv}= 5.12×10^{-5} g cm^{-3} [222],

ΔP_{wv} is the water vapour pressure differences between two sides of the membrane (Pa) at different temperature; at 20°C, 65%RH; ΔP_{wv} = 2.33×10^{3} Pa, at 40°C, 65%RH; ΔPwv = 7.37×10^{3} Pa [223],

L is the membrane thickness (cm).

Water vapour permeability coefficient, J_{total}, of each NIPAAM-g-PVDF membrane is calculated based on the equation (7-2) and shown in Table 7.9 below.

Table 7.9 Water vapour permeability coefficient, J_{total}, of the NIPAAM-g-PVDF and PVDF membranes

Samples	**Thickness (cm)**	***WVTR*** **(g m^{-2} $(24h)^{-1}$)**		***J_{total}*** **(cm^3 cm^{-2} s^{-1} $(Pa/cm)^{-1}$)**	
		20°C	**40°C**	**20°C**	**40°C**
A1	0.147	55.0	193.0	6.63×10^{-9}	2.49×10^{-9}
A2	0.078	60.1	208.8	3.85×10^{-9}	1.43×10^{-9}
A3	0.092	119.7	118.6	9.03×10^{-9}	9.56×10^{-10}
J1	0.071	160.9	380.4	9.37×10^{-9}	2.37×10^{-9}
J2	0.036	195.5	365.1	5.77×10^{-9}	1.15×10^{-9}
U4	0.057	63.1	134.9	2.95×10^{-9}	6.74×10^{-10}

7.2.3.1 The influence of membrane thickness on water vapour permeability coefficient

The relationship between the thickness of the heat-pressed NIPAAM-g-PVDF membranes and their water vapour permeability coefficients at 20°C and 40°C is shown in Figure 7.14 and Figure 7.15, respectively.

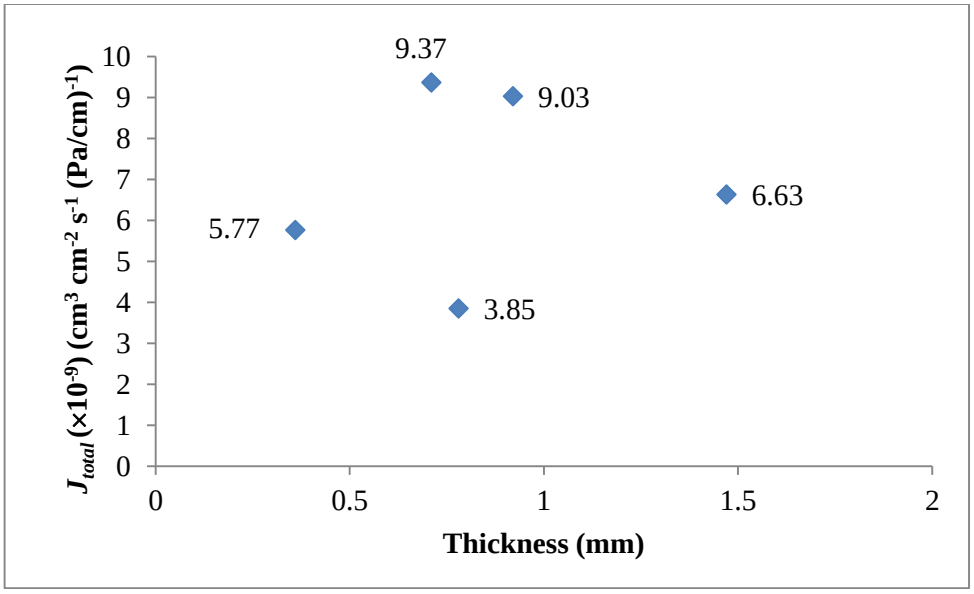

Figure 7.14 Water vapour permeability coefficient (J_{total}) at 20°C vs Thickness of the heat-pressed NIPAAM-g-PVDF membranes

It is found in Figure 7.14 that there is not an apparent trend between the water vapour permeation coefficient and the membrane thickness as a whole. In order to exclude such influence being caused by different production methods, the influences of the membrane thickness on permeability coefficient are discussed below. For the three membranes (A1, A2, and A3) made from thermally induced method, the thickest heat-pressed NIPAAM-g-PVDF membrane (1.47 mm) has smaller J_{total} (6.63×10^{-9} cm^3 cm^{-2} s^{-1} (Pa/cm)$^{-1}$) than the J_{total} (9.03×10^{-9} cm^3 cm^{-2} s^{-1} (Pa/cm)$^{-1}$) of the thinner membrane (0.92 mm). For the membranes (J1 and J2) made from plasma grafted method, the thinnest heat-pressed NIPAAM-g-PVDF membrane (0.36 mm) has the smaller J_{total} (5.77×10^{-9} cm^3 cm^{-2} s^{-1} (Pa/cm)$^{-1}$) than that (9.37×10^{-9} cm^3 cm^{-2} s^{-1} (Pa/cm)$^{-1}$) of the thicker membrane (0.78 mm). Therefore, it is concluded that the J_{total} at 20°C of the heat-pressed NIPAAM-g-PVDF membranes does not have an apparent trend with their thickness as a whole, but for the membranes made from plasma grafted method, thinner membrane does have a greater permeation coefficient.

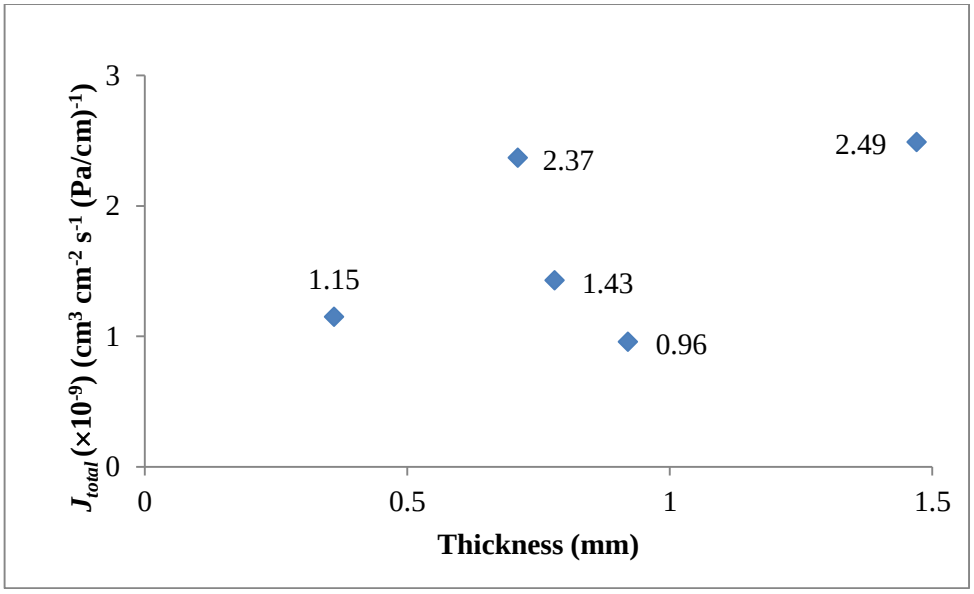

Figure 7.15 Water vapour permeability coefficient (J_{total}) at 40°C vs Thickness of the heat-pressed NIPAAM-g-PVDF membranes

It is found in Figure 7.15 that the water vapour permeation coefficient at 40°C of the heat-pressed NIPAAM-g-PVDF membranes has a moderate relationship with their thickness as a whole (R^2=0.3067). However, it is found in the three membranes made from thermally induced method (A1, A2, and A3), the thickest heat-pressed NIPAAM-g-PVDF membrane (1.47 mm) has the greatest water vapour permeation coefficient (2.49×10^{-9} cm^3 cm^{-2} s^{-1} (Pa/cm)$^{-1}$) in comparison with the other two thinner membranes; such tread is also found true for the two membranes made from plasma grafted method (J1 and J2); the thicker heat-pressed membrane (0.71 mm) has a greater permeation coefficient (2.37×10^{-9} cm^3 cm^{-2} s^{-1} (Pa/cm)$^{-1}$) than that (1.15×10^{-9} cm^3 cm^{-2} s^{-1} (Pa/cm)$^{-1}$) of the thinner membrane (0.36 mm). Therefore, it is concluded that the water vapour permeation coefficient at 40°C of the heat-pressed NIPAAM-g-PVDF membranes increases with the increase of their thickness. This trend interestingly opposes with the trend of the membranes made from plasma membranes at 20°C.

7.2.3.2 The influence of membrane porous structure on water vapour permeability coefficient

The characteristics of the pore size distribution of the heat-pressed NIPAAM-g-PVDF membranes were shown in Section 7.1, it is noted that they were measured at 20°C, and the porous structure of the heat-pressed NIPAAM-g-PVDF membranes at 40°C could not be measured due to the limitation of the mercury intrusion porosimetry.

Therefore, the porous structures discussed below are the pore characteristics at 20°C only.

7.2.3.2.1 The influence of membrane total pore volume on vapour permeability coefficient

The relationship between the total pore volume of the heat-pressed NIPAAM-g-PVDF membranes and their water vapour permeation coefficient at 20°C and 40°C is shown in Figure 7.16 and Figure 7.17, respectively.

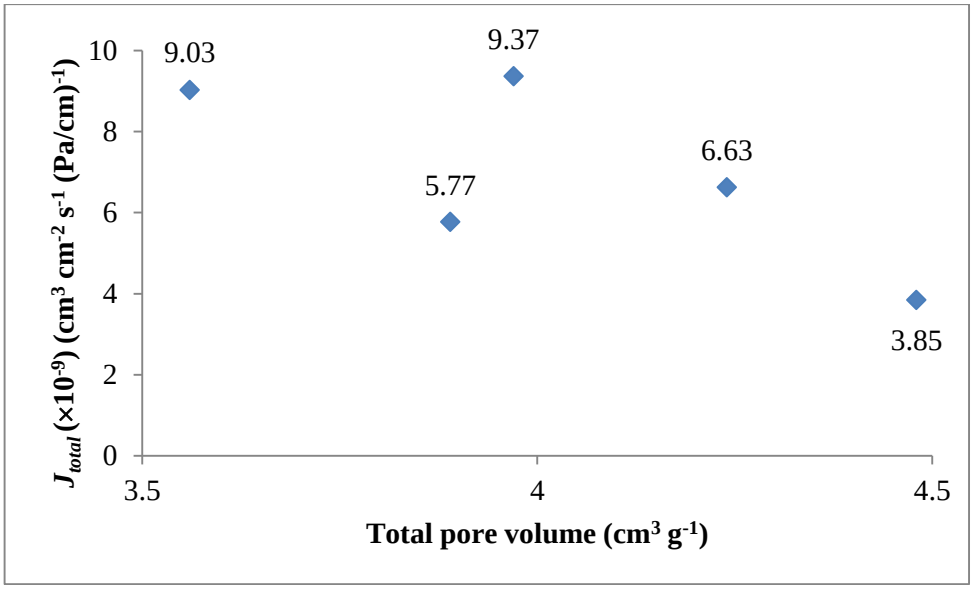

Figure 7.16 Water vapour permeability coefficient (J_{total}) at 20°C and Total pore volume of the heat-pressed NIPAAM-g-PVDF membranes

It is found in Figure 7.16 that the permeation coefficient of the heat-pressed NIPAAM-g-PVDF membranes has a strong linear relationship with their total pore volumes, J_{total} decreases with the increase of the total pore volume. For the membranes (A1, A2 and A3) made from thermal induced method, in which the membrane having the greatest total pore volume (4.48 cm^3 g^{-1}) appears to have the smallest J_{total} (3.85×10^{-9} cm^3 cm^{-2} s^{-1} (Pa/cm)$^{-1}$) and the membrane having the smallest total pore volume (3.56 cm^3 g^{-1}) appears to have the greatest J_{total} (9.03×10^{-9}cm^3 cm^{-2} s^{-1} (Pa/cm)$^{-1}$). However, for the membranes (J1 and J2) made from plasma grafted method, while the total pore volumes of the two membranes have a small difference of 2% (3.89 and 3.97 cm^3 g^{-1}), their permeation coefficient are about 58% different (5.77×10^{-9} and 9.37×10^{-9}cm^3 cm^{-2} s^{-1} (Pa/cm)$^{-1}$). Therefore, the water vapour permeation coefficient, J_{total}, of the heat-pressed NIPAAM-g-PVDF membrane at

20°C is influenced by its total pore volume but total pore volume might not be a decisive factor.

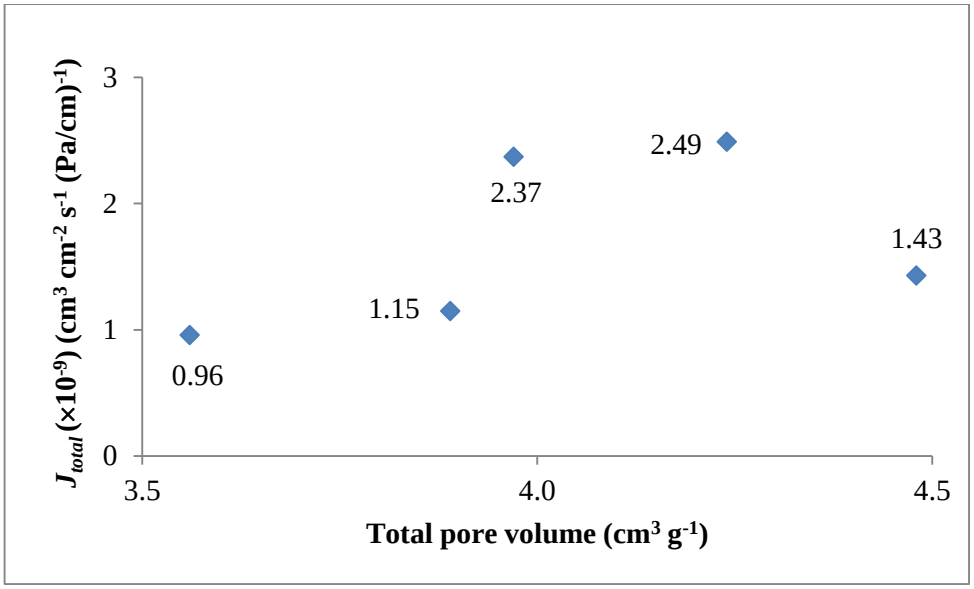

Figure 7.17 Water vapour permeability coefficient (J_{total}) at 40°C vs Total pore volume of the heat-pressed NIPAAM-g-PVDF membranes

It is found in Figure 7.17 that there is a moderate correlation between the water vapour permeation coefficient of the membranes at 40°C and the total pore volume as a whole when considering the membrane having smallest total pore volume (3.56 cm^3 g^{-1}) appears to have smallest J_{total} (9.6×10^{-10} cm^3 cm^{-2} s^{-1} $(Pa/cm)^{-1}$) and R^2 = 0.1879. However, when considering the membranes made from thermally induced method (A1, A2, and A3), the membrane having the greatest total pore volume (4.48 cm^3 g^{-1}) has smaller J_{total} (1.43×10^{-9} cm^3 cm^{-2} s^{-1} $(Pa/cm)^{-1}$) than the J_{total} (2.49×10^{-9} cm^3 cm^{-2} s^{-1} $(Pa/cm)^{-1}$) of the smaller total pore volume 4.24 cm^3 g^{-1}. Also, the membranes made from plasma-grafted method (J1 and J2), the total pore volumes of the two membranes have a small difference of 2% (3.89 and 3.97 cm^3 g^{-1}), their permeation coefficients are massively different at 106% (2.37×10^{-9} and 1.15×10^{-9} cm^3 cm^{-2} $s^{-1}(Pa/cm)^{-1}$). Therefore, the water vapour permeation coefficient of the heat-pressed NIPAAM-g-PVDF membranes at 40°C increases with the increase of total pore volume.

In summary, the water vapour permeation coefficient (J_{total}) of the heat-pressed NIPAAM-g-PVDF membranes at 20°C and 40°C is influenced by their total pore volume but total pore volume might not be a decisive factor.

7.2.3.2.2 The influence of membrane average pore diameter on water vapour permeability coefficient

The relationship between the average pore diameters and water vapour permeability coefficient of the heat-pressed NIPAAM-g-PVDF membranes at below and above LCST of NIPAAM is shown in Figure 7.18 and Figure 7.19, respectively.

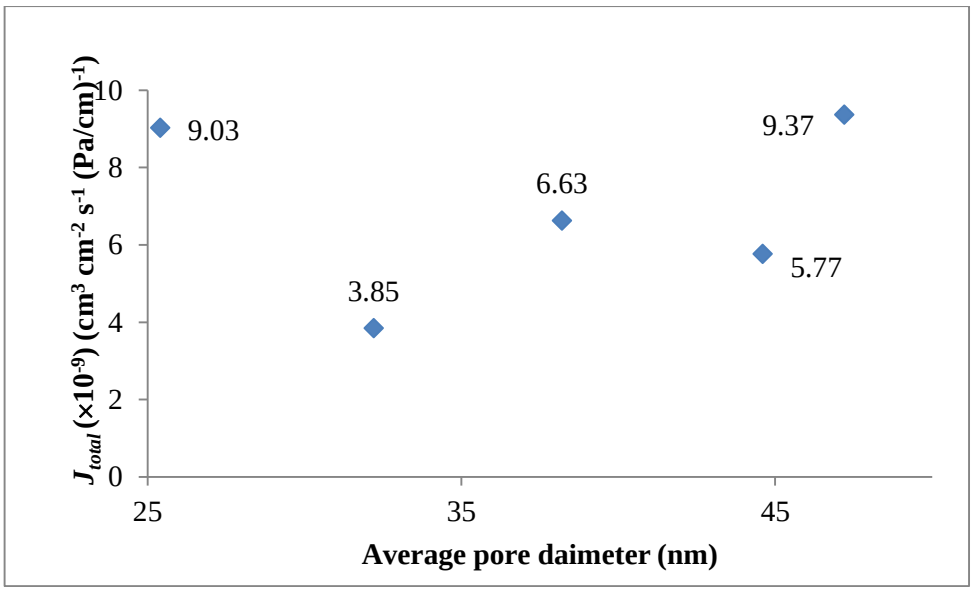

Figure 7.18 Water vapour permeability coefficient (J_{total}) at 20°C vs their average pore diameter of the heat-pressed NIPAAM-g-PVDF membranes

It is found in Figure 7.18 that there is not apparent trend between the water vapour permeation coefficient at 20°C and the average pore diameter as a whole. For the three membranes made from thermally induced method (A1, A2, and A3), the membrane having the smallest average pore diameter (25.4 nm) has greatest J_{total} (9.03×10^{-9} cm^3 cm^{-2} s^{-1} (Pa/cm)$^{-1}$) than the J_{total} (3.85×10^{-9} and 6.63×10^{-9} cm^3 cm^{-2} s^{-1} (Pa/cm)$^{-1}$) of the membrane having the greater average pore diameters 32.2 nm, 38.2 nm. For the membranes (J1 and J2) made from plasma grafted method, the membrane having a smaller average pore diameter (44.6 nm) has the smaller J_{total} (5.77×10^{-9} cm^3 cm^{-2} s^{-1} (Pa/cm)$^{-1}$) than that (9.37×10^{-9} cm^3 cm^{-2} s^{-1} (Pa/cm)$^{-1}$) of the membrane having a greater average pore diameters. Moreover, the average pore diameter of the two membranes have a small difference of 5.8% while the difference of their water vapour permeation coefficient is about 28%.

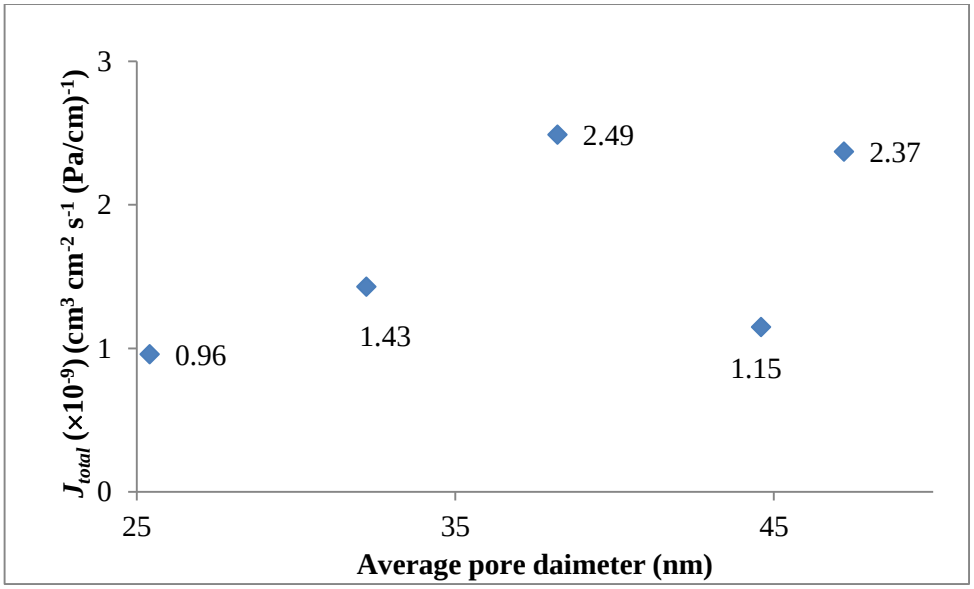

Figure 7.19 Water vapour permeability coefficient (J_{total}) at 40°C vs their average pore diameters of the heat-pressed NIPAAM-g-PVDF membranes

It is found in Figure 7.19 that there is a moderate correlation between the water vapour permeation coefficient of the copolymer membranes at 40°C and their average pore diameters as a whole ($R^2 = 0.2875$). However, when considering the membranes made from thermally induced method (A1, A2, and A3), the membrane having the greatest average pore diameter (38.2 nm) has the greatest J_{total} (2.49×10^{-9} cm^3 cm^{-2} s^{-1} (Pa/cm)$^{-1}$) than the J_{total} (9.6×10^{-10} cm^3 cm^{-2} s^{-1} (Pa/cm)$^{-1}$) of the smallest average pore diameters (25.4 nm). In contrast, the membranes made from plasma method (J1 and J2), the membranes having greater average pore diameters (47.2 nm) has greater J_{total} (2.37×10^{-9} cm^3 cm^{-2} s^{-1} (Pa/cm)$^{-1}$) and the membrane having the smaller average pore diameter (44.6 nm) has higher J_{total} (1.15×10^{-9} cm^3 cm^{-2} s^{-1} (Pa/cm)$^{-1}$). These two membranes have a small difference of average pore diameter at 5.8% while their permeation coefficients are massively different at 106%.

Therefore, permeation coefficient at 20°C and 40°C of the heat-pressed NIPAAM-g-PVDF membranes is not influenced by their average pore diameters.

7.2.3.2.3 The influence of membrane porosity on water vapour permeability coefficient

The relationship between the membrane porosity and the water vapour permeation coefficient of the heat-pressed NIPAAM-g-PVDF membranes at 20°C and 40°C (below and above LCST of NIPAAM) is shown in Figure 7.20 and Figure 7.21, respectively.

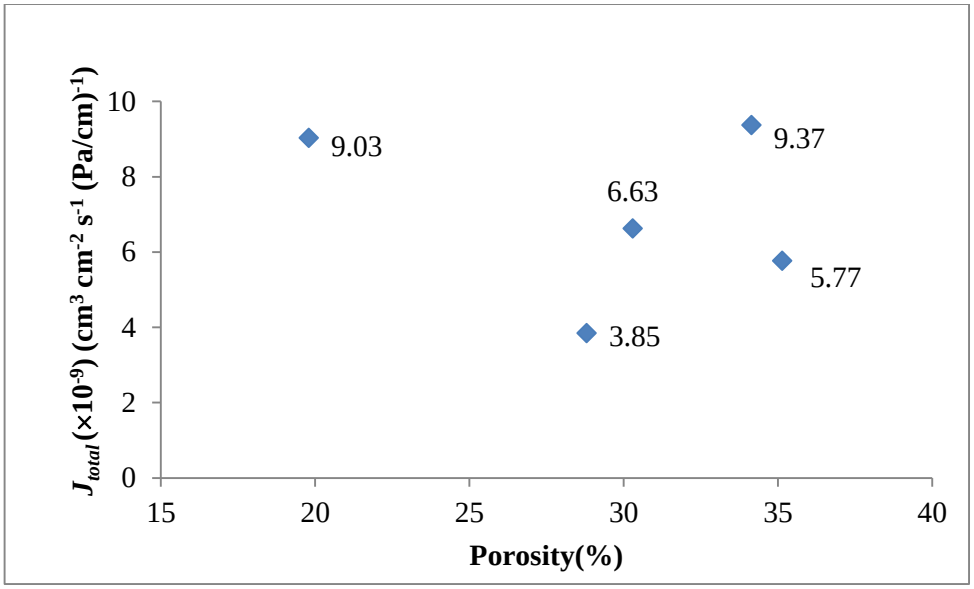

Figure 7.20 Water vapour permeability coefficient (J_{total}) at 20°C vs their porosity of the heat-pressed NIPAAM-g-PVDF membranes

It is found in Figure 7.20 that there is a weak correlation between the water vapour permeation coefficient at 20°C and the porosity as a whole (R^2 = 0.0593). For the three membranes made from thermally induced method (A1, A2, and A3), there is no an apparent trend between the permeation coefficient and the porosity as the membrane having the smallest porosity (19.79%) has greatest J_{total} (9.03×10^{-9} cm^3 cm^{-2} s^{-1} (Pa/cm)$^{-1}$) than the J_{total} (3.85×10^{-9} and 6.63×10^{-9} cm^3 cm^{-2} s^{-1} (Pa/cm)$^{-1}$) of the membrane having the porosity of 28.80% and 30.29%. For the membranes J1 and J2, the membrane having a smaller porosity (34.14%) has the greater J_{total} (9.37×10^{-9} cm^3 cm^{-2} s^{-1} (Pa/cm)$^{-1}$) than that (5.77×10^{-9} cm^3 cm^{-2} s^{-1} (Pa/cm)$^{-1}$) of the membrane having a greater porosity (35.14%). At 20°C, the porosity of the two membranes have a small difference of 2%, while their water vapour permeation coefficient are massively different approximately 58.4%.

Therefore, the water vapour permeation coefficient at 20°C of the heat-pressed NIPAAM-g-PVDF membranes is not influenced by their porosity.

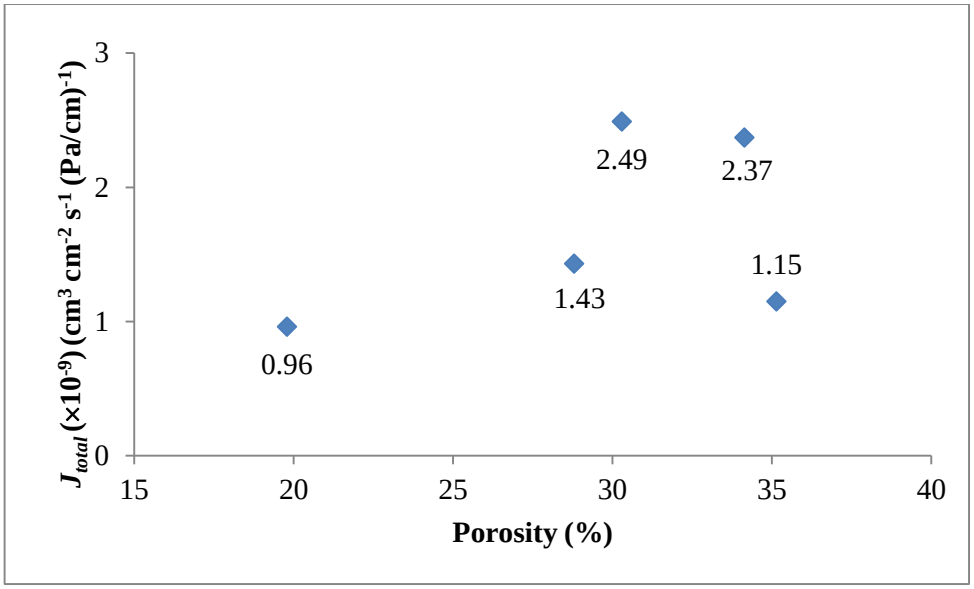

Figure 7.21 Water vapour permeability coefficient (J_{total}) at 40°C vs Porosity of the heat-pressed NIPAAM-g-PVDF membranes

It is found in Figure 7.21 that there is a moderate correlation between the water vapour permeation coefficient of the membranes at 40°C and the porosity as a whole (R^2 =0.2169). However, when considering the membranes made from thermally induced method (A1, A2, and A3), the membrane having the greatest porosity (30.29%) has the greatest J_{total} (2.49×10^{-9} cm^3 cm^{-2} s^{-1} $(Pa/cm)^{-1}$) than the J_{total} (9.6×10^{-10} cm^3 cm^{-2} s^{-1} $(Pa/cm)^{-1}$) of the smallest average pore diameters (19.79%). Also, the membranes made from plasma method (J1 and J2), the membranes having greater porosity (35.14%) has smaller J_{total} (4.03×10^{-9} cm^3 cm^{-2} s^{-1} $(Pa/cm)^{-1}$) and the membrane having the smaller porosity (34.14%) has higher J_{total} (9.28×10^{-9} cm^3 cm^{-2} s^{-1} $(Pa/cm)^{-1}$). At 40°C, the porosity of the two membranes had a small difference of 2%, while their permeation coefficient are massively different approximately 105.5%. Therefore, permeation coefficient at 40°C of the heat-pressed NIPAAM-g-PVDF membranes may be influenced by their porosity.

7.2.3.3 The influence of membrane crystallinity on water vapour permeability coefficient

The relationship between the water vapour permeation coefficient of the heat-pressed NIPAAM-g-PVDF membranes at 20°C and 40°C and their crystallinity are shown in Figure 7.22 and Figure 7.23, respectively.

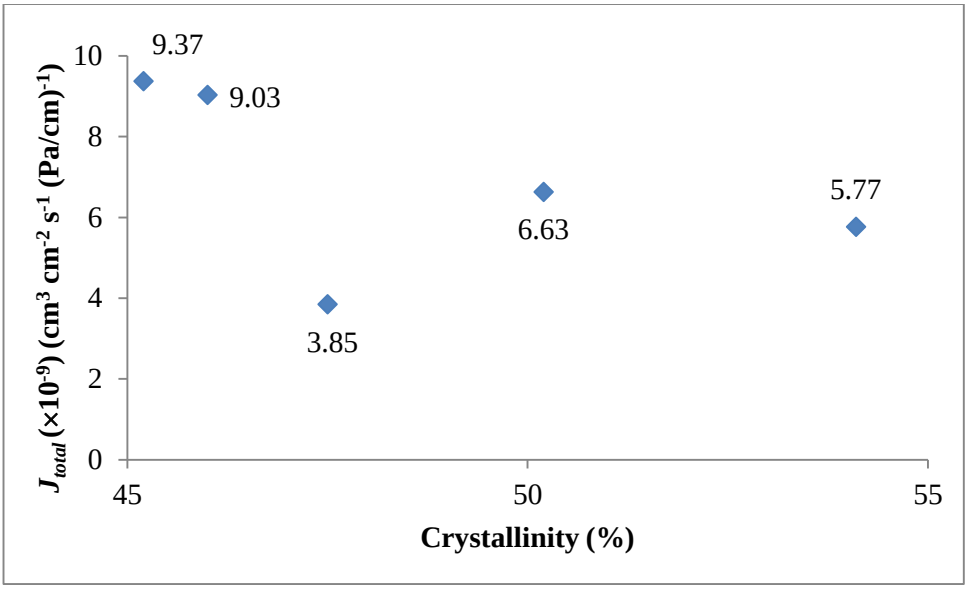

Figure 7.22 Water vapour permeability coefficient (J_{total}) of the heat-pressed NIPAAM-g-PVDF membranes at 20°C vs their crystallinity

It is found in Figure 7.22 that there is a moderate correlation between the permeation coefficient of the membranes at 20°C and crystallinity as a whole (R^2 = 0.2664). For the three membranes made from thermally induced method (A1, A2, and A3), there is no an apparent trend between the water vapour permeation coefficient and the crystallinity as the membrane having the smallest crystallinity (46.0%) has greatest J_{total} (9.03×10-9 cm^3 cm^{-2} s^{-1} (Pa/cm)$^{-1}$) than the J_{total} (3.85×10^{-9} and 6.63×10^{-9} cm^3 cm^{-2} s^{-1} (Pa/cm)$^{-1}$) of the membranes having the crystallinity of 47.5% and 50.2%. For the membranes (J1 and J2) made from plasma grafted method, the membrane having a smaller crystallinity (45.2%) has the greater J_{total} (9.37×10^{-9} cm^3 cm^{-2} s^{-1} (Pa/cm)$^{-1}$) than that (5.77×10^{-9} cm^3 cm^{-2} s^{-1} (Pa/cm)$^{-1}$) of the membrane having a greater crystallinity (54.1%). The crystallinity of the two membranes had a massively difference of 19.7%, while their permeation coefficient are massively different approximately 28%.

Therefore, the permeation coefficient at 20°C of the heat-pressed NIPAAM-g-PVDF membranes is not influenced by the crystallinity.

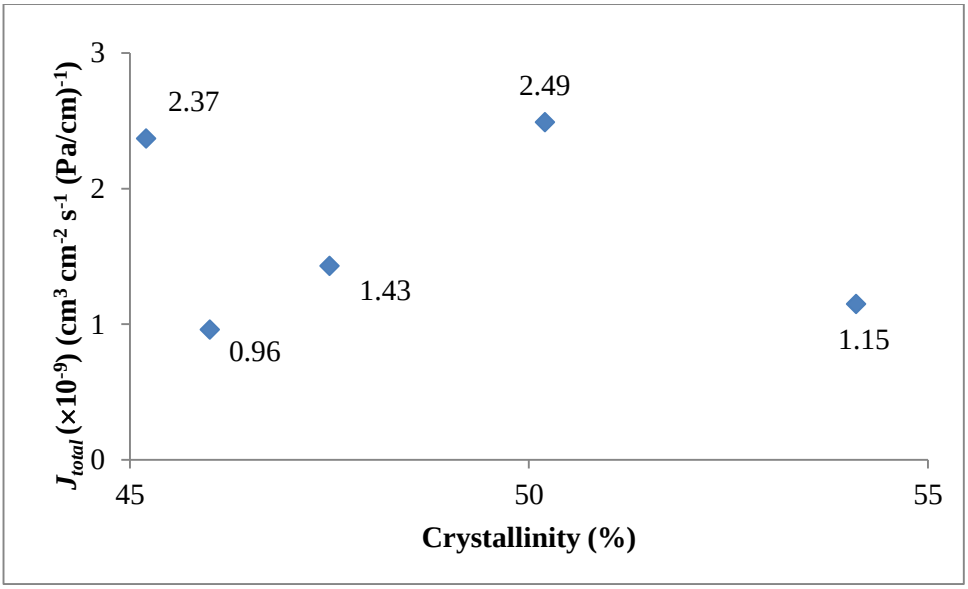

Figure 7.23 Water vapour permeability coefficient (J_{total}) at 40°C vs Crystallinity of the heat-pressed NIPAAM-g-PVDF membranes

However, it is found in Figure 7.23 that there is a weak correlation between the permeation coefficient of the membranes at 40°C and the crystallinity as a whole (R^2 =0.0317). However, when considering the membranes made from thermally induced method (A1, A2, and A3), the membrane having the greatest crystallinity (50.2%) has the greatest J_{total} (2.49×10^{-9} cm^3 cm^{-2} s^{-1} (Pa/cm)$^{-1}$) than the J_{total} (9.6×10^{-10} cm^3 cm^{-2} s^{-1} (Pa/cm)$^{-1}$) of the smallest crystallinity (46.0%). Also, in the membranes made from plasma method (J1 and J2), the membrane having greater crystallinity (54.1%) has smaller J_{total} (1.15×10^{-9} cm^3 cm^{-2} s^{-1} (Pa/cm)$^{-1}$) and the membrane having the smaller porosity (45.2%) has higher J_{total} (2.37×10^{-9} cm^3 cm^{-2} s^{-1} (Pa/cm)$^{-1}$). At 40°C, the crystallinity of the two membranes had a small difference of 19.7%, while their permeation coefficient is massively different approximately 106%.

Therefore, permeation coefficient at 40°C of the heat-pressed NIPAAM-g-PVDF membranes may be influenced by their crystallinity but it might not be a decisive factor.

7.3 Liquid chemical permeation properties of the NIPAAM-g-PVDF copolymer membranes

The dynamic permeation rate of the heat-pressed NIPAAM-g-PVDF membranes is studied using the same method described in the Section 6.3. The steady state permeation rate, corresponding permeation coefficient and the breakthrough time at 1 µg cm^{-2} min^{-1}, of n-hexane through the heat-pressed NIPAAM-g-PVDF membranes

are discussed, and the influences of the structural parameters of the membranes on these permeation properties are investigated.

7.3.1 Dynamic permeation rate and breakthrough time

The dynamic permeation rate of n-hexane permeating through the heat-pressed NIPAAM-g-PVDF membranes is presented in Figure 7.24 and the breakthrough time at the permeation rate of 1 μg cm^{-2} min^{-1} is summarised in Table 7.10.

Table 7.10 Breakthrough time of the heat-pressed NIPAAM-g-PVDF membrane

Membranes	**Breakthrough time at permeation rate of 1 μg cm^{-2} min^{-1} (minutes)**
A1	4
A2	1
A3	56
J1	4
J2	4

It is found in Figure 7.24 that the dynamic rate of the membranes made from different copolymerisation methods varies massively. Among the three heat-pressed NIPAAM-g-PVDF copolymer membranes made from the thermally induced copolymerisation method, the two membranes (A1 and A2) have a greater mass ratio of NIPAAM: PVDF (1:1 and 1:10) exhibit small breakthrough time (approximately 4 minutes and 1 minutes, respectively); while the membrane (A3) containing smaller proportion of NIPAAM components (1:100) has the greatest breakthrough time (about 60 minutes). Therefore, it is apparent that the proportion of NIPAAM in the copolymer membranes significantly affects the breakthrough time.

However, the two heat-pressed NIPAAM-g-PVDF membranes (J1 and J2) made from the plasma induced copolymerisation method have a breakthrough time of 4 minutes, it is noticed that they are also much smaller than the breakthrough time (15 minutes) of the heat-pressed PVDF membrane (see membrane U4 in Section 6.3).

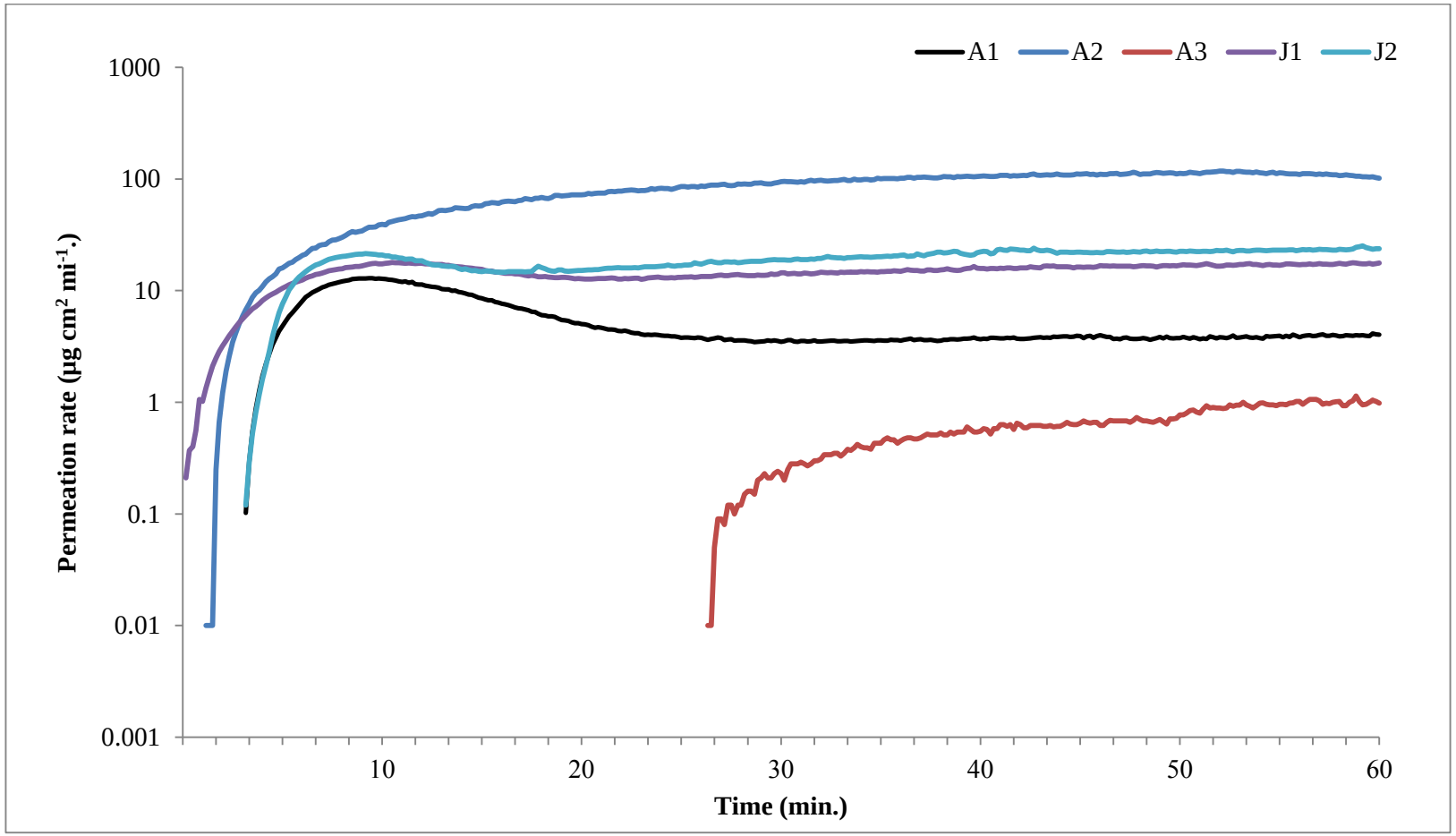

Figure 7.24 The dynamic permeation rate of NIPAAM-g-PVDF copolymer membranes

7.3.2 Permeation coefficient at steady state

Similar to the water vapour permeation coefficient (J_{total}) of the *WVTR* at Section 7.2, based on the volumetric flow rate of n-hexane through a unit cross-section area of the porous membranes ($J_{total\text{-}hexane}$) described by Henry's law in equation (2-6), the permeation coefficient of water vapour through a membrane ($J_{total\text{-}hexane}$) is described in equation (7-3) below (also see equation 2-7);

$$J_{total-hexane} = R_{hexane} \times \frac{L}{\Delta P_{hexane}} \quad (7\text{-}3)$$

where

$J_{total\text{-}hexane}$ is the permeation coefficient of n-hexane permeation through of membrane ($cm^3\ cm^{-2}\ s^{-1}\ (Pa/cm)^{-1}$),

R_{hexane} is the dynamic permeation rate of the membranes ($cm^3\ cm^{-2}\ s^{-1}$),

ΔP_{hexane} is the pressure of n-hexane between two sides of the membrane (Pa); ΔP_{hexane} = 17 kPa at 20°C [224].

However, the dynamic permeation rate at time is calculated based on equation (3-3) as indicated in equation (7-4);

$$R_{hexane} = \frac{\boldsymbol{\varphi_i} \times 10^{-6}}{60 \times \rho_{hexane}} \quad (7\text{-}4)$$

where

φ_i is the dynamic permeation rate at time t_i, ($\mu g\ cm^{-2}\ min^{-1}$) as shown in equation (3-3);

ρ_{hexane} is the density of n-hexane vapour is three times of air at the same temperature; At 20˚C, $\rho_{hexane} = 3 \times 0.0012\ g\ cm^{-3} = 0.0036\ g\ cm^{-3}$ [224].

Based on the dynamic permeation rate of the heat-pressed NIPAAM-g-PVDF membranes shown in Figure 7.24, the steady state permeation rate, the time for permeation rate to reach steady state and the permeation coefficient of n-hexane through the membranes are summarised in Table 7.11.

Table 7.11 Steady state permeation coefficient of the NIPAAM-g-PVDF membranes

Membranes	**Thickness (cm)**	**Steady state permeation rate ($\mu g\ cm^{-2}\ min^{-1}$)**	**Time for permeation rate reaching steady state (minutes)**	**$J_{total\text{-}hexane}$ ($cm^3\ cm^{-2}\ s^{-1}\ (Pa/cm)^{-1}$)**
A1	0.147	13	10	5.20×10^{-10}
A2	0.078	72	20	1.53×10^{-9}
A3	0.092	1	56	2.51×10^{-11}
J1	0.036	17	10	3.29×10^{-10}
J2	0.057	20	10	1.96×10^{-10}

It is found in Table 7.11 that the steady state permeation rate of the heat-pressed NIPAAM-g-PVDF membranes made from the thermally induced copolymerisation method is significantly different. It takes a longer time (56 minutes) for the membrane containing the smallest proportion of NIPAAM component in the membrane to reach its steady state permeation rate, which is also the smallest. Moreover, the steady state permeation rate of the heat-pressed NIPAAM-g-PVDF copolymer membranes produced from the plasma induced copolymerisation method is not significant different (17 minutes and 20 minutes) and they reached the steady state permeation rate in 10 minutes for both of the membrane.

7.3.3 Relationship between breakthrough time and the structure of NIPAAM-g-PVDF copolymer membranes

The influences of three membrane structural parameters related to the liquid permeation through the heat-pressed NIPAAM-g-PVDF membranes: thickness, average pore diameter and total pore volume, on their breakthrough time are discussed below.

7.3.3.1 The influence of membrane thickness on breakthrough time

According to Darcy's law described in equation (3-4), the volumetric flow rate of fluid flow through a unit cross-section area is inversely proportional to the thickness, and the relationship between the breakthrough time and thickness of these copolymer membranes is shown in Figure 7.25.

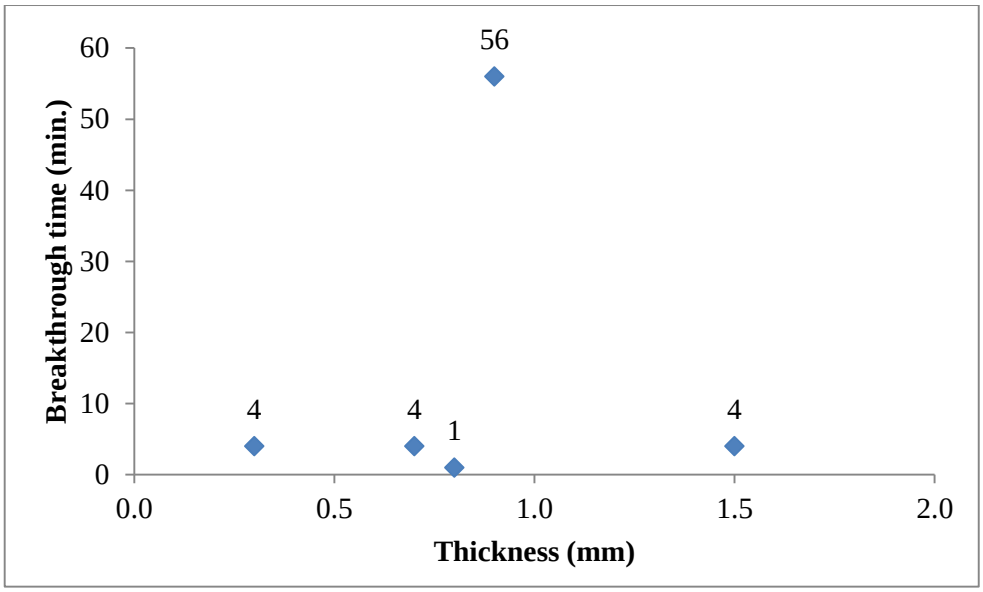

Figure 7.25 Breakthrough time vs thickness

It is found in Figure 7.25 that the thickest heat-pressed NIPAAM-g-PVDF membrane (1.47 mm) which had similar level of breakthrough time (4 minutes) to the thinner membrane (0.3 mm and 0.7 mm). In addition, the two heat-pressed NIPAAM-g-PVDF membranes have similar membrane thickness (0.8 mm) having the smallest and greatest breakthrough time (1 minutes and 56 minutes) respectively. Therefore, we may conclude that the thickness of the heat-pressed NIPAAM-g-PVDF membranes has little effect on their breakthrough time, and it is noted that this conclusion is different from the trend for the heat-pressed PVDF membranes shown in the section 6.3.

7.3.3.2 The influence of porous structure on breakthrough time

In the Section 6.2, it was found that the passage of liquid chemical through the heat-pressed PVDF membranes is related to their porous structure. In this section, the effect of the membrane porous structure on the breakthrough time on the NIPAAM-g-PVDF copolymer membranes are investigated.

7.3.3.2.1 The influence of total pore volume on breakthrough time

The relationship between the breakthrough time and the total pore volume of the heat-pressed copolymer membranes is presented in Figure 7.26.

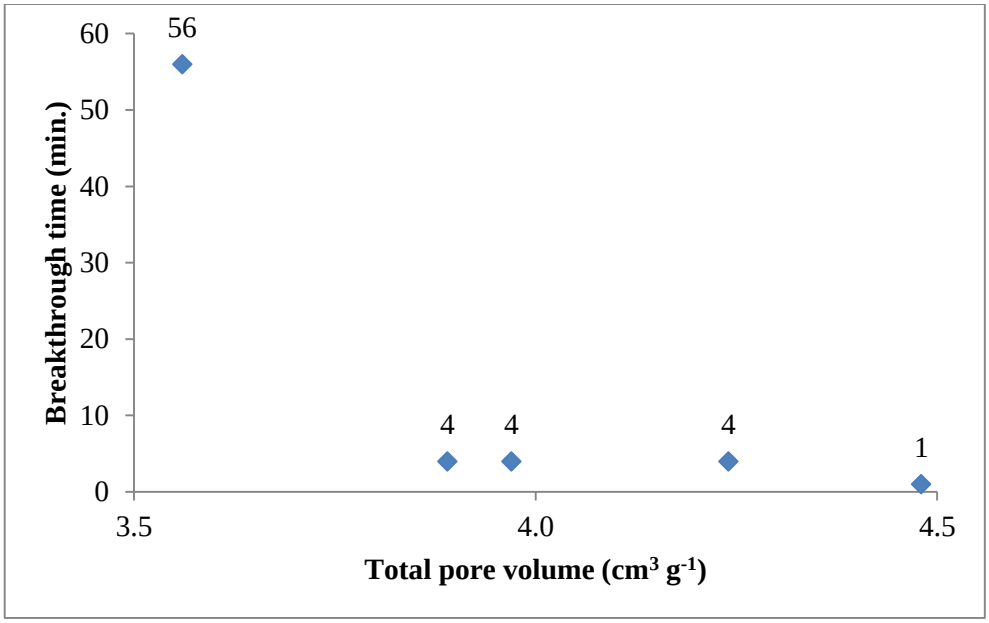

Figure 7.26 Breakthrough time vs Total pore volume of heat- NIPAAM-g-PVDF membranes

It is found in Figure 7.26 that the heat-pressed NIPAAM-g-PVDF copolymer membranes which has smallest total pore volume (3.56 cm^3 g^{-1}) has the greatest breakthrough time (56 minutes), while the membranes having the greatest total pore volume (4.48 cm^3 g^{-1}) has the smallest breakthrough time (1 minute). The other three heat-pressed NIPAAM-g-PVDF membranes having slightly different total pore volume (3.89, 3.97 and 4.24 cm^3 g^{-1}) all have similar level of breakthrough time at 4 minutes. Therefore, the breakthrough time of the heat-pressed NIPAAM-g-PVDF copolymer membrane decreases with the increase of their total pore volume.

7.3.3.2.2 The influence of average pore diameter on breakthrough time

The relationship between the breakthrough time and the average pore diameters of the heat-pressed NIPAAM-g-PVDF membranes is shown in Figure 7.27.

It is found in Figure 7.27 that the heat-pressed NIPAAM-g-PVDF copolymer membrane having the smallest average pore diameter (25.4 nm) shows the greatest breakthrough time (56 minutes) in comparison with that (1 to 4 minutes) of the other four membranes having greater pore diameters (32.2 to 47.2nm). However, there is not a clear relationship between the average pore diameters of the other four heat-pressed NIPAAM-g-PVDF membranes and their breakthrough time. As it was revealed in the Section 6.4 that the combined effect of membrane thickness and the average pore diameter has a clear influence on the breakthrough time of the heat-pressed PVDF membranes, this combined effect of membrane thickness and the

average pore diameter of the NIPAAM-g-PVDF copolymer membranes on their breakthrough time are also thus shown in Figure 7.28.

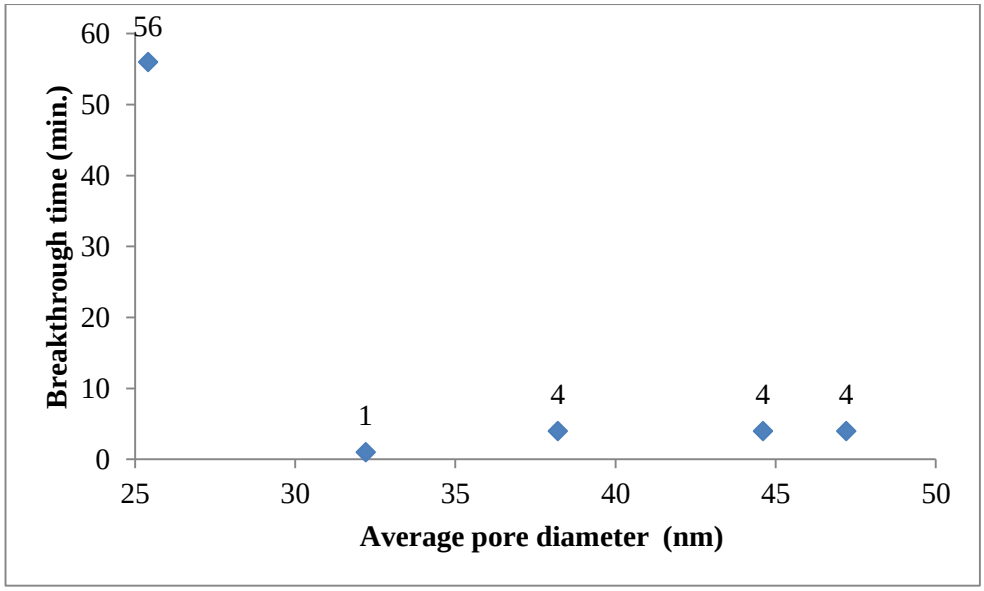

Figure 7.27 Breakthrough time vs Average pore diameter of heat-pressed NIPAAM-g-PVDF membranes

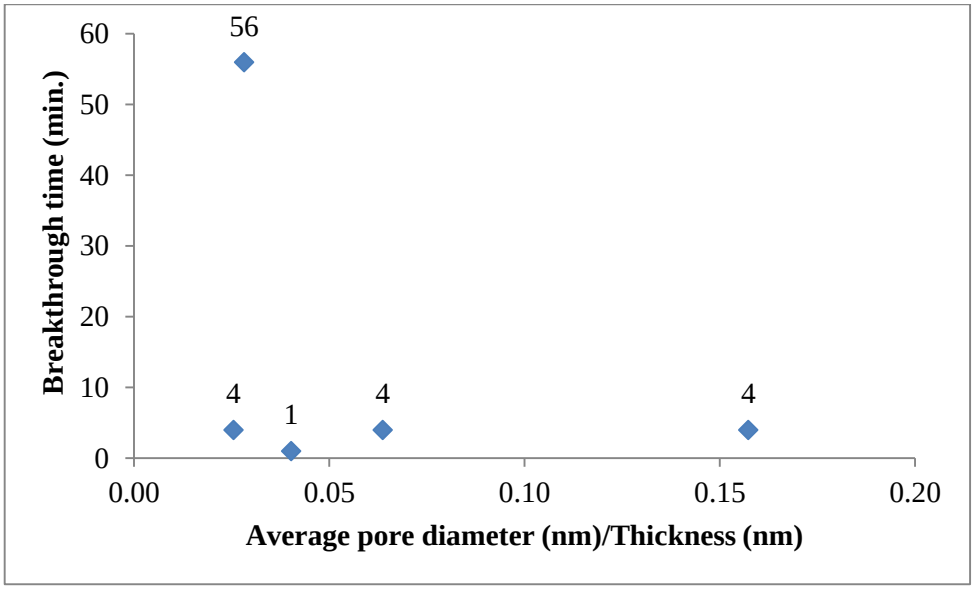

Figure 7.28 Breakthrough time vs Average pore diameters and thickness of heat-pressed NIPAAM-g-PVDF membranes

It is found in Figure 7.28 that, unlike heat-pressed PVDF membrane, there is not a clear trend between the membrane thickness and the average pore diameter for the copolymer membranes.

7.3.3.2.3 The influence of porosity on breakthrough time

The relationship between the breakthrough time and the porosity of the heat-pressed NIPAAM-g-PVDF membranes is shown in Figure 7.29.

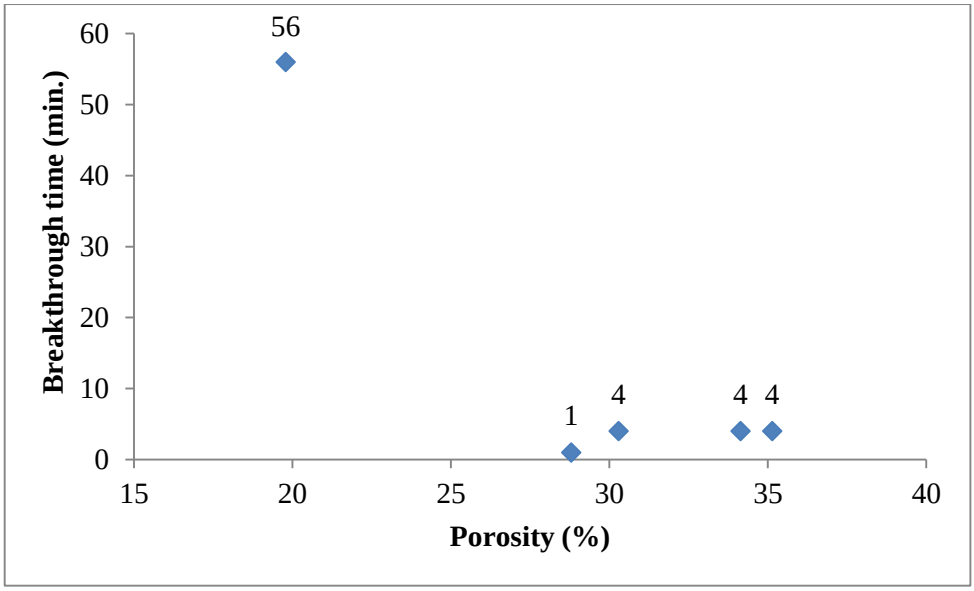

Figure 7.29 Breakthrough time vs Porosity of heat-pressed NIPAAM-g-PVDF membranes

It is shown in Figure 7.29 that the heat-pressed NIPAAM-g-PVDF membrane having the smallest porosity (19.79%) shows the greatest breakthrough time (56 minutes), but it is not a clear trend between the membrane porosity and their breakthrough time (1 to 4 minutes).

7.3.3.3 The influence of membrane crystallinity on breakthrough time

The relationship between the breakthrough time and crystallinity of the heat-pressed NIPAAM-g-PVDF membranes is shown in Figure 7.30.

Again, it is found in Figure 7.30 that heat-pressed NIPAAM-g-PVDF membrane having smaller crystallinity (46%) shows the greatest breakthrough time (56 minutes) while the other four heat-pressed NIPAAM-g-PVDF membranes which have different levels of crystallinity (45.2%, 47.5%, 50.2% and 54.1%) do not show a clear trend. With consideration of the combined effect of membrane thickness and crystallinity on the breakthrough time of the heat-pressed PVDF membranes discussed in the section 6.4, the combined effect of both crystallinity and thickness of the copolymer membranes on their breakthrough time is also shown in Figure 7.31. It is found in the

Figure 7.30 that the combined effect of membrane thickness and crystallinity have no influence on the copolymer membranes.

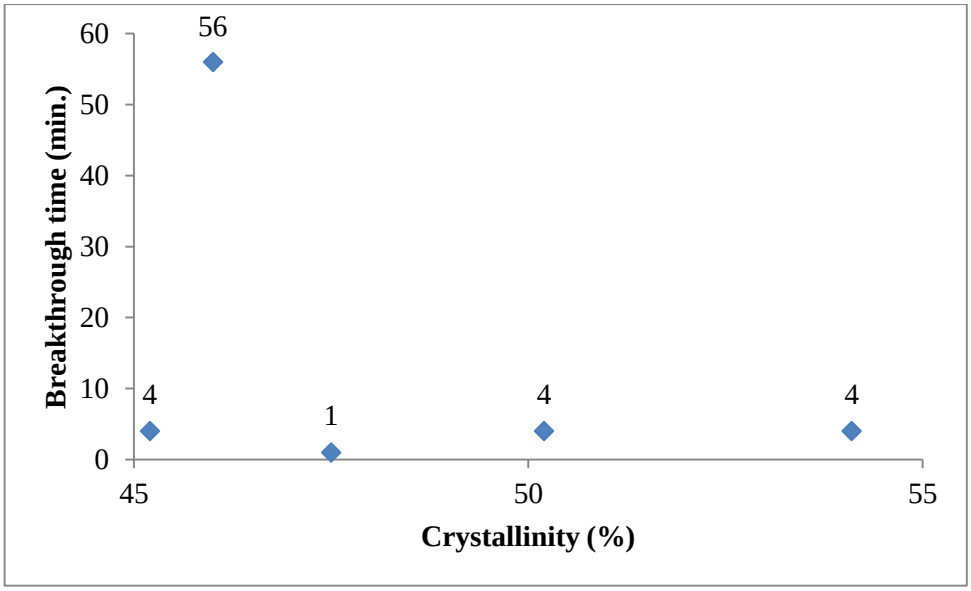

Figure 7.30 Breakthrough time vs Crystallinity of heat-pressed NIPAAM-g-PVDF membranes

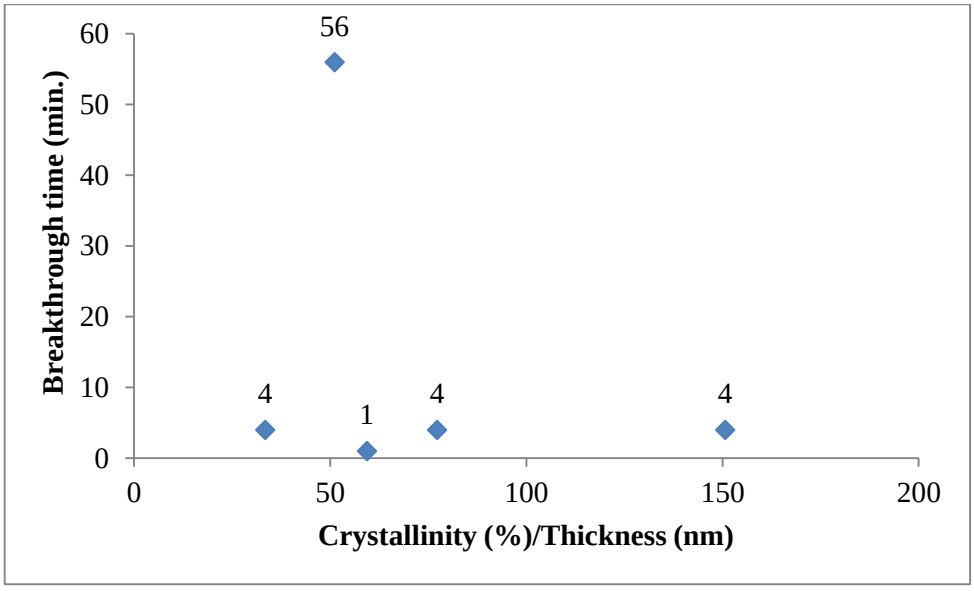

Figure 7.31 Breakthrough time vs Crystallinity and thickness of heat-pressed NIPAAM-g-PVDF membranes

In a summary, it seems that there is not a clear relationship between membrane structural parameters and their breakthrough time for these copolymer membranes. However, it is certain that one of the membranes has the smallest total pore volume, pore diameter and porosity always has the longest breakthrough time. This trend and its causes need further investigation.

7.3.4 Relationship between permeation rate and the structure of NIPAAM-g-PVDF copolymer membranes

Similar to the breakthrough time, the three parameters e.g. the thickness, the porous structure and the crystallinity also influence the liquid permeation rate of the heat-pressed NIPAAM-g-PVDF membranes, as indicated in the Section 7.3.1, so their influences are discussed below.

7.3.4.1 The influence of membrane thickness on steady state permeation rate

As mentioned before, the thickness of the membrane is one of the factors needs to be considered based on Henry's law, the relationship between the permeation rate at the steady state and the membrane thickness is thus shown in Figure 7.32.

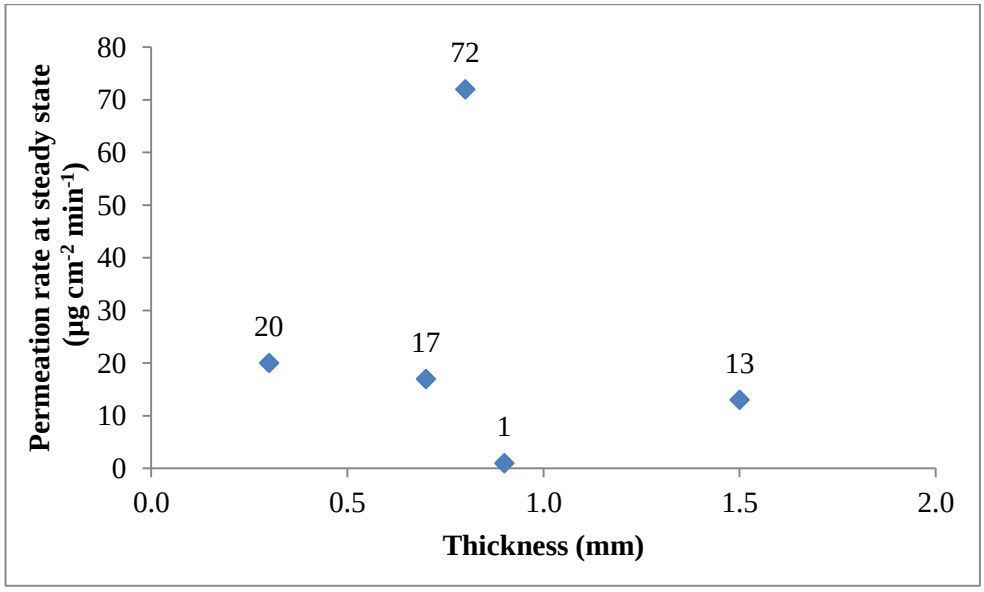

Figure 7.32 Permeation rate at steady state vs Thickness

It is found in Figure 7.32 that, except one membrane (A2) which has the greatest steady state permeation rate (72 μg cm^{-2} min^{-1}), the other four heat-pressed NIPAAM-g-PVDF membranes roughly have a trend that the permeation rate decreases with the increase of the membrane thickness. Also, the thickest membrane (1.5 mm) does show a smaller permeation rate (13 μg cm^{-2} min^{-1}). Therefore, it is concluded that the permeation rate of the heat-pressed NIPAAM-g-PVDF membranes are related to their thickness; so it is also necessary to examine the combined effect of the membrane thickness and other structure parameters on the permeation rate (2-7).

7.3.4.2 The influence of porous structures on steady state permeation rate

The relationships between the permeation rate at the steady state and the porous structural parameters of the heat-pressed NIPAAM-g-PVDF membranes e.g. total pore volume, average pore diameter and porosity are discussed below.

7.3.4.2.1 The influence of total pore volume on steady state permeation rate

The relationship between permeation rate and total pore volume of the heat-pressed NIPAAM-g-PVDF membranes is shown in Figure 7.33.

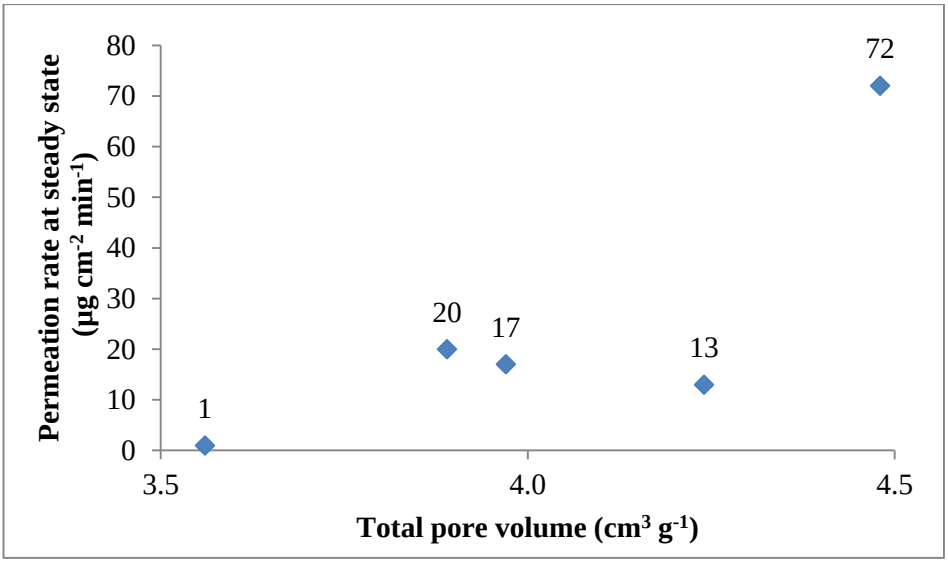

Figure 7.33 Permeation rate at steady state vs Total pore volume of heat-pressed NIPAAM-g-PVDF membranes

It is found in Figure 7.33 that the heat-pressed NIPAAM-g-PVDF membrane which has smallest total pore volume (3.56 $cm^3\ g^{-1}$) has the smallest permeation rate at steady state at 1 µg $cm^{-2}\ min^{-1}$ while the membrane having the greatest total pore volume (4.48 $cm^3\ g^{-1}$) has the greatest permeation rate at 72 µg $cm^{-2}\ min^{-1}$. The other three heat-pressed NIPAAM-g-PVDF membranes having slightly different total pore volumes (3.89, 3.97 and 4.24 $cm^3\ g^{-1}$) all have different level of permeation rate at 20, 17 and 13 minutes, respectively. Therefore, the permeation rate of the heat-pressed NIPAAM-g-PVDF copolymer membrane increases with the increase of their total pore volume.

7.3.4.2.2 The influence of average pore diameter on steady state permeation rate

The relationship between the permeation rate and the average pore diameter of the heat-pressed NIPAAM-g-PVDF membranes is indicated in Figure 7.34.

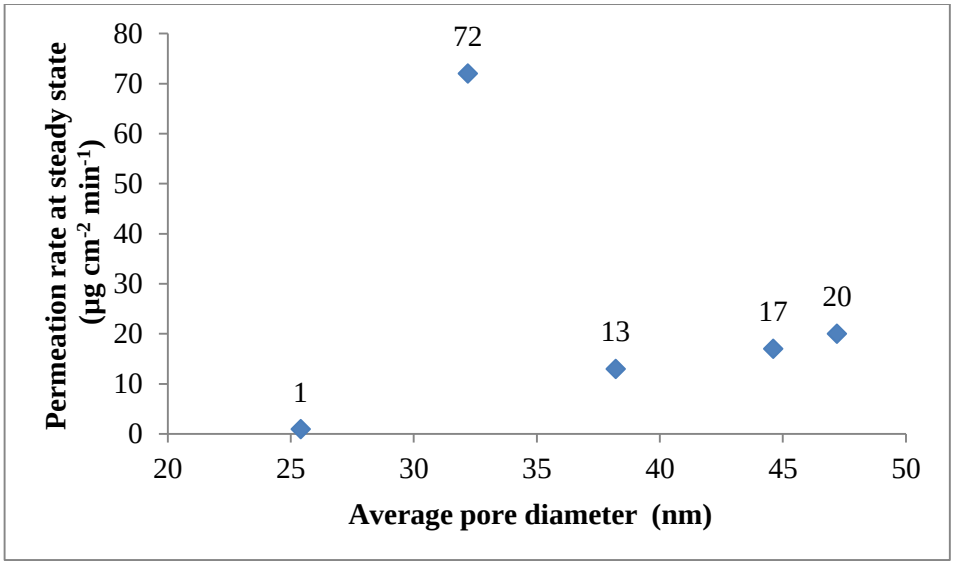

Figure 7.34 Permeation rate at steady state vs Average pore diameters of heat-pressed NIPAAM-g-PVDF membranes

It is found in Figure 7.34 that the heat-pressed NIPAAM-g-PVDF membranes which has smallest average pore diameter (25.4 nm) has the smallest permeation rate at 1 µg cm^{-2} min^{-1}, while the membrane having the greater average pore diameter (32.2 nm) has the greatest permeation rate (72 minute). However, the other three membranes have slightly different average pore diameters (38.2 nm, 44.6 and 47.2 nm) show an increasing trend between their average pore diameters and permeation rates (13 to 20 minutes).

Moreover, the combined effect of membrane thickness and the average pore diameters has a clear influence on the breakthrough time of the heat-pressed PVDF membranes as indicated in Section 6.4. It is thus the combined effect of membrane thickness and the average pore diameter of the copolymer membranes on their permeation rate are indicated in Figure 7.35.

It is found in the Figure 7.35 that, unlike heat-pressed PVDF membrane, there is not a clear trend between the membrane thickness and the average pore diameters to the permeation rate for the copolymer NIPAAM-g-PVDF membranes.

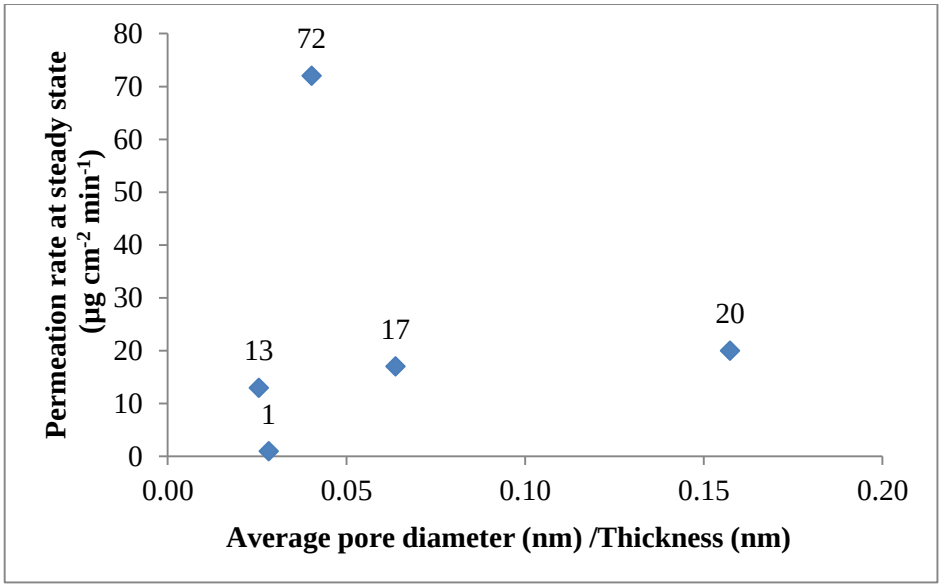

Figure 7.35 Permeation rate at steady state vs Average pore diameters and thickness of heat-pressed NIPAAM-g-PVDF membranes

7.3.4.2.3 The influence of porosity on steady state permeation rate

The relationship between the permeation rate and the porosity of the heat-pressed NIPAAM-g-PVDF membranes is indicated in Figure 7.36.

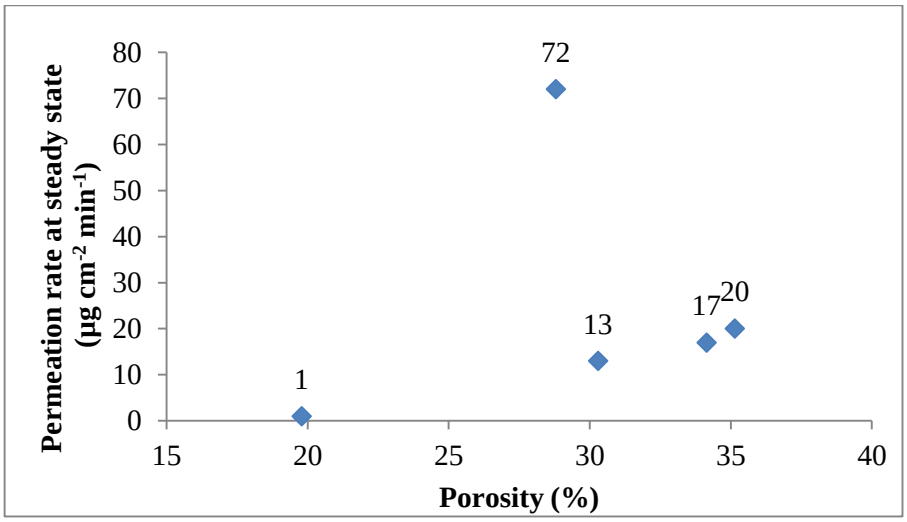

Figure 7.36 Permeation rate at steady state vs Porosity of heat-pressed NIPAAM-g-PVDF membranes

It is found in Figure 7.36 that the heat-pressed NIPAAM-g-PVDF membranes which has smallest porosity (19.79%) has the smallest permeation rate at 1 µg cm^{-2} min^{-1}, while the membrane having the greater porosity (28.8%) has the greatest permeation rate (72 minute). However, the other three membranes have slightly different average

pore diameters (30.29%, 34.14% and 35.14%) show an increasing trend between their average pore diameters and permeation rates (13 to 20 minutes).

7.3.4.3 The influence of membrane crystallinity on steady state permeation rate

The relationship between the permeation rate and the crystallinity of the heat-pressed NIPAAM-g-PVDF membranes is shown in Figure 7.37.

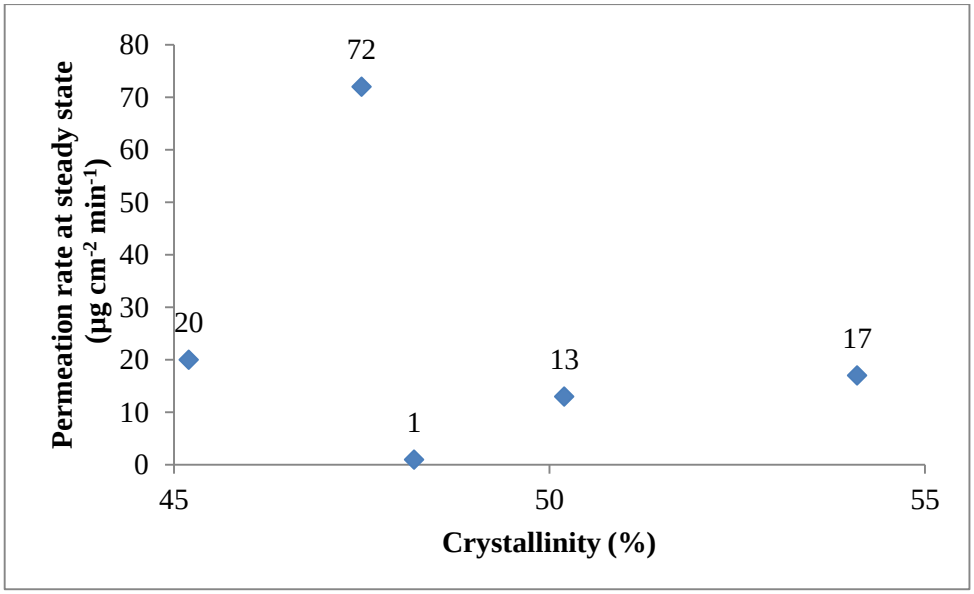

Figure 7.37 Permeation rate at steady state vs Crystallinity

It is found in Figure 7.37 that the membrane having smaller crystallinity (46%) has the greatest permeation rate at 72 μg cm^{-2} min^{-1}. which has smallest porosity (19.79%) has the smallest permeation rate at 1 μg cm^{-2} min^{-1}, while the other four membranes roughly have a trend that the permeation rate decreases with the increases of the crystallinity. Therefore, it is concluded that the permeation rate of the heat-pressed NIPAAM-g-PVDF membranes are not related to their crystallinity; so it is also necessary to examine the combined effect of the crystallinity and other structure parameters on the permeation rate (2-7) such as thickness as indicated in Figure 7.38.

It is found in Figure 7.38 that there is not a clear trend between the membrane thickness and their crystallinity to the permeation rate for the copolymer NIPAAM-g-PVDF membranes.

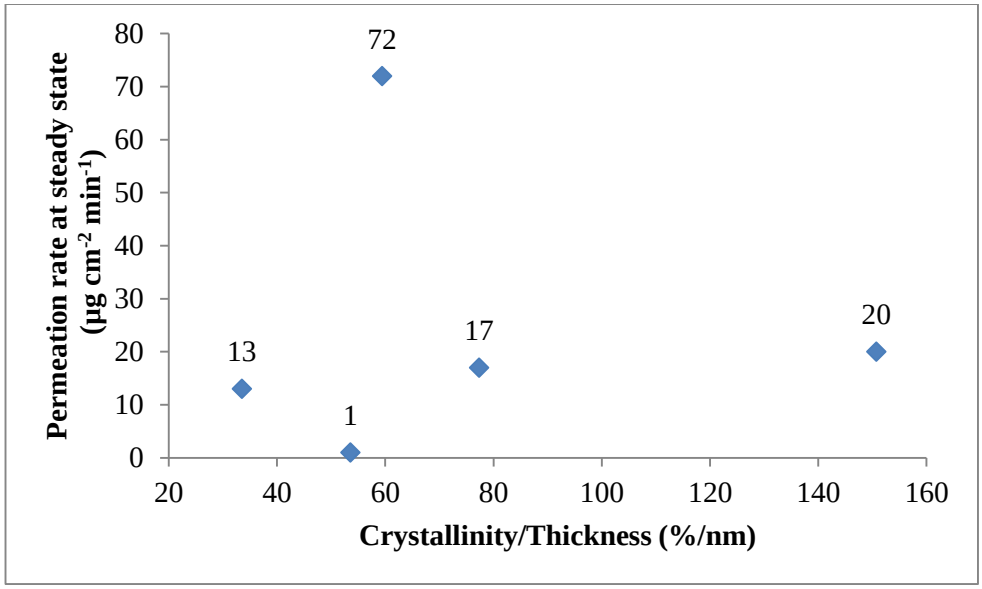

Figure 7.38 Permeation rate at steady state vs Crystallinity of heat-pressed NIPAAM-g-PVDF membranes

In a summary, it seems that there is not a clear relationship between membrane structural parameters and their permeation rate for these copolymer membranes. However, it is certain that one of the membranes has the smallest total pore volume, pore diameter and porosity always has the smallest permeation rate. This trend and its causes need further investigation.

7.4 Mechanisms of water vapour and liquid chemicals permeation through NIPAAM-g-PVDF copolymer membranes

As discussed in Section 7.3, there were three liquid transmission mechanisms which were involved in liquid chemical permeation through the resultant nanoporous membranes: the fluid permeation through both the PVDF and the NIPAAM components of the NIPAAM-g-PVDF membranes, and the fluids flow through the porous structure of the membranes. The solution-diffusion model uses to describe the total water vapour permeation coefficient, J_{total}, ($cm^3\ cm^{-2}\ s^{-1}\ (Pa/cm)^{-1}$), defined as the volume of water vapour passing through a unit area of NIPAAM-g-PVDF copolymer per unit time, with a unit pressure gradient across the sample, is shown in equation (7-5) below;

$$J_{total} = J_{PVDF} + J_{Pore} + J_{NIPAAM} \quad (7\text{-}5)$$

where

J_{PVDF} is the water vapour permeability coefficient through the PVDF component ($cm^3\ cm^{-2}\ s^{-1}\ (Pa/cm)^{-1}$),

Jpore is the water vapour permeability coefficient through the pores in the membrane ($cm^3\ cm^{-2}\ s^{-1}\ (Pa/cm)^{-1}$),

J_{NIPAAM} is water vapour permeability coefficient through the NIPAAM component of the membrane ($cm^3\ cm^{-2}\ s^{-1}\ (Pa/cm)^{-1}$).

The water vapour permeability coefficient of the PVDF and NIPAAM components are described by Henry's law shown in equations (7-6) and (7-7), respectively;

$$J_{PVDF} = S_{PVDF} \cdot D_{PVDF} \cdot X \tag{7-6}$$

$$J_{NIPAAM} = S_{NIPAAM} \cdot D_{NIPAAM} \cdot Y \tag{7-7}$$

where

S_{PVDF} is the solubility coefficient of PVDF in water ($cm^3\ cm^{-3}\ Pa^{-1}$) (see the calculation below),

S_{NIPAAM} is the solubility of NIPAAM in water ($cm^3\ cm^{-3}\ Pa^{-1}$),

D_{PVDF} is the diffusivity coefficient of PVDF ($cm^2\ s^{-1}$) in water, which is between $8\sim10\times10^{-6}$ ($cm^2\ s^{-1}$) [225],

D_{NIPAAM} is the diffusivity of NIPAAM in water at 25°C is 3.2×10^{-8} $cm^2\ s^{-1}$ [226] another water diffusion coefficient through NIPAAM = $(2.3\sim3.6)\times10^{-7}$ $cm^2\ s^{-1}$ [227],

X and Y are the proportions of PVDF and NIPAAM in NIPAAM-g-PVDF membrane (%) respectively, and X+Y=100%.

Also, the water permeability of PVDF membrane (P_{PVDF}) at 23°C and 38°C of Solef® PVDF 1010 is 0.2 and 0.6 g mm m^{-2} $24h^{-1}$, respectively [228]. They are used to represent the water vapour permeability of PVDF membrane (P_{PVDF}) at 20°C and 40°C respectively. It is noted that the water vapour pressure difference across the membrane at 20°C and 40°C is 8.15×10^2 Pa and 2.58×10^3 Pa, respectively [224]. Therefore, the water vapour permeability coefficients of PVDF membrane (J_{PVDF}) at 20°C and 40°C are obtained according to equation 7.2.

At 20°C;

$$J_{PVDF} = 0.2 \times \frac{1}{24\times3600\times10^6\times1.73\times10^{-5}} \times \frac{0.1}{8.15\times10^2}$$

$$= 1.64\times10^{-11}(cm^3cm^{-2}s^{-1}\ (Pa/cm)^{-1}).$$

At 40°C;

$$J_{PVDF} = 0.6 \times \frac{1}{24 \times 3600 \times 10^6 \times 5.12 \times 10^{-5}} \times \frac{0.1}{2.28 \times 10^3}$$
$$= 5.95 \times 10^{-12} \text{ (cm}^3\text{cm}^{-2}\text{s}^{-1}\text{ (Pa/cm)}^{-1}\text{).}$$

It is also noted that, the diffusion coefficient of water at 20°C is 8.71×10^{-9} cm^2 s^{-1} [229],[230]. Thus, its solubility coefficients (S_{PVDF}) at 20°C and 40°C is shown below,

At 20°C;

$S_{PVDF} = \frac{J_{PVDF}}{D_{PVDF}} = \frac{1.64 \times 10^{-11}}{8.71 \times 10^{-9}} = 1.88 \times 10^{-4}$ cm^3 cm^{-3} Pa^{-1}, and

at 40°C;

$S_{PVDF} = \frac{J_{PVDF}}{D_{PVDF}} = \frac{5.95 \times 10^{-12}}{8.71 \times 10^{-9}} = 6.77 \times 10^{-5}$ cm^3 cm^{-3} Pa^{-1}, respectively.

The effect of temperature on the diffusivity of fluid through the nanopores of NIPAAM-g-PVDF copolymer membranes can be described by using the concept of effective diffusion coefficient in a 'hindered diffusion' model (see equation 7-8), it explains the contribution of partial unblocking on increased diffusivity [231]. The effective diffusion coefficient (D_{eff}) is determined by two major factors: the steric restriction resulted from the pore blocking and the interaction between the wall surface of pore and the fluid;

$$D_{eff} = \frac{\Phi D_\infty}{K} \quad (7\text{-}8)$$

where

K is a hydrodynamic factor due to the surface interaction between the pore wall and the fluid,

D_∞ is the bulk diffusivity of the fluid depending on the temperature,

Φ is the partition coefficient caused by steric restriction, and Φ is the production of membrane porosity (ε) and available area in a pore (φ), where $\varphi = (1-\lambda)^2$ and λ is the ratio of the diameters of the fluid molecules to the diameter of the pores. The diameter of solute is 2.75 Å. The diameter of pores in the NIPAAM-g-PVDF membrane is measured by using porosimetry, it is usually smaller at a temperature lower than LCST (e.g. 20°C) than that at a temperature higher than LCST (e.g., 40°C).

Therefore, from equation (7-5), it is written the total permeation of water vapour transport through membrane as equation (7-9).

$$J_{total} = (S_{PVDF} \cdot D_{PVDF} \cdot X) + (\frac{J_{Pore}}{\Delta P_{wv}} \cdot L) + (S_{NIPAAM} \cdot D_{NIPAAM} \cdot Y) \quad (7\text{-}9)$$

From equation (7-9), the water vapour permeability coefficient of the heat-pressed pristine PVDF membrane and the NIPAAM-g-PVDF membranes at 20°C and at 40°C is calculated as shown Table 7.12 and Table 7.13, respectively. Moreover, the percentage of the combined water permeability coefficient through the pores in the membrane and the water permeability coefficient through the NIPAAM component ($Q_{J_{NIPAAM}+J_{total}}$ contributed to the water vapour permeability coefficient of the PVDF and NIPAAM-g-PVDF membrane is also calculated using equation (7-10) below;

$$Q_{J_{NIPAAM}+J_{total}} = \frac{J_{NIPAAM}+J_{Pore}}{J_{total}} \times 100\% \quad (7\text{-}10)$$

The ratio of the total of water vapour permeability through the membrane between 20°C and 40°C ($R_{J_{total}}$) are calculated in equation (7-11) and results are shown in Table 7.14.

$$R_{J_{total}} = \frac{J_{total}\ at\ 20\ ^{\circ}C}{J_{total} at\ 40\ ^{\circ}C} \quad (7\text{-}11)$$

Additionally, the water vapour permeability coefficient through the pores and the NIPAAM components of the membranes, ($J_{NIPAAM}+J_{pore}$) between 20°C and 40°C ($R_{J_{NIPAAM}+J_{Pore}}$) is calculated in equation (7-12) and shown in Table 7.14.

$$R_{J_{NIPAAM}+J_{Pore}} = \frac{J_{NIPAAM}+J_{pore}\ at\ 20\ ^{\circ}C}{J_{NIPAAM}+J_{pore} at\ 40\ ^{\circ}C} \quad (7\text{-}12)$$

Table 7.12 Water vapour permeability coefficient at 20°C of the nanoporous PVDF and NIPAAM-g-PVDF membranes

Membranes	J_{total} **(cm^3 cm^{-2} s^{-1} (Pa/cm)$^{-1}$)**	X **(%)**	Y **(%)**	J_{PVDF} **(cm^3 cm^{-2} s^{-1} (Pa/cm)$^{-1}$)**	$J_{NIPAAM}+ J_{pore}$ **(cm^3 cm^{-2} s^{-1} (Pa/cm)$^{-1}$)**	$Q_{J_{NIPAAM}+J_{total}}$ **(%)**
A1	6.63×10^{-9}	85.45	14.55	1.19×10^{-10}	6.51×10^{-9}	98.2
A2	3.85×10^{-9}	94.00	6.00	1.31×10^{-10}	3.71×10^{-9}	96.6
A3	9.03×10^{-9}	98.95	1.05	1.38×10^{-10}	8.90×10^{-9}	98.5
J1	9.37×10^{-9}	99.85	0.15	1.39×10^{-10}	9.23×10^{-9}	98.5
J2	5.77×10^{-9}	99.93	0.07	1.39×10^{-10}	5.63×10^{-9}	97.6
U3	2.95×10^{-9}	100.00	0.00	1.39×10^{-10}	2.81×10^{-9}	95.3

Where

J_{total} are obtained from Table 7.9

J_{PVDF} = 1.64×10^{-11} (cm^3 cm^{-2} s^{-1} (Pa/cm)$^{-1}$) at 20°C (see Page 226)

Y and X is the estimated proportion of NIPAAM (wt%) and PVDF (wt%) in the resultant NIPAAM-g-PVDF copolymer membrane, respectively, as shown in Table 7.3 and X=100 – Y (wt%)

$J_{NIPAAM} + J_{pore} = J_{total} - (J_{PVDF}\times X)$

Table 7.13 Water vapour permeability coefficient at 40°C of the nanoporous PVDF membrane and NIPAAM-g-PVDF membranes

Membranes	J_{total} **(cm^3 cm^{-2} s^{-1} (Pa/cm)$^{-1}$)**	X **(%)**	Y **(%)**	J_{PVDF} **(cm^3 cm^{-2} s^{-1} (Pa/cm)$^{-1}$)**	$J_{NIPAAM}+J_{pore}$ **(cm^3 cm^{-2} s^{-1} (Pa/cm)$^{-1}$)**	$Q_{J_{NIPAAM}+J_{total}}$ **(%)**
A1	2.49×10^{-9}	85.45	14.55	5.04×10^{-11}	2.44×10^{-9}	98.0
A2	1.43×10^{-9}	94.00	6.00	5.54×10^{-11}	1.37×10^{-9}	96.1
A3	9.56×10^{-10}	98.95	1.05	5.83×10^{-11}	8.98×10^{-10}	93.9
J1	2.37×10^{-9}	99.85	0.15	5.89×10^{-11}	2.31×10^{-9}	97.5
J2	1.15×10^{-9}	99.93	0.07	5.89×10^{-11}	1.09×10^{-9}	94.9
U3	6.74×10^{-10}	100.00	0.00	5.90×10^{-11}	6.15×10^{-10}	91.2

Where

J_{total} are obtained from Table 7.9

$J_{PVDF} = 5.95\times10^{-12}$ cm^3 cm^{-3} Pa^{-1} at 40°C (see Page 227)

Y and X is the estimated proportion of NIPAAM (wt%) and PVDF (wt%) in the resultant NIPAAM-g-PVDF copolymer membrane, respectively, as shown in Table 7.3 and $X=100-Y$ (wt%)

$J_{NIPAAM} + J_{pore} = J_{total} - (J_{PVDF}\times X)$

Table 7.14 Ratio of J_{NIPAAM} + J_{pore} and J_{total} between 20°C and 40 °C

Samples	J_{total} **($cm^3\ cm^{-2}\ s^{-1}\ (Pa/cm)^{-1}$)**		$R_{J_{total}}$	$J_{NIPAAM} + J_{pore}$ **($cm^3\ cm^{-2}\ s^{-1}\ (Pa/cm)^{-1}$)**		$R_{J_{NIPAAM}+J_{Pore}}$
	20°C	40°C		20°C	40°C	
A1	6.63×10^{-9}	2.49×10^{-9}	2.7	6.51×10^{-9}	2.44×10^{-9}	2.7
A2	3.85×10^{-9}	1.43×10^{-9}	2.7	3.71×10^{-9}	1.37×10^{-9}	2.7
A3	8.90×10^{-9}	8.98×10^{-10}	9.9	8.90×10^{-9}	8.98×10^{-10}	9.9
J1	9.37×10^{-9}	2.37×10^{-9}	4.0	9.23×10^{-9}	2.31×10^{-9}	4.0
J2	5.77×10^{-9}	1.15×10^{-9}	5.0	5.63×10^{-9}	1.09×10^{-9}	5.2
U3	2.95×10^{-9}	6.74×10^{-10}	4.4	2.81×10^{-9}	6.15×10^{-10}	4.6

It is found in Table 7.12, Table 7.13 and Table 7.14 that the water vapour permeability coefficients of the PVDF membrane and NIPAAM-g-PVDF membranes are temperature independent. The water vapour permeability coefficient of both PVDF membrane and NIPAAM-g-PVDF at 20°C is much greater than that at 40°C. NIPAAM is hydrophilic at 20°C which is below its LCST of NIPAAM (i.e., 30°C). Its molecular chains are bonded with the molecules of water vapour and allow it permeates through the NIPAAM-g-PVDF structure easier. At temperature 40°C, which above the LCST of NIPAAM, NIPAAM exhibits a hydrophobic and shrunken state above its LCST [154], the NIPAAM side chains on the membrane surface (including the surfaces of the pores) is hydrophobic and these membranes exhibit the same water vapour permeation behaviour as the hydrophobic membrane [152], [153]. Therefore, water vapour permeability coefficients of the NIPAAM-g-PVDF membrane, J_{NIPAAM} +J_{pore} and J_{total} at 40°C are smaller than that at 20 °C.

It is also found in Table 7.14 that the ratio of the water vapour permeability coefficients at 20°C and 40°C vary with the proportion of the NIPAAM in the copolymer membranes. This indicates that there are different mechanisms of water vapour permeation through the copolymers containing different proportion of NIPAAM components. The ratio of J_{total} between 20°C and 40°C, $R_{J_{total}}$, for both PVDF membrane (U4) and the NIPAAM-g-PVDF membranes containing a small proportion of NIPAAM components (A3, J1 and J2) is much greater (around 4.0~9.9) than that of the NIPAAM-g-PVDF membranes containing greater proportion of NIPAAM components (A1 and A2) (about 2.7).

As water vapour hardly permeates through PVDF polymers, it is believed that water vapour permeability coefficient of pure PVDF membrane (U4), which does not contain any NIPAAM, is mainly due to water vapour permeates through the pores of the porous membrane (4.7% at 20°C and 8.8% at 40°C). However, NIPAAM-g-PVDF copolymer membranes (A1, A2, A3, J1 and J2), the water vapour permeates through the membranes not only via the pores but also through the NIPAAM components. Therefore, membranes containing greater proportion of NIPAAM allow water vapour through the smart pores formed between PVDF and NIPAAM which changes significantly with environmental temperature and this leads to a relative greater J_{total} at 40°C; while the pores of the membranes containing no or little NIPAAM components does not have such properties.

It is found that the water vapour permeability coefficient of both NIPAAM component and pores in the copolymer membranes contribute to the total water vapour permeability coefficient, J_{total}, up to 98.5% at 20°C and up to 98.0% at 40°C.

Moreover, the water vapour permeability coefficients through the pores and NIPAAM components of the NIPAAM-g-PVDF membranes, (J_{NIPAAM} + J_{pore}), at 20°C and 40°C as shown in Table 7.14 have similar trends to J_{total}. The ratio of $R_{J_{NIPAAM}+J_{Pore}}$ for both PVDF membrane (U4) and the NIPAAM-g-PVDF membranes containing a small proportion of NIPAAM components (A3, J1 and J2) is much greater (around 4.0-9.9) than that of the NIPAAM-g-PVDF membranes containing greater proportion of NIPAAM components (A1 and A2) (about 2.7).

It is thus concluded that water vapour permeability coefficient is influenced by both NIPAAM and the porous structure of the copolymer membrane.

Similar to water vapour permeate through the copolymer membranes, the mechanism of liquid chemicals permeation of n-hexane through NIPAAM-g-PVDF membrane, equation (7-7) can be applied with changes of some parameters, as shown in equation (7-13);

$$J_{total-hexane} = (S_{PVDF-hexane} \cdot D_{PVDF-hexane} \cdot X) + (\frac{J_{Pore}}{\Delta P_{hexane}} \cdot L) + (S_{NIPAAM-hexane} \cdot D_{NIPAAM-hexane} \cdot Y) \quad (7\text{-}13)$$

where

$J_{total\text{-}hexane}$ is the total permeation of n-hexane transport through the membrane ($cm^3\ cm^{-2}\ s^{-1}\ (Pa/cm)^{-1}$),

$S_{PVDF\text{-}hexane}$ is the solubility of PVDF in hexane ($cm^3\ cm^{-3}\ Pa^{-1}$),

$D_{PVDF\text{-}hexane}$ is the diffusivity of PVDF in hexane ($cm^2\ s^{-1}$),

$S_{NIAAM\text{-}hexane}$ is the solubility of NIPAAM in n-hexane at 25°C ($cm^3\ cm^{-3}\ Pa^{-1}$),

$D_{NIPAAM\text{-}hexane}$ is the diffusivity of NIPAAM in n-hexane ($cm^2\ s^{-1}$).

It was reported that permeability flux of n-hexane permeation through PVDF membrane at the temperature of around 50-60°C was 0.01-0.03 g mm m^{-2} $24h^{-1}$ [227]. There is no data reported for the permeability of n-hexane permeation through the PVDF membranes at 20°C.

We do not have any data for n-hexane permeation through NIPAAM component ($J_{NIPAAM\text{-}hexane}$) except it is known that the permeation coefficient of methanol through NIPAAM [222] at 21°C is between 1.8×10^{-5} and 3.9×10^{-5} $cm^2\ s^{-1}$. Therefore, it is assumed that the diffusion coefficient of n-hexane through NIPAAM at 21°C is at 1.8×10^{-5} $cm^2\ s^{-1}$ [223]. Based on the report that NIPAAM is insoluble in n-hexane [233], it is assumed that $S_{NIAAM\text{-}hexane}$ is negligible. Therefore, the permeability of n-

hexane through NIPAAM component (J_{NIPAAM}) is also negligible, and we assume that the permeability of n-hexane through a NIPAAM-g-PVDF copolymer membrane depends mainly on the permeability through the pores as shown in equation (7-14).

$$J_{Htotal} = \frac{J_{HPore}}{\Delta P_{hexane}} \cdot L \quad (7\text{-}14)$$

Therefore, the mechanism of the water vapour permeation and liquid chemicals permeation through NIPAAM-g-PVDF copolymer membranes mainly depends on the porous structure of the NIPAAM-g-PVDF membrane, while it is noticed that the pore structures of the copolymer membranes changes with the environmental temperatures.

7.5 Conclusions

The water vapour transmission properties of heat pressed NIPAAM-g-PVDF membranes is investigated. It is found that the water vapour permeability coefficient through the membrane at both 20°C and 40°C are influenced by the membrane thickness, the total pore volume and the porosity of the membranes. Moreover, both breakthrough time and the permeation rate of the heat-pressed NIPAAM-g-PVDF membranes are influenced by their thickness and their average pore diameter. An analysis of the mechanism of the total water vapour permeability coefficient and the total of n-hexane permeability coefficient through the heat-pressed NIPAAM-g-PVDF membranes leads to the finding that the proportion of NIPAAM components in the copolymer membranes and their porous structures play an important role in the water vapour permeability coefficient, it is believed that the conclusions apply to the case of chemical permeation through the copolymer membranes as well.

Chapter 8 Conclusions and further work

The aim of this research is to develop a smart barrier membrane material to be used as a protection layer in chemical protective clothing to improve the moisture management property of the membrane while maintaining its protection properties. To accomplish the aim of the research, thermosensitive nanoporous NIPAAM-g-PVDF membranes produced using two different methods are investigated. The influence of the nanoporous membrane structure on both the water vapour transfer and the liquid chemical permeation properties of the produced membranes are studied. The main conclusions drawn from the previous chapters are summarised below and the comments for the future work are proposed.

8.1 Main findings

Based on the objectives of this research, the main findings are summarised below;

1. Thermo-sensitive NIPAAM-g-PVDF copolymers are produced by using two different modified copolymerisation methods in this research, the direct route of thermally induced copolymerisation method in ozone activated PVDF polymers and the modified oxygen plasma induced copolymerisation in porous PVDF membranes. In the modified thermally induced grafted copolymerisation via a direct copolymerisation process, NIPAAM-g-PVDF copolymer materials are obtained by adding NIPAAM monomer solution into ozone activated PVDF solution in NMP. The process makes the drying process of activated PVDF unnecessary. In the modified oxygen plasma induced copolymerisation process, NIPAAM molecules are filled in the macropores and mesopores and grafted on the surface of the plasma treated PVDF porous membrane.

2. Nanoporous NIPAAM-g-PVDF copolymer membranes are produced by using heat-press process. It is evident that the processing time duration, heating temperature and the number of layer of the porous membrane influence the nanoporous structure of the copolymer membranes and liquid chemical permeation properties of the membrane.

3. The thermal sensitive moisture transfer properties of these nanoporous NIPAAM-g-PVDF copolymer membranes as a novel smart barrier material for chemical protective clothing are studied in this research.

4. An analysis of the water vapour permeation coefficient of the NIPAAM-g-PVDF membranes at different temperatures indicates that the proportion of NIPAAM components significantly affects the water vapour permeation coefficients of the copolymer membranes, the copolymer membranes containing greater proportion of NIPAAM components have greater permeation coefficients at 40°C (above LCST of NIPAAM) than that of the copolymer membranes containing smaller proportion of NIPAAM components.at the same temperature. It is believed that the difference of the permeation coefficient for different copolymer membranes is primarily due to the pore sizes formed between NIPAAM and PVDF in the copolymer increases when the environmental temperature is above LCST of NIPAAM. It is also found that the influence of the PVDF components on the total water vapour permeability coefficient of the copolymer membranes is negligible.

5. The water vapour transmission properties of the nanoporous NIPAAM-g-PVDF membranes investigated by using a modified upright cup method based on BS 7209:1990 at both 20°C and 40°C are also influenced by the membrane thickness, the total pore volume, the porosity, and the crystallinity of the membranes in addition to the proportion of NIPAAM components in the copolymer.

6. For a comparison purpose, the mechanism for water vapour permeation through conventional barrier membranes are studied using the same modified upright cup method. It is found that the water vapour flowing through conventional porous barrier membranes obeys Darcy's Law and mainly transports through pores in the membrane. The water vapour transmission rate (*WVTR*) at 40°C is greater than that at 20°C, and the theoretical ratio of volumetric water vapour transmission rate through porous barrier materials between 40°C and 20°C (65%) is 3.16 based on Darcy's law.

7. It was found this ratio of *WVTR* of thin and porous nonwoven fabrics is greater than 3.16, and this indicates that either greater water vapour condensation in the fabric pores at 20°C or additional diffusion mechanism promoting the moisture transfer at 40°C. It is also found that, the ratio of *WVTR* of thick, coated and laminated membranes of the chemical protective clothing was less than 3.16 which is an indication that the water vapour transfer through these types of fabrics might depends on diffusion and permeation process rather than following Darcy's law in macroposous.

8. The liquid chemical permeation properties, e.g. the dynamic permeation rate, breakthrough time and the steady-state permeation rate both commercially barrier fabrics and the new NIPAAM-g-PVDF membranes are studied by using a modified permeation test system based on BS ISO 6529:2013, with using n-hexane as the challenge permeant. Total permeability coefficient of n-hexane through the NIPAAM-g-PVDF copolymer nanoporous membranes is significantly influenced by the porous structure of the membranes.

9. The breakthrough time and steady-state permeation rate of the NIPAAM-g-PVDF copolymer membranes are influenced by their thickness, total pore volume, average pore diameters, and porosity.

10. Fluids (water vapour and liquid chemicals) transport through three different areas of the thermos-sensitive NIPAAM-g-PVDF nanoporous membranes, the pores, crystallised area and amorphous area of NIPAAM-g-PVDF polymers. The NIPAAM polymers grafted on the surface of the copolymers are thermo-sensitive and reacts to the environmental temperature, this leads the sizes and maybe the geometries of the pores formed by the copolymers to be thermos-sensitive. The thermos-sensitive pores is the primarily factor influencing the fluid transport properties of the copolymer nanoporous membranes responsive to the environmental temperature.

8.2 Further works

To understand the structure and properties of the thermos-sensitive NIPAAM-g-PVDF copolymer membranes, the further work are proposed below.

1. The pore size distribution of the nanoporous NIPAAM-g-PVDF membranes is characterised by using mercury porosimetry which could only be operated at 20°C, therefore the change of the pore sizes of the thermos-sensitive NIPAAM-g-PVDF copolymers responding to the changes of the environmental temperatures could not be characterised currently. It would better establish an alternative method to enable the characterisation of the porous structure of the porous NIPAAM-g-PVDF membranes at 40°C.

2. The liquid chemical permeation properties of the thermo-sensitive NIPAAM-g-PVDF copolymer membranes have not yet been investigated at the temperature (e.g. at 40°C) above the LCST of NIPAAM. It would therefore be

interesting to investigate whether the NIPAAM-g-PVDF copolymer membranes have similar liquid chemical permeation properties at different environmental temperatures.

3. In this research, only *WVTR* of the nanoporous NIPAAM-g-PVDF membranes were investigated, thermal resistance (R_{ct}) and water vapour resistance (R_{et}) could not be analysed due to the limitation of the dimension of the copolymer membranes produced. The methods to produce the heat-pressed NIPAAM-g-PVDF membranes need to be improved to obtain the membranes of larger sizes to enable the investigation of the thermal resistance and water vapour resistance by using the sweating guard hotplate method.

4. PVDF polymer is used as the main barrier polymers to copolymerise with NIPAAM monomers to produce thermosensitive barrier copolymer membranes; however, PVDF is a fluorine polymer which might have potential environmental concern in future application, the copolymerisation of NIPAAM with other alternative barrier polymer materials to produce new thermosensitive copolymer membranes needs to be investigated.

5. It is shown in this research that the NIPAAM-g-PVDF copolymers obtained from different copolymerisation methods have different structure and properties, so alternative copolymerisation methods are worthy of investigated. For example, the following methods are worthy of being explored.

   (a) The NIPAAM and PVDF copolymerisation via atom transfer radical polymerization method is one of the copolymerisation methods which could be used to synthesis the NIPAAM-g-PVDF copolymer materials in the further work.

   (b) The plasma activation of PVDF polymers using various gases; for example, mixture of argon gas and oxygen gas, to activate porous PVDF membranes for copolymerisation with NIPAAM monomers to obtain alternative types of NIPAAM-g-PVDF copolymer membranes.

References

1. Wood, L., *Research and Markets: Global chemical protective clothing market 2015-2019: Key Vendors are 3M, Ansell, E.I. Du Pont De Nemours and Company, Honeywell International, Kimberley-Clark, Royal TenCate and Teijin Aramid*. [Online]. 2015. [Accessed 27/07/2015]; Available from: http://uk.reuters.com/article/2015/02/04/research-and-markets-idUKnBw046280a+100+BSW20150204.
2. Boopathi, M., B. Singh, and R. Vijayaraghavan, *A review on NBC body protective clothing.* The Open Textile Journal, 2008.
3. Stull, J.O., *Issues and challenges in chemical protective clothing.* Ergonomics of protective clothing, 2000: p. 222.
4. Koszewska, M., *Development prospects of Polish protective clothing market after 1 May 2004. Threats and opportunities'*. Fibres & Textiles in Eastern Europe, 2004. **12**(4): p. 48.
5. Schild, H.G., *Poly(N-isopropylacrylamide): experiment, theory and application.* Progress in Polymer Science, 1992. **17**(2): p.163-249.
6. Hu, J., H. Meng, G. Li and S.I. Ibekwe, *A review of stimuli-responsive polymers for smart textile applications.* Smart Materials and Structures, 2012. **21**(5): p.053001.
7. Crespy, D. and R.M. Rossi, *Temperature-responsive polymers with LCST in the physiological range and their applications in textiles.* Polymer, 2007. **56**: p.1461-1468.
8. Great Britain. Health and Safety Executive. Personal protective equipment at work: Personal Protective Equipment at Work Regulations 1992 (as amended). Sudbury: HSE Books, 2005.
9. Occupational Safety and Health Administration. OSHA Technical Manual in Section VIII: Chapter 1 Chemical Protective Clothing.
10. Truong, Q. and E. Wilusz, *Chemical and Biological Protection*. In Scott, R.A. ed. Textile for protection. Boca Raton:Woodhead Publishing; CRC, 2005.
11. Rock, M. Chemical Protective Fabric. US20060234573 A1. 2006.
12. Gopalakrishnan, D., M. Nithiyakumar, and A.Nayaket, Development of chemical protective clothing. [Online]. 2015. [Accessed 09/01/2015]. Available from: http://www.fibre2fashion.com/industry-article/1/85/development-of chemical -protective-clothing6.asp.
13. Schreuder-Gibson, L. Heidi, Q. Truong, J.E. Walker, J.R. Owens, J.D. Wander, and W.E. Jones, *Chemical and biological protection and detection in fabrics for protective clothing.* MRS Bulletin, 2003. **28**(08): p. 574-578.

14. Ishizaki, K., S. Komarneni, and M. Nanko, *Porous materials: process technology and applications*. 1998, Dordrecht; London: Kluwer Academic.
15. Ellis, L.F., *Chemical-resistant breathable textile laminate*. EP1757197 A2. 2007.
16. Mordecai, M. and J. Snedeker, *Protective coat for emergency responders*. US7921471 B2. 2011.
17. Sen, A.K., *Coated textiles: principles and applications.* 2001, Boca Raton, FL; London: Taylor & Francis.
18. Microgard Limited, *Microchem 4000*, 2011.
19. Todd, R.C., *Chemical protective clothing.* Occupational Health & Safety, 2001. **70**(8): p.36.
20. American Society for Testing and Materials, *ASTM F739 Standard test method for permeation of liquids and gases through protective clothing materials under conditions of continuous contact*. 2012, ASTM: Philadelphia.
21. National Fire Protection Association, *NFPA 1991: Standard on vapor-protective ensembles for hazardous materials emergencies*. 2005, NFPA.
22. American Society for Testing and Materials, *ASTM F903-10 Standard test method for resistance of materials used in protective clothing to penetration by liquids*. 2006, ASTM: Philadelphia.
23. National Fire Protection Association, *NFPA 1992 Standard on liquid splash-ensembles and clothing for hazardous materials emergencies*. 2005, NPFA.
24. Brouwer, D.H., R.J. Aitken, R. Oppl, and J.W. Cherrie, J.W., *Concepts of skin protection: considerations for the evaluation and terminology of the performance of skin protective equipment*. Journal of Occupational and Environmental hygiene, 2005. **2**(9): p.425-434.
25. British Standards Institute, *BS EN 340:1993: Protective clothing. General requirements*. 1993, BSI.
26. British Standards Institute, *BS EN 943-1:2002: Protective clothing against liquid and gaseous chemicals, aerosols and solid particles. Performance requirements for ventilated and non-ventilated "gas-tight" (Type 1) and "non-gas-tight" (Type 2) chemical protective suits*. 2002, BSI.
27. British Standards Institute, *BS EN ISO 13982-1:2004: Protective clothing for use against solid particulates. Performance requirements for chemical protective clothing providing protection to the full body against airborne solid particulates (type 5 clothing)*. 2005, BSI.
28. Lovasic, S., *Chemical Protective Clothing.* Chemical Engineering, 2011. **118**(3): p. 51-53.
29. Microgard Limited, *Microchem 2500*, 2011.
30. Microgard Limited, *Microchem 3000*, 2011.

31. DuPont, *Tyvek: Instructions for Use*, 2010.
32. DuPont, *Tychem F: Instructions for Us*e, 2010.
33. DuPont, *Tychem F2: Instructions for Use*, 2010.
34. DuPont, *Tychem C2: Instructions for Use*, 2010.
35. Microgard Limited, *Microgard Product Catalogue*, 2011.
36. DuPont, *DuPont Permeation Guide*. 2013.
37. Kissa, E., *Wetting and Wicking.* Textile Research Journal, 1996. **66**(10): p.660-668.
38. Deryagin, B.V. and N.V. Churaev, *Structure of water in thin layers.* Langmuir, 1987. **3**(5): p.607-612.
39. Wenzel, R.N., *Resistance of solid surfaces to wetting by water.* Industrial & Engineering Chemistry, 1936. **28**(8): p.988-994.
40. Cassie, A.B.D. and S. Baxter, *Wettability of porous surfaces.* Transactions of the Faraday Society, 1944. **40**: p.546-551.
41. Grundke, K., M. Nitschke, S. Minko, M. Stamm, C. Froeck, F. Simon, S. Uhlmann, K. Poschel, and M. Motornov, *Merging two concepts: Ultrahydrophobic polymer surfaces and switchable wettability.* Contact angle, Wettability and Adhesion, 2003. **3**: p.267-291.
42. British Standards Institute, *BS EN ISO 6529:2013: Protective clothing. Protection against chemicals. Determination of resistance of protective clothing materials to permeation by liquids and gases*. 2013, BSI.
43. Raheel, M., *Protective clothing systems and materials*. 1994, New York: Marcel Dekker.
44. Chao, K.P., P.H. Lee, and M.J. Wu, *Organic solvents permeation through protective nitrile gloves.* Journal of Hazardous Materials, 2003. **99**(2): p.191-201.
45. Mellström, G.A., *Comparison of chemical permeation data obtained with ASTM and ISO permeation test cells-I. the ASTM standard test procedure.* Annals of occupational hygiene, 1991. **35**(2): p.153-166.
46. Perkins, J.L. and M. You, *Predicting temperature effected on chemical protective clothing permeation.* American Industrial Hygiene Association Journal, 1992. **53**(2): p.77-83.
47. Guo, W., *Modelling of solubility parameters and permeation data of organix solvents in butyl gloves*. Ph.D. thesis, 2006, University of Akron.
48. Chao, K.P., J.S Lai, H.C. Lin, and Y.P. Hsu, *Comparison of permeability determined by permeation cell and immersion methods for organic solvents through protective gloves.* Polymer Testing, 2006. **25**(7): p.975-984.

49. Labruyère, C., G. Gorrasi, F. Monteverde, M. Alexandre, and P. Dubois, *Transport properties of organic vapours in silicone/clay nanocomposites.* Polymer, 2009. **50**(15): p.3626-3637.
50. Barton, A.F.M., *CRC handbook of solubility parameters and other cohesion parameters*. 1983, Boca Raton: CRC Press.
51. Hansen, C.M., *The universality of the solubility parameter.* Product R&D, 1969. **8**(1): p.2-11.
52. Reddy, K.K., T. Kawakatsu, J.B. Snape, and M. Nakajima, *Membrane concentration and separation of L-aspartic acid and L-phenylalanine derivatives in organic solvents.* Separation Science and Technology, 1996. **31**(8): p.1161-1178.
53. Gabler, W.J., *Adapting air sampling methods for the detection of toxic industrial chemicals on NFPA 1994 permeation resistance test*, MSc thesis, 2014, North Carolina University.
54. Perkins, J.L. and A.D. Tippit, *Use of three-dimensional solubility parameter to predict glove permeation.* American Industrial Hygiene Association Journal, 1985. **46**(8): p.455-459.
55. Seader, J.D. and E.J. Henley, *Separation process principles*. Vol. 2nd. 2006, Hoboken, N.J: Wiley.
56. Vahdat, N., *Permeation of protective clothing materials by methylene chloride and perchloroethylene.* American Industrial Hygiene Association Journal, 1987. **48**(7): p.646-651.
57. Chao, K.P., Y.P. Hsu, and S.Y. Chen, *Permeation of aromatic solvent mixtures through nitrile protective gloves.* Journal of Hazardous Materials, 2008. **153**(3): p.1059-1066.
58. Schwope, A.D., P.P. Costas, J.O. Jackson, Stull, J.O. and D.J. Weitzman, *Guidelines for the selection of chemical protective clothing*, In. Schwope, A.D. ed. Cincinnati, Ohio: American Conference of Governmental Industrial Hygienists. 1983.
59. Raheel, M., *Modern textile characterization methods*. 1996: Taylor & Francis.
60. British Standards Institute, *BS EN ISO 6530:2005: Protective clothing. Protection agaist liquid chemicals. Test method for resistance of materials to penetration by liquids*. 2005, BSI.
61. American Society for Testing and Materials, *ASTM International technical committee F23 on personal protective clothing and equipment*. 1977, ASTM.
62. Stull, J.O., D.F. White, and T.C. Greimel, *A comparison of the liquid penetration test with other chemical-resistance test and its application in determining the performance if protective clothing.* Performance of Protective Clothing : Fourth Volume, 1992. **1133**: p.123-140.

63. British Standard Institute, *BS ISO 13994:1998 Clothing for protection against liquid chemicals-Determination of the resistance of protective clothing materials to penetration by liquids under pressure*. 1999, BSI: London.
64. Stull, J.O., *Considerations for design and selection of chemical-protective clothing.* Journal of Hazardous Materials, 1987. **14**(2): p.165-189.
65. British Standards Institute, *BS EN 374-3:2003: Protective gloves against chemicals and micro-organisms. Determination of resistance to permeation by chemicals*. 2003, BSI: London.
66. American Society for Testing and Materials, *ASTM F1383 Standard test method for permeation of liquids and gases through protective clothing materials under conditions of intermittent contact*. 2012, ASTM: Philadelphia.
67. American Society for Testing and Materials, *ASTM F1407 Standard test method for resistance of chemical protective clothing materials to liquid permeation-permeation cup method*. 1999, ASTM: Philadelphia.
68. American Society for Testing and Materials, *ASTM D5886 Standard guide for selection of test methods to determine rate of fluid permeation through geomembranes for specific applications*. 2011, ASTM: Philadelphia.
69. Stull, J.O., *Civillain protection and protection of inductrial workers from chemicals*. In Scott, R.A. ed. Textile for protection. Boca Raton:Woodhead Publishing; CRC, 2005.
70. British Standards Institute, *BS EN 14325:2004 Protective clothing against chemicals-Test methods and performance classification of chemical protective clothing materials, seams, joins and assemblages*. 2004, BSI: London.
71. British Standards Institute, *BS EN ISO 7730:2005: Ergonomics of the thermal environment. Analytical determination and interpretation of thermal comfort using calculation of the PMV and PPD indices and local thermal comfort criteria*. 2006, BSI.
72. Fanger, P.O., *Thermal comfort: analysis and applications in enivironmental engineering*. 1972, New York; London: McGraw-Hill Book Company.
73. Li, Y., *The science of clothing comfort.* Textile Progress, 2001. **31**(1): p.1-135.
74. Rissanen, S. and H. Rintamäki, *Thermal responses and physiological strain in men wearing impermeable and semipermeable protective clothing in the cold.* Ergonomics, 1997. **40**(2): p.141-150.
75. Arens, E. and H. Zhang, *The skin's role in human thermpregulation and comfort*, In N. Pan and P. Gibson, ed. Thermal and moisture transport in fibrous materials. CRC Press; Woodhead: Cambridge. 2006. p.560-597.
76. She, F. and L. Kong, *Theoretical investigation of heat and moisture transfer through porous textile materials.* Research Journal of Textile and Clothing, 2000. **4**(1): p.37-41.

77. Den Hartog, E., G. Havenith, and S. Martini, *Heat stress in chemical protective clothing: porosity and vapour resistance.* Ergonomics, 2011. **54**(5): p.497-507.
78. Lotens, W.A., F.J.G. Van De Linde, and G. Havenith, *Effects of condensation in clothing on heat transfer.* Ergonomics, 1995. **38**(6): p.1114-1131.
79. Holmer, I., *Protective clothing and heat stress.* Ergonomics, 1995. **38**(1): p.166 -182.
80. Sybilska, W. and R. Korycki, *Analysis of coupled heat and water vapour transfer in textile laminates with a membrane.* Fibres & Textiles in Eastern Europe, 2010. **18**(3): p.65-69.
81. Incropera, F.P., *Introduction to heat transfer*. Vol. 5. 2007, Hoboken: Wiley.
82. Lee, S.C., *Effect of fiber orientation on thermal radiation in fibrous media.* International Journal of Heat and Mass Transfer, 1989. **32**(2): p.311-319.
83. Gretton, J.C., D.B. Brook, H.M. Dyson, and S.C. Harlock, *Moisture vapor transport through waterproof breathable fabrics and clothing systems under a temperature gradient.* Textile Research Journal, 1998. **68**(12): p.936-941.
84. Zheng, Q., B. Yu, S. Wang, and L. Luo, *A diffusivity model for gas diffusion through fractal porous media.* Chemical Engineering Science, 2012. **68**(1): p.650-655.
85. Prahsarn, C., R.L. Barker, and B.S. Gupta, *Moisture vapor transport behavior of polyester knit fabrics.* Textile Research Journal, 2005. **75**(4): p.346-351.
86. Lee, S. and S.K. Obendorf, *Barrier effectiveness and thermal comfort of protective clothing materials.* The Journal of The Textile Institute, 2007. **98**(2): p.87-98.
87. Branson, D.H., J.O. Dejonge, and D. Munson, *Thermal response associated with prototype pesticide protective clothing.* Textile Research Journal, 1986. **56**(1): p.27-34.
88. W.L. Gore & Associates Inc., *Protection you can wear*. Elkton 2005.
89. Rissanen, S., I. Jousela, and H. Rintamaki. *Impact of NBC protective clothing on the performance of medical task in warm and cool environmentals*. The 13th International conference on environmental ergonomics. 2009. Boston. p.108-112.
90. Avellini, B.A., *Physiological evaluation of chemical protective clothing*. 1983, DTIC Document.
91. British Standards Institute, *ISO 8301:1991 Thermal insulation. Determination of steady-state thermal resistance andrelated properties. Heat flow meter apparatus*. 1991, BSI.
92. British Standards Institute, *ISO 8302:1991 Thermal insulation. Determination of steady-state thermal resistance and related properties. Guarded hot plate apparatus*. 1991, BSI.

93. American Society for Testing and Materials, *ASTM C177 Standard test method for steady-state heat flux measurements and thermal transmission properties by means of the guarded-hot-plate apparatus*. 2013, ASTM: Philadelphia.
94. American Society for Testing and Materials, *ASTM C518 Standard Test Method for Steady-State Thermal Transmission Properties by Means of the Heat Flow Meter Apparatus*. 2010, ASTM: Philadelphia.
95. British Standards Institute, *BS EN ISO 11092:2014: Textiles. Physiological effects. Measurement of thermal and water-vapour resistance under steady-state conditions (sweating guarded-hotplate test)*. 2014, BSI.
96. American Society for Testing and Materials, *ASTM E96 Standard Test Methods for Water Vapor Transmission of Materials*. 2014, ASTM: Philadelphia.
97. British Standards Institute, *BS 7209:1990: Specification for water vapour permeable apparel fabrics*. 1990, BSI.
98. British Standards Institute, *BS EN ISO 15496:2004: Textiles. Measurement of water vapour permeability of textiles for the purpose of quality control*. 2004, BSI.
99. Jianhua, H. and Q. Xiaoming, *Comparison of test methods for measuring water vapor permeability of fabrics.* Journal of Textile Research, 2008. **29**(8): p.45-47.
100. Gibson, P., C. Kendrick, D. Rivin, L. Sicuranza, and M. Charmchi, *An automated water vapor diffusion test method for fabrics, laminates, and films.* Journal of Industrial Textiles, 1995. **24**(4): p.322-345.
101. McCullough, E.A., M. Kwon, and H. Shim, *A comparison of standard methods for measuring water vapour permeability of fabrics.* Measurement Science and Technology, 2003. **14**(8): p.1402.
102. Zhong, W. and N. Pan, *Development in clothing protection technology*. In Pan, N. and G. Sun, ed. Functional smart textiles using stimuli-sensitive polymers. Woodhead publishing: Oxford, 2011.
103. Gugliuzza, A. and E. Drioli, *A review on membrane engineering for innovation in wearable fabrics and protective textiles.* Journal of Membrane Science, 2013. **446**(0): p.350-375.
104. Gorey, C. and I.C. Escobar, *N-isopropylacrylamide (NIPAAM) modified cellulose acetate ultrafiltration membranes.* Journal of Membrane Science, 2011. **383**(1-2): p.272-279.
105. Iwata, H. M. Oodate, Y. Uyama, H. Amemiya, and Y. Ikada, *Preparation of temperature-sensitive membranes by graft polymerization onto a porous membrane.* Journal of Membrane Science, 1991. **55**(1-2): p.119-130.
106. Okano, M.N.T. and F.M. Winnik, *Poly (N-isopropylacrylamide)-based smart surfaces for cell sheet tissue engineering.* Material Matters, 2010. **5**: p.56.

107. Agrawal A.K. and M. Jassal, *Functional smart textiles using stimuli-sensitive polymers*. In Pan, N. and G. Sun, ed. Functional smart textiles using stimuli-sensitive polymers. Woodhead publishing: Oxford. 2011.
108. Huang, J., Z. Huang, Y. Bao and Z. Weng, *Thermosensitive poly(N-isopropylacrylamide-co-acrylonitrile) hydrogels with rapid response.* Chinese Journal of Chemical Engineering, 2006. **14**(1): p.87-92.
109. Park, C.W., S.M. Cho, and B.K. Kim, *Synthesis and properties of thermosensitive polyurethane-b-poly(N-isopropyl acrylamide).* Reactive & Functional Polymers, 2006. **66**(6): p.585-591.
110. Pan, Y.V., R.A. Wesley, R. Luginbuhl, D.D. Denton, and B.D. Ratner, *Plasma polymerized N-isopropylacrylamide: Synthesis and characterization of a smart thermally responsive coating.* Biomacromolecules, 2001. **2**(1): p.32-36.
111. Wang, X.L. and M.G. McCord, *Grafting of poly(N-isopropylacrylamide) onto nylon and polystyrene surfaces by atmospheric plasma treatment followed with free radical graft copolymerization.* Journal of Applied Polymer Science, 2007. **104**(6): p.3614-3621.
112. Kim, S.Y., T. Kanamori, and T. Shinbo, *Preparation of thermal-responsive poly(propylene) membranes grafted with N-isopropylacrylamide by plasma-induced polymerization and their permeation.* Journal of Applied Polymer Science, 2002. **84**(6): p.1168-1177.
113. Chen, K.S., J.C. Tsai, C.W. Chou, M.U. Yang, and J.M. Yang, *Effects of additives on the photo-induced grafting polymerization of N-isopropylacrylamide gel onto PET film and PP nonwoven fabric surface.* Materials Science and Engineering: C, 2002. **20**(1): p.203-208.
114. Xie, R., L.Y. Chu, W.M. Chen, W. Xiao, H.D. Wang, and J.B. Qu, *Characterization of microstructure of poly(N-isopropylacrylamide)-grafted polycarbonate track-etched membranes prepared by plasma-graft pore-filling polymerization.* Journal of Membrane Science, 2005. **258**(1–2): p.157-166.
115. Gupta, B., S. Mishra, and S. Saxena, *Preparation of thermosensitive membranes by radiation grafting of acrylic acid/N-isopropyl acrylamide binary mixture on PET fabric.* Radiation Physics and Chemistry, 2008. **77**(5): p.553-560.
116. Ying, L., E.T. Kang, and K.G. Neoh, *Characterization of membranes prepared from blends of poly(acrylic acid)-graft-poly(vinylidene fluoride) with poly(N-isopropylacrylamide) and their temperature- and pH-sensitive microfiltration.* Journal of Membrane Science, 2003. **224**(1-2): p.93-106.
117. Ueberschlag, P., *PVDF piezoelectric polymer.* Sensor Review, 2001. **21**(2): p. 118-125.
118. Zhao, Y.H., B.K. Zhu, X.T. Ma, and Y.Y. Xu, *Porous membranes modified by hyperbranched polymers: I. Preparation and characterization of PVDF*

membrane using hyperbranched polyglycerol as additive. Journal of Membrane Science, 2007. **290**(1-2): p.222-229.

119. Nunes, J.S., A. Wu, J. Gomes, V. Sencadas, P. M. Vilarinho, and S. Lanceros-Méndez, *Relationship between the microstructure and the microscopic piezoelectric response of the α- and β-phases of poly(vinylideneisopropanol fluoride).* Applied Physics A, 2009. **95**: p.875-880.
120. Branciforti, M.C., Sencadas, V. Lanceros-Mendez, S. and Gregorio, R., *New technique of processing highly oriented poly(vinylidene fluoride) films exclusively in the β phase.* Journal of Polymer Science Part B: Polymer Physics, 2007. **45**(19): p.2793-2801.
121. Sencadas, V., R. Gregorio, and S. Lanceros-Mendez, *to β Phase Transformation and Microestructural Changes of PVDF Films Induced by Uniaxial Stretch.* Journal of Macromolecular Science, Part B: Physics, 2009. **48**(3): p.514-525.
122. Lushcheĭkin, G., *New polymer-containing piezoelectric materials.* Physics of the Solid State, 2006. **48**(6): p.1023-1025.
123. Huang, S.I. and H. Chen, *Study on the improvement of hydrophobicity of PVDF films.* Journal of Thermoplastic Composite Materials, 2010: p.1-8.
124. Kuo, C.Y. H.N. Lin, H.A. Tsaia, D.M. Wang, and J.Y. Lai, *Fabrication of a high hydrophobic PVDF membrane via nonsolvent induced phase separation.* Desalination, 2008. **233**(1-3): p.40-47.
125. Zheng, Z., Z.Gu, R. Huo, and Y.Ye , *Superhydrophobicity of polyvinylidene fluoride membrane fabricated by chemical vapor deposition from solution.* Applied Surface Science, 2009. **255**(16): p.7263-7267.
126. Han, S., W.K. Choi, K. H. Yoon, and S.K. Koh., *Surface reaction on polyvinylidenefluoride (PVDF) irradiated by low energy ion beam in reactive gas environment.* Journal of Applied Polymer Science, 1999. **72**(1): p.41-47.
127. Oh, S.J., N. Kim, and Y.T. Lee, *Preparation and characterization of PVDF/TiO2 organic-inorganic composite membranes for fouling resistance improvement.* Journal of Membrane Science, 2009. **345**(1-2): p.13-20.
128. Zhang, M.G., Q.T. Nguyen, and Z. Ping, *Hydrophilic modification of poly (vinylidene fluoride) microporous membrane.* Journal of Membrane Science, 2009. **327**(1-2): p.78-86.
129. Braesch-Andersen, S., *PVDF membrane*. 2007. U.S. Patent US8,859,219 B2.
130. Joseph, R., R. Shelma, A. Rajeev, and C.V. Muraleedharan, *Characterization of surface modified polyester fabric.* Journal of Materials Science-Materials in Medicine, 2009. **20**: p.153-159.

131. Choi, S. and Z. Jiang, *A novel wearable sensor device with conductive fabric and PVDF film for monitoring cardiorespiratory signals.* Sensors and Actuators A: Physical, 2006. **128**(2): p.317-326.
132. Liu, Q., Z.Zhu, , X. Yang, X. Chen, and Y. Song, *Temperature-sensitive porous membrane production through radiation co-grafting of NIPAAm on/in PVDF porous membrane.* Radiation Physics and Chemistry, 2007. **76**(4): p.707-713.
133. Guo, Y., X. Feng, L. Chen, Y. Zhao, and J. Bai, *Influence of the coagulation-bath temperature on the phase-separation process of poly(vinylidene fluoride)-graft-poly(N-isopropylacrylamide) solutions and membrane structures.* Journal of Applied Polymer Science, 2010. **116**(2): p. 1005-1009.
134. Ebnesajjad, S. and P.R. Khaladkar, *Properties of neat (unfilled) and filled fluoropolymers*, in *Fluoropolymers Applications in the Chemical Processing Industries*, S.E.R. Khaladkar, ed. 2004, William Andrew Publishing: Norwich, NY. p.15-115.
135. Fargere, T., M. Abdennadher, M. Delmas and B. Boutevin, *Synthesis of graft polymers from an ozonized ethylene vinyl acetate copolymer (EVA). I. Study of the radical polymerization of styrene initiated by an ozonized EVA.* Journal of Polymer Science Part A: Polymer Chemistry, 1994. **32**(7): p.1377-1384.
136. Pacetti, S.D. and S.F.A. Hossainy, *Functionalised chemically inert polymers for coatings*. 2013. U.S. Patent 8,021,676.
137. Liu, Y., J.Y. Lee, E.T. Kang, P. Wang, and K.L. Tan, *Synthesis, characterization and electrochemical transport properties of the poly(ethyleneglycol)-grafted poly(vinylidenefluoride) nanoporous membranes.* Reactive and Functional Polymers, 2001. **47**(3): p.201-213.
138. Inagaki, N., *Plasma surface modification and plasma polymerization*. 1996: CRC Press.
139. Bryjak, M., I. Gancarz, and K. Smolinska, *Plasma nanostructuring of porous polymer membranes.* Advances in Colloid and Interface Science, 2010. **161**(1): p.2-9.
140. Arefi, F., V. Andre, P. Montazer-Rahmati and J. Amouroux, *Plasma polymerization and surface treatment of polymers.* Pure and applied chemistry, 1992. **64**(5): p.715-723.
141. Kull, K.R., M.L. Steen, and E.R. Fisher, *Surface modification with nitrogen-containing plasmas to produce hydrophilic, low-fouling membranes.* Journal of Membrane Science, 2005. **246**(2): p.203-215.
142. Biederman, H., *Plasma polymer films*. 2004, London: Imperial College Press.
143. Kaynak, A., T. Mehmood, X. J. Dai, K. Magniez and A. Kouzani, *Study of radio frequency plasma treatment of PVDF tilm using Ar, O_2 and (Ar + O_2) gases for improved polypyrrole adhesion.* Materials, 2013. **6**(8): p.3482-3493.

144. Momose, Y., M. Noguchi, and S. Okazaki, *Ar, O_2 and CF_4 plasma treatment of poly-(vinylidene fluoride), polyimide and polyamidoimide and its relationship to wettability.* Nuclear Instruments and Methods in Physics Research Section B: Beam Interactions with Materials and Atoms, 1989. **39**(1): p.805-808.
145. Pawde, S. and K. Deshmukh, *Surface characterization of air plasma treated poly vinylidene fluoride and poly methyl methacrylate films.* Polymer Engineering & Science, 2009. **49**(4): p.808-818.
146. Li, Y., L.Y. Chu, J.H. Zhu, H.D. Wang, S.L. Xia, and W.M. Chen, *Thermoresponsive gating gharacteristics of poly(N-isopropylacrylamide)-grafted porous poly(vinylidene fluoride) membranes.* Industrial & Engineering Chemistry Research, 2004. **43**(11): p.2643-2649.
147. Feng, X., Y. Guo, X. Chen, Y.Zhao, J.Li, X. He, and L. Chen, *Membrane formation process and mechanism of PVDF-g-PNIPAAm thermo-sensitive membrane.* Desalination, 2012. **290**(0): p.89-98.
148. Jian, C., L. Jiding, and C. Cuixian, *Surface modification of polyvinylidene fluoride (PVDF) membranes by low-temperature plasma with grafting styrene.* Plasma Science and Technology, 2009. **11**(1): p.42.
149. Mangindaan, D., I. Yared, H. Kurniawan, J.R. Sheu, and M.J. Wang, *Modulation of biocompatibility on poly(vinylidene fluoride) and polysulfone by oxygen plasma treatment and dopamine coating.* Journal of Biomedical Materials Research Part A, 2012. **100A**(11): p.3177-3188.
150. Boutevin, B., J.J. Robin, and A. Serdani, *Synthesis and applications of graft copolymers from ozonized poly(vinylidene fluoride)-II.* European Polymer Journal, 1992. **28**(12): p.1507-1511.
151. Wang, W.Y. and L. Chen, *"Smart" membrane materials: Preparation and characterization of PVDF-g-PNIPAAm graft copolymer.* Journal of Applied Polymer Science, 2007. **104**(3): p.1482-1486.
152. Zhao, Y., H. Zhao, L. Chen, X. Feng, Q. Zhang, J. Wang, and R. Zhang, *Thermo-responsive modification and properties study of PVDF flat membrane.* Journal of Polymer Research, 2013. **20**(1): p.1-8.
153. Lin, X.K., X. Feng, L. Chen, and Y.P. Zhao, *Characterization of temperature-sensitive membranes prepared from poly(vinylidene fluoride)-graft-poly(N-isopropylacrylamide) copolymers obtained by atom transfer radical polymerization.* Frontiers of Materials Science in China, 2010. **4**(4): p.345-352.
154. Ke, Z., B. Dai, L. Li, G. Yan, and D. Zhou, *Thermoresponsive surface prepared by atom transfer radical polymerization directly from poly(vinylidene fluoride) for control of cell adhesion and detachment.* Journal of Applied Polymer Science, 2010. **115**(2): p.976-980.

155. Akerman, S., P. Viinikka, B. Svarfvar, K. Putkonen, K. Järvinen, K. Kontturi, J. Näsman, A. Urtti, and P.Paronen, *Drug permeation through a temperature-sensitive poly(N-isopropylacrylamide) grafted poly(vinylidene fluoride) membrane.* International Journal of Pharmaceutics, 1998. **164**(1-2): p.29-36.
156. Van Herk, A.M. and M. Monteiro, *Heterogeneous Systems*, in *Handbook of Radical Polymerization*. 2003, John Wiley & Sons, Inc. p.301-331.
157. Ying, L., E.T. Kang, and K.G. Neoh, *Synthesis and characterization of poly(N-isopropylacrylamide)-graft-poly(vinylidene fluoride) copolymers and temperature-sensitive membranes.* Langmuir, 2002. **18**(16): p.6416-6423.
158. Ying, L., E. T. Kang, K. G. Neoh, K. Kato and H. Iwata, *Novel Poly(N-isopropylacrylamide)-graft-poly(vinylidene fluoride) copolymers for temperature-sensitive microfiltration membranes.* Macromolecular Materials and Engineering, 2003. **288**(1): p.11-16.
159. Ying, L., E. T. Kang, K. G. Neoh, K. Kato and H. Iwata, *Drug permeation through temperature-sensitive membranes prepared from poly(vinylidene fluoride) with grafted poly(N-isopropylacrylamide) chains.* Journal of Membrane Science, 2004. **243**(1–2): p.253-262.
160. Xie, R., Y. Li, and L.Y. Chu, *Preparation of thermo-responsive gating membranes with controllable response temperature.* Journal of Membrane Science, 2007. **289**(1–2): p.76-85.
161. Chen, K.S., S.C. Liao, S.W.Lin, S.H. Tsao, T.H.Ting, N. Inagaki, H.M. Wu, and W.Y. Chen, *The film deposition via atmospheric pressure plasma from ethanol and He mixing gases.* Surface and Coatings Technology, 2013. **231**(0): p.408-411.
162. Kuo, Y.L., K.H. Chang, T.S. Hung, K.S. Chen, and N.Inagaki, *Atmospheric-pressure plasma treatment on polystyrene for the photo-induced grafting polymerization of N-isopropylacrylamide.* Thin Solid Films, 2010. **518**(24): p.7568-7573.
163. Chu, L.Y., T. Niitsuma, T. Yamaguchi, and S.Nakao, *Thermoresponsive transport through porous membranes with grafted PNIPAM gates.* AIChE Journal, 2003. **49**(4): p. 896-909.
164. Mulder, M., *Basic principles of membrane technology*. 1996, Dordrecht; London: Kluwer Academic.
165. Madaeni, S.S. and A.H. Taheri, *Effect of casting solution on morphology and performance of PVDF microfiltration membranes.* Chemical Engineering & Technology, 2011. **34**(8): p.1328-1334.
166. Wang, X., L. Zhang, D. Sun, Q. An, and H. Chen, *Effect of coagulation bath temperature on formation mechanism of poly(vinylidene fluoride) membrane.* Journal of Applied Polymer Science, 2008. **110**(3): p.1656-1663.

167. Thürmer, M.B., P. Poletto, M. Marcolin, J. Duarte, and M. Zeni, *Effect of non-solvents used in the coagulation bath on morphology of PVDF membranes.* Materials Research, 2012. **15**: p.884-890.
168. Rendle, D.F., *A guide to materials characterisation and chemical analysis.* Journal of Applied Crystallography, 1991. **24**(3): p.265-266.
169. Smith, R.M., *Understanding mass spectra: a basic approach*. 2004, New York; Chichester: Wiley-Interscience.
170. Lavagnini, I., *Quantitative applications of mass spectrometry*. 2006, Chichester: John Wiley.
171. Seah, M.P., I.S. Gilmore, and S.J. Spencer, *Quantitative XPS: I. Analysis of X-ray photoelectron intensities from elemental data in a digital photoelectron database.* Journal of Electron Spectroscopy and Related Phenomena, 2001. **120**(1–3): p.93-111.
172. Balcı, M., *Basic ^{1}H- and ^{13}C-NMR spectroscopy*. 2005, Amsterdam; London: Elsevier.
173. Malz, F. and H. Jancke, *Validation of quantitative NMR.* Journal of Pharmaceutical and Biomedical Analysis, 2005. **38**(5): p.813-823.
174. Mao, N. and S.J. Russell, *Characterisation, testing and modelling of nonwoven fabrics*. In S.J. Russell, ed. Handbook of nonwovens. CRC Press: Boca Raton, Fla; Cambridge, 2007.
175. Giesche, H., *Mercury porosimetry: a general (practical) overview.* Particle & particle systems characterization, 2006. **23**(1): p.9-19.
176. Kong, Y. and J.N. Hay, *The measurement of the crystallinity of polymers by DSC.* Polymer, 2002. **43**(14): p.3873-3878.
177. Stuart, B.H., *Polymer Analysis*. 2008: Wiley.
178. Gorji, M., A.A.A. Jeddi, and A.A. Gharehaghaji, *Fabrication and characterization of polyurethane electrospun nanofiber membranes for protective clothing applications.* Journal of Applied Polymer Science, 2012. **125**(5): p.4135-4141.
179. Schick, C., *Differential scanning calorimetry (DSC) of semicrystalline polymers.* Analytical and Bioanalytical Chemistry, 2009. **395**(6): p.1589-1611.
180. Teyssedre, G., A. Bernes, and C. Lacabanne, *Influence of the crystalline phase on the molecular mobility of PVDF*. Journal of Polymer Science Part B: Polymer Physics, 1993. **31**(13): p.2027-2034.
181. Palacio, L., P. Prádanos, J.I. Calvo, and A. Hernández, *Porosity measurements by a gas penetration method and other techniques applied to membrane characterization.* Thin Solid Films, 1999. **348**(1-2): p.22-29.

182. Webb, P.A., *An introduction to the physical characterization of materials by mercury intrusion porosimetry with emphasis on reduction and presentation of experimental data.* 2001.
183. British Standards Institute, *BS 12154:2014 Determination of density by volumetric displacement. Skeleton density by gas pycnometry*. 2014, BSI.
184. British Standards Institute, *BS 2782-6 Method 630A:1994, ISO 4593:1993: Methods of testing plastics. Dimensional properties. Determination of thickness by mechanical scanning of flexible sheet*. 1994, BSI.
185. British Standards Institute, *BS 2471:2005 Textiles. Woven fabrics. Determination of mass per unit length and mass per unit area*. 2005, BSI.
186. Mazzuchetti, G., G. Lopardo, and R. Demichelis, *Influence of nonwoven fabrics' physical parameters on thermal and water vapor resistance.* Journal of Industrial Textiles, 2007. **36**(3): p.253-264.
187. Shabaridharan and A. Das, *Study on heat and moisture vapour transmission characteristics through multilayered fabric ensembles.* Fibers and Polymers, 2012. **13**(4): p.522-528.
188. Wexler, A., *Vapor pressure formulation for water in range 0 to 100℃. A revision.* Journal of Research of the National Bureau of Standards, 1976. **80**: p.775-785.
189. Gibson, P.W., *Effect of temperature on water vapor transport through polymer membrane laminates.* Polymer Testing, 2000. **19**(6): p.673-691.
190. Huang, J. and Y. Chen, *Effect of environmental parameters on water vapor transfer of fabrics.* The Journal of The Textile Institute, 2010. **102**(1): p.50-56.
191. Korson, L., W. Drost-Hansen, and F.J. Millero. *Viscosity of water at various temperatures*. The Journal of Physical Chemistry, 1969. 73(1): p.34-39.
192. Chatterjee, P.K. and B.S. Gupta, *Absorbent technology*. Vol. 13. 2002, Amsterdam; Oxford: Elsevier Science.
193. Huang, R.Y. and V.J. Lin, *Separation of liquid mixtures by using polymer membranes. I. Permeation of binary organic liquid mixtures through polyethylene.* Journal of Applied Polymer Science, 1968. **12**(12): p.2615-2631.
194. Powell, S. and B. Vernon, *Localized delivery system for phenstatin using n-isopropylacrylamide*. 2004, US 20040052761 A1
195. Du, M., *The thermal insulation properties of a flexible methyltrimethoxysialne (MTMS) based silicone aerogel and its application on aerogel-spacer fabric composites*, Ph.D. thesis. 2014, University of Leeds.
196. Cao, J.H., B. Zhu, D. Zuo, Y. Xu, and J. Li, *Microporous PVDF-HFP based polymer membranes formed from supercritical CO_2 induced phase seperation.* Chinese Journal of Polymer Science, 2008. **26**(01): p.13-21.

197. Suzuki, H. and K. Naoi, *Fabrication processes for electrodes for electrochemical devices, and electrochemical device fabrication process*. 2011, TDK Corporation.
198. Ferro, L., O. Scialdone, and A. Galia, *Preparation of pH sensitive poly(vinilydenefluoride) porous membranes by grafting of acrylic acid assisted by supercritical carbon dioxide.* The Journal of Supercritical Fluids, 2012. **66**(0): p.241-250.
199. Fargere, T., et al., *Determination of peroxides and hydroperoxides with 2,2-diphenyl-1-picrylhydrazyl (DPPH). Application to ozonized ethylene vinyl acetate copolymers (EVA).* European Polymer Journal, 1995. **31**(5): p.489-497.
200. Kedare, S.B. and R. Singh, *Genesis and development of DPPH method of antioxidant assay.* Journal of food science and technology, 2011. **48**(4): p.412-422.
201. Zhang, X., S. Heinonen, and E. Levanen, *Applications of supercritical carbon dioxide in materials processing and synthesis.* RSC Advances, 2014. **4**(105): p.61137-61152.
202. Montes, A., A. Tenorio, M. D. Gordillo, C. Pereyra, and E.J. Martinez de La Ossa, *Screening design of experiment applied to supercritical antisolvent precipitation of amoxicillin: Exploring new miscible conditions.* The Journal of Supercritical Fluids, 2010. **51**(3): p.399-403.
203. Wang, X. and M.G. McCord, *Grafting of poly(N-isopropylacrylamide) onto nylon and polystyrene surfaces by atmospheric plasma treatment followed with free radical graft copolymerization.* Journal of Applied Polymer Science, 2007. **104**(6): p.3614-3621.
204. Sun, B., Y. Lin, and P. Wu, *Structure analysis of poly (N-isopropylacrylamide) using near-infrared spectroscopy and generalized two-dimensional correlation infrared spectroscopy.* Applied spectroscopy, 2007. **61**(7): p.765-771.
205. Hu, J.L., B.H. Liu, and W.G. Liu, *Temperature/pH dual sensitive N-isopropylacrylamide/polyurethane copolymer hydrogel-grafted fabrics.* Textile research journal, 2006. **76**(11): p.853-860.
206. Barth, A. and C. Zscherp, *What vibrations tell about proteins.* Quarterly Reviews of Biophysics, 2002. **35**(04): p.369-430.
207. Lanceros-Méndez, S., J. F. Mano, A. M. Costa, and V. H. Schmidt, *FTIR and DSC studies of mechanically deformed β-PVDF films.* Journal of Macromolecular Science, Part B, 2001. **40**(3-4): p.517-527.
208. Shivapooja, P., L.K. Ista, H.E. Canavan, and G.P. Lopez, *ARGET–ATRP synthesis and characterization of PNIPAAm brushes for quantitative cell detachment studies.* Biointerphases, 2012. **7**(1-4): p.1-9.

209. Everett, D., *Manual of symbols and terminology for physicochemical quantities and units, Appendix II: Definitions, terminology and symbols in colloid and surface chemistry*. Pure and Applied Chemistry, 1972. 31(4): p.577-638.
210. British Standards Institute, *BS ISO 9277:2010: Determination of the specific surface area of solids by gas adsorption. BET method*. 2010, BSI.
211. British Standards Institute, *BS EN 828:2013: Adhesives. Wettability. Determination by measurement of contact angle and surface free energy of solid surface*. 2013, BSI.
212. Buonomenna, M. G., P. Macchi, M. Davoli, and E. Drioli, *Poly(vinylidene fluoride) membranes by phase inversion: the role the casting and coagulation conditions play in their morphology, crystalline structure and propertie*s. European Polymer Journal, 2007. 43(4): p.1557-1572.
213. Kuo, C., H. Lin, H. Tsai, D. Wang, and J. Lai, *Fabrication of a high hydrophobic PVDF membrane via nonsolvent induced phase separation*. Desalination, 2008. 233(1-3): p.40-47.
214. Yeow, M.L., Y.T. Liu, and K. Li, *Morphological study of poly(vinylidene fluoride) asymmetric membranes: Effects of the solvent, additive, and dope temperature*. Journal of Applied Polymer Science, 2004. 92(3): p.1782-1789.
215. Cao, J., H. Zhang, W. Xu, and X. Li, *Poly(vinylidene fluoride) porous membranes precipitated in water/ethanol dual-coagulation bath: The relationship between morphology and performance in vanadium flow battery*. Journal of Power Sources, 2014. 249(0): p. 84-91.
216. Cardoso, V.F., G. Minas, C. M. Costa, C. J. Tavares, and S. Lanceros-Mendez, *Micro and nanofilms of poly(vinylidene fluoride) with controlled thickness, morphology and electroactive crystalline phase for sensor and actuator applications.* Smart Materials and Structures, 2011. **20**(8): p.087002.
217. Ooi, B.S., N.S.M. Yatim, A.L. Ahmad, and S.O. Lai, *Preparation of polyvinylidene fluoride membrane via dual coagulation bath system and its wettability study.* Journal of Applied Polymer Science, 2012. **124**(S1): p.E225-E232.
218. Holmes, J.L., C. Aubry, and P.M. Mayer, *Assigning structures to ions in mass spectrometry*. 2007, Boca Raton: CRC Press.
219. Lanceros-Mendez, S., V.J.G. Da Silva, and R.G. Filho, *Non-Porous Polyvinylidene Fluoride (Pvdf) Films in the Beta Phase and Processing Method Thereof*. 2008, EP 1913082.
220. British Standards Institute, *BS ISO 15901-1:2005: Pore size distribution and porosity of solid materials by mercury porosimetry and gas adsorption. Mercury porosimetry*. 2006, British Standards Institute.

221. Platzer, N., *Encyclopedia of PVC.* Journal of Polymer Science Part C: Polymer Letters, 1988. **26**(6): p.273-273.
222. Arndt, K.F., D. Kuckling, and A. Richter, *Application of sensitive hydrogels in flow control*. Polymers for Advanced Technologies, 2000. **11**(8-12): p.496-505.
223. Lide, D.R. *CRC Handbook of chemistry and physics: A Ready-reference book of chemical and physical data*. CRC-Press, 1995.
224. Smallwood, I.M. Handbook of organic solvent properties. New York;London: Arnold, 1996.
225. Bottino, A., G. Camera-Roda, G. Capannelli, and S. Munari, *The formation of microporous polyvinylidene difluoride membranes by phase separation.* Journal of Membrane Science, 1991. **57**(1): p.1-20.
226. Taşdelen, B., N. Kayaman-Apohan, O. Güven, and B.M. Baysal, *Swelling and diffusion studies of poly(N-isopropylacrylamide/itaconic acid) copolymeric hydrogels in water and aqueous solutions of drugs.* Journal of Applied Polymer Science, 2004. **91**(2): p.911-915.
227. Gehrke, S., *Synthesis, equilibrium swelling, kinetics, permeability and applications of environmentally responsive gels*. In K. Dušek, ed. Responsive Gels: Volume Transitions II. Springer Berlin Heidelberg, 1993. p.81-144.
228. Solvey Solexis, *Solef® & Hylar® PVDF Polyvinylidene fluoride Design and Processing Guide*. [Online] 2006. Accessed 05/07/15]. Available from: https://www.equflow.com/sites/default/files/bijlagen/bestanden/ solef_ hylar_ 2009.pdf
229. Hansen, C.M., *Water transport and condensation in fluoropolymer films.* Progress in Organic Coatings, 2001. **42**(3-4): p.167-178.
230. Hansen, C.M. and L. Just, *Erratum to "Water transport and condensation in fluoropolymer films" [Prog. Org. Coat. 142 (2001) 167-178]*. Progress in Organic Coatings, 2002. **44**(3): p.259-259.
231. Bohrer, M.P., G.D. Patterson, and P.J. Carroll, *Hindered diffusion of dextran and ficoll in microporous membranes.* Macromolecules, 1984. **17**(6): p.1170-1173.
232. Smallwood, I.M. *Handbook of organic solvent properties*. New York; London: Arnold, 1996.
233. Galaev, I. and B. Mattiasson, *Smart Polymers for Bioseparation and Bioprocessing*. Taylor & Francis. 2001.